The Pennsylvania State University

The Graduate School

Department of Materials Science and Engineering

PHASE TRANSITIONS IN $Ag(Ta_XNb_{1-X})O_3$ THIN FILMS

A Dissertation in

Materials Science and Engineering

by

Raegan Johnson

Submitted in Partial Fulfillment
of the Requirements
for the Degree of

Doctor of Philosophy

December 2011

The dissertation of Raegan Johnson was reviewed and approved* by the following:

Susan Trolier-McKinstry
Professor of Ceramic Science and Engineering
Dissertation Advisor
Chair of Committee

Clive A. Randall
Professor of Materials Science and Engineering

L. Eric Cross
Professor of Electrical Engineering

Venkatraman Gopalan
Professor of Materials Science and Engineering

Ian M. Reaney
Professor of Materials Science and Engineering
University of Sheffield, Sheffield, UK
Special Member

Joan M. Redwing
Professor of Materials Science and Engineering
Chair of Intercollege Graduate Degree Program in Materials Science and Engineering

*Signatures are on file in the Graduate School

ABSTRACT

A large number of perovskite materials undergo cooperative rotations of the oxygen octahedral framework. To date, there has been relatively little work studying how strain might be used to modify these common phase transitions, especially in materials with complex tilt systems. This work aims to gain a fundamental understanding of the relationship between tilt and strain.

The first objective of this dissertation was to obtain structural details on relaxed epitaxial $Ag(Ta_xNb_{1-x})O_3$ (ATN) films. These results provided a baseline for measurements on strained films. $Ag(Ta_{0.5}Nb_{0.5})O_3$ films grown on (001) oriented $SrRuO_3/LaAlO_3$ and $LaAlO_3$ substrates were characterized by electron diffraction and high resolution X-ray diffraction (XRD). It was found that the ATN films exhibited octahedral rotations characteristic of the *Pbcm* space group, similar to those seen in bulk materials; however, the temperature of the M_3-M_2 phase transition was suppressed by ~250 K due to the fact that the correlation length for rotations about c_{pc} was significantly reduced (pc = pseudo-cubic). The average off-center B-cation displacements, which signify the degree of long-range order for these local cation positions, were negligibly small compared to bulk materials, as inferred from the near-zero intensity of the ¼(00*L*)-type reflections. On cooling, pronounced ordering of B-cation displacements occurred at ~60 K, which is significantly below bulk (~310 K). The onset of this ordering coincides with a broad maximum in relative permittivity as a function of temperature. It is believed that point and planar defects in thin ATN films disrupt the complex sequence of in-phase and anti-phase rotations around c_{pc}, thereby reducing the effective strength of interactions between the tilting and cation displacements.

The second objective was to perform structural studies on compressively strained $Ag(Ta_{0.5}Nb_{0.5})O_3$ films. Phase transitions in coherent $Ag(Ta_{0.5}Nb_{0.5})O_3$ films on $SrTiO_3$ (001) substrates were characterized by high resolution X-ray diffraction and transmission electron

microscopy. The compressively strained films were found to undergo the same phase transition sequence as bulk materials: cubic (C) ↔ tetragonal (T) ↔ orthorhombic (O) ↔ orthorhombic (M_3). However, the biaxial in-plane strain stabilized the tetragonal and orthorhombic phases, expanding these phase fields by a total of ~280 °C. The compressive strain state also favors domain states in which the *c*-axis is directed out-of-plane. Consequently, unit cell quadrupling in the M_3 phase and the in-phase tilt of the T phase both occur around the out-of-plane direction. In contrast, bulk materials and relaxed films are poly-domain, with the complex tilt system occurring along all three of the orthogonal axes. Compressively strained films are in the M_3 phase at room temperature rather than in the M_2 phase as is observed in bulk. These results demonstrate unambiguously that strain engineering in systems with *complex* tilt sequences such as $Ag(Ta_{0.5}Nb_{0.5})O_3$ is feasible and open up the possibility of modifying properties by manipulation of the pertinent octahedral tilt transition temperature in a wide range of functional ceramics.

The third objective was to examine coherent $Ag(Ta_{0.5}Nb_{0.5})O_3$ films under tensile strain that had been deposited on $(Ba_{0.4}Sr_{0.6})TiO_3/LaAlO_3$ (001) and $KTaO_3$ substrates. Unlike the poly-domain nature of bulk materials or relaxed films, these films exhibited a domain structure with the *c*-axis aligned primarily along the in-plane axes. In addition, it is believed that the tilt angle of the oxygen octahedra was significantly reduced, as was evidenced by the weaker superlattice reflection intensity. It was determined that films under tensile strain undergo the same phase transition sequence as bulk materials and other thin films. Similar to films under compressive strain, an expansion of the tetragonal and orthorhombic phase fields was observed in $ATN/(Ba_{0.4}Sr_{0.6})TiO_3/LaAlO_3$ due to the closer lattice match between the film and the pseudosubstrate in these temperature regimes. These films under tensile strain showed T and O phase fields that were collectively ~ 270 °C wider than that of bulk materials. In addition, it was found that the films were in the M_3 phase at room temperature rather than M_2 observed in bulk.

This work demonstrates that, in addition to compressive strain, tensile strain can be used to strain engineer materials with complex tilt systems and complicated phase transition sequences.

The fourth objective was to develop a measurement technique for the "roto"-electric effect and then test $AbNbO_3$ as a candidate rotoelectric. In perovskite materials, the tilting of the oxygen octahedra can lead to new symmetries that include such rotations. This, in turn, can introduce new properties related to these symmetries. For example, in the "roto"-electric effect the rotation of the oxygen octahedra is altered by an applied electric field. An experiment was developed to test this relationship using $AgNbO_3$ as a model system. The intensity of superlattice reflections were measured at the Advanced Photon Source as a function of electric field for a pure $AgNbO_3$ single crystal, a $(Ag_{0.95}Li_{0.05})NbO_3$ single crystal, and an $AgNbO_3$ thin film. Model calculations demonstrated that if the tilt angle was modified by the electric field, a change in superlattice peak intensity should have been observed. However, in the samples tested, no change was observed, suggesting that the octahedra in $AgNbO_3$ do not undergo a substantial change in tilt as a function of electric field. This experiment provides a foundation for similar measurements on other material systems.

TABLE OF CONTENTS

LIST OF FIGURES

LIST OF TABLES

ACKNOWLEDGEMENTS

First and foremost, I would like to thank my advisor Dr. Susan Trolier-McKinstry. I would have never accomplished this work without her help and guidance. I owe her my deepest gratitude for believing in me even when I didn't have the confidence to believe in myself.

I would like to thank my committee members, Dr. Clive Randall, Dr. L. Eric Cross, Dr. Venkat Gopalan, Dr. Ian Reaney, and Dr. Elizabeth Dickey for pushing the limits of my knowledge. Their advice and outside perspective was greatly appreciated.

I was fortunate to participate in a project that involved many collaborators. Having had the opportunity to work with such brilliant people was priceless. Much of the TEM work was performed by Drs. Ian Reaney and Yisong Han at the University of Sheffield. Their insight into the ATN system and knowledge and interpretation of the TEM data is greatly appreciated. Drs. Dillon Fong and Tim Fister at Argonne National Lab did a phenomenal job of introducing me to synchrotron X-ray diffraction experiments. An extra thank you goes to Dillon for patiently answering my questions regarding data analysis and interpretation. Lastly, I would like to thank Igor Levin at NIST for his TEM expertise and passion for the ATN system. His timely paper that provided gory details of bulk $AgNbO_3$ was a huge inspiration in this work.

I would like to thank the Advance Photon Source (APS) staff members, Jenia Karapetrova and Peter Baldo, for ensuring the experiments ran smoothly and quickly.

A special thanks goes to Dan Marincel, Dan Tinberg, Derek Wilke, and Charley Yeager who were willing to work long hours and often stay up all night taking measurements at APS. Most of the data in this dissertation could not have been obtained without their help.

I would also like to thank the MRL technical staff: Mark Angelone, Amanda Baker, Charley Cole, Maria DiCola, Bill Drawl, Pam Garito, Chris Jabco, Beth Jones, Maria Klimkiewicz, Tim Klinger, Jeff Long, Joe Lonjin, Paul Moses, Gaylord Shawver, Scott Stringer,

and Nichole Wonderling. Their knowledge was helpful and their patience appreciated. Thanks to Joanne Aller, Kathy Gummo, Donna Lucas, and Susie Sherlock for helping with the non-technical details that us scientists try to avoid.

Finally, I would like to thank the past and present group members of the STM group: Raja Bharadwaja, Patamas Bintachitt, Ichiro Fujii, Lauren Garten, Flavio Griggio, Eunki Hong, Ryan Keech, Song Won Ko, Sun Young Lee, Dan Marincel, Adarsh Rajashekhar, Dan Tinberg, Margeau Wallace, Aaron Welsh, Derek Wilke, Jung In Yang, Charley Yeager, Hong Goo Yeo, and Wanlin Zhu.

Funding for this work was obtained from the National Science Foundation (grants DMR-0602770 and DMR-0820404).

Chapter 1

Introduction

Many different A- and B-site cations can be accommodated in the perovskite ABO_3 structure, making it possible to synthesize a large number of solid solutions with this arrangement. Depending on the stoichiometry, perovskite materials have useful properties such as high permittivities and high piezoelectric constants, magnetism, pyroelectricity, metallic conductivity, and superconductivity. Industrial uses for materials with the perovskite structure include dielectric layers in capacitors, microwave dielectrics, infrared imagers, ultrasound transducers, ink-jet printers, fuel-injectors, and micro-positioners, among others.[1]

Although a large number of different cations can sit on the A- and B-sites of the perovskite structure, the relative sizes of these cations can induce distortions in the structure. For example, when the size A-site cation is too small for its interstice, the oxygen octahedra typically tilt or rotate in order to reduce the volume of the interstice. A number of technologically important perovskite structures undergo octahedral tilt; these include, but are not limited to, $Pb(Zr,Ti)O_3$, $SrTiO_3$, $(Na,Bi)TiO_3$, $LaAlO_3$, $LaNiO_3$, $SrRuO_3$, and $BiFeO_3$.[2] Tilt or rotation of the oxygen octahedra tends to occur when the Goldschmidt tolerance factor (Equation 1-1), is less than one.[2, 3]

$$t = \frac{r_A + r_O}{\sqrt{2}(r_B + r_O)}$$

Equation 1-1

Here, r_A is the ionic radius of the A-site cation, r_B is the ionic radius of the B-site cation and r_O is the radius of the oxygen ion.

As will be discussed in more detail in Chapter 2, rotation of the oxygen octahedra is coupled with strain in the lattice. The goal of this work is to understand the relationship between strain and octahedral tilt. Using thin films, a biaxial strain can be applied to a perovskite material at levels well above the cracking point of the bulk counterpart.[4] Typically, this is achieved by growing coherent films on substrates with similar lattice parameters. For films of sufficiently small thickness, biaxial strain levels up to a few percent can be tolerated. Such strains are often used to tune transition temperatures, including the paraelectric to ferroelectric transition temperature.[4-9] The work presented in this dissertation describes how the introduction of biaxial strain in $Ag(Ta_xNb_{1-x})O_3$ modifies the tilt system and tilt transition temperatures of the material. Through such strain engineering, it may be possible to manipulate octahedral rotations and the associated transition temperatures to produce devices with desired properties

1.1 Organization of dissertation

The material used in this study was $Ag(Ta_xNb_{1-x})O_3$ because it exhibits multiple tilt systems and undergoes a complex phase transition sequence as a function of temperature. Thin films of this material were studied to assess both the tilt system and phase transition temperature sequence as a function of strain. Chapter 2 will provide a detailed background of the perovskite structure and octahedral tilting. An in-depth look at the $Ag(Ta_xNb_{1-x})O_3$ system will also be provided. Here, differences between the phases will be detailed. An overview of current literature reporting on the relationship between strain and octahedral tilt will be discussed. Chapter 2 will conclude with the industrial uses for Ag $(Ta_xNb_{1-x})O_3$ materials. Chapter 3 outlines the experimental procedures used throughout this study. This includes synthesis of samples and the measurement techniques used. Chapter 4 discusses results on structural studies of relaxed

$Ag(Ta_{0.5}Nb_{0.5})O_3$ films on $LaAlO_3$ and $SrRuO_3/LaAlO_3$ substrates. The information in this chapter provides a baseline for the studies of films that are under biaxial compressive and tensile strain. Chapter 5 examines how the phase transitions in $Ag(Ta_{0.5}Nb_{0.5})O_3$ thin films are affected by compressive strain. In Chapter 6, tilt transitions in coherently strained films under tensile strain are discussed. Chapter 7 is devoted to search for a link between octahedral tilt and applied electric field, the so-called "roto-electric effect". Finally, Chapter 8 will provide conclusions for relaxed and coherently strained $Ag(Ta_xNb_{1-x})O_3$ films presented in this dissertation, as well as suggested future work.

Chapter 2

Background

This chapter will provide a background into octahedral tilting, and discuss why it occurs in perovskite structures and how tilting is related to strain. A review of recent research related to strain and octahedral tilt is also given. Then, a detailed look at the $Ag(Ta_xNb_{1-x})O_3$ system will follow. The chapter will conclude with a discussion of $Ag(Ta_xNb_{1-x})O_3$ as a functional material.

2.1 The perovskite structure and the oxygen octahedra

The perovskite structure has the general chemical formula ABO_3 and is shown in Figure 2-1a. The prototypical paraelectric phase typically observed at elevated temperatures has cubic $Pm\bar{3}m$ symmetry. In the cubic perovskite structure, the A-site cations (grey) sit at corners of the cube, the B-site cation (green) is located at the center of the cube and the oxygen atoms (red) occupy the face center positions. Oftentimes, the structure is viewed in terms of the polyhedra centered on the B-site cation. This is known as the oxygen octahedra and is shown in green in Figure 2-1b.

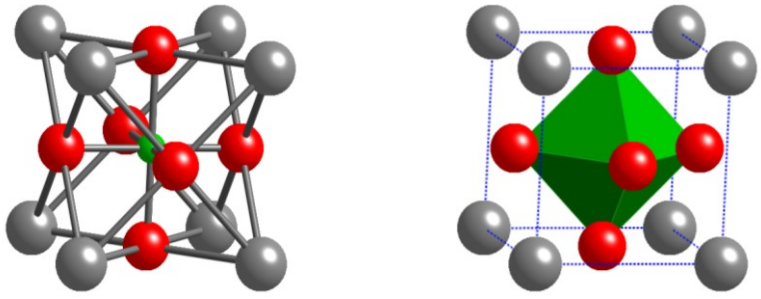

(a) (b)

Figure 2-1 (a) The prototypical perovskite structure with chemical formula ABO_3. One oxygen octahedra is highlighted in (b).

2.1.1 Octahedral tilt transitions

Materials with the perovskite structure typically undergo phase transitions; these include ferroelectric, antiferroelectric, octahedral tilt and incommensurate phase transitions. One of the most common structural changes in perovskites occurs when the oxygen octahedra undergo cooperative motions about a specific crystallographic axis in order to reduce the coordination volume of the A-site cation. The phase transition associated with this change is often referred to as a tilt transition. During these phase transitions, the octahedra tilt or rotate along one or more of the three pseudo-cubic axes as is shown in Figure 2-2.

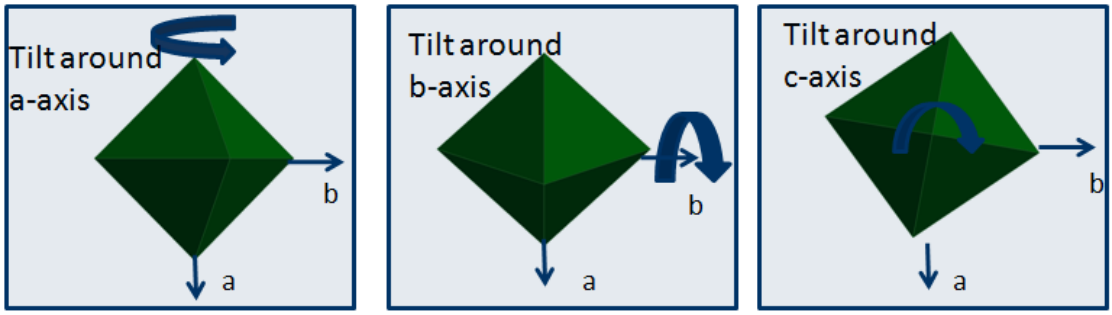

Figure 2-2 Rotation or tilt of the oxygen octahedra can occur around the three crystallographic pseudo-cubic axes in perovskite materials.

The notation used to describe the different tilt systems in perovskites was developed by Glazer.[2, 10] Glazer notation uses a set of three letters, *a*, *b*, and *c*, to describe the magnitude of tilt about the [100], [010] and [001] pseudo-cubic axes, respectively. If the tilt magnitude is the same along two or more axes, then the letter is repeated. When one octahedron rotates along one of the pseudo-cubic axes, then all adjacent octahedra in a plane perpendicular to the tilt axis are forced to rotate in an opposite sense to avoid breaking B – O bonds. That is, all octahedra in the plane undergo cooperative rotations. However, there are two choices for the stacking of layers perpendicular to the tilt axis. Figure 2-3 shows a two dimensional representation of two

successive planes of octahedra tilted about the *c*-axis. If the 1st and 2nd layers of octahedra superimpose on one another, this is known at in-phase tilt and a superscript "+" is used in Glazer notation (Figure 2-3a). If the two adjacent layers do not superimpose, as is shown in Figure 2-3(b), then this is known as anti-phase tilt and a superscript "–" is used. If no tilt occurs about a specific direction, then a superscript 0 is used. The full Glazer notation for the schematic in Figure 2-3(b) is $a^0a^0c^-$, meaning there is no tilt about the *a*- or *b*-axes, and anti-phase tilt about the *c*-axis.

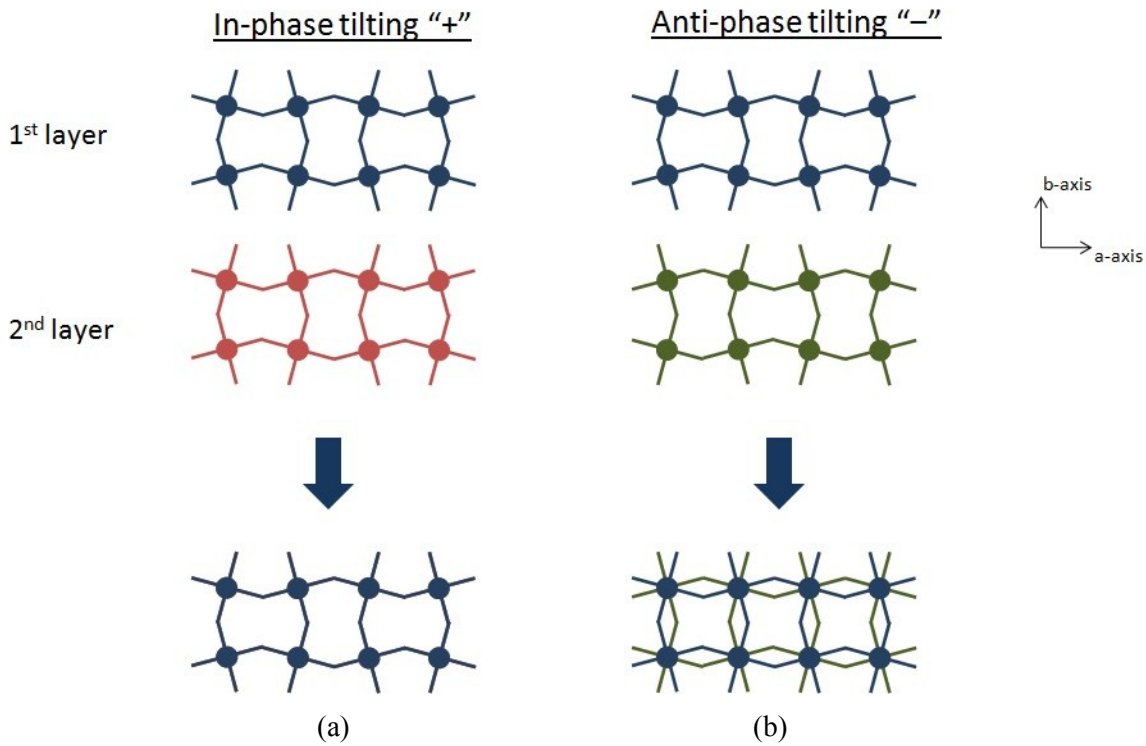

Figure 2-3 Two dimensional representation of adjacent layers of tilted octahedra; the B cations are shown as circles. The lines show the bonds to adjacent anions. (a) For tilt about the *c*-axis, two adjacent layers superimpose when the tilt system is in-phase. (b) If the tilt system is anti-phase, then two adjacent layers have an opposite sense of tilt.

2.1.1.1 Common perovskites that undergo tilt

Various combinations of in-phase, anti-phase and no-tilt are possible in the perovskite structure. Tilting typically occurs when the tolerance factor is less than 1 due to the fact that the

A-site cation is too small for the volume of its interstice.[11] There are a total of 23 possible tilt systems in the perovskite family; examples of some of which are listed in Table 2-1.[2, 12, 13] It is worth noting that several materials such as $NaNbO_3$, $AgNbO_3$, and $KMnF_3$ have multiple tilt transitions.

Table 2-1 Tilt systems found in perovskite electroceramics.

Material	Tilt System	Space Group	Ref
$NaNbO_3$ (T_2 phase)	$a^0a^0c^+$	C4/mmb	[2]
$SrTiO_3$ (< 110 K)	$a^0a^0c^-$	I4mmm	[2]
$KMnF_3$	$a^0a^0c^-$	F4/mmc	[2]
$LaAlO_3$	$a^-a^-a^-$	$R\bar{3}c$	[14]
$BiFeO_3$	$a^-a^-a^-$	R3c	[15]
$Pb(Zr_{0.90}Ti_{0.10})O_3$	$a^-a^-a^-$	R3c	[16]
$LaNiO_3$	$a^-a^-a^-$	$R\bar{3}c$	[2]
$(La_{0.67}Sr_{0.33})MnO_3$	$a^-a^-a^-$	$R\bar{3}c$	[17]
$DyScO_3$	$a^-a^-c^+$	Pbnm	[18]
$SrRuO_3$	$a^-a^-c^+$	Pbnm	[19]
$CaTiO_3$	$a^-a^-c^+$	Pbnm	[20]
$NaNbO_3$ (room temperature P phase)	$a^-b^+a^-/a^-b^-a^-$	Pbma	[2, 21]

2.1.1.2 Detection of octahedral tilting in perovskites

For antiferrodistortive phase transitions such as octahedral tilting, the unit cell contains an integer number of formula units exceeding one, whereas the cubic prototype has one ABO_3/unit cell. For example, the unit cell may double or quadruple along any of the three

primary pseudo-cubic axes. In some cases, the new unit cell will be rotated 45° with respect to the original pseudo-cube thus producing a lattice parameter $\sqrt{2}a_{pc}$ (pc = pseudocubic). The subscript pc here denotes the pseudocubic unit cell. The increase in the unit cell size will produce additional weak reflections on the half-integral and/or quarter-integral reciprocal lattice planes and can be detcted in diffraction patterns. The two types of tilt, in-phase (+) and anti-phase (–), give rise to two distinct types of reflections in reciprocal space. The + type tilts produce reflections of the type odd-odd-even while the – tilts produce odd-odd-odd reflections. General rules were developed by Glazer and are reproduced in Table 2-2.[10]

Table 2-2 Glazer's rules for superlattice reflections arising from in-phase and anti-phase tilt of the oxygen octahedra. *e* = even indices, *o* = odd indices.[10]

Tilt	Reflection	Example
a^+	½{*eoo*} with $K \neq L$	½{213} or ½{031}
b^+	½{*oeo*} with $H \neq L$	½{123} or ½{103}
c^+	½{*ooe*} with $H \neq K$	½{312} or ½{130}
a^-	½{*ooo*} with $K \neq L$	½{131} or ½{113}
b^-	½{*ooo*} with $H \neq L$	½{311} or ½{113}
c^-	½{*ooo*} with $H \neq K$	½{131} or ½{311}

The superlattice reflections due to tilting of the oxygen octahedra can be detected in diffraction patterns through the use of X-rays, neutrons and electrons. The intensity of the superlattice reflections for most perovskite materials is on the order of 0.01-1% of the maximum intensity. This weak intensity makes it difficult to detect superlattice reflections using a lab-source X-ray system. Therefore, synchrotron X-ray diffraction, neutron diffraction and transmission electron microscopy (TEM) are typically used to characterize tilt

in perovskite structures. Figure 2-4 shows an electron diffraction pattern along the [010] direction of $CaTiO_3$.[3] In this case, the in-phase tilt is about the [010] axis. The octahedral tilting can be distinguished by the presence of ½{*oeo*}-type reflections that are highlighted in the figure.

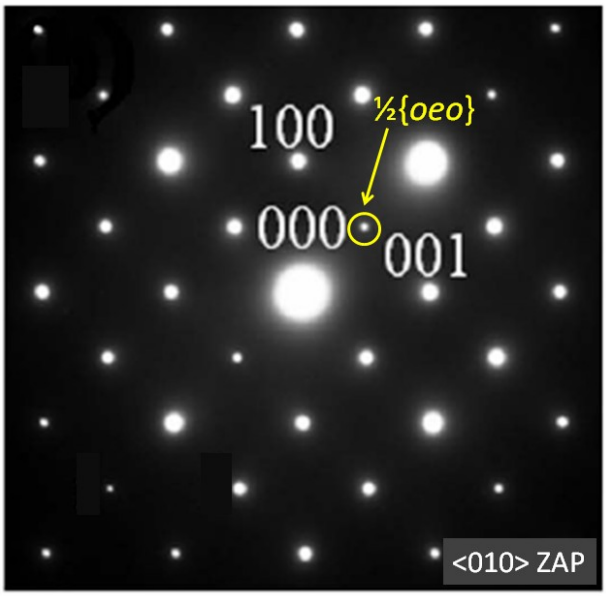

Figure 2-4 Electron diffraction pattern obtained from $CaTiO_3$. $CaTiO_3$ has a tilt system $a^-a^-c^+$. This diffraction pattern, looking down the [010] axis, shows clear ½{*oeo*}-type reflections that are characteristic of in-phase tilting.[3]

From a mathematical standpoint, the existence or absence of specific superlattice reflections can be determined using the structure factor. In diffraction, the intensity of peaks is proportional to the square of the structure factor F_{hkl} given as

$$F_{hkl} = f_{O^{2-}} \sum_n \exp[2\pi i(hu_n + kv_n + lw_n)]$$

When considering reflections due to tilt, only the oxygen sublattice needs to be considered. In the equation above, $f_{O^{2-}}$ is the oxygen ion form factor, the position of the n^{th} oxygen atom within the unit cell is given by (*u,v,w*) and *h*, *k*, and *l* are the Miller indices of the Bragg peak. Because peak intensity is proportional to the square of the structure factor, the existence of a particular superlattice reflection can be determined by calculating the structure factor. Consider $LaNiO_3$,

which has 24 oxygen atoms in the unit cell due to the tilt system $a^-a^-a^-$. The tilt angle about each of the three pseudo-cubic axes is 5.2°.[22] Based on Glazer's rules given in Table 2-2, one would expect

$a^-a^-a^-$ to produce ½{*ooo*}-type reflections. Select superlattice reflections along with the corresponding square of the structure factor are shown in Table 2-3 for $LaNiO_3$. The square of the structure factor given in the table is summed over all eight domain variants of $LaNiO_3$. As expected based on Glazer's rules, finite intensities exist for ½{*ooo*}-type reflections but not for ½{*ooe*}-type reflections. In addition, reflections of the type ½{*ooo*} in which *H*=*K*=*L* do not show intensity.

Table 2-3 Superlattice reflections and the square of the structure factor for several reflections of $LaNiO_3$. $LaNiO_3$ has the tilt system $a^-a^-a^-$ with a tilt angle of 5.2° about each axis. The structure factor is based on the oxygen sublattice and is calculated for X-rays.

Superlattice Reflection	$(\text{Structure Factor})^2$
½(113)	~ 318
½(311)	~ 294
½(115)	~ 280
½(111)	0
½(312)	0

2.1.2 Octahedral tilt and strain

When a material undergoes tilting of the oxygen octahedra, a strain is introduced into the lattice. This phenomenon is shown schematically in Figure 2-5. In the figure, the closed circles represent B-site cations and the lines represent the axes of the octahedra. When octahedra in a perovskite structure are untilted, the repeat distance is simply one octahedron (Figure 2-5a). As a

result, the distance between B-site cations is the lattice parameter of the perovskite structure. In contrast, when the octahedra tilt or rotate in a simple pattern, the repeat unit becomes two octahedra, thus doubling the length of the unit cell edges (Figure 2-5b). As this happens, the distance between two adjacent B-site cations is shorter than that of the untilted case. Therefore, the volume of the psuedocubic unit cell changes as a result of tilt and a strain is introduced in the lattice. In other words, strain and tilt are related. The goal of this project is to understand the relationship between tilt and strain by using strain engineering in epitaxial perovskite thin films.

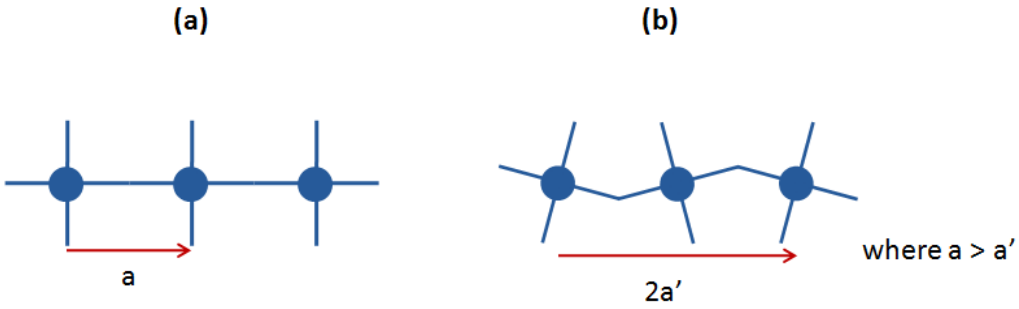

Figure 2-5 Schematic showing a 2-dimensional representation of (a) three untilted octahedra and (b) three tilted octahedra. The solid circles represent the B-site cations while the lines represent the two axes of the octahedra. A series of tilted octahedra will double the unit cell and decrease the distance between the B-site cations as compared to the untilted case.

2.2 Strain engineering

As was stated in the last section, octahedral tilting is related to strain. However, the relationship between strain and tilt is not well understood. One means to probe this relationship would be to induce a strain in the lattice, and study the tilt structure. In bulk materials, hydrostatic pressure is often used to induce strain in the lattice. Alternatively, materials under biaxial strain can also be studied in the form of thin films on crystalline substrates. When one material is deposited onto a substrate, large strains can be induced due to differences in crystal symmetry, lattice parameter and thermal expansion coefficients between the film and substrate.

2.2.1 Biaxial strain in epitaxial thin films

The growth and deposition of epitaxial thin films allows for introduction of biaxial strain into the film. Epitaxial growth occurs when the crystal structure of the grown film has both in-plane and out-of-plane registry to the substrate.[23, 24] It is possible to grow films such that the in-plane lattice parameter is constrained by that of the substrate, thus preventing the film from attaining its bulk equilibrium value. These types of films are called coherently strained films. Growth of high quality, coherently strained epitaxial films is possible when the difference between the lattice parameters of the film and substrate is small at growth temperatures. In addition, the surface energies of the film and substrate should be comparable. The lattice mismatch, *f*, is often defined as

$$f = \frac{a_f - a_s}{\frac{1}{2}(a_f + a_s)} \approx \frac{a_f - a_s}{a_s}$$

Equation 2-1

where a_f is the lattice parameter of the film and a_s is the lattice parameter of the substrate.[23, 24]

During the initial stages of growth, the film will adopt a lattice parameter constrained by that of the underlying layer (in many cases identical to that of the substrate). This is shown in Figure 2-6a and Figure 2-6b. As a result, the film is under stress along the in-plane (*x* and *y*) directions of the film. Typically, the films remained strained to the substrate until a critical thickness is reached. At this point, dislocations start forming as a means of reducing the stress in the film, as is shown in Figure 2-6c.

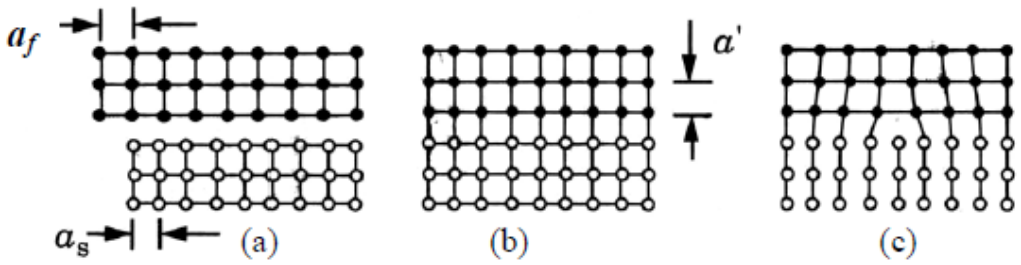

Figure 2-6 Schematic showing lattice mismatch between film and substrate (a) prior to film deposition, (b) during initial stages of growth and (c) after a dislocation is formed in the film as a method of relieving stress.[24]

The point at which dislocations start forming in epitaxial films can be calculated using the Matthews-Blakeslee criterion. At small thicknesses, there is a competition between the strain energy in the lattice and the strain energy associated with the formation of dislocations. The Matthews-Blakeslee criterion describes the relationship between the critical thickness of the film, h, and the strain, ε:

$$\varepsilon = \frac{b}{8h\pi(1+\upsilon)}\ln\left(\frac{4h}{b}\right)$$

Equation 2-2

where b is the Burger's vector and υ is Poisson's ratio.[24, 25] Above the critical thickness, dislocations are favored to relieve the stress in the film. In many cases, relaxation by dislocation formation occurs above this critical thickness due to kinetic limitations.

2.2.2 Bi-axial strain effects on phase transitions

As a result of the large strains present in epitaxial thin films, the properties can differ from the intrinsic properties of the unstrained bulk counterparts. For example, $SrTiO_3$, which is cubic above 105 K and paraelectric above 0 K, has been shown to exhibit strain-induced ferroelectricity in thin films at room temperature.[5] Similarly, the ferroelectric transition

temperature of coherently strained $BaTiO_3$ was increased by 500 °C and the remanent polarization was enhanced by 250% compared to bulk materials.[8] Several groups have reported the structural phase transition in $SrRuO_3$ thin films.[6, 26-28] Under biaxial compressive stress, $SrRuO_3$ thin films exhibit a tetragonal phase rather than the orthorhombic phase stable in bulk $SrRuO_3$.[28] The observed phase is strongly dependent on the lattice mismatch between the $SrRuO_3$ film and the substrate. At low mismatch values the film remained orthorhombic, however, at higher lattice mismatch values the structure of the film was tetragonal. For $SrRuO_3$ films on $SrTiO_3$ substrates, it was found that the film remained tetragonal well above the tetragonal-cubic phase transition temperature reported for bulk materials.[27] In addition, it has been reported that the orthorhombic transition temperature of coherently strained $SrRuO_3$ thin films shifts by nearly 250 °C.[26]

Besides altering phase transition temperatures, biaxial strain has also been used to control the domain state in materials. For example, Vailionis *et al.* and Maria *et al.*, showed that epitaxial $SrRuO_3$ films on miscut $SrTiO_3$ substrates exhibited a single domain structure.[27, 29] It has also been shown that the domain structure of $PbTiO_3$ thin films changes as a function of thickness as a method of relieving stresses.[30]

2.2.3 Mechanical constraint effects on octahedral tilt

The relative stability of octahedrally tilted phases under different strain conditions has received little attention until recently. Research by He *et al.* showed that the tilt transition temperature of $SrTiO_3$ is dependent on biaxial strain.[6, 7, 31] In that work, superlattice reflections due to octahedral tilting were examined as a function of temperature. An increase in the tilt transition temperature was observed when the $SrTiO_3$ film was coherently strained to an underlying $SrRuO_3$ layer (Figure 2-7). From a theoretical standpoint, phase field modeling

suggests that the tilt transition temperature of $SrTiO_3$ is weakly coupled to strain. However, uncertainty in some of the constants leads to uncertainty in the predicted transition temperatures, as is evidenced by the shaded regions in Figure 2-8.[32-34] Both tensile and compressive strain along the in-plane direction appear to increase the tilt transition temperature for films, with larger effects observed for compressive strain.[6, 7, 35]

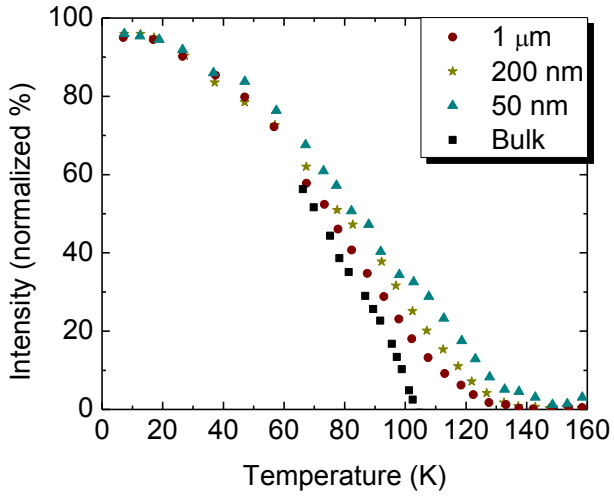

Figure 2-7 The superlattice intensity as a function of temperature for $SrTiO_3$ thin films on $SrRuO_3$. As a result of strain, the transition temperature of the octahedral tilt transition was shifted to higher temperatures. Plot adapted from He *et al.*[6, 7]

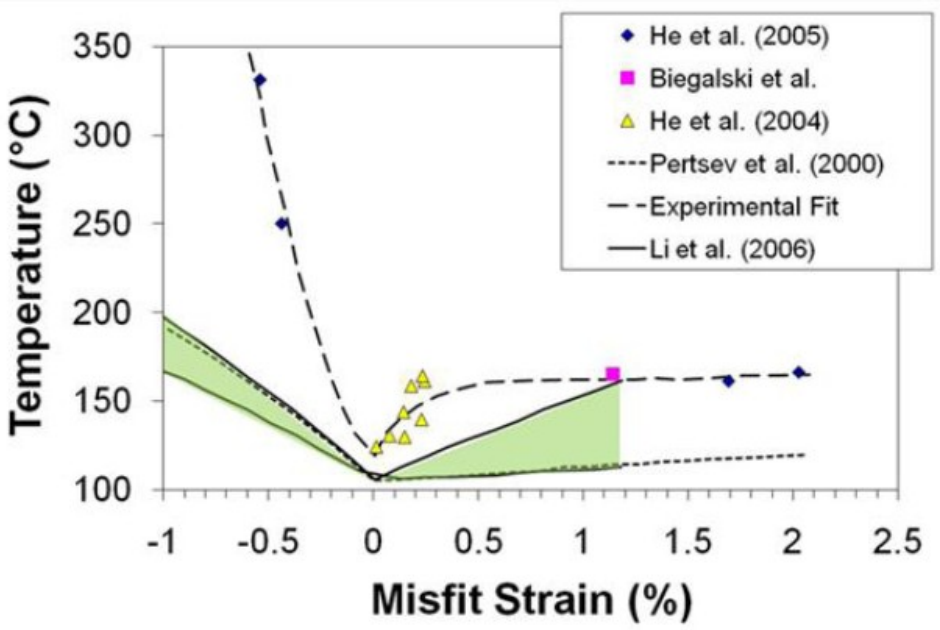

Figure 2-8 The strain phase diagram for $SrTiO_3$. Above the line the material is untilted, while a tilted phase is favored below the line. Data obtained using a combination of experimental data [6, 7, 35] and phenomenological modeling.[32-34] The shaded regions indicate uncertainty in the calculated tilt transition temperature. Figure from [36].

The tilt angle of the oxygen octahedra has been shown to depend on the strain in the lattice in some perovskite materials. In Figure 2-9, density functional theory (DFT) was used to calculate the degree of tilt or rotation in $LaAlO_3$ as a function of strain. $LaAlO_3$ has an $a^-a^-a^-$ tilt system.[37] In this work, the authors refer to "tilt" as rotation of the octahedra about an in-plane axes while "rotation" refers to rotation of the octahedra about the $[001]_{pc}$ or out-of-plane axis. As was demonstrated in Figure 2-5, a rotation about the *c*-axis reduces the *a*- and *b*- lattice parameters. Thus, if the material is in a state of biaxial compressive strain, rotation of the oxygen octahedra about the out-of-plane axis would be favored, as shown in the schematic in Figure 2-10a. Conversely, if the material is in a state of tensile strain, rotation of the oxygen octahedra about the in-plane axes could be favored (Figure 2-10b). This is also predicted from density functional theory calculations.[37]

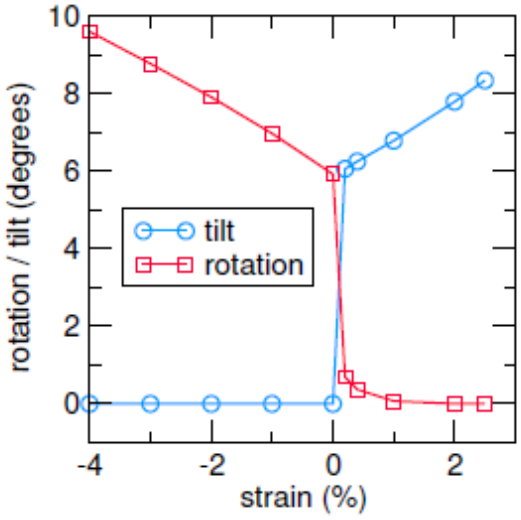

Figure 2-9 (a) Density functional theory (DFT) calculations showing tilt angle as a function of strain for $LaAlO_3$.[37], [22]

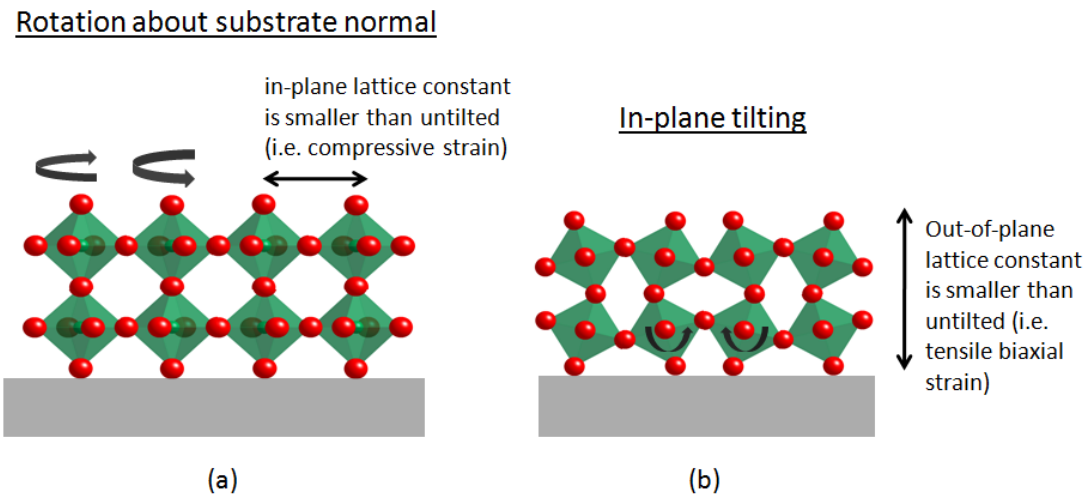

Figure 2-10 Schematic showing that (a) compressive strain favors octahedral rotation about the out-of-plane axis and (b) tensile strain would favor tilt about an in-plane axis.

Experimental measurements were performed on $LaNiO_3$ thin films to confirm the theoretical results discussed above. For that purpose, $LaNiO_3$ films ($a^-a^-a^-$ tilt system) were deposited on $SrTiO_3$ and $LaAlO_3$ substrates to induce a tensile and compressive strain state, respectively.[22] X-ray diffraction was used to record the intensity of specific superlattice

reflections. These intensities were used to calculate tilt angles from the structure factor. To describe the structure, the tilt angles α and β were defined for octahedral tilt about an in-plane axis and γ referred to the tilt angle about the out-of-plane axis. Table 2-4 summarizes the results showing that a compressive strain leads to larger tilt about the out-of-plane axis while tensile strain enhances the tilt angle about the in-plane axes.[22] These results agree with the density functional theory calculations. Interestingly, when DFT was used to calculate the bond angles and bond lengths based on the experimental lattice parameters (see Figure 2-11), it was found that the Ni-O bond length was altered as a function of strain.[22] This suggests that strain can also distort the octahedra; the octahedra may not behave rigidly in all perovskite systems under the influence of strain. Although not as direct, experimental results that demonstrated changes in tilt magnitude as function of strain were obtained on $La_{0.67}Sr_{0.33}MnO_3$ and $SrRuO_3$ thin films deposited on a variety of substrates that induced different levels of compressive and tensile strain into the films.[17]

Table 2-4 Tilt angle of $LaNiO_3$ in an unstrained state, a compressively strained state and a state of tensile strain. As predicted using DFT calculations, a larger tilt angle was observed for films under compressive strain while tensile strain enhances tilt about the in-plane axes.[22]

Angle	Unstrained	Compressive (-1.1 %)	Tensile (1.7 %)
α	5.2°	1.7 ± 0.2°	7.1 ± 0.2°
β	5.2°	1.7 ± 0.2°	7.1 ± 0.2°
γ	5.2°	7.9 ± 0.2°	0.3 ± 0.7°

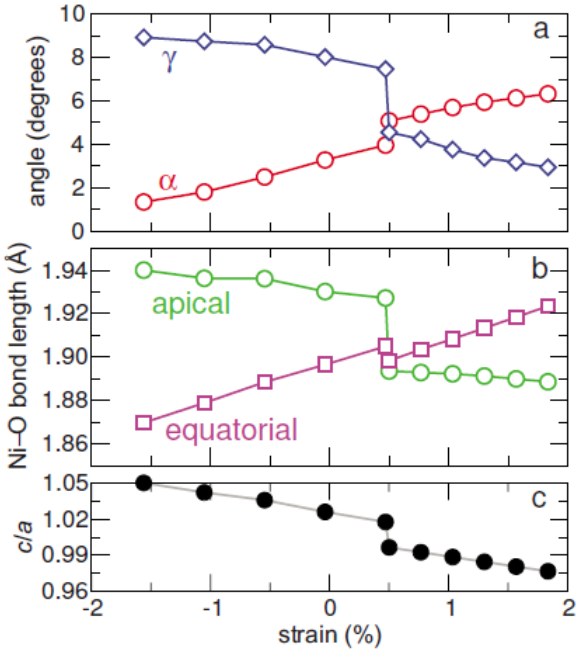

Figure 2-11(a) Density functional theory calculated rotation angles, (b) Ni-O bond lengths and (c) *c/a* ratio as a function of strain.[22]

The effect of strain on tilt angle has also been studied through the use of superlattice structures. Synchrotron X-ray diffraction was used to measure octahedral rotations in $(LaNiO_3)_n/(SrMnO_3)_m$ superlattices. $LaNiO_3$ undergoes octahedral rotations with the $a^-a^-a^-$ tilt system. $SrMnO_3$, on the other hand, is cubic with no octahedral rotations. Figure 2-12a shows the intensity of the ½113 reflection for different *m* to *n* ratios.[38] The peak intensity is related to the magnitude of the octahedral tilt angle. When the number of $SrMnO_3$ layers was large and the number of $LaNiO_3$ layers was small (i.e. $m > n$; L1S2 in the figure) then the octahedral rotations of $LaNiO_3$ were nearly nonexistent. Conversely, when $m < n$ (L4S2 in the figure), large rotations were present in the $LaNiO_3$. In addition, the bond angles of $SrMnO_3$ were reduced, indicating that the oxygen octahedra in the $SrMnO_3$ layer were also rotated.[38] These results correlate well with density functional theory calculations for other systems suggesting that the anti-phase tilt pattern in a $SrTiO_3$ substrate propagates across the interface into the originally cubic $SrFeO_3$ film.[39]

The data is demonstrated schematically in Figure 2-12b. As was found in both these cases, strain can be used to manipulate collective motion of the octahedra.

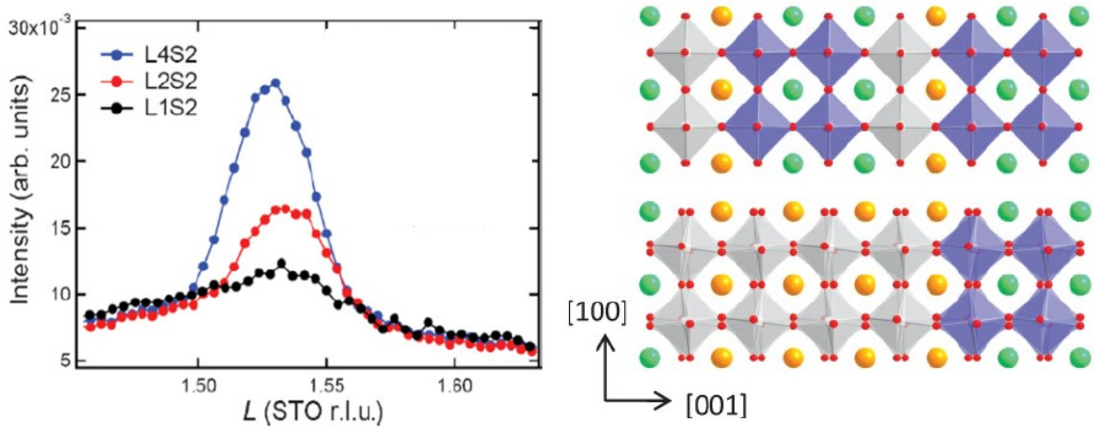

(a) (b)

Figure 2-12 (a) The intensity of the ½113 peak in $LaNiO_3$ as a function of *m* to *n* ratio in the $(LaNiO_3)_n/(SrMnO_3)_m$ superlattice structure. As the thickness of the tilted $LaNiO_3$ layer decreases, the intensity, and hence tilt angle, also decreases. L4S2 = 4 layers of $LaNiO_3$ plus 2 layers of $SrMnO_3$.[38] (b) Schematic demonstrating results from May *et al.* showing that the number of monolayers in a superlattice has a profound impact on the tilt angle of the oxygen octahedra. The top figure shows that the tilt angle is strongly suppressed in the superstructure consisting of 1 layer of $LaNiO_3$ with 2 layers of $SrMnO_3$ (L1S2). The bottom figure shows larger tilt angles for the superstructure consisting of 4 layer of $LaNiO_3$ with 2 layers of $SrMnO_3$ (L4S2).[38]

2.3 $Ag(Ta_xNb_{1-x})O_3$

The work presented in this dissertation examines how strain affects tilt transitions in the solid solution $Ag(Ta_xNb_{1-x})O_3$. This section will describe the important aspects of the crystal structure of $Ag(Ta_xNb_{1-x})O_3$, including octahedral tilting and cation ordering. Then, an overview of ATN as material for practical applications will be discussed.

2.3.1 The $Ag(Ta_xNb_{1-x})O_3$ phase diagram

$Ag(Ta_xNb_{1-x})O_3$ (ATN) was used in the work because it has a complex tilt system and a compound phase transition sequence. These factors, in addition to the fact that ATN has lattice parameters near that of common substrates, make ATN a good model system to study the relationship between octahedral rotation and strain. The phase diagram for ATN is shown in Figure 2-13.[40, 41] $Ag(Ta_xNb_{1-x})O_3$ has a perovskite-like structure that is cubic at high temperatures and undergoes a series of reversible phase transitions that include tetragonal, orthorhombic and M phases.[41-44] The M phases were originally thought to be monoclinic, but have more recently been confirmed to be orthorhombic.[43, 44] The space group and tilt system (denoted using Glazer notation) are given in Figure 2-13 for each crystallographic phase. It is important to note that the T, O and M phases all have different space groups that arise from octahedral-tilting instabilities. Conversely, the three M phases have the same space group and same tilt system. The difference between these phases will be discussed later and involve subtle, non-symmetry breaking cation displacements.

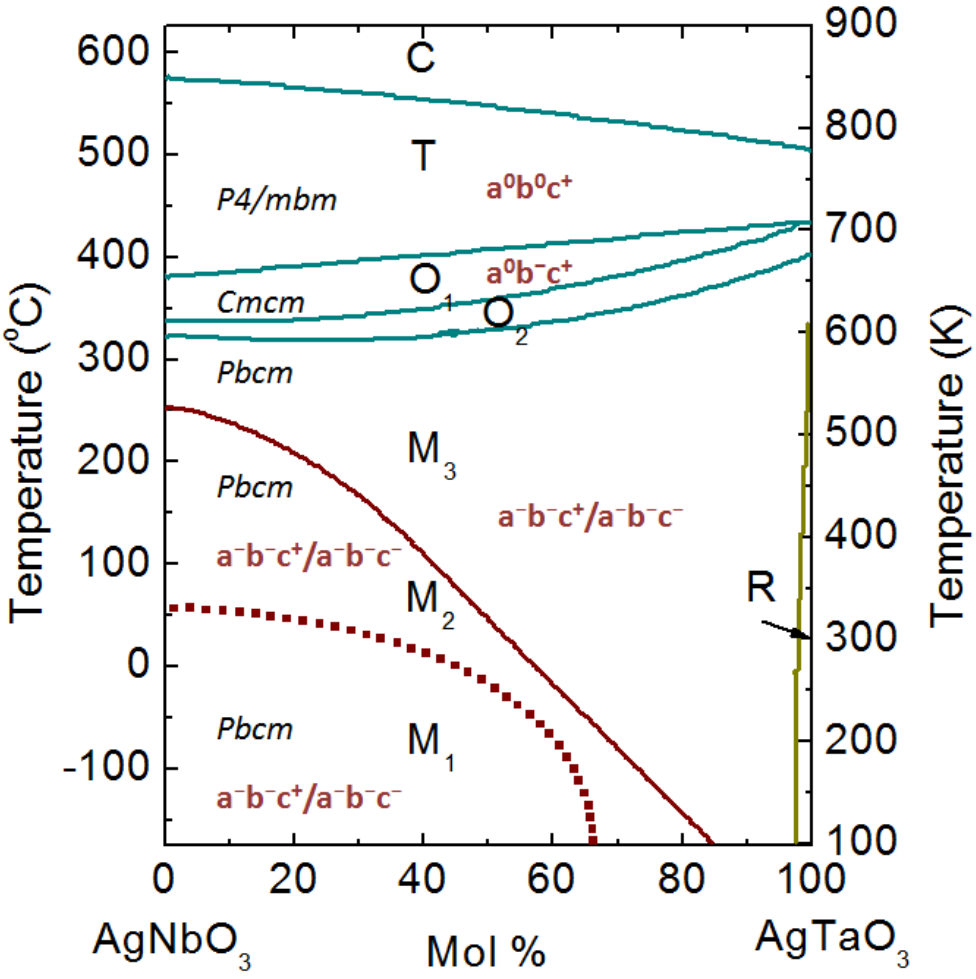

Figure 2-13 Phase diagram of $Ag(Ta_xNb_{1-x})O_3$ solid solution. C = cubic, T = tetragonal, O_1 and O_2 = orthorhombic, M_1, M_2, M_3 = "M" phases. (Redrawn from ref. [40, 41].)

As was mentioned, ATN undergoes a complex sequence of octahedral tilt transitions that arise because the Ag ion is too small for the available volume. According to Reaney *et al.*, perovskite structures will tend to undergo octahedral tilt if the tolerance factor is less than 1.0. Table 2-5 shows typical ranges of tolerance factors in perovskite structures and the associated tilt systems.[11] Based on the ionic radii of Ag^+, Nb^{5+} and O^{2-} with their respective coordination

numbers, the tolerance factor of $AgNbO_3$ is ~ 0.96.[45] Therefore, the complex tilt system found in ATN is not surprising.

Table 2-5 Tolerance factor range and associated tilt systems found in perovskite materials.[11]

Tolerance Factor	Tilt
0.985 < t < 1.06	No tilt
0.964 < t 0.985	Anti-phase
t < 0.964	In-phase and anti-phase

2.3.2 High temperature phases of $Ag(Ta_xNb_{1-x})O_3$

At high temperatures, $Ag(Ta_xNb_{1-x})O_3$ is cubic with a *Pm3m* space group that is typical of the perovskite structure. Because the material is cubic and no tilting exists in this phase, the unit cell can be defined by $a_{pc}\ x\ a_{pc}\ x\ a_{pc}$ where a_{pc} ~ 3.96Å in the cubic phase.[44] As the material cools from the cubic phase, it transitions into the tetragonal phase with a *P4/mbm* space group and an $a^0a^0c^+$ tilt system. Due to the tilting of the octahedra, the unit cell has lattice parameters of approximately $\sqrt{2}a_{pc}\ x\ \sqrt{2}a_{pc}\ x\ a_{pc}$, where two of the principal vectors are rotated by 45° with respect to the original cube. Figure 2-14 shows eight octahedral units for ATN in the tetragonal phase. The in-phase tilt found in this phase field can be detected through the presence of ½{*ooe*}-type superlattice reflections.

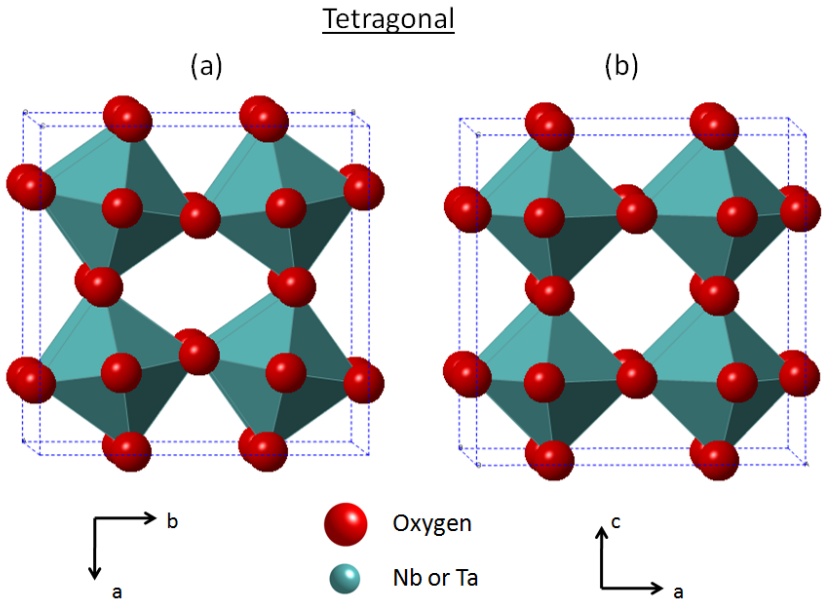

Figure 2-14 Eight pseudo-cubic units of tetragonal ATN looking down the (a) *c*-axis and the (b) *b*-axis. The tilt system for the T phase is $a^0a^0c^+$. The Ag ions are hidden for clarity.

As ATN cools from the tetragonal phase, it undergoes an orthorhombic phase transition. In this phase the pseudo-cubic unit cell is $2a_{pc}$ x $2a_{pc}$ x $2a_{pc}$ due to the $a^0b^-c^+$ tilt system. Figure 2-15 shows a schematic of the orthorhombic unit cell with in-phase tilting about the *c*-axis and anti-phase tilting about the *b*-axis. The co-existence of both in-phase and anti-phase tilting will lead to ½{*ooe*} and ½{*ooo*} reflections in diffraction patterns.

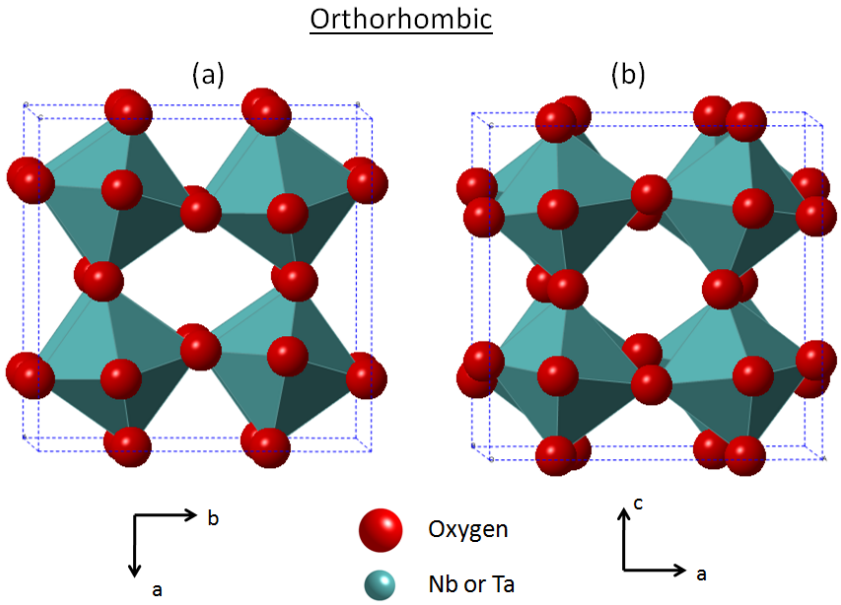

Figure 2-15 The orthorhombic unit cell of ATN looking down the (a) *c*-axis and the (b) *b*-axis. The in-phase tilting is visible along the *c*-axis while the anti-phase tilt can be seen along the *b*-axis. The tilt system for the O phase is $a^0b^-c^+$. The silver ions are hidden for clarity.

2.3.3 M phases of $Ag(Ta_xNb_{1-x})O_3$

Two important structural features of the M phases include tilting of the oxygen octahedra and local cation displacements. This section will describe these differences in detail.

2.3.3.1 Octahedral tilt in the M phases of $Ag(Ta_xNb_{1-x})O_3$

At room temperature, $Ag(Ta_xNb_{1-x})O_3$ (ATN) exhibits an orthorhombic perovskite-related structure with *Pbcm* symmetry. The unit cell has lattice parameters $\sqrt{2}a_{pc} \times \sqrt{2}a_{pc} \times 4a_{pc}$ where $a_{pc} \sim 3.96$ Å corresponds to the cubic phase. Throughout this dissertation, the unit cell will be given in reference to the pseudo-cubic unit cell unless otherwise noted. If clarification is required, a subscript *pc* will be used. In ATN, the oxygen octahedra undergo cooperative

rotations of the [NbO_6] and [TaO_6] framework. The room temperature tilt system is $a^-b^-c^-/a^-b^-c^+$, meaning that there is anti-phase tilting about the *a*- and *b*-axes and a periodic sequence of two similarly rotated octahedra and two octahedra rotated in an opposite sense about the *c*-axis. It is this combined in-phase and anti-phase tilt that leads to the quadrupling of the unit cell along the *c*-axis as is shown in Figure 2-16. The supercell structure of ATN results in ½- and ¼-order reflections which can be observed in diffraction patterns. In particular, ½{*ooo*} reflections correspond to the in-phase tilting in the M phase while ½{*ooo*} ± ¼{00*L*} are due to the quadrupling of the unit cell from tilt.

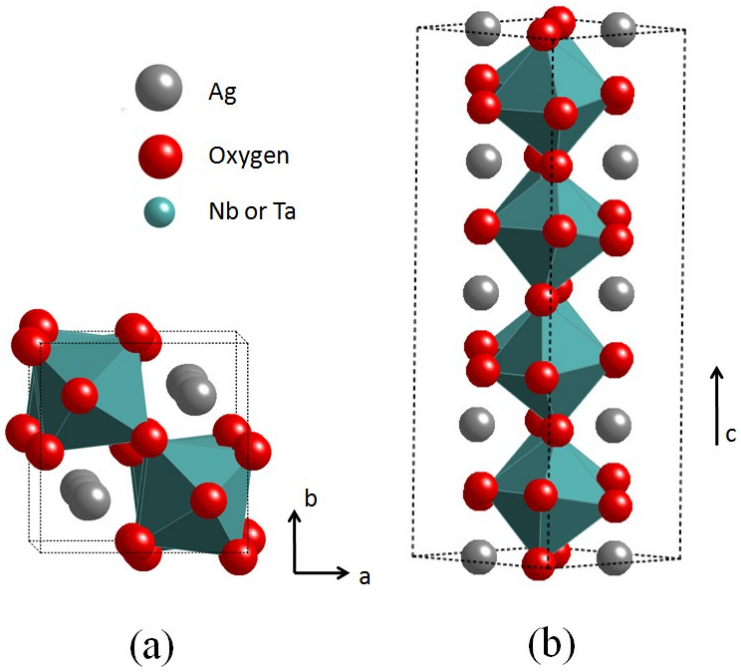

Figure 2-16 Room temperature structure of $AgNbO_3$ (a) viewed down the c-axis showing the combined in-phase and anti-phase tilting and (b) viewed along $<110>_o$ ($<111>_{pc}$) showing quadrupling of the unit cell along the c-direction.

2.3.3.2 B-site cation ordering in the M phases of $Ag(Ta_xNb_{1-x})O_3$

As was mentioned previously, all three of the M phases have the same space group and same tilt system, however, the electrical properties are distinct.[46, 47] A diffuse peak develops in the temperature dependent permittivity at the $M_3 - M_2$ phase transition. The M_1 phase is weakly ferroelectric. It was not until work by Levin *et al.* that the underlying structural differences between these phases was fully understood.[43]

Through x-ray diffraction, neutron diffraction, TEM and extended X-ray absorption fine structure (EXAFS), Levin *et al.* determined that the Nb cations exhibit local off-center displacements in $AgNbO_3$. The displacements of the B-site cations are illustrated in Figure 2-17. In the high temperature phases (i.e. T and O), Nb atoms displace along any one of the eight ⟨111⟩ type directions with equal probability (Figure 2-17c). Thus, on average, the Nb atoms appear to be located at the center of the unit cell in the O and T phases. In the M phases, the local displacements of the Nb atoms show partial ordering. Instead of being distributed equally amongst the eight sites, two of the eight sites are favored. This is shown in Figure 2-17b where the different sized spheres represent the probability of displacements. Below ~ 175 °C in $AgNbO_3$, the Nb atoms "lock in" to only two of the possible eight sites (Figure 2-17a). Thus, on average, the Nb atoms displace along ⟨110⟩. That, in turn, is coupled to an expansion along the equator and a contraction along the apex of the oxygen octahedra. Prior to Levin's work, other authors reported splitting of the 002_{pc} peak via x-ray diffraction at the M_2-M_3 phase transition.[41, 42, 44] It is now believed that the distortion of the oxygen octahedra, which is due to the "locking-in" of the Nb atoms, gives rise to the observed peak splitting ($002_{pc} = 008_o$ and 220_o) shown in Figure 2-18 for bulk $AgNbO_3$. Due to the $a^-b^-c^- / a^-b^-c^+$ tilting in the M phases, the symmetry restrictions constraining the Nb atoms to their ideal central position at higher temperatures has been lifted, thereby promoting partial ordering of the local Nb displacements.

As the temperature decreases, this ordering becomes more pronounced and long range, while the magnitude of the Nb displacements increases.

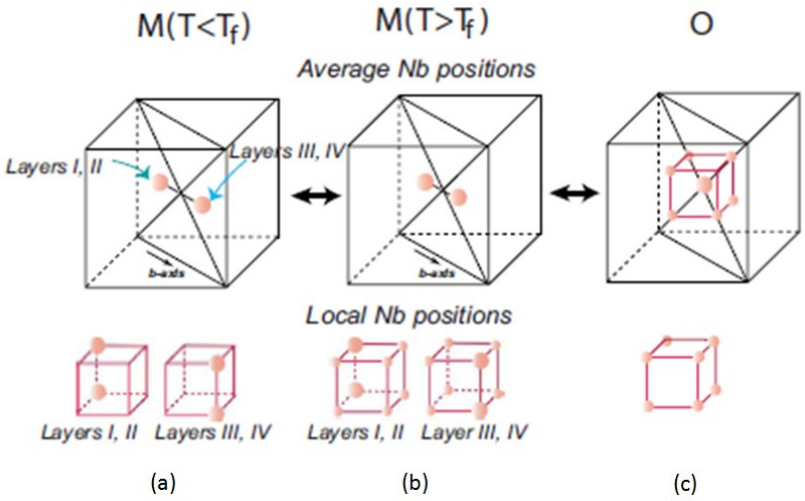

Figure 2-17 B-site cation displacements in bulk $AgNbO_3$ for the (a) M_2, (b) M_3 and (c) O phases. $T_f \sim 175$ °C. Below T_f, the Nb cations preferentially order along only two of the <111> directions of the pseudo-cube. This leads to an average displacement along <110>. Above T_f (i.e. in the M_3 phase), the Nb cations show partial ordering. In the O phase, the Nb cations displace randomly along the eight <111> directions. Figures from Levin *et al.*[43]

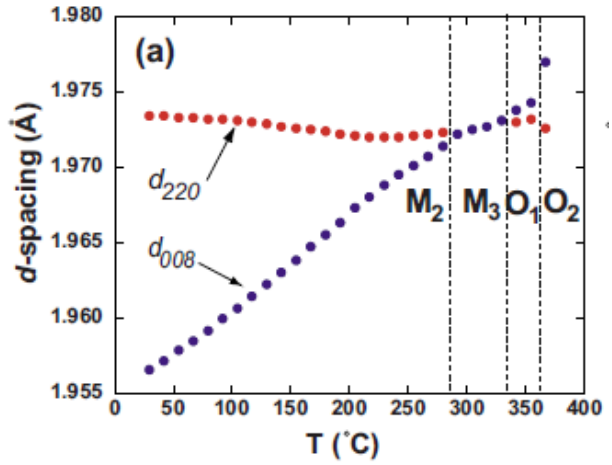

Figure 2-18 The splitting of the $008_{pc} = 008_o + 220_o$ peaks becomes pronounced in the M_2 phase of bulk $AgNbO_3$. The long range ordering of B-cation displacements distorts the oxygen octahedra, which leads to the observed splitting.[43]

Levin *et al.* suggested that the M_2-M_3 phases represent different stages in partial cation ordering, rather than two distinct phases. In the ATN phase diagram, shown in Figure 2-13, it can be seen in the M_2-M_3 transition temperature decreases as the Ta concentration increases. This

occurs because Ta^{5+} has a smaller ionic polarizabilty [40, 48] than Nb^{5+} and thus disturbs the long range ordering of the B-cation displacements. When the long range order is disrupted, the M_2-M_3 transition temperature is suppressed.

In bulk $AgNbO_3$, sheets of diffuse intensity, which are associated with long range ordering of Nb displacements, are observed in electron diffraction patterns.[43] A similar phenomenon is also observed in the orthorhombic phases of $BaTiO_3$ and $KNbO_3$, and are reportedly due to correlated B-cation displacements within linear -B-B-B- [001] chains.[49] It is believed $AgNbO_3$ undergoes similar chain-like ordering. Figure 2-19 shows the chain-like correlations of Nb cations which displace along the [111] and [11$\bar{1}$] directions. If chain 1 and chain 2 occur in a random mixture, then this is equivalent to an average displacement of Nb cations along the [110] direction with additional disordered local displacement components along [001] and [00$\bar{1}$].[43]

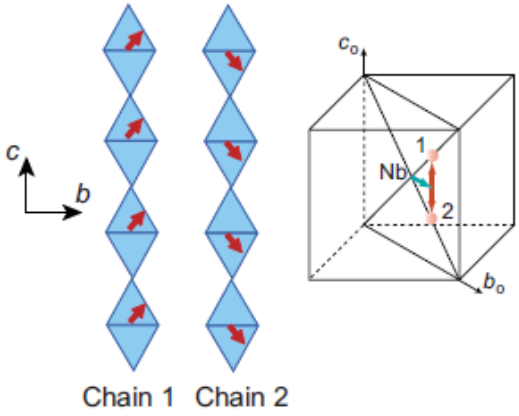

Figure 2-19 Schematic showing the chain-like correlations of the B-site cations which displace along [111] and [11$\bar{1}$] directions. The chain-like structure of Nb ordering leads to quadrupling of the unit cell along the *c*-axis. Figures from Levin *et al.*[43]

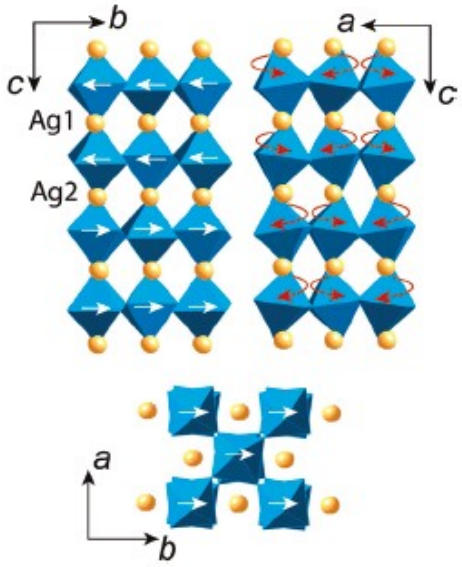

Figure 2-20 Schematic showing the correlation between B-site cation displacements and direction of octahedral tilt in the M phases of $AgNbO_3$.[40]

As observed in Figure 2-20, the chain-like correlations of B-site cations lead to a periodicity of 4 cells (along the *c*-axis) which is strongly linked to the tilting of the oxygen octahedra.[40, 43] Both structures will quadruple the unit cell; the two phenomena can be distinguished from one another in diffraction patterns. The $a^-b^-c^-/a^-b^-c^+$ tilt system will produce reflections of the type ½(*ooo*) ± ¼{00*L*}. The ordering of the B-site cations will lead to ¼{00*L*} reflections flanking a Bragg peak. Figure 2-21 shows a simulated diffraction pattern along the [130] zone axis pattern (ZAP) of $AgNbO_3$. In these figures, the spots at ½311 ± ¼{00*L*} are due to the $a^-b^-c^-/a^-b^-c^+$ tilt system in the M phases. The 311 ± ¼{00*L*} reflections are associated with B-site cation ordering. In Figure 2-21a these spots are stronger than in Figure 2-21b, as can be expected because the B-cation displacements show pronounced ordering in the M_2 phase and partial ordering in the M_3 phase.

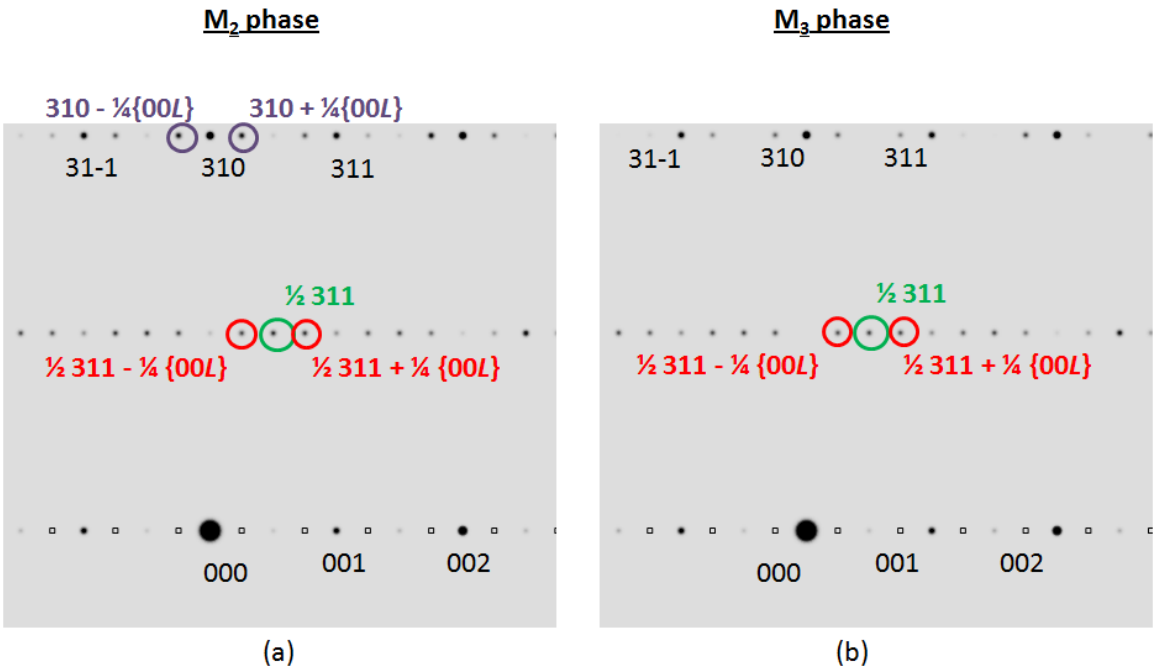

Figure 2-21 Simulated electron diffraction pattern along the $[130]_{pc}$ = $[240]_o$ zone axis for the (a) M_2 and (b) M_3 phases. The 311 ± ¼{00*L*} reflections are due to long range ordering of B-site cations. The intensity of these reflections in the M_3 phase is weaker than in the M_2 phase due to only partial B-site cation ordering in M_3. The ½311 ± ¼{00*L*} spots occur from the quadrupling of the unit cell due to the octahedral tilt system $a^-b^-c^-/a^-b^-c^+$. The squares in the bottom row represent spots that appear due to double diffraction.

2.3.4 $Ag(Ta_xNb_{1-x})O_3$ as a functional material

$Ag(Ta_xNb_{1-x})O_3$ solid solutions are notable amongst other dielectric ceramics because of the unique combination of large, temperature stable permittivity and modest dielectric losses at microwave frequencies.[50-53] Most interesting is the diffuse maximum in permittivity that is associated with high frequency dielectric relaxation due to B-site cation displacements. This broad peak, which occurs during the M_2-M_3 phase transition, can be tracked as a function of Nb composition as is shown in Figure 2-22.[46] For device applications, compositions of interest occur near x = 0.5 because the diffuse maximum in permittivity appears in the device working temperature regime.

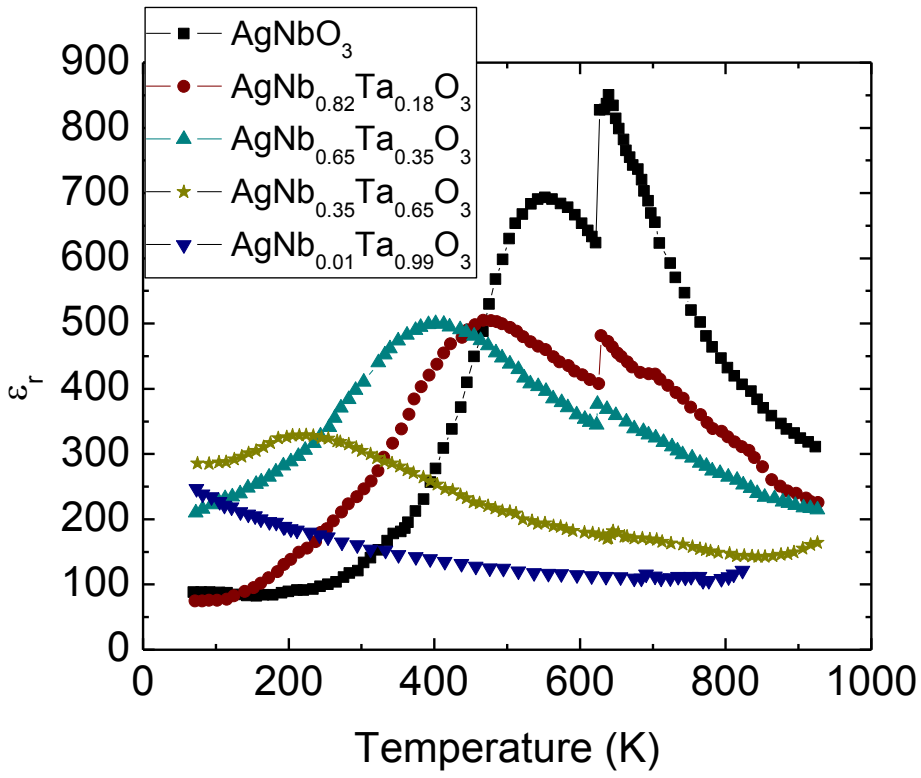

Figure 2-22 Temperature dependent permittivity for five different Nb compositions of the $Ag(Ta_xNb_{1-x})O_3$ solid solution. The broad peak in permittivity occurs at the M_2-M_3 phase transition and is strongly dependent on Nb concentration. Plot reconstructed from reference [46].

To date, $Ag(Ta_xNb_{1-x})O_3$ has been synthesized in bulk and thin film form. Conventional solid-state processing techniques are used to fabricate ceramics.[40, 41, 43, 47, 50-64] However, the processing can prove difficult, as metallic silver often occurs.[51] At 2 GHz, $Ag(Ta_{0.5}Nb_{0.5})O_3$ has been shown to have a $Q \times f$ value of ~ 753 GHz and a permittivity of ~ 410.[50, 62] Dielectric losses remain low at high frequencies, making ATN suitable for microwave device applications.[64] For the x=0.5 composition, temperature coefficient of capacitance values are modest. Valant *et al.* synthesized a composite of 45 wt. % $Ag(Ta_{0.35}Nb_{0.65})O_3$ and 55 wt. % $Ag(Ta_{0.65}Nb_{0.35})O_3$ to obtain a temperature coefficient of capacitance of < 50 ppm/K.[63] In addition, ceramics processed with x = 0.5 show a change in capacitance, $\Delta C/C$, of less than 8%

over the temperature range -20 °C to 120 °C at 1 MHz, which makes $Ag(Ta_{0.5}Nb_{0.5})O_3$ a potential candidate for devices that require stability in electrical properties over a range of temperatures.[50]

Due to the demand for miniaturized devices, thin films of $Ag(Ta_xNb_{1-x})O_3$ have been explored. The two primary thin film deposition techniques reported include pulsed laser deposition (PLD) [65-69] and chemical solution deposition.[70] X-ray diffraction and electrical measurements were performed on $Ag(Ta_{0.38}Nb_{0.62})O_3$ films deposited via PLD on $Pt_{0.8}Ir_{0.2}$ and $(La_{0.7}Sr_{0.3})CoO_3/LaAlO_3$ substrates.[66] These films were epitaxial, but showed evidence of the secondary phase natrotantite, $Ag_2Nb_4O_{11}$. Interestingly, the temperature dependent permittivity data suggested that the M_1-M_2 phase transition was suppressed ~ 60 K while the M_2-M_3 transition temperature was shifted down 50 K. The origin of this discrepancy was not addressed. A ferroelectric response was observed in these films at 125 K.[66] Films of the same composition deposited on $LaAlO_3$ substrates showed loss tangents of 0.0033 at 1 MHz with permittivity of 224 at 1 kHz.[65] Epitaxial films with the end members $AgNbO_3$ and $AgTaO_3$ have been grown on $LaAlO_3$ substrates and coplanar waveguide interdigital capacitor structures then fabricated. A fraction of natrotantite phase also appeared in these films. The devices showed favorable dielectric properties with ~0.1 loss tangent at 20 GHz.[69] $Ag(Ta_{0.5}Nb_{0.5})O_3$ films on $LaAlO_3$ that were grown via PLD exhibited secondary phase, however, the full width at half maximum (FWHM) of the 002 reflection was reasonable at ~ 0.2°. Coplanar waveguide interdigital capacitors were also fabricated using these films. Loss tangents as low as 0.068 were recorded at 20 GHz.[68]

Sakurai *et al.* also used pulsed laser deposition to deposit ATN films on crystalline substrates.[71] The deposition temperature was higher than Koh *et al.* and Kim *et al.* (700 °C versus 550 °C) and the laser energy density was a factor of two higher. No oxygen pressure was given in the article by Sakurai *et al.*[71] In the report, $AgNbO_3$ films were grown on (001), (110)

and (111) $SrTiO_3$ substrates. The major fraction of all three films was epitaxial; however, each had small amounts of misorientation and/or secondary phase in the X-ray diffraction patterns. Overall, the films seemed to be better quality than Koh *et al.* and Kim *et al.* The dielectric permittivity was highest in (001) oriented films which was attributed to the polarization lying in-plane.[71] Interestingly, the polarization-electric field behavior showed different behavior for the films; the (001) films showed anti-ferroelectric behavior at high fields while the (110) and (111) films showed ferroelectric behavior. Contrary to what was observed by Koh *et al.*, the temperature dependent permittivity of (001) $AgNbO_3$ thin films was nearly identical to that observed in bulk materials.[72] It is unknown why the films from the two groups showed different phase transition temperatures as was evidenced through the dielectric data.

Thin films of ATN have also been deposited using a chemical solution deposition technique. This method was attempted to avoid the silver losses observed in some PLD growths. $AgNbO_3$, $Ag(Ta_{0.5}Nb_{0.5})O_3$, and $AgTaO_3$ films were deposited on $SrRuO_3/LaAlO_3$ (001) substrates. Films were epitaxial and free of secondary phases, however, some (110) oriented material existed.[73, 74] In contrast, films deposited on $Pt/Ti/SiO_2/Si$ substrates from the same solution were mostly natrotantite thus proving perovskite-like substrates necessary for ATN film growth.[70, 73-75] $Ag(Ta_{0.5}Nb_{0.5})O_3$ films on $SrRuO_3/LaAlO_3$ showed low losses and reasonable permittivities at room temperature.[75] Similar to what was observed by Koh *et al.*, the temperature dependent permittivity of these films showed significantly different behavior than the bulk counterpart.[70, 75] Figure 2-23 shows the aforementioned permittivity data for $Ag(Ta_{0.5}Nb_{0.5})O_3$.[70] As can be seen in the plot, the diffuse maximum associated with the M_2-M_3 phase transition has been suppressed ~ 250K. The structural origin of this discrepancy was not addressed by Telli *et al.* and will be the motivation of Chapter 4.

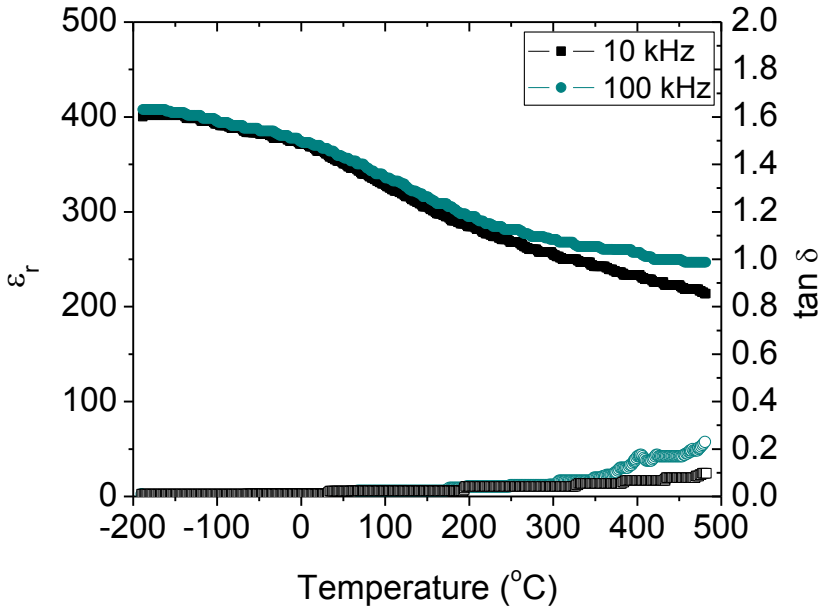

Figure 2-23 Temperature dependent permittivity of $Ag(Ta_{0.5}Nb_{0.5})O_3$ films on $SrRuO_3/LaAlO_3$ substrates grown by a chemical solution deposition method. Plot redrawn from the corresponding reference.[70]

Besides being an attractive candidate for microwave device applications, ATN also shows promise as a piezoelectric material. Piezoelectric materials are used in a variety of applications such as medical ultrasound transducers, miniaturized sensors and actuators, and sonar applications due to their ability to convert electrical energy into mechanical energy (and vice versa). However, most prominent piezoelectric ceramics contain lead. The European Union has banned lead from the majority of electronic components, prompting a world-wide search for a lead-free piezoelectric ceramic with comparable properties. Theoretical calculations using $AgNbO_3$ as an end member for $PbTiO_3$, $BaZrO_3$, and $BaTiO_3$ have shown that these solid solutions possess a morphotropic phase boundary with favorable piezoelectric properties [76], making $Ag(Ta_xNb_{1-x})O_3$ a potential end member candidate for lead-free piezoelectrics.

Chapter 3

Experimental Procedure

This chapter will detail the procedure used to deposit and characterize $Ag(Ta_xNb_{1-x})O_3$ thin films. A description of the solution preparation and film deposition process will be given. The structure of the films was characterized using X-ray diffraction and transmission electron microscopy (TEM); these experiments are described. The procedure used to measure the dielectric properties of the films is then detailed. Finally, the preparation and characterization of single crystals will be outlined.

3.1 Choice of substrates

The goal of this dissertation was to understand the relationship between octahedral tilt and strain in a material; therefore, careful consideration of the type of substrate was required. $Ag(Ta,Nb)O_3$ has a perovskite-like structure with a pseudo-cubic lattice parameter close to that of a variety of commercially available single crystal substrates. The room temperature lattice parameters for $AgNbO_3$ and $Ag(Ta_{0.5}Nb_{0.5})O_3$ are given in Table 3-1.

Table 3-1 Room temperature pseudo-cubic lattice parameters of $AgNbO_3$ and $Ag(Ta_{0.5}Nb_{0.5})O_3$.[40, 43]

	$AgNbO_3$	$Ag(Ta_{0.5}Nb_{0.5})O_3$
a	3.926 Å	3.906 Å
b	3.9654 Å	3.936 Å
c	3.912 Å	3.918 Å

The choice of a substrate was based on the lattice parameter mismatch with the film (i.e. strain in the film), crystal structure, and presence or absence of octahedral tilting. Table 3-2 shows a list of potential substrates considered in this dissertation. The strain in Table 3-2 is calculated from the room temperature lattice parameters of bulk $Ag(Ta_{0.5}Nb_{0.5})O_3$. Here, the strain state is defined by

$$\% \text{ strain} = \frac{a_{ATN} - a_{substrate}}{a_{substrate}}$$

Equation 3-1

where a_{ATN} is the room temperature lattice parameter of $Ag(Ta_{0.5}Nb_{0.5})O_3$ and $a_{substrate}$ is the room temperature lattice parameter of the substrate in question.

Table 3-2 Potential substrates with room temperature lattice parameters near that of ATN. The tilt system, crystal structure of the substrate is also shown. The calculated strain state in $Ag(Ta_{0.5}Nb_{0.5})O_3$ is shown for each pseudo-cubic axes.

Substrate	Lattice parameter (Å)	Crystal Structure	Tilt	% Strain in $Ag(Ta_{0.5}Nb_{0.5})O_3$		
				a	*b*	*c*
$LaAlO_3$	3.79	rhombohedral	$a^-a^-a^-$	-2.97	-3.726	-3.268
$SrTiO_3$	3.905	cubic	none	-0.023	-0.805	-0.332
$SrRuO_3$	3.93	rhombohedral	$a^-a^-c^+$	0.617	-0.170	0.306
$(Ba_{0.4}Sr_{0.6})TiO_3$	3.94	cubic	none	0.847	0.059	0.535
$KNbO_3$	3.989	cubic	none	2.127	1.329	1.811

3.1.1 Commercially available substrates

In this work, substrates were purchased from MTI Corporation (Richmond, CA) or Crystec (Germany). For relaxed films, the substrate of choice was $LaAlO_3$ (LAO) single crystals. $LaAlO_3$ is a rhombohedral perovskite (a = 3.79 Å) with the $a^-a^-a^-$ tilt system below 525 °C.

Although $LaAlO_3$ does undergo tilt, the comparatively large difference in lattice parameter between ATN and $LaAlO_3$ allowed for easy distinction between superlattice reflections due to the substrate and film. Electrical measurements were performed on relaxed films deposited on $SrRuO_3/LaAlO_3$ substrates. The lattice parameter of $SrRuO_3$ (SRO) is 3.93 Å, which is extremely close to the lattice parameter of ATN. In addition, $SrRuO_3$ has the tilt system $a^-a^-c^+$. As a result, $SrRuO_3$ was not used in structural measurements because it was impossible to differentiate between the superlattice reflections due to the ATN film and the superlattice reflections due to the $SrRuO_3$ layer.

Substrates for coherently strained films were required to have lattice parameters near that of ATN to enable a film of several tens of nm in thickness before dislocation formation.[25] In addition, a cubic substrate with no octahedral tilt was preferred. $SrTiO_3$ has a smaller lattice parameter than ATN, inducing a compressive strain of ~0.8% along the *b*-axis, ~0.3% along the *c*-axis and negligible strain along the *a*-axis. In addition, the oxygen octahedra of $SrTiO_3$ (STO) do not undergo tilt above 105 K. Using the Matthews-Blakeslee criterion,[25] the critical thickness of ATN on $SrTiO_3$ was ~60 nm (calculations based on the longest lattice parameter b ~ 3.94 Å). Therefore, $SrTiO_3$ was a good choice for films under compressive strain. For films under tensile strain, a solid solution of $SrTiO_3$ and $BaTiO_3$ was used, as it also had zero tilt. The $(Ba_{1-x}Sr_x)TiO_3$ with x=0.6 was chosen to produce ~ 0.8% tensile strain along *a*-axis, negligible strain along *b*-axis and ~ 0.5% strain about the *c*-axis in $Ag(Ta_{0.5}Nb_{0.5})O_3$.

3.1.2 Deposition of $SrRuO_3/LaAlO_3$

In some cases, commercial substrates were not available; one example is strontium ruthenate. $SrRuO_3$ was employed for electrical measurements as a bottom electrode due to the

fact that it is conductive, has the perovskite structure and yielded pure perovskite phase ATN films. The $SrRuO_3$ films were deposited via pulsed laser deposition using a procedure developed by Maria.[29] The deposition conditions for $SrRuO_3$ are shown in Table 3-3. Prior to deposition, the substrates were cleaned in acetone, methanol and isopropanol in an ultrasonic bath for 5 minutes each. The substrate was then attached to the heater mount using silver paste. $SrRuO_3$ films were deposited using a Compex KrF 102 laser with a wavelength of 248 nm and energy density of ~ 2 J/cm^2. A target made of $SrRuO_3$ ceramic (Target Materials, Inc., Columbus, OH) was used. The substrate temperature was 680 °C. The chamber pressure was 160 mTorr in the presence of 90% oxygen / 10% O_3. Based on the shape of the plume, the target to substrate distance was set to 8 cm. A deposition time of 10 minutes with a laser repetition rate of 10 Hz produced a film of approximately 200 nm thick. Films were inspected for second phases using X-ray diffraction.

Table 3-3 PLD deposition conditions used to grow $SrRuO_3$ films.

Parameter	Value
Deposition Temperature	680 °C
Chamber Pressure	160 mTorr
Target to Substrate Distance	8 cm
Deposition Time	10 min
Laser Fluence	200 mJ
Energy Density	~ 2 J/cm^2
Cool Down Pressure	100 mTorr
Ambient Gas	90% O_2 / 10% O_3

3.1.3 Deposition of (Ba,Sr)TiO_3 buffer layer

There are very few commercially available substrates that impose a tensile strain on ATN films that are also cubic and show no octahedral tilting. For measurements of the octahedral tilting in coherent films, it is helpful to use an untilted substrate to avoid interference of the superlattice lines. As a result, in this work, a buffer layer film of $(Ba_{1-x}Sr_x)TiO_3$ (BST) was deposited to provide a surface for coherent ATN films with tensile strains. Chemical solution deposited BST films were too porous to use for ATN deposition. Therefore, a pulsed laser deposition route was utilized. Powders of $(Ba_{1-x}Sr_x)TiO_3$ with x=0.6 were processed by Beth Jones at the Materials Research Laboratory. X-ray diffraction confirmed the material was free of second phase and had a lattice parameter of 3.94 Å. Powders were pressed into targets and sintered (also by Beth Jones). The final pellet was used as the target material for PLD depositions. The PLD procedure was similar to that used with $SrRuO_3$ depositions. Initial deposition parameters were based on those found in literature.[77-79] The pressure and target-to-substrate distance were adjusted from these base values to ensure the sample was positioned in the middle of the diffuse region of the laser plume. The final deposition parameters are shown in Table 3-4. After deposition, films were annealed at 1000 °C for 3 hours to improve the density and provide a smooth surface for deposition of ATN films.

Table 3-4 Pulsed laser deposition parameters used to grow of $(Ba_{0.4}Sr_{0.6})TiO_3$ thin films.

Parameter	Value
Deposition Temperature	780 °C
Chamber Pressure	100 mTorr
Target to Substrate Distance	7 cm
Deposition Time	10 min
Laser Fluence	200 mJ
Energy Density	~ 2 J/cm^2
Frequency	10 Hz
Cool Down Pressure	100 mTorr
Ambient Gas	90% O_2 / 10% O_3

3.2 Chemical solution deposition of $Ag(Ta_{1-x}Nb_x)O_3$ thin films

There are two reported techniques used to deposit $Ag(Ta_xNb_{1-x})O_3$ (ATN) thin films: pulsed laser deposition[65, 66, 71, 80] (PLD) and chemical solution deposition.[73, 75, 81] ATN films deposited via PLD typically show existence of secondary phase due to the volatility of silver. Therefore, chemical solution deposition was used to deposit films in this dissertation.

3.2.1 ATN solution preparation

The procedure for depositing $Ag(Ta_xNb_{1-x})O_3$ thin films using a chemical deposition route was introduced by Telli[70] in his doctoral dissertation and is outlined in Figure 3-1. Niobium (V) ethoxide ($Nb(OCH_2CH_3)_5$) [with a purity of 99.95% on a trace metals basis (Sigma-Aldrich, Inc.)] and tantalum (V) ethoxide ($Ta(OCH_2CH_3)_5$) [with a purity of 99.999% (metals basis) (Alfa Aesar)] or tantalum (V) ethoxide [purity of 99.98% (metals basis) (Sigma-Aldrich

Inc.)] were used. These precursors were added to high purity 2-methoxyethanol [purity ≥99.9% (Sigma-Aldrich, Inc. CHROMASOLV® line brand)]. The mixture was distilled at 110 °C for 2 minutes to remove low boiling point impurities such as water. The solution was then mixed at 110 °C for 1 hour. In a separate flask, silver nitrate [Premion® 99.9995% (metals basis) (Alfa Aesar)] or silver nitrate [purity 99.9999% (metals basis) (Sigma-Aldrich, Inc.)] was dissolved in anhydrous pyridine [98% (Sigma-Aldrich, Inc.)] at room temperature. This solution was then mixed for 1 hour at room temperature. The two solutions were combined and mixed at 110 °C for 5 minutes. The final molarity of the solution was typically 0.3 molar for the relaxed films and 0.1 molar for the coherently strained films. For structural measurements, films with x=0 and 0.5 were synthesized. Additional compositions, including x=0.16, 0.33, and 0.5 with 5% excess silver were deposited for electrical measurements.

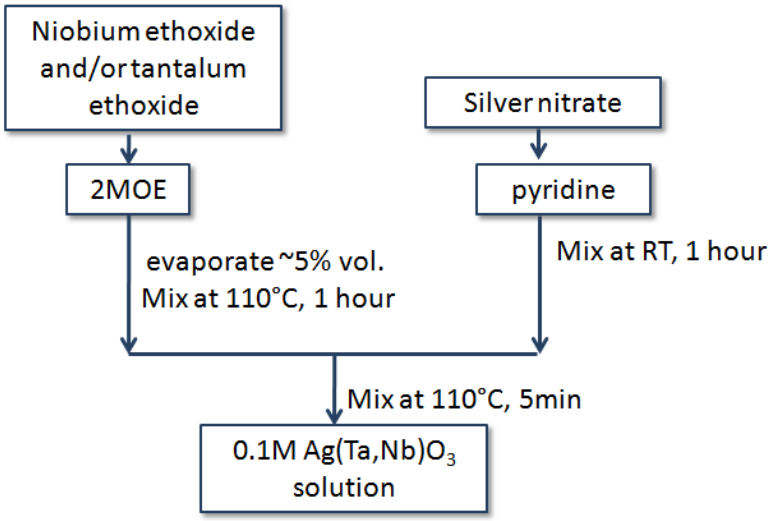

Figure 3-1 Flow diagram used to make $Ag(Ta_xNb_{1-x})O_3$ (ATN) solution. The niobium and tantalum precursors were mixed in 2-methoxyethanol (2MOE) at high temperatures for 1 hour. The silver precursor was dissolved in pyridine and mixed at room temperature for one hour. The two solutions were combined and mixed at 110 °C for 5 minutes. The final solution was 0.1 or 0.3 Molar.

3.2.2 ATN film deposition

Figure 3-2 outlines the procedure used to deposit ATN films on crystalline substrates. In this work, the films were deposited on $LaAlO_3$, $SrRuO_3/LaAlO_3$, $SrTiO_3$, $(Ba,Sr)TiO_3/LaAlO_3$ and $KTaO_3$ substrates. Previous work showed that perovskite based single crystal substrates facilitated growth of the ATN perovskite phase rather than a Ag-deficient natrotantite phase.[70] The (100) $LaAlO_3$, $SrTiO_3$ and $KTaO_3$ substrates were purchased from MTI Corporation (Richmond, CA).

Before deposition, the substrates were rinsed in acetone, dried with nitrogen, then rinsed in isopropanol and dried with nitrogen. They were then heated using a Rapid Thermal Annealing (RTA) furnace at 700 °C for 1 minute in air with a 10 °C/sec ramp rate. For films deposited on $SrTiO_3$, the solution did not wet to the surface very well. As a result, 2-methoxyethanol (2MOE) was spun on the substrate at 1500 rpm for 30 sec. This was followed by heating steps at 200 °C for 20 sec and 450 °C for 20 sec. All substrates were cooled to room temperature before dispensing the ATN solution. The solution was spun on the substrates at 1500 rpm for 30 sec. Two pyrolysis steps were performed at 200 °C and 450 °C, both for 20 sec. The films were then crystallized at 750 °C in flowing oxygen for 1 min. An RTA was used to ensure the ramp rate was 100 °C/sec. For the relaxed films, the 0.3 M solution was used; 5 layers were deposited and crystallized to reach a film thickness of ~225 nm. The coherently strained films were deposited using 0.1 M solution. One layer was used to obtain a film thickness of ~15 nm. The film deposition process is outlined in Figure 3-2.

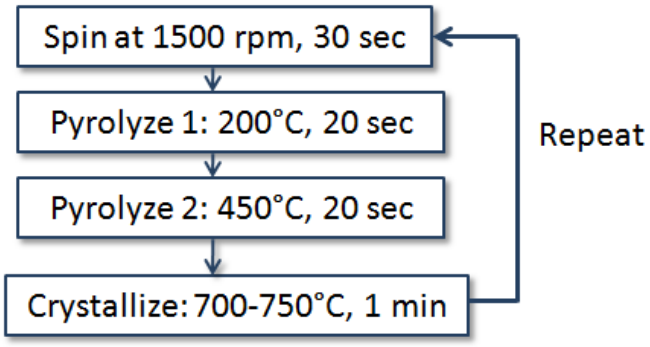

Figure 3-2 Flow diagram used to deposit ATN films on crystalline substrates.

3.3 Structural characterization

The quality of the crystalline nature of the ATN films was determined using X-ray diffraction and transmission electron microscopy (TEM). X-ray diffraction (XRD) measurements were initially performed on lab source diffractometers to determine the crystalline quality of the films. Select samples were measured using the synchrotron at the Advanced Photon Source at Argonne National Laboratory. TEM samples were examined at the University of Sheffield and National Institute of Standards and Technology (NIST).

3.3.1 2-circle X-ray diffraction

A Scintag Pad V powder diffractometer (Scintag Inc., Cupertino, CA) operating in θ-2θ mode was used to examine the out-of-plane orientation of the films. The radiation source was a Cu K_α X-ray tube. Typical XRD generator settings were 35 kV and 30 mA. Scans ranged from 15° – 90° 2θ with a 0.02° step size and a 1.0 sec count time. Samples were mounted to a zero background holder made from a highly miscut Si single crystal. These measurements were primarily used to determine if there were any second phases in the films. Due to a relatively large

beam spot, the samples had to be cleaved to 7 mm *x* 7 mm to remove edge effects (these tended to produce second phases and/or secondary orientations). Table 3-5 shows the PDF card numbers used to determine specific phases found in the films.

Table 3-5 XRD PDF card numbers for different materials used in this study.

Material	PDF #
$AgNbO_3$	00-022-0471
$Ag(Ta_{0.5}Nb_{0.5})O_3$	01-89-7738
Ag_2NbO_{11} (natrotantite)	00-021-1086
Ag	00-004-0783
$LaAlO_3$	01-073-3684
$SrTiO_3$	00-005-0634
$SrRuO_3$	01-088-0013
RuO_3	00-040-1290
$Ba_{0.5}Sr_{0.5}TiO_3$	00-039-1395

3.3.2 4-circle X-ray diffraction

Off-axis peaks were examined using a Philips X'Pert Pro MRD high resolution 4-circle diffractometer (PANalytical Inc., Tempe, AZ). The diffractometer was equipped with a graphite hybrid monochromator which selectively collimated Cu $K_{\alpha 1}$ radiation. Figure 3-3 shows a schematic of a 4-circle diffractometer. The sample sits on the ω axis, allowing it to rock back and forth. The detector sits on the 2θ axis. The χ axis moves along an arc. The sample can spin about an axis normal along the φ axis.

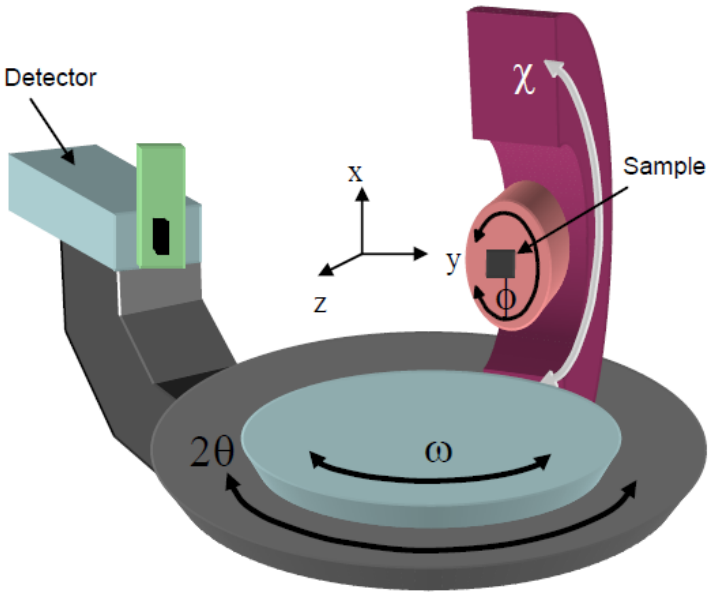

Figure 3-3 A schematic of a 4-circle diffractometer such as the Philips X'Pert Pro MRD used in this study.[82]

A zero background holder made from highly miscut Si was used to ensure there were no peaks from the sample mount. In order to align the beam and sample, first, the detector was aligned to the direct beam by rocking 2θ until a maximum in intensity was observed. Then the sample was moved along the z-axis into the path of the beam until the intensity was cut in half. A rocking curve about ω was performed to ensure the sample was oriented parallel to the beam. The sample was then moved to a substrate position (usually 002_{pc}) to align to an out-of-plane peak. Alignment scans were performed by moving the sample along the ω, 2θ, χ, *x*, and *y* axes. After the sample was aligned to the substrate, θ-2θ scans and rocking curve (ω) scans were performed on both the film and the substrate peaks. A scan range of 15° – 115° 2θ was utilized with a step size of 0.2° and 0.5 sec per step. Rocking curves were typically acquired over a 4° range in *ω* with a 0.01 step size and count time of 0.5 sec. Out-of-plane lattice parameters were determined from the peak positions of the rocking curve scans. In order to assess the epitaxy and in-plane lattice parameters of the film, the 101_{pc} and/or 202_{pc} peak was used. The sample was moved to χ =

45° and φ was rotated until the substrate peak was detected. Then, φ, χ and 2θ were adjusted to properly align the substrate peak. θ-2θ scans and rocking curves were performed to locate the film peak and determine the in-plane lattice parameter, respectively. A φ scan with range 360° was performed to prove epitaxy.

3.3.3 Synchrotron X-ray diffraction

Superlattice reflections due to octahedral tilting were detected using synchrotron X-ray diffraction. When ATN undergoes tilt, the unit cell is doubled ($a^0a^0c^+$ or $a^0b^-c^+$) or quadrupled ($a^-b^-c^-/a^-b^-c^+$) along one or more of the three principle pseudocubic axes. These tilt systems can be detected through superlattice reflections at ½ and ¼ positions of a Bragg peak. The intensity of these superlattice reflections is too weak to be detected using a lab source diffractometer, particularly for thin films. As a result, an X-ray beam with a large photon flux is necessary. For this work, the samples were measured at the Advanced Photon Source at Argonne National Lab due to the high brilliance of the X-ray beam that allowed for detection of weak superlattice peaks from thin layers. Temperature dependent X-ray measurements were performed at beamline 33BM using a Huber 4-circle diffractometer. The energy used in experiments was 21 keV, which allowed for a large region of reciprocal space to be mapped. The sample was mounted to a temperature stage designed for *in-situ* deposition of films.[83] Scans through reciprocal space or scans of any of the four motors were controlled using SPEC software.

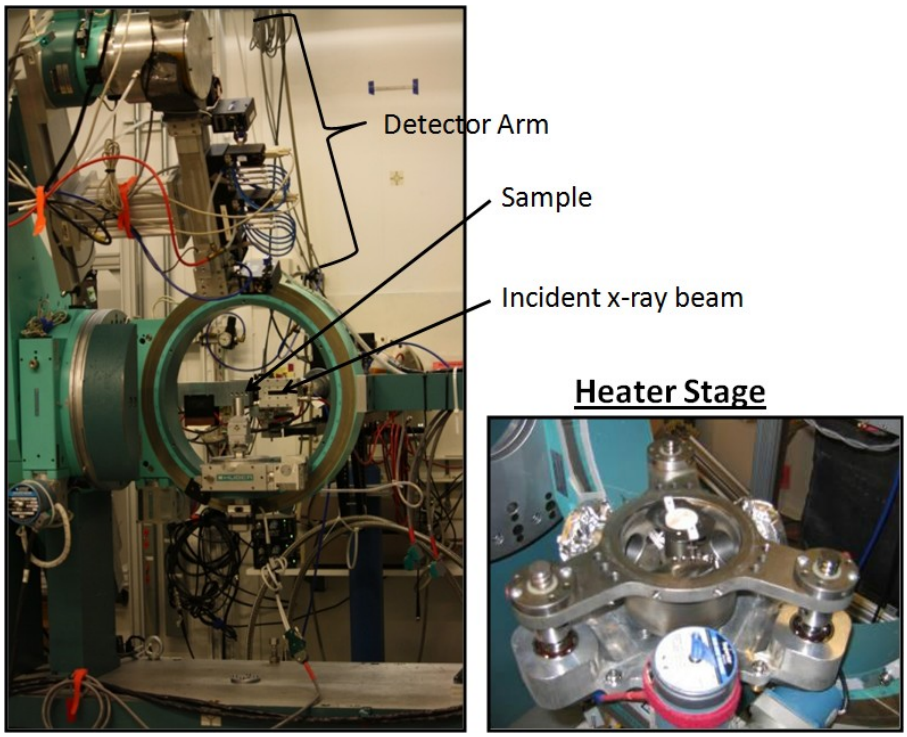

Figure 3-4 Huber diffractometer at the Advanced Photon Source; the setup shown here is installed at beamline 33BM.

Prior to performing measurements at temperature, the orientation of the crystal needed to be determined. An out-of-plane peak (008_{pc} or 004_{pc}) was located, followed by two off-axis peaks (typically 011_{pc} and 113_{pc}). The locations of these three peaks provided an alignment matrix so that the software could search for any other Bragg peak. Bragg peaks due to the ATN film were then located and recorded at room temperature. The sample was heated to 600 °C or 650 °C and measurements were recorded on cooling. Both out-of-plane and in-plane Bragg peaks were measured to enable d-spacing and lattice parameter calculations. All peaks were scanned in θ, 2θ, χ, and φ to ensure the sample was at the center of the diffractometer. Scans in θ (for out-of-plane peaks) and φ (for in-plane peaks) were recorded. In addition, scans in reciprocal space were also measured to look for peak splitting. Superlattice reflections characteristic of the T, O and M tilt phases were also recorded. These included $\frac{1}{2}\{ooe\}$, $\frac{1}{2}\{ooo\}$ and $\frac{1}{2}\{ooo\} \pm \frac{1}{4}\{00L\}$ peaks (o = odd, e = even). Peaks due to long range B-site cation ordering appeared at $\frac{1}{4}\{00L\}$ positions

flanking main Bragg peaks (i.e. 011). All superlattice peaks were aligned in θ, 2θ, χ, and φ. Phi and *L*-scans were recorded for each superlattice reflection.

The temperature of the heater was calibrated using the known thermal expansion coefficient of the substrate. At each temperature step, one out-of-plane Bragg peak and 2 to 3 off-axis Bragg peaks were recorded for the substrate. Using three Bragg peaks, the lattice parameter was calculated using the Nelson-Riley approach.[84] The lattice parameter was then compared to the reported lattice parameter based on the thermal expansion coefficient of the substrate and an error was estimated.[85, 86] For the experiments performed in this dissertation, the actual temperature differed by less than 10% from the heater stage reading.

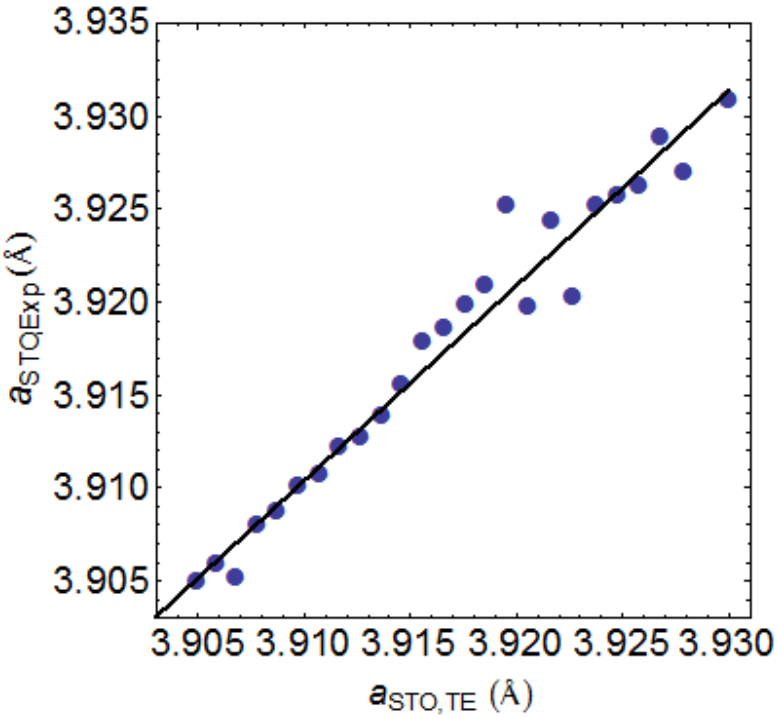

Figure 3-5 Experimental lattice parameter of $SrTiO_3$ ($a_{STO, Exp}$) vs. calculated lattice parameter based on the thermal expansion coefficient ($a_{STO, TE}$). The black line is a linear fit to the data. This data was used for temperature calibration of the heater stage in the high temperature X-ray diffraction experiments.

Phase transition temperatures of the ATN films were determined by calculating the d-spacing from Bragg peaks. Reciprocal space scans (i.e. *L*-scan, *HKL*-scan) of the film Bragg peaks were fit using a Pseudo-Voigt function:[87, 88]

$$I = A_o \left[\mu \frac{2}{\pi} \frac{w}{4(x-x_c)^2+w^2} + (1-\mu) \frac{\sqrt{4\ln 2}}{\sqrt{\pi} w} e^{\frac{-4\ln 2}{w^2}(x-x_c)^2} \right] + C$$

where A_o is the amplitude, w is the full width at half maximum of the peak, x_c is the center position of the peak, C is a constant and μ is the profile shape factor which will act as a weight between the Gaussian and Lorentzian components. For multiple peaks, a second set of parameters was added to the equation. In the case when peaks had a linear background, a linear term was added to the equation (e.g. A_1x). All peaks were fit using Mathematica. Peak positions were extracted from x_c values and the d-spacing and lattice parameters were calculated from x_c. Integrated intensities were calculated based on the peak fittings of the superlattice reflections. d-spacings and integrated intensities were plotted as a function of temperature in order to determine the phase transition temperatures.

3.3.4 Transmission electron microscopy

For transmission electron microscopy (TEM) observation, cross-sectional and plan-view thin foils were prepared by conventional sample preparation techniques including polishing and argon ion beam milling using a Gatan ‘duo ion mill’ operated at 6 kV with a combined gun current of 0.6 mA. The Gatan ‘duo ion mill’ – a high angle, relatively slow ion-beam thinner – reduces the possibility of *in-situ* ion beam heating which may modify the structures of the ATN and SRO layers. The sample microstructures at room temperature were characterized in Philips EM430 and JEOL 3010 instruments using selected area electron diffraction and diffraction

contrast imaging. The low temperature diffraction experiment was carried out in a liquid He sample holder using a Hitachi H-8000 TEM. The diffraction patterns were collected every 10 K. High resolution imaging and electron diffraction were performed in a JEOL 2010f TEM, operated at 200 kV. Simulations of diffraction intensities were accomplished using a Windows version of EMS. TEM preparation and imaging were performed by Yisong Han at the University of Sheffield.

High-resolution phase-contrast TEM (HRTEM) and high-angle annular dark-field (HAADF) STEM images were also utilized in this work courtesy of Igor Levin at NIST. For these experiments cross-sectional samples were prepared using conventional mechanical sectioning, polishing, and dimpling to a thickness of 30 microns. The thinning was completed until perforation in the Gatan Precision Ion Polishing System (PIPS) operated at 4.5 kV and an ion-beam angle of 4.5 degree. Previously, this procedure was shown to provide artifact-free TEM samples of bulk $AgNbO_3$ and $Ag(Nb,Ta)O_3$.[40, 43] The samples were analyzed using an FEI Titan TEM/STEM operated at 300 kV. Both HRTEM and HAADF STEM images were recorded with the incident electron beam parallel to the [100] zone axis. HAADF images are formed using electrons scattered to high angles and therefore are sensitive to atomic numbers of the scattering atoms; therefore, this technique is often referred to as Z-contrast imaging.

3.4 Electrical property measurements

Dielectric property measurements of the ATN films were performed on capacitor structures. This section will describe the process of depositing the top electrodes as well as the technique use to obtain dielectric measurements.

3.4.1 Lift-off process of top electrodes

The top electrodes were patterned using a photolithographic lift-off process. The films were first heated at 100 °C for 30 seconds to dry the surface. Then LOR 5A lift-off resist (MicroChem Corp. Newton, MA) was spun on the sample at 4000 rpm for 40 seconds. This resist was cured at 180 °C for 2 minutes. Photoresist (Shipley 1811) was then spun on at 4000 rpm for 40 seconds and soft baked at 100 °for 1 minute. A Suss MJB3 mask aligner was used to generate UV exposure from a Hg vapor lamp operating at 300 W for 90 seconds. The mask pattern provided circular features ranging from ~50 – 200 μm in diameter. The photoresist and LOR were developed using CD-26 (Shipley, Marlboro, MA) for ~ 2 minutes. After this, samples were rinsed in DI water and dried with nitrogen. The pattern was checked in a microscope to ensure proper exposure and development.

Access to the bottom electrode could not be obtained by a wet etch method since the ATN film did not etch in either a buffered HF etch or HCl. As a result, a deep scratch was made on the surface of the film in order to expose the $SrRuO_3$. During sputter deposition of the Pt, a conductive layer coated the sides of the scratch mark, thus making a connection to the bottom electrode.

After patterning, platinum was sputter deposited using a Kurt J. Lesker CMS-18 sputter system. The metal was DC bias sputtered from a Pt target at a power density of 4.4 W/cm^2 at 2.5 mtorr in Ar. The deposition was performed at room temperature with a target-to-substrate distance of ~ 120 mm. The 7 minute deposition time produced a Pt layer ~ 1000 Å thick. After sputtering, the sample was soaked in acetone to remove the Pt from unwanted areas. The film was rinsed and dried with N_2. To remove excess LOR, the sample was soaked in CD-26, rinsed with water and then dried. The samples were annealed at 500 °C for 1 minute in a rapid thermal annealing furnace to improve the interface between the metal and the dielectric film.

3.4.2 Dielectric measurements on ATN films

Dielectric property measurements were performed on capacitor structures with $SrRuO_3$ acting as the bottom electrode, the ATN film was the insulating material and Pt was the top electrode. The permittivity was calculated using

$$\varepsilon_r = \frac{Ct}{\varepsilon_o A}$$

where C is the measured capacitance in Farads, t is the capacitor thickness, ε_o is the permittivity of free space and A is the area of the top electrode.

Contact to the bottom and top electrodes were made using point probes (Probing Solutions, Inc. NV). Capacitance and loss measurements were performed using Hewlett-Packard 4192A LF Impedance Analyzer (Hewlett-Packard, Palo Alto, CA). Measurements were made from 0.1 kHz to 100 kHz with a 30 mV oscillating voltage.

All temperature dependent measurements were measured using a HP4284 LCR meter at 10 and 100 kHz with a 30 mV oscillating voltage. High temperature measurements were made while heating the sample from room temperature to 300 °C at a rate of 3 °C/min using a probe station with a heating stage. The low temperature measurements were conducted in a Delta Design 9023 furnace. The sample was heated to 200 °C and the dielectric measurements were performed while cooling to -170 °C at 3 °C/min.

Polarization-electric field measurements were obtained using RT66A Standardized Ferroelectric Test System (Radiant Technologies Inc. Albuquerque NM). Electric field values as high as 300 kV/cm were applied. All measurements were performed at 100 Hz.

3.4.3 Wire bonding

To conduct electrical measurements at temperature, several top electrode spots were wire bonded to a DIP package using gold wire. A wedge bonder (K&S model 4123), Kulicke & Soffa Industries Inc. was used. The first bond was applied to the contact pad on the DIP package; the second bond was applied to the top electrode. Table 3-6 shows the wire-bonding parameters used in this work.

Table 3-6 Parameters used to wire-bond the electrodes of a sample to the contact pads on the DIP package.

Set point	1st bond	2nd bond
Loop = 2.5 Temperature = 50 °C		
Search	2	1
Force	7.4	6.7
Time	5.8	4.8
Power	4	5

3.5 Single crystals

Part of the work in this dissertation involved structural studies on single crystals of $AgNbO_3$. $AgNbO_3$ single crystals were donated by Antoni Kania at the University of Silesia in Poland. $(Ag_{1-x}Li_x)NbO_3$ single crystals were donated by Satoshi Wada at the University of Yamanashi in Japan. The crystals were $\{001\}_{pc}$ oriented. Laue diffraction was required to determine the orientation of the crystal to ensure it was cut and polished appropriately. Synchrotron X-ray diffraction was performed at Argonne National Laboratory to monitor the superlattice reflections as a function of electric field.

3.5.1 Laue diffraction

Samples were mounted to a goniometer that allowed for small adjustments in x, y, and tilt angle. The diffractometer used was a Laue diffractometer (Multiwire Laboratory, Ltd. Ithaca, NY) with the software program Northstar to analyze the data in real-time and obtain still images. Using the real-time function, the position and tilt of the crystal was adjusted until it was aligned directly along the [001] crystallographic axis.

3.5.2 Single crystal sample preparation

After the crystal was aligned along <001>, an initial polishing step was performed while the sample was still in the Laue sample mount. The crystal was then removed from the sample mount and further polished on both sides of the crystal using 600 grit SiC polishing powder. The sample was polished to thickness of 0.5 – 1.0 mm.

Platinum electrodes were deposited on both sides of the crystal using the Bal Tec SDC 050 Sputter coater. Prior to deposition, the edges of the crystal were taped with Kapton tape to prevent a conductive pathway along the sides. A Pt thickness of ~1000 Å was deposited on each side. The samples were then annealed at 500 °C for 30 minutes in a box furnace.

3.5.3 Electrical characterization of single crystals

Prior to performing structural measurements under the application of an electric field, initial electrical measurements were performed on the $AgNbO_3$ and $(Ag_{0.95}Li_{0.5})NbO_3$ crystals to ensure that the crystal quality was sufficient. Permittivity and loss tangent were recorded as a function of temperature in a Delta Design 9023 furnace. An HP4284 LCR meter at 10 and 100

kHz with a 1 V oscillating voltage was used. Polarization-electric field measurements were acquired on a custom polarization measurement system. This system allowed for a time dependent applied field with voltage amplifier (TREK 609C-6 HV/DC amplifier). The crystals were immersed in Galden oil (H7-200 Solvay Solexis, Thorofare, New Jersey) to prevent breakdown in air. Leakage current as a function of applied field and time was also measured. An HP4140B pA meter/DC voltage source with a Kepco (BOP 1000M) amplifier were used. Current values were determined at different voltages with a four minute wait time prior to recording data.

3.5.4 Synchrotron X-ray diffraction of single crystals

In order to search for the roto-electric effect in $AgNbO_3$ single crystals, an experiment measuring tilt angle as a function of electric field was designed. A method of calculating tilt angle in perovskite materials using synchrotron X-ray diffraction was outlined by May.[22] In that work, the intensity of the superlattice reflections due to octahedral tilting was compared to the intensity calculated from the structure factor. Intensity ratios between different peaks allowed for the experimental calculation of tilt angle. A comparable method was adopted here. The high brilliance, monochromatic X-ray source of a synchrotron was required for these experiments to observe changes in superlattice reflection intensity and position. Beamline 33BM at the Advanced Photon Source at Argonne National Lab was used.

A sample holder was designed to allow X-ray measurements to be collected while the sample was exposed to an electric field. The crystal was first mounted to a glass slide using CircuitWorks® CW2400 silver epoxy. Two small wires were connected to the top and bottom electrode surfaces of the crystal using epoxy. This setup was then mounted to the goniometer head of the Huber 4-circle diffractometer. SPEC software was used to control the voltage and manipulate the θ, 2θ, χ and φ motor positions. The voltage was supplied using a Keithley 2410

1100 V source meter (Keithley, Cleveland, Ohio). This device allowed for simultaneous measurements of source voltage as well as current through the sample. By recording current, the crystal could be monitored for potential dielectric breakdown.

The orientation of the crystal was determined by first aligning θ, 2θ and χ to an out-of-plane peak (004_{pc}). Then, two in-plane peaks (101_{pc} and 113_{pc}) were located and the motor positions aligned to these peaks. The $AgNbO_3$ crystal was indexed using pseudo-cubic lattice parameters. A number of superlattice reflections were then located and their positions were recorded. Repeat measurements were performed at 0 V at each peak to test for reproducibility. φ scans were then recorded at different electric field values. A dramatic increase in current was observed when the electric field was applied and the X-ray beam was illuminating the sample. Therefore, the amount of time that a voltage was applied to the sample was kept to a minimum to prevent premature breakdown. Numerous scans at 0 V were performed between voltage steps to increase the statistical significance of the measurement.

Chapter 4

Phase Transitions in Relaxed $Ag(Ta_xNb_{1-x})O_3$ Thin Films*

The goal of this dissertation is to study tilt transitions in biaxially strained $Ag(Ta_xNb_{1-x})O_3$. However, before such studies can be performed, a solid understanding of the structure and phase transitions in relaxed films is required. This chapter describes characterization of relaxed epitaxial films. First, simulations of ATN diffraction patterns were examined and the importance of peak splitting and superlattice reflections discussed. Then, TEM and X-ray diffractions results of relaxed ATN films are presented. Finally, a discussion of the structure of such films is given.

4.1 Simulated diffraction studies of $Ag(Ta_xNb_{1-x})O_3$

$Ag(Ta_xNb_{1-x})O_3$ (ATN) has a perovskite-like structure that undergoes slight distortions as a function of temperature and composition. The subtle changes can be detected through high-resolution diffraction methods. In these distorted perovskite structures, the material is typically poly-domain. An example of this for $AgNbO_3$ is shown in Figure 4-1. The figure demonstrates that the 002 plane of the prototypical cubic perovskite is equivalent to the 008_o and 220_o planes of the orthorhombic M_1 phase in $AgNbO_3$. (Unless otherwise noted, all Miller indices will be referenced to the pseudo-cubic unit cell.) In reality, there are slight differences in the spacings of these two planes as was described in Section 2.3.3.2. Figure 4-2 shows a simulated diffraction pattern near the 002 (i.e. 008_o and 220_o) peaks of $AgNbO_3$. In an ideal situation, clear splitting is observed (Figure 4-2a), however, most X-ray diffraction peaks exhibit broadening due to

* Parts of this chapter appear in Y. Han, I. M. Reaney, R. L. Johnson-Wilke, M. B. Telli, D. S. Tinberg, I. Levin, D. D. Fong, T. T. Fister, S. K. Streiffer, and S. Trolier-McKinstry, *Journal of Applied Physics*, **107** (2010)

instrumental effects and the two peaks may look more like that shown in Figure 4-2b. These can be resolved using peak fitting functions (for example pseudo-Voigt or Gaussian).

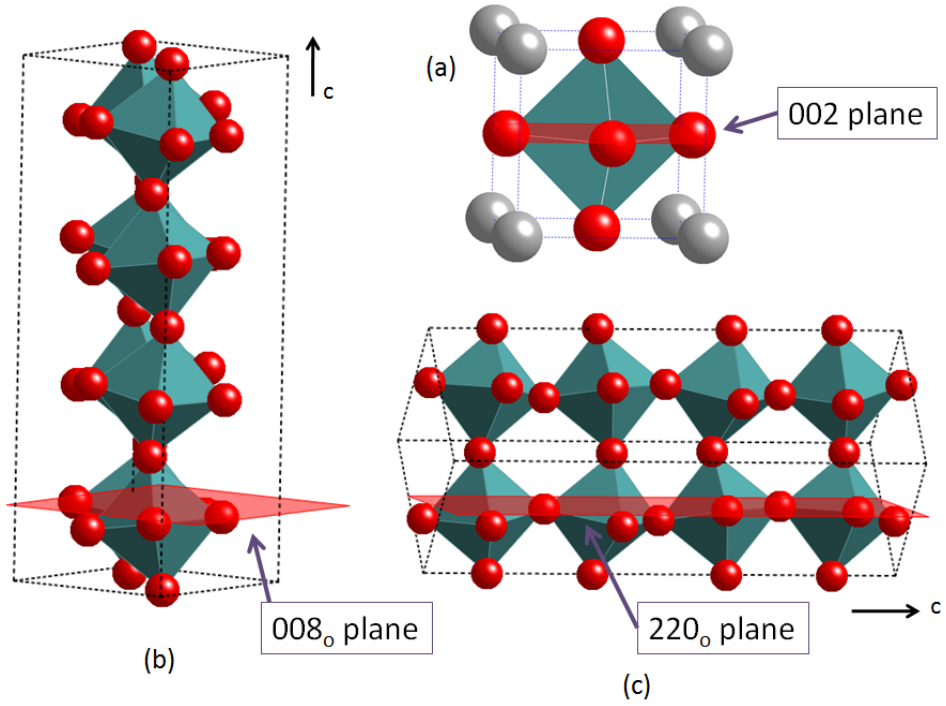

Figure 4-1 Simulated multi-domain structure of $AgNbO_3$. The (a) 002 pseudocubic plane is equivalent to the (b) 008_o and (c) 220_o orthorhombic planes in the M_1 phase. The slightly different spacing of these two planes will lead to dissimilar peak positions in diffraction patterns.

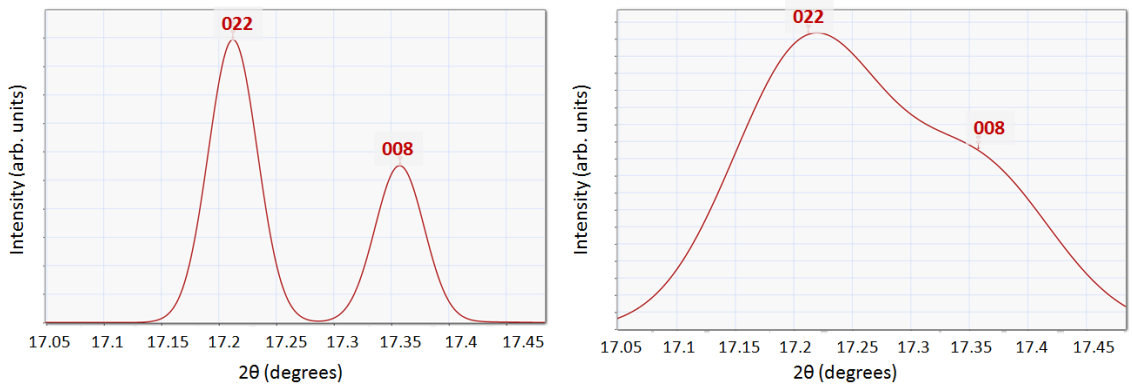

Figure 4-2 Simulated X-ray diffraction pattern of $AgNbO_3$ in the M_1 phase near the 002 peak for a photon energy of 21 keV. (a) In the ideal case, clear peak splitting is observed due to the poly-domain structure. However, (b) instrumental broadening causes the two peaks to overlap, so they are not as readily distinguishable.

Depending on the phase of ATN, most of the pseudo-cubic Bragg reflections will exhibit splitting due to the poly-domain nature of the structure. Table 4-1, Table 4-2, and Table 4-3 show the equivalent orthorhombic or tetragonal indices for the 002, 101 and 111 pseudo-cubic reflections, respectively. These tables also include $\Delta 2\theta$ that was calculated for an X-ray energy of 21 keV, the energy used in most experiments throughout this dissertation. The important thing to note is the relatively small degree of splitting observed in the M_3 phase as compared to the M_2 and M_1 phases. The origin of this discrepancy is due to displacement of B-site cations as was described in Section 2.3.3.2. Such a difference allows for easy distinction between the M_3 and M_2 phases. In this work, peak splitting was a useful tool in determining phase transition sequences in the ATN films.

Table 4-1 The equivalent orthorhombic and tetragonal peaks for the 002 pseudo-cubic reflection. The split (in degrees 2θ) is also given. Values were calculated for $AgNbO_3$ with a photon energy of 21 keV. When three reflections are observed, as in the O phase, the split between the first two peaks and between the second two peaks are listed.

	002_c	Δ2θ (degrees)
M_1 (26 K)	$220_o + 008_o$	0.1455
M_2 (423 K)	$220_o + 008_o$	0.1453
M_3 (573 K)	$220_o + 008_o$	0.0036
O phase (645 K)	$004_o + 040_o + 400_o$	0.0351, 0.0154
T phase (733 K)	$002_T + 220_T$	0.056

Table 4-2 The equivalent orthorhombic and tetragonal peaks for the 101 pseudo-cubic reflection. The split (in degrees 2θ) is given for $AgNbO_3$ with a photon energy of 21 keV. The first Δ2θ value represents the split between the first two reflections. The second Δ2θ refers to the difference between the second two peaks.

	101_c	Δ2θ (degrees)
M_1 (26 K)	$020_o + 114_o + 200_o$	0.113, 0.0102
M_2 (423 K)	$020_o + 114_o + 200_o$	0.1104, 0.007
M_3 (573 K)	$020_o + 114_o + 200_o$	0.0358, 0.0382
O phase (645 K)	$022_o + 202_o + 220_o$	0.0055, 0.0123
T phase (733 K)	$111_T + 020_T$	0.0197

Table 4-3 The equivalent orthorhombic and tetragonal peaks for the 111 pseudo-cubic reflection. The split (in degrees 2θ) is given for $AgNbO_3$ with a photon energy of 21 keV. The tetragonal and orthorhombic phases do not show peak splitting along the 111 pseudo-cubic direction.

	111_c	Δ2θ (degrees)
M_1 (26 K)	$024_o + 204_o$	0.1006
M_2 (423 K)	$024_o + 204_o$	0.1264
M_3 (573 K)	$024_o + 204_o$	0.0606

$Ag(Ta_xNb_{1-x})O_3$ undergoes multiple tilt systems as a function of temperature (Section 2.3), each of which can be detected using superlattice reflections in diffraction patterns. Table 2-2 lists the types of reflections that are present for in-phase and anti-phase rotations. In ATN, anti-phase tilting is observed in the M phases and in the O phase, which have the tilt systems $a^-b^-c^-/a^-b^-c^+$ and $a^0b^-c^+$, respectively. Based on Glazer's rules, anti-phase rotations should produce reflections of the type ½{*ooo*}. Figure 4-3a shows simulated diffraction pattern around the ½113 pseudo-cubic reflection. CrystalDiffract and CrystalMaker were used to model the different phases of $AgNbO_3$ based on crystallographic data in the corresponding references.[43, 44] The figure clearly shows finite intensity of the ½113 reflection when the material is in the M_1, M_2, M_3 and O phases. However, no signature is observed in the T phase. In-phase tilt should lead to ½{*ooe*} type reflections. Figure 4-3b shows that the T phase has a dominant ½312 peak compared to the other phases, as would be expected for an $a^0a^0c^+$ arrangement. The M and O phases do show finite intensities for ½312 as shown in the inset, however, they are significantly weaker than that of the T phase. Mixed tilt systems (i.e. systems that exhibit both in-phase and anti-phase tilting), such as the one found in the O phase, have the tendency to produce reflections of the type ½{*oee*}.[3] Based on the simulations for ½212, one would expect to see finite intensity of this peak in the O phase only (Figure 4-3c). These three superlattice reflections can be

used to differentiate the tilt phases in the ATN system. In this work, the ½{*ooo*} and ½{*ooe*} peaks were widely used to distinguish phases.

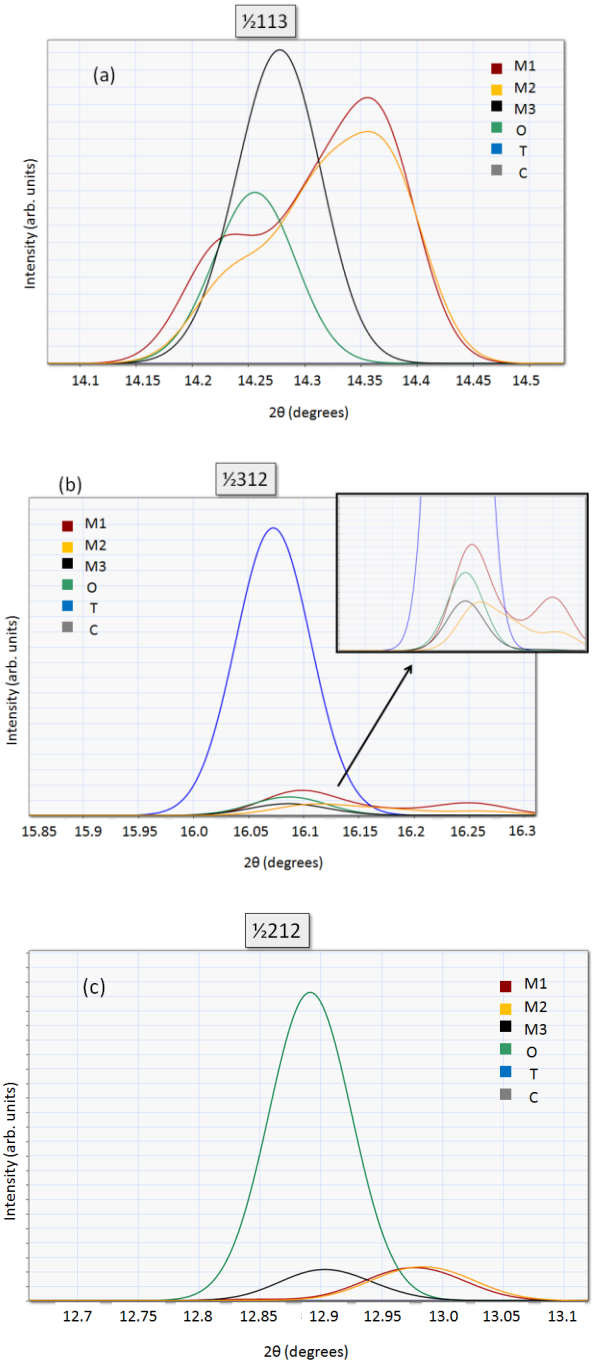

Figure 4-3 Simulated X-ray diffraction patterns of the (a) ½113, (b) ½312, and (c) ½212 pseudo-cubic superlattice reflections.

4.2 Results and discussion

Telli *et al.* showed that the dielectric behavior of ATN thin films differs from that of bulk ceramics, which suggests that the two may have different phase transition sequences.[75] However, no direct evidence for a change in the symmetry/tilt system in such films has been reported. The purpose of this chapter is to combine electron diffraction and high resolution X-ray diffraction to determine the structure and tilt system of ATN thin films as a function of temperature and thereby interpret the dielectric behavior.

4.2.1 Temperature dependent permittivity

The procedure for depositing and characterizing $Ag(Ta_xNb_{1-x})O_3$ (ATN) thin films was described in detail in Chapter 3. ATN films with thicknesses from 100 nm – 250 nm were prepared on $LaAlO_3$ substrates. As reported previously, the ATN thin films investigated here showed high permittivities over a wide temperature range, with a broad permittivity maximum below -170 °C (~100 K), Figure 4-4.[75] The minor discontinuity of the data near room temperature results from differences in measurement apparatus and is not a characteristic of the film. The peak permittivity of the film occurs at a significantly different temperature than in bulk, where the diffuse maximum occurs near 40 °C (~ 315 K) in response to the M_2-M_3 transition (Figure 4-4).[41, 46]

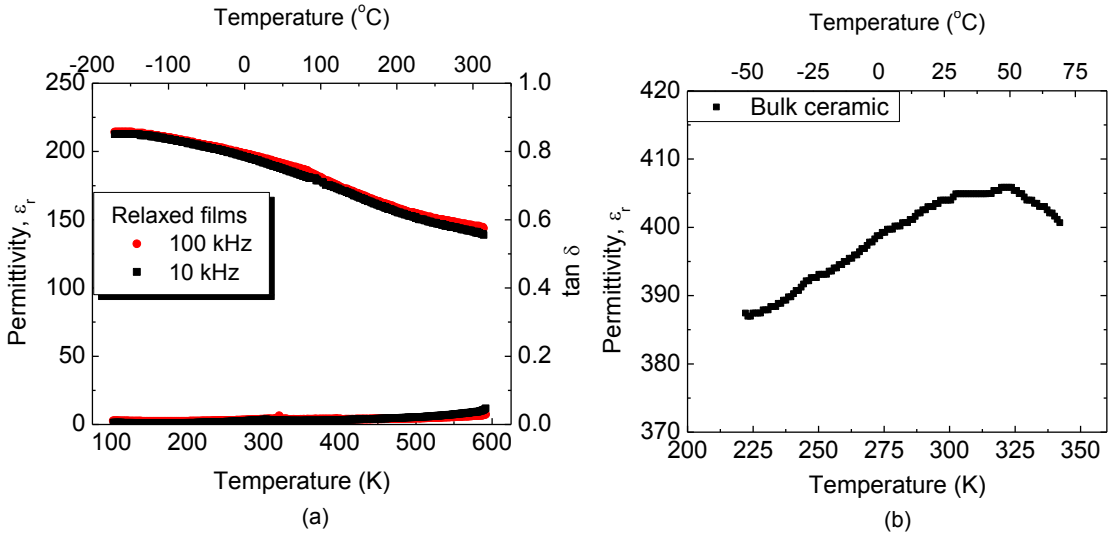

Figure 4-4 Temperature dependent permittivity for $Ag(Ta_{0.5}Nb_{0.5})O_3$ (a) thin films and (b) bulk ceramics. (Bulk data from [53]).

4.2.2 Room temperature X-ray diffraction

The resulting films are epitaxial with room temperature pseudo-cubic lattice parameters of 3.929 Å (out-of-plane) and 3.914 Å (in-plane). Figure 4-5a shows the out-of-plane θ-2θ scan of $Ag(Ta_{0.5}Nb_{0.5})O_3$ on (001) $LaAlO_3$ substrates. The films are free of secondary phases. Epitaxy was demonstrated by the phi scan shown in Figure 4-5b. The rocking curve FWHM of the 002 ATN peak is 1.22° (Figure 4-4a). Figure 4-6b shows the rocking curve of the ATN 202 peak which exhibited a FWHM of 1.44°.

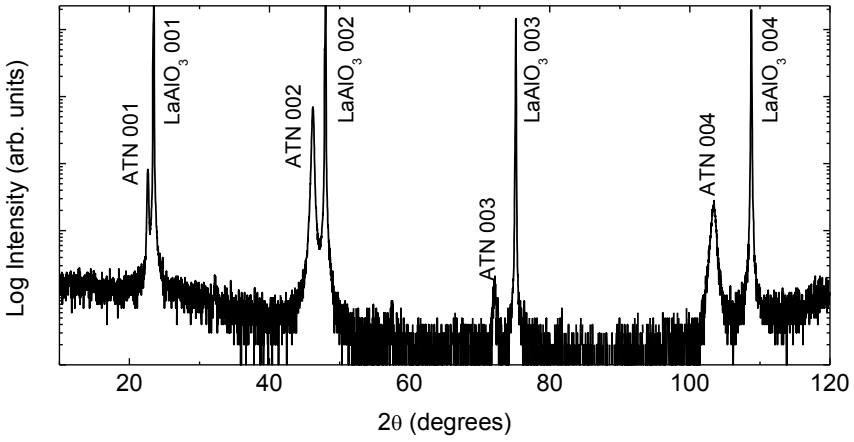

(a)

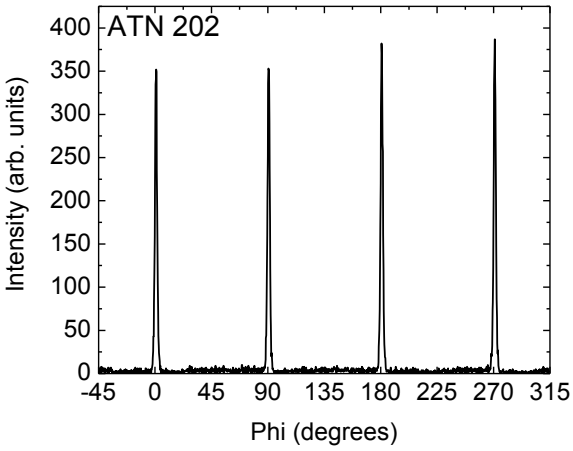

(b)

Figure 4-5 (a) θ-2θ and (b) φ scan for $Ag(Ta_{0.5}Nb_{0.5})O_3$ film on (001) $LaAlO_3$.

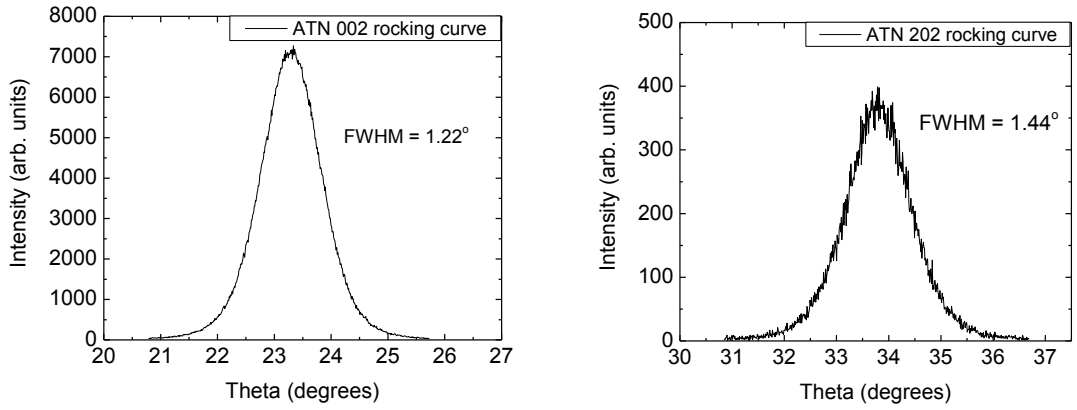

(a) (b)

Figure 4-6 Rocking curves and the corresponding FWHM of ATN (a) 002 and (b) 202 peaks.

4.2.3 Room temperature transmission electron microscopy

Figure 4-7a and Figure 4-7b are two-beam dark-field images of plan-view and cross-sectional TEM foils from an ATN/SRO/LAO sample crystallized at 700 °C. Figure 4-7b reveals sharp ATN/SRO and SRO/LAO interfaces, suggesting limited interdiffusion. However, there is evidence of planar defects parallel to the substrate surface (arrowed). These are believed to arise from the multi-step spin-coating/crystallization process adopted in the chemical solution deposition route. The plan and cross-sectional views of this sample also illustrate that the ATN layer is composed of slightly misoriented regions with interfaces roughly normal to the substrate surface, 200 nm to 500 nm in size. Similar size regions were also observed for ATN films deposited directly on LAO substrates and crystallized at 700 °C, as shown in Figure 4-7c.

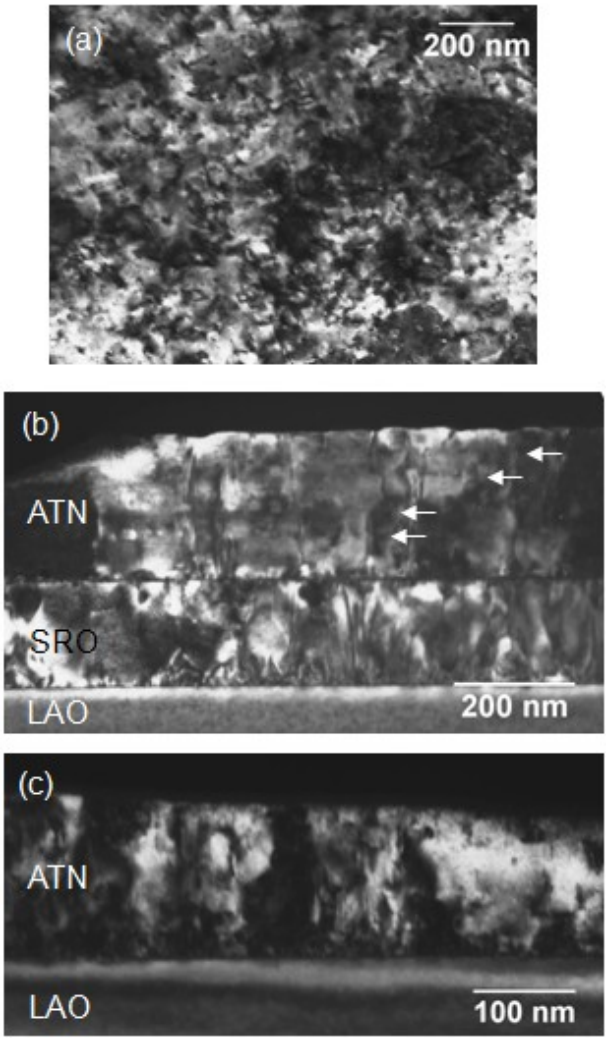

Figure 4-7 (a) Plan-view and (b) cross-sectional TEM images of an ATN/SRO/LAO sample crystallized at 700°C and (c) cross-sectional TEM image of an ATN/LAO crystallized at 700°C. Arrows mark planar defects.

4.2.4 ½311 ± ¼{00*L*} reflections due to tilt

To investigate the tilt system of the ATN layers, electron diffraction data were recorded from both plan-view and cross-sectional samples of films crystallized at 700°C. Diffraction patterns recorded in [103]-type orientations (Figure 4-8) featured superlattice reflections with diffraction vectors of a general form $g = ½(ooo) \pm ¼\{00L\}$ ("o" refers to odd *hkl* indexes) as

expected for bulk *Pbcm* structure with $a^-b^-c^+/a^-b^-c^-$ tilting (see Section 2.3.3.1). However, these superlattice reflections (Figure 4-8a) are much weaker compared to bulk (Figure 4-8b) and acquire streaks of diffuse intensity along the *c*-axis, which suggests that both the tilting angle and the correlation length for a complex sequence of in-phase and antiphase octahedral rotations around *c*-axis in thin films is appreciably reduced.

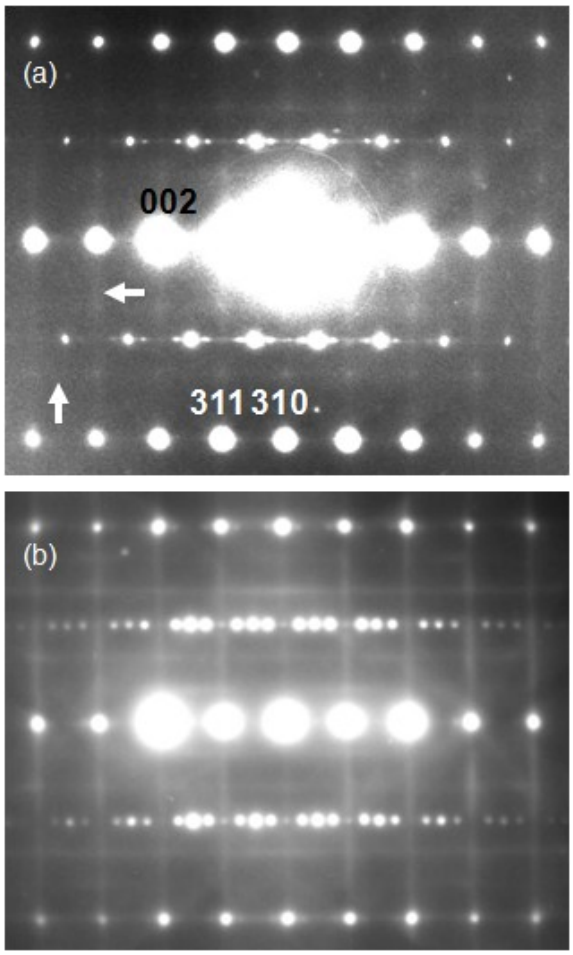

Figure 4-8 Electron diffraction patterns recorded along the [130] zone axis from (a) an ATN/SRO/LAO thin film and (b) an $Ag(Ta_{0.5}Nb_{0.5})O_3$ bulk sample, respectively. The pattern for a thin film exhibits two types of pronounced diffuse scattering: [001] rods passing through ½113-type reflections and streaks (indicated using arrows) that represent intersections of {100} diffuse sheets by the Ewald sphere. The rods are associated with a tilting disorder around *c* whereas the diffuse sheets reflect chain-like correlations among ⟨100⟩ components of local B-cation displacements. The faint ring in (a) is likely due to redeposited Ag or Ag_2O.

Figure 4-9 is a high resolution XRD profile showing the region of reciprocal space around the $Ag(Ta_{0.5}Nb_{0.5})O_3$ ½311 peak. For bulk ATN, superstructure satellites of the type ±¼(00*L*) are expected to flank the main perovskite reflection; from simulations, the intensity of these satellites should be approximately a factor of 3 less than that of the ½311 peak. However, the intensity experimentally observed at the ½311 ± ¼(00*L*) positions in thin ATN films at room temperature (arrowed in Figure 4-9) are approximately a factor of 10 less than the ½311, consistent with the electron diffraction data. The existence of the ½311 ± ¼(00*L*) reflections confirms that the films are in one of the M phases at room temperature.

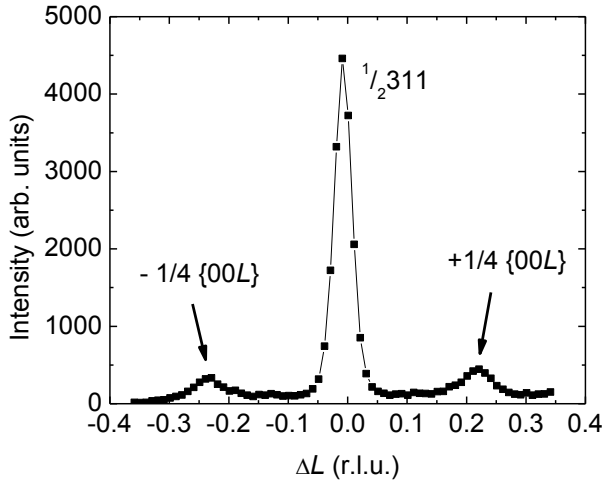

Figure 4-9 Diffraction from an epitaxial $Ag(Ta_{0.5}Nb_{0.5})O_3$ film on (001) $LaAlO_3$. The difference in reciprocal lattice L [Δ*L* (rlu)] is given with respect to the $LaAlO_3$ substrate. The quarter-order reflections appear as satellites on the ½311 peak.

4.2.4.1 ± ¼{00L} reflection due to B-site cation ordering

Surprisingly, diffraction patterns of thin films recorded along low-index ⟨100⟩ and ⟨110⟩ zone axis directions (Figure 4-10a and b) exhibit no detectable ¼(00*L*) reflections, whereas

discrete ¼(00*L*) spots are clearly observed in the analogous patterns for bulk crystallites (Figure 4-10c, d, e). The structural origin of this discrepancy becomes evident from computer simulations of electron/x-ray diffracted intensities: in the ATN system; $g = ½(ooo)+¼\{00L\}$ reflections are dominated by octahedral tilting whereas $¼\{00L\}$ reflections are determined entirely by displacements of cations (Ag, Nb, Ta) from their central positions in the ideal perovskite structure (see Section 2.3.3).[43] Thus, it is believed that the magnitudes of cation off-center displacements in these thin films are significantly reduced compared to bulk. Figure 4-11 shows the x-ray diffraction pattern scanned in the L-direction about the 011 peak. As is seen in the figure, there is noticeable intensity at the $¼\{00L\}$ positions, however, this intensity is about 0.016% of the intensity of the 011 peak. The relatively weak quarter order reflection in films suggests that there exists partial ordering of the B-site cations, however, this ordering is short range, as is typical of the M_3 phase. The data suggest that ATN films are in the M_3 phase, rather than the M_2 phase at room temperature.

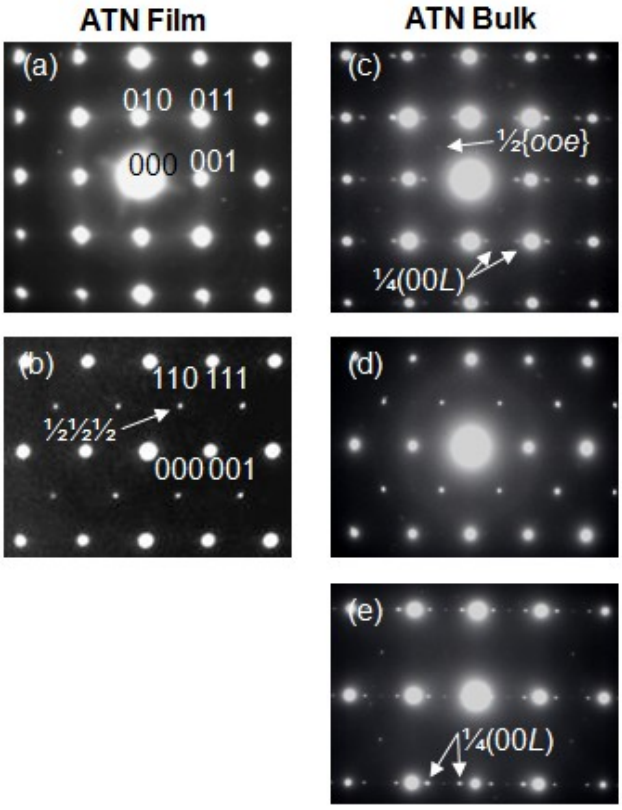

Figure 4-10 (a) <100> and (b) <110> electron diffraction patterns from $Ag(Ta_{0.5}Nb_{0.5})O_3$ films deposited on SRO/LAO and crystallized at 700 °C. (c) [100], (d) [101], and (e) [110] from bulk ATN.

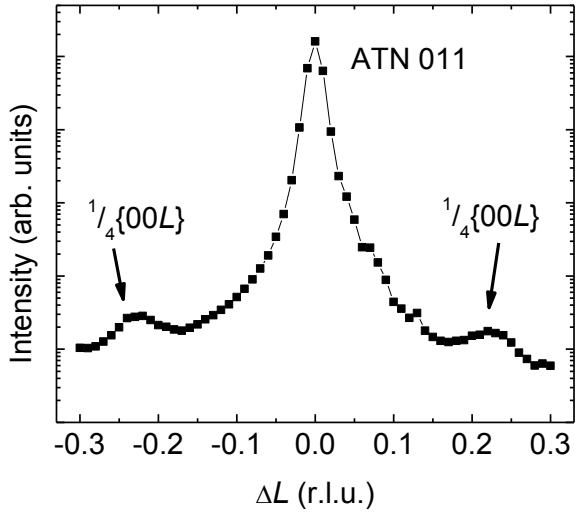

Figure 4-11 XRD showing the ¼ order peaks flanking the 011 peak for relaxed $Ag(Ta_{0.5}Nb_{0.5})O_3$ films. These quarter order reflections are substantially lower in intensity than expected for the M_2 phase.

In addition to diffuse rods through the tilting superlattice reflections, [103] patterns (Figure 4-8) reveal diffuse streaks (indicated using arrows) that represent traces of diffuse intensity sheets passing through all fundamental reflections perpendicular to the three ⟨100⟩ directions. Previous studies of $AgNbO_3$ confirmed these sheets to originate from the local Nb-cation displacements correlated along the -B-B-B- chains.[43] According to Levin *et al*.,[43] Nb cations in $AgNbO_3$ are locally displaced along ⟨111⟩ directions and, in the high-temperature polymorphs (i.e. C, T, O, and M_3), exhibit disorder among the 8 displaced positions. Our results confirm the presence of similar B-cation displacement correlations along the -Nb-Ta-Nb- chains and the associated 8-site displacive disorder in thin ATN films at room temperature.

4.2.5 Low temperature TEM

Figure 4-12 shows low-temperature diffraction patterns recorded along the ⟨100⟩ zone axis from a cross section of the ATN/SRO/LAO sample. Distinct ¼{00*L*}-type reflections emerged below ~ -210 °C (~60 K). The appearance of discernable intensity for these reflections signifies ordering of local Nb/Ta displacements, which is manifested in the increasing average off-center B-cation displacements. Such displacements can be viewed as an order parameter.[43] Despite extreme care, sample drift during film exposures (30 seconds) resulted in some overlap between the ATN and SRO layers giving rise to the SRO's ½{*ooe*} and ½{*eeo*} spots in the diffraction patterns. However, the ¼(00*L*)-type reflections are unique to *Pbcm* structure and, as such, are characteristic of the ATN layer.

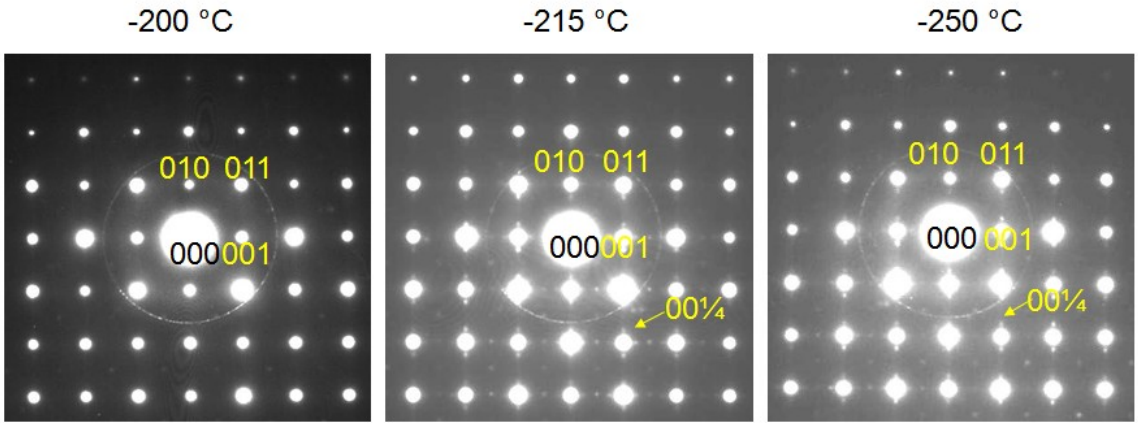

Figure 4-12 Electron diffraction patterns from the $Ag(Ta_{0.5}Nb_{0.5})O_3$ films deposited on SRO/LAO(001) crystallized at 700 °C, along the <100> zone axis, recorded at (a) -200 °C (~ 70 K) , (b) -210 °C (~60 K) and (c) -250 °C (~25 K), respectively. The faint ring is likely due to redeposited Ag or Ag_2O.

4.2.6 Phase identification using temperature dependent X-ray diffraction

Figure 4-13 shows the room temperature XRD data for the $Ag(Ta_{0.5}Nb_{0.5})O_3$ film (008 peak). No evidence of peak splitting is observed, consistent with the ATN film being in the M_3 rather than the M_2 or M_1 phase at room temperature[43]. Temperature dependent X-ray diffraction data for the ATN films are shown in Figure 4-14. The d-spacing of the 008 peak shows no evidence of splitting from room temperature up to ~250 °C (525 K), consistent with the M_3 phase in which the 880_o and $0\ 0\ 32_o$ remain unresolved. On further heating, the ATN films transform to the O phase between 250 °C (525 K) and 275 °C (550 K), to the T phase between 325 °C (600 K) and 350 °C (625 K) and finally to cubic prototype between 525 °C (800 K) and 555 °C (830 K). Figure 4-15 shows the FWHM of the 008 peak as a function of temperature in terms of θ. Anomalies are observed at temperatures consistent with those observed in the d-spacings. However, the O – T and T - C phase transitions recorded for thin film ATN are ~ 50 °C lower than those reported for bulk.[41] The high temperature transitions are largely driven by the

low tolerance factor associated with $Ag(Ta_xNb_{1-x})O_3$ solid solution and are therefore nearly independent of the Nb/Ta ratio unlike the M transitions.

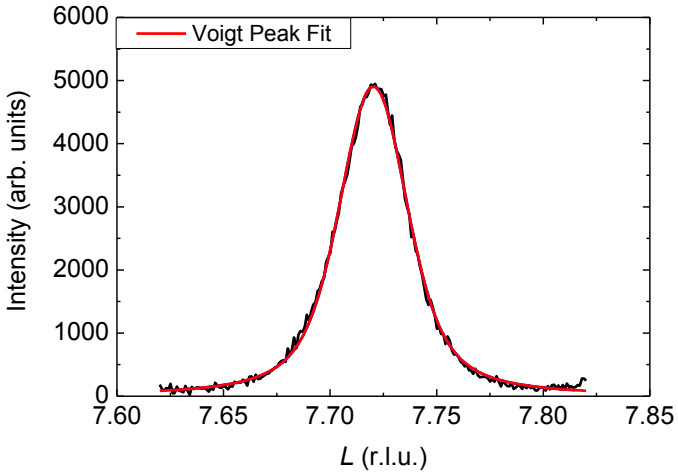

Figure 4-13 XRD trace of the 008 peak at room temperature for $Ag(Ta_{0.5}Nb_{0.5})O_3$ film. The reciprocal lattice unit *L* is referenced to the substrate (LAO) lattice parameter, 3.79 Å. The ATN film shows no indication of splitting, suggesting that at room temperature the film is in the M3 phase. Black line = experimental data, red line = fit.

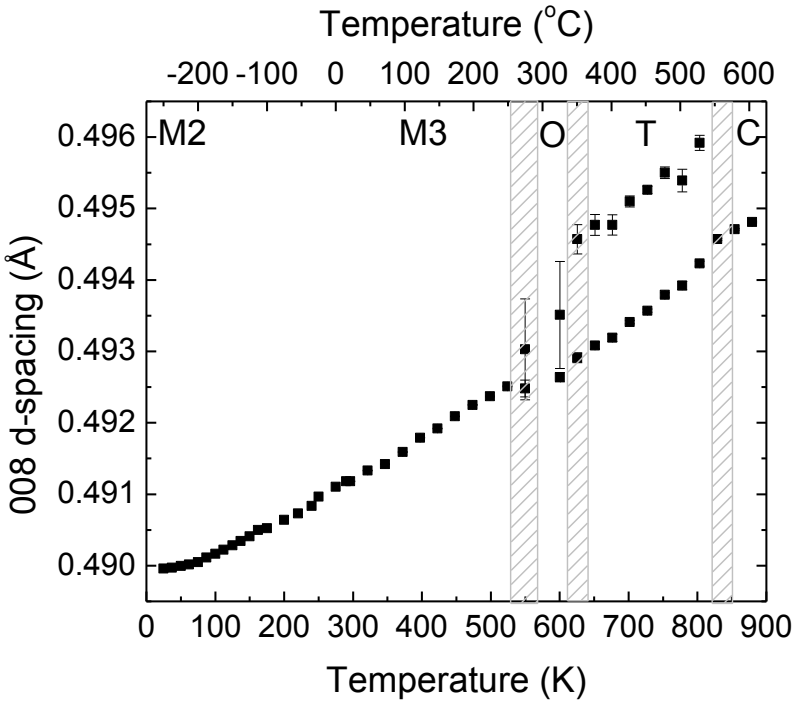

Figure 4-14 d-spacing as a function of temperature for the $008_{pc} = 880_o + 0\ 0\ 32_o$ peaks (M_3 phase), $008_{pc} = 0\ 0\ 16_o + 0\ 16\ 0_o$ peaks (O phase), and $008_{pc} = 008_T + 880_T$ peaks (T phase). Shaded regions indicate some uncertainty in the fits near phase transitions. The O phase is also shaded due to the fact that the chi squared values between a one peak fit and a two peak fit were similar. It is believed that the data presented represent the better fit.

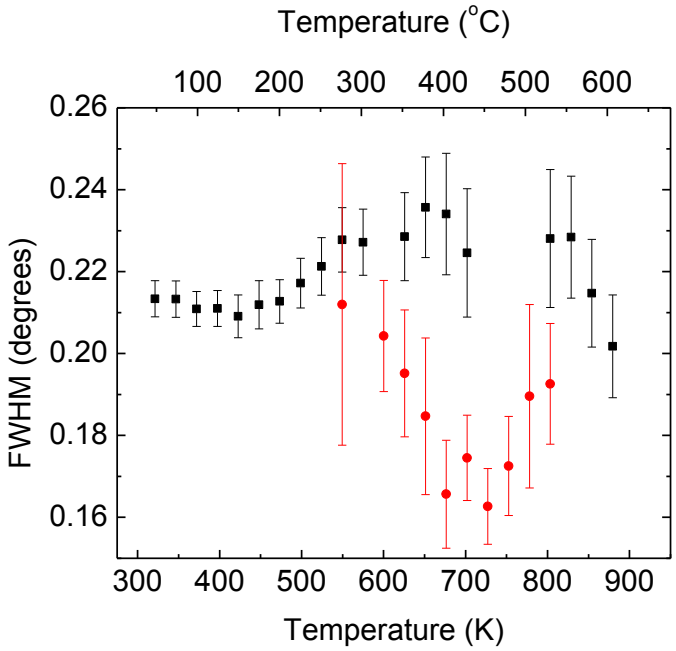

Figure 4-15 FWHM of the 008_p peak in terms of theta for $Ag(Ta_{0.5}Nb_{0.5})O_3$ films as a function of temperature. Anomalies occur between 250 °C (525 K) and 275 °C (550 K) suggesting the M_3 to O phase transition; between 325 °C (600 K) and 350 °C (625 K) where the O to T phase transition occurs; and between 525 °C (800 K) and 555 °C (830 K) suggesting the film transitions to cubic around this temperature. Black points represent FWHM when the peaks were fit with a single peak. Red points represent the FWHM when the peaks were fit with two peaks; the data shown is the more intense of the two peaks.

Figure 4-16a,b shows the d-spacings for the 444 and 404 Bragg peaks of the ATN films, respectively. In ATN, the 444 Bragg peak should not show discernable splitting in the C, T, and O phases, however, peak splitting should be resolvable in the M phases. From the experimental data, it can be seen that the 444 peak is a single peak from high temperatures down to 275 °C (~550 K). Below 275 °C (~550 K) a shoulder appears and the data can be fit with two peaks. This indicates that M_3-O transition occurs at ~275 °C (~550 K), which is consistent with the results for the d-spacing of the 008 peak. Likewise, the 044 Bragg peak should have no discernable splitting in the C, T, O, or M_3 phases, while splitting should be detectable in the M_2 and M_1 phases. As is seen in Figure 4-16b, the 044 peak shows no observable peak splitting in the temperature range

tested. This data provides further indication that the relaxed ATN films are in the M_3 phase at room temperature rather than the M_2 phase.

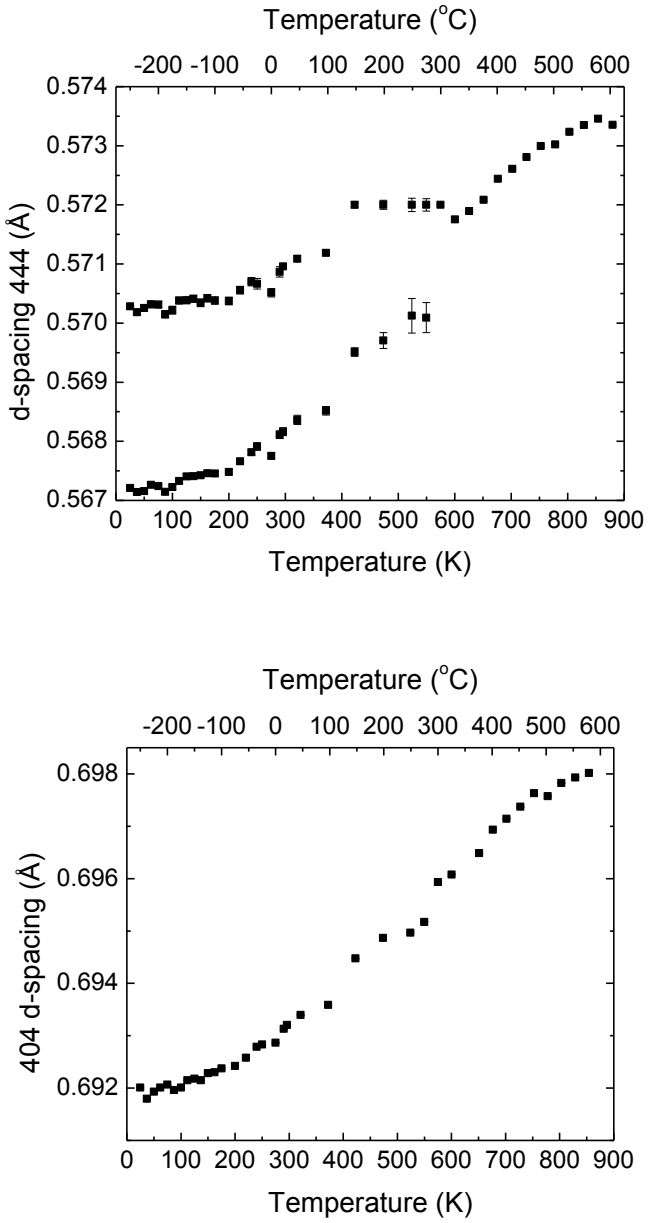

Figure 4-16 d-spacing of 444_c and 404_c Bragg peaks. (a) The 444_c peak shows no splitting from 300 °C (575 K) up to high temperatures, indicating that the film is in the C, T or O phases over this temperature range. The 444_c peak shows splitting below 275 °C (550 K), indicating the phase transition to one of the M phases. (b) The 404_c peak shows no splitting from room temperature up to 575 °C (850 K). This is consistent with the film being in the M_3, O, T or C phases over this temperature range.

4.2.7 Temperature dependence of superlattice reflections

The phase transitions can be confirmed by examining various superlattice reflections. Figure 4-17 shows the normalized integrated intensities for both the ½311 and ½321 peaks of the relaxed ATN film. The ½311 peak dominates at low temperatures as would be expected for the M phases. Both the ½311 and ½321 reflections show finite intensity characteristic of $a^0b^-c^+$ tilting in the O phase. Finally, the intensity of the ½321 peak dominates in the T phase, which has in-phase tilting. These phase transitions correlate with the data in Figure 4-14.

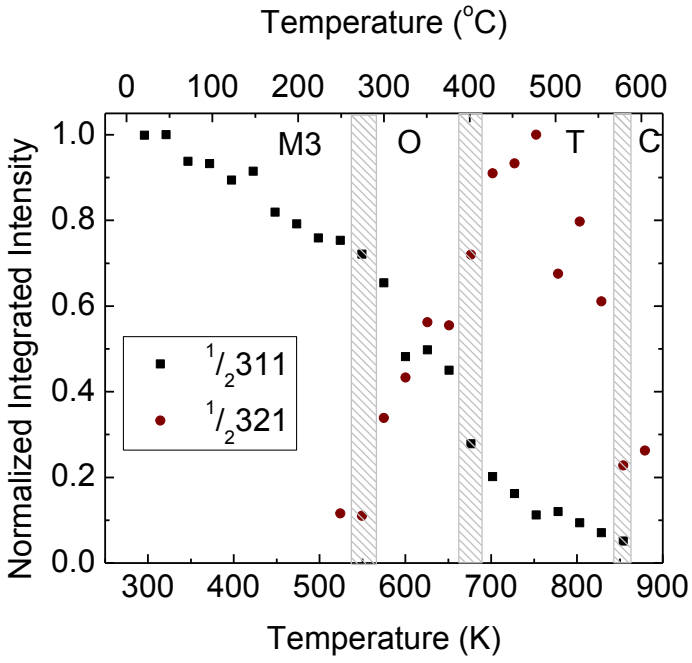

Figure 4-17 Normalized integrated intensity of ½311 and ½321 superlattice reflections. As was described earlier in the chapter, the ½311 peak indicated anti-phase tilting present in the M phases while the in-phase tilt of the T phase leads to the ½321 peak. The O phase should have finite intensity for both the ½311 and ½321 reflections.

The quarter order reflections due to the $a^-b^-c^-/a^-b^-c^+$ octahedral tilting were characterized as a function of temperature and used to estimate the M_3-O phase transition. These superlattice reflections effectively vanish above ~ 325 °C (~ 600 K) as is observed in Figure 4-18.

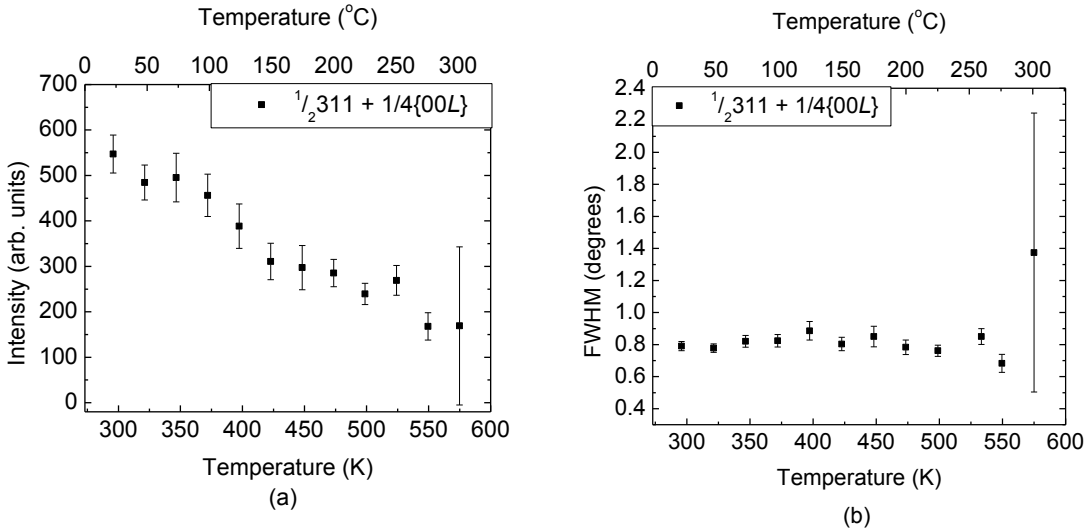

Figure 4-18 (a) Integrated intensity and (b) FWHM of ½311 + ¼{00*L*}. The peaks vanished at 325 °C (~ 600 K) and above.

4.2.8 Low temperature X-ray diffraction

X-ray diffraction data was obtained down to ~ 25 K to search for the M_2-M_3 phase transition. Through TEM electron diffraction and electrical measurements, it was estimated that this transition occurred at -200 °C (70 K). Figure 4-14 and Figure 4-16 include the low temperature data for the d-spacings of the 008, 404 and 444 peaks. Despite the fact that peak splitting of the 008 peak should be resolvable in the M_2 phase, it was difficult to fit the data with two peaks. As a result, the FWHM of the single peak was used instead to detect phase transitions. Figure 4-19 shows an increase in the response as the temperature decreases, suggesting that the material is approaching the M_2 phase. A leveling off of the FWHM near -215 °C (60 K) indicates that ATN may be in the M_2 phase; this temperature correlates well with the TEM and dielectric data which showed the transition to occur near -215 °C (60 K) and -200 °C (73 K), respectively.

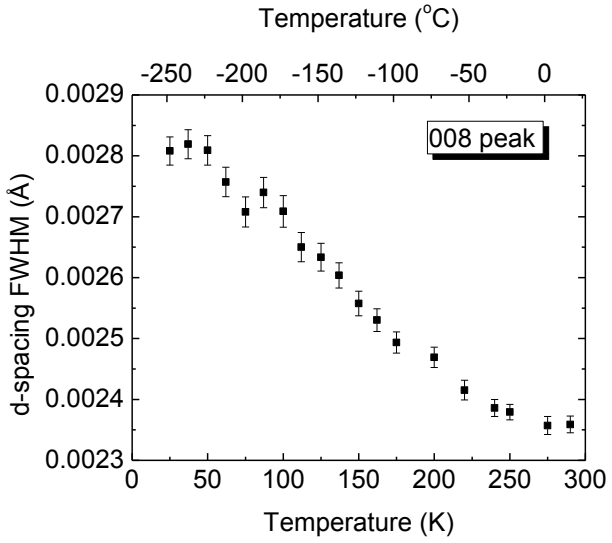

Figure 4-19 FWHM of 008 d-spacing as a function of temperature obtained during low temperature measurements. Although no obvious splitting of the peak occurred, the FWHM did increase as the temperature decreased, indicating the material was approaching the phase transition into the M_2 phase.

The M_2 phase exhibits long range ordering of the B-site cation displacements, which is evident through ¼$\{00L\}$ reflections. Figure 4-20 shows that the integrated intensity increases as the temperature decreases, suggesting that the long range ordering of the B-site cations becomes more pronounced.

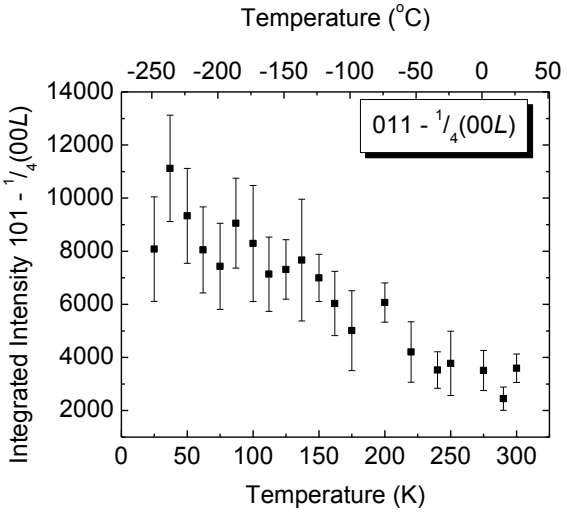

Figure 4-20 Integrated intensity of 101 – ¼{00*L*} as a function of temperature. The constant increase in peak intensity as temperature decreases indicates that the B-site cations are exhibiting pronounced ordering.

4.2.9 Discussion

In previous studies it has been demonstrated that tilting in bulk $AgNbO_3$, $a^-b^-c^-/a^-b^-c^+$, is concurrent with long-range antipolar ordering of local Nb displacements.[43] Recent studies confirmed that this complex tilting promotes ordering of Nb local positions and the resulting pattern of average Nb displacements adopts the *Pbcm* symmetry of the tilted octahedral framework. Nevertheless, some positional disorder for Nb is retained in the structure as evidenced by the diffuse intensity sheets observed in electron diffraction patterns. The M_3-M_2 line in the phase diagram (Figure 2-13) marks the onset of a pronounced ordering of the local B-cation displacements.[43] A broad dielectric maximum coincides with the temperature of this ordering. Nb promotes ordering of the Nb/Ta displacements because its greater ionic polarizability.[48] This is reflected in the bulk M_3-M_2 transition temperature decreasing rapidly with increasing Ta concentration.

These results indicate that local displacement correlations along the -Nb-Ta-Nb- chains in the ATN thin films are still significant enough to produce pronounced diffuse scattering sheets in electron diffraction. However, both $a^-b^-c^-/a^-b^-c^+$ tilting and ordering of Nb/Ta displacements in thin film ATN appear at much lower temperatures compared to bulk. This difference can be attributed to a relatively high concentration of point and planar defects in the films, as evident in the TEM results, which show a limited correlation length for the complex sequence of in-phase and antiphase rotations around the *c*-axis required in the *Pbcm* structure. By analogy with $AgNbO_3$, the limited spatial extent of $a^-b^-c^-/a^-b^-c^+$ tilting is expected, in turn, to inhibit long-range ordering of Nb/Ta displacements. As in bulk ceramics, in the ATN films the broad dielectric peak coincides with the onset of strong B-cation displacive ordering.

Shifts in T_C can also be induced by stresses in thin films due to substrate constraints or lattice parameter mismatch. However, the M transitions in ATN are non-symmetry breaking and do not have a strong ferroelastic component.[75] It is unlikely therefore that stresses in the ATN film are large enough to cause a substantial change in the M_3-M_2 phase transition temperature. Moreover, the film is in a relaxed state with lattice parameters similar to those of the bulk ceramic (out-of-plane = 3.93±0.01 Å and in-plane = 3.92±0.01 Å).

More generally, stress may also be induced in thin films by thermal expansion mismatch, which for ATN and LAO is estimated to be 57 MPa. Suchanicz *et al.* found that axial pressures up to 80 MPa changed the phase transition temperatures by ≤ 25 ºC.[75] Therefore, it is concluded that point and planar defects are the primary cause for the suppression in the M_3-M_2 phase transition temperature.

Point defects are difficult to detect even in bulk ceramics, but it is possible that the low crystallization temperatures of chemical solution deposited ATN layers (700 °C) compared to the sintering temperature of bulk ceramics (1200 °C) results in a high concentration of point defects. These defects can arise from residual carbon, oxygen vacancies associated with low local oxygen

pressures during annealing, any segregation of the Ag during processing, or a variety of other factors. Planar defects are far more visible and the highly perturbed diffraction contrast present in the images in Figure 4-7 confirms a high density of faults in the structure. As the Nb concentration increases, stronger correlations among local B-cation displacements reduce the driving force required for their long-range ordering. Therefore, the effect of defects is expected to be diminished. Indeed, in $AgNbO_3$ films, a significant ordering of Nb displacements is observed already at room temperature as evidenced by discrete, relatively strong ¼{00*L*} reflections in the ⟨001⟩ diffraction patterns (

Figure 4-21a) and also by splitting of the 008 peak typical of either the M_2 or M_1 phases (Figure 4-21b).

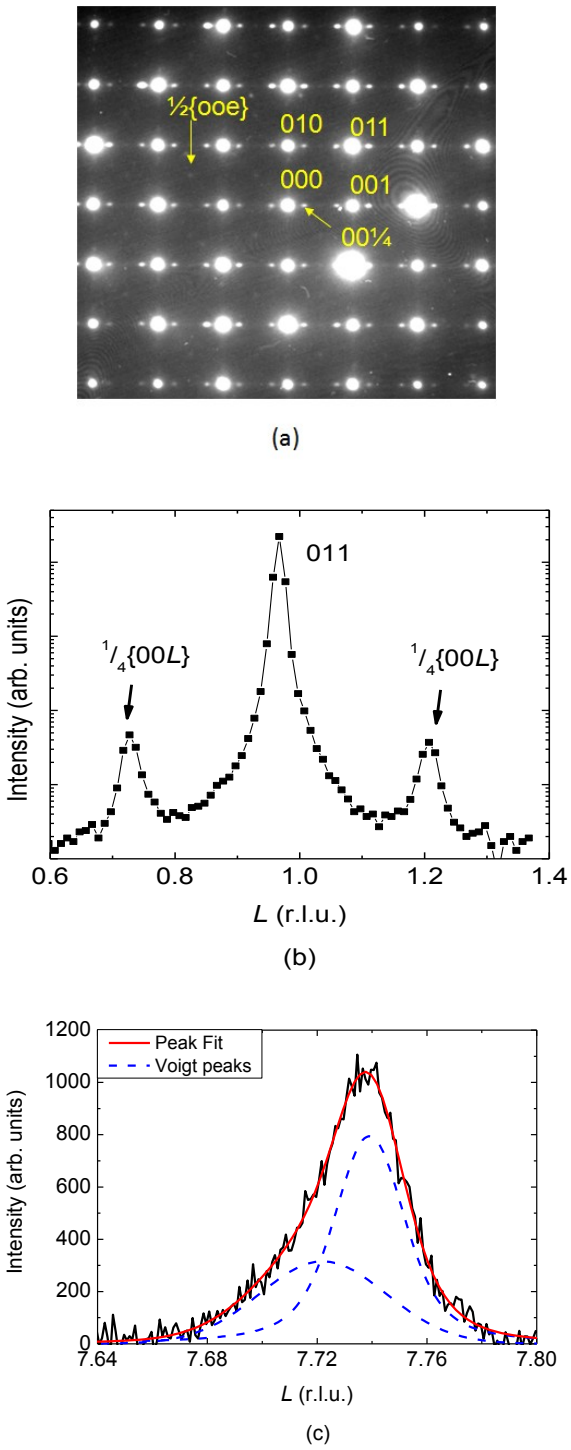

Figure 4-21 (a) <100> pseudocubic zone axis electron diffraction patterns from an $AgNbO_3$ film deposited on SRO/LAO(001) and crystallized at 700°C showing ¼{00*L*} reflections similar to bulk. (b) XRD profile showing the quarter order reflections flanking the 011 peak. (c) XRD trace of the $AgNbO_3$ 008 peak showing clear evidence of splitting indicating that the film is in the M_2 or M_1 phase at room temperature. The reciprocal lattice unit *L* is referenced to the substrate (LAO) lattice parameter, 3.79 Å. Black line = experimental data, blue line = Voigt peaks, red line = overall peak fit.

4.2.9.1 Dielectric measurements in ATN films with other compositions

The phase transitions of other ATN compositions was estimated through the use of dielectric measurements. Figure 4-22 shows the temperature dependent permittivity response for $Ag(Ta_xNb_{1-x})O_3$ films with x = 0, 0.16, 0.33 and 0.5. The diffuse maximum observed is due to the M_2-M_3 phase transition and can be seen to decrease in temperature as the Ta concentration increases. Dielectric data for bulk materials is shown in Figure 2-22. In this plot, the broad permittivity maximum shifts to lower temperatures with increasing Ta content due to the fact that Ta has a lower polarizability than Nb and will thus disrupt the long range ordering of B-cation displacements. In films, a similar trend is observed; however, all compositions see a suppression of the M_2-M_3 transition as compared to the bulk counterparts, suggesting that in films the B-cation displacive ordering undergoes a more severe disruption across the entire system. In films, unlike bulk, the M_3-O transition was not observed in the permittivity data. The reason for this discrepancy is unknown at this time.

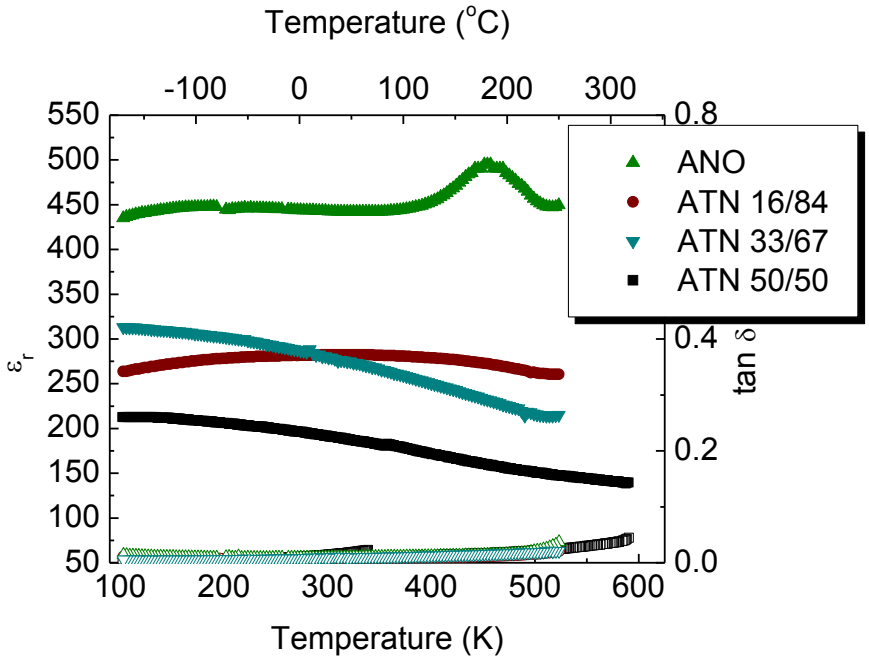

Figure 4-22 Temperature dependent permittivity of $Ag(Ta_xNb_{1-x})O_3$ with x = 0, 0.16, 0.33, and 0.5. The diffuse maximum in permittivity can be seen to decrease with increasing Ta content suggesting that the M_2-M_3 phase transition is suppressed in films of all compositions. Filled symbols are for the permittivity; open symbols were the measured loss tangents.

4.2.9.2 Summary of phase transitions in $Ag(Ta_{0.5}Nb_{0.5})O_3$ films

The information on phase transitions associated with tilt or the ordering of B-cation displacements in relaxed $Ag(Ta_{0.5}Nb_{0.5})O_3$ films are summarized by superimposing them on the bulk phase diagram, as shown in Figure 4-23. The phase transitions of the films are denoted using stars. In the relaxed films, the high temperature C-T, T-O and O-M_3 transitions occur at similar temperatures to bulk materials, however a suppression of the M_3-M_2 transition was observed in films of all compositions.

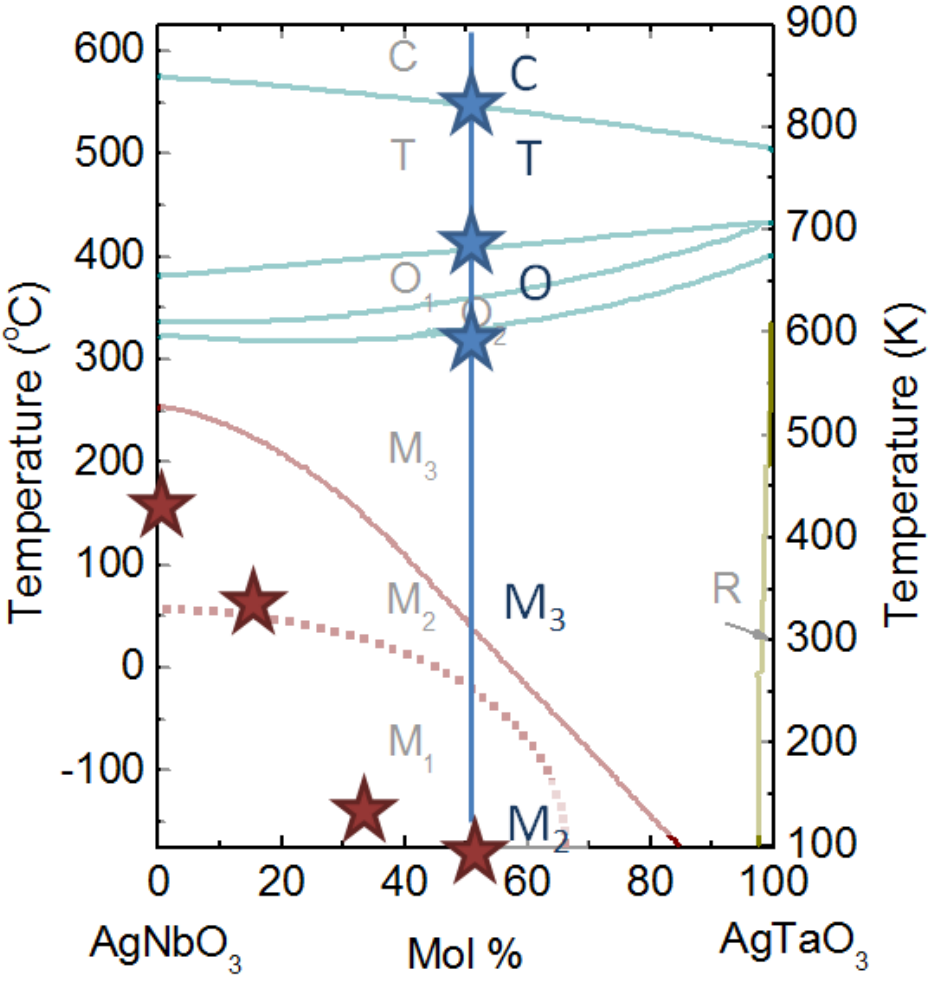

Figure 4-23 Phase transitions for relaxed $Ag(Ta_xNb_{1-x})O_3$ films superimposed on the bulk phase diagram. The stars indicate the phase transition temperatures of the film. The gray text represents the bulk phases while the black text refers to the films.

4.3 Conclusions

Electron diffraction data from ATN layers deposited on SRO/LAO(001) and LAO(001) confirm that the films adopt a complex octahedral tilted structure with *Pbcm* symmetry and

$\sqrt{2}a_{pc}\times\sqrt{2}a_{pc}\times 4a_{pc}$ unit cell. However, in the films, the correlation length for the sequence of in-phase and antiphase rotations about *c*-axis is significantly reduced. Similar to bulk materials, the ATN films exhibit local off-center displacements of B-cations along 8 non-equivalent ⟨111⟩ directions that give rise to {100} diffuse intensity sheets. B-cations are randomly distributed among these 8-sites as inferred from the lack of significant average B-cation displacements. In the ATN films, ordering of local displacements, which coincides with a broad maximum of dielectric constant, occurs around ~ 210 °C (60 K) as opposed to ~ 40 °C (310 K) in bulk. Such strong suppression of B-cation displacive ordering in thin films compared to bulk samples is attributed to a significant concentration of point and planar defects which reduce the correlation length for complex octahedral rotations about the *c* axis and, thus, weaken the interactions between the tilting and B-cation displacements that are key to the ordering.

Chapter 5

Tilt Transitions in Compressively Strained $Ag(Ta_xNb_{1-x})O_3$ Thin Films [†]

As was discussed in earlier chapters, this dissertation aims at understanding the relationship between octahedral rotations and strain through the use of biaxial stress in thin films. This chapter will detail results of phase transitions, specifically tilt transitions, in $Ag(Ta_xNb_{1-x})O_3$ films under compressive strain. Initial measurements confirming the quality of the films will first be presented. Then, results from TEM and synchrotron X-ray diffraction will be used to determine the phase transition sequence of compressively strained $Ag(Ta_{0.5}Nb_{0.5})O_3$. Finally, a model to describe the findings will be presented.

5.1 Compressively strained $AgTa_{½}Nb_{½}O_3$

$Ag(Ta_xNb_{1-x})O_3$ thin films were deposited on $SrTiO_3$ substrates using the experimental procedure outlined in Section 3.2. In this work, the film thickness was ~ 15 nm. As described previously, $SrTiO_3$ has a smaller lattice parameter than $Ag(Ta_{0.5}Nb_{0.5})O_3$, meaning the film is under compressive strain.

[†] Most of this chapter appears in R. L. Johnson-Wilke, D. S. Tinberg, C.B. Yeager, Y. Han, I. M. Reaney, I. Levin, D. D. Fong, T. T. Fister, and S. Trolier-McKinstry (accepted *Phys. Rev. B*)

5.1.1 Room temperature X-ray diffraction

Prior to performing TEM and synchrotron X-ray diffraction measurements on the samples, room temperature experiments were performed on a lab source diffractometer. Figure 5-1a shows the out-of-plane θ-2θ pattern of $Ag(Ta_{0.5}Nb_{0.5})O_3$ (ATN) films on $SrTiO_3$ obtained with Cu K_α radiation. The scan shows the films are free of second phase and do not exhibit regions of misorientation. The rocking curves about the 002 ATN and $SrTiO_3$ peaks are shown in Figure 5-1b. These scans have been normalized to the intensity and center position of the two peaks. The full width at half maximum (FWHM) of the film and substrate were 0.061° ± 0.002° and 0.020° ± 0.005°, respectively. Due to the coherent nature of the ATN films, locating an off-axis peak was extremely difficult and, as a result, a phi scan was not obtained.

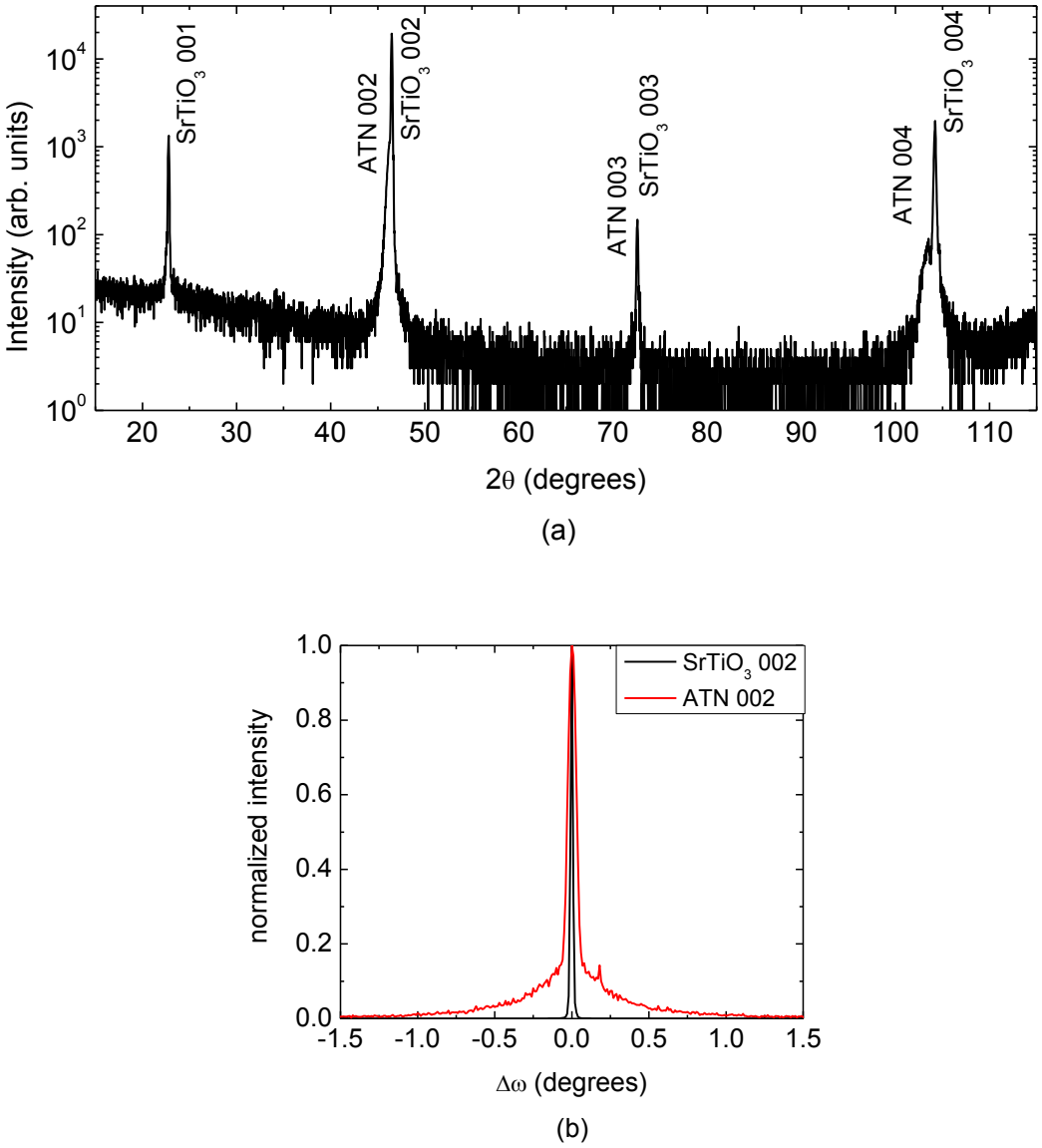

Figure 5-1 (a) Out-of-plane θ-2θ diffraction pattern for $Ag(Ta_{0.5}Nb_{0.5})O_3$ films grown on $SrTiO_3$. (b) Normalized rocking curve of the 002 peak for both ATN and the underlying substrate. The FWHM of ATN was 0.061 ± 0.002°. $SrTiO_3$ had a FWHM of 0.020 ± 0.005°. The intensity was normalized and the peak positions centered on $\omega = 0$ for comparison purposes.

$Ag(Ta_{0.5}Nb_{0.5})O_3$ films of different thickness were deposited and their rocking curves measured to determine the optimal film thickness for further experiments. Figure 5-2 shows such data for samples with thicknesses of 7.5 nm, 15 nm, and 30 nm. Although all films show some

material which is coherent, it is fairly clear that as the thickness increases, the fraction of relaxed material also increases. This is evidenced by the "skirt" at the bottom of the curve. To avoid complications due to this relaxed material, 15 nm was used as an optimized thickness, because it had minimal relaxation. In addition, it was thicker than the 7.5 nm film, thus providing a larger volume of matter for diffraction experiments.

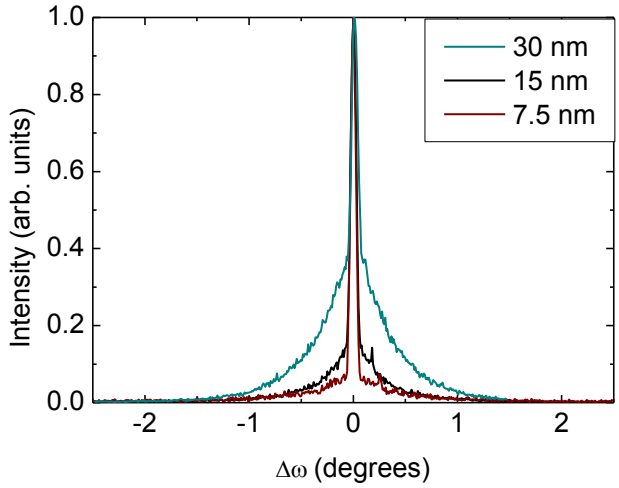

Figure 5-2 Rocking curve of the 002 reflection for three ATN films of different thicknesses. The "skirt" on the lower portion of the curve is likely due to some fraction of the film being in a relaxed state.

5.1.2 Room temperature phase identification of ATN films on $SrTiO_3$

Phase identification of films with $Ag(Ta_{0.5}Nb_{0.5})O_3$ and $AgNbO_3$ compositions was performed using synchrotron X-ray diffraction. A reciprocal space map around the 113 Bragg peak (Figure 5-3) shows that the in-plane lattice parameters of $Ag(Ta_{0.5}Nb_{0.5})O_3$ film are identical to the in-plane lattice parameters of the substrate, since *H* and *K* are the same for both peaks. For bulk ceramics, the room temperature lattice parameters are a = 5.5238 Å, b = 5.5673 Å, and c = 15.6721 Å.[40] Conversion to pseudocubic lattice parameters yields a_{pc} = 3.9059 Å, b_{pc} = 3.9366 Å, and c_{pc} = 3.918 Å. $SrTiO_3$ has a lattice parameter of 3.905 Å, which induces an in-plane

compressive strain of ~0.8% along the *b*-axis, ~0.3% along the *c*-axis, and negligible strain along the *a*-axis. The strain state is similar at elevated temperatures.

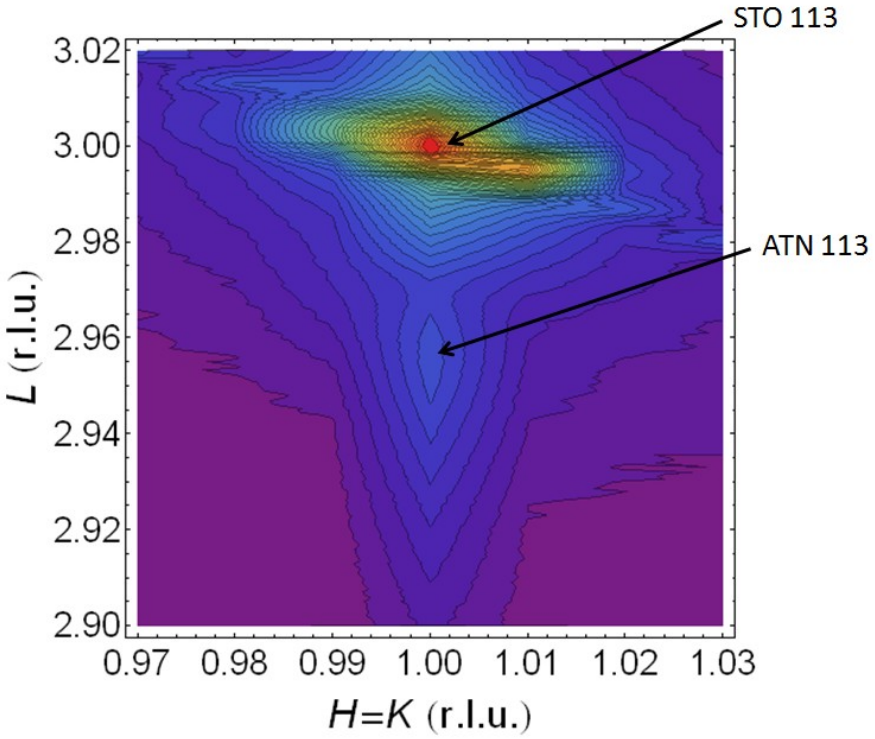

Figure 5-3: Room temperature reciprocal space map around the 113 peak of a coherently strained $Ag(Ta_{0.5}Nb_{0.5})O_3$ film on $SrTiO_3$. The film peak has the same *H* and *K* values as $SrTiO_3$, indicating that the film is coherently strained. The intensity is plotted on a log scale. Reciprocal lattice units (r.l.u.) are referenced to the room temperature lattice parameter of $SrTiO_3$.

Figure 5-4 shows a high-resolution transmission electron micrograph (HRTEM) of the $Ag(Ta_{0.5}Nb_{0.5})O_3$ film on $SrTiO_3$. The images show a clean interface between the film and substrate with no evidence for dislocations, porosity or Ag precipitates.

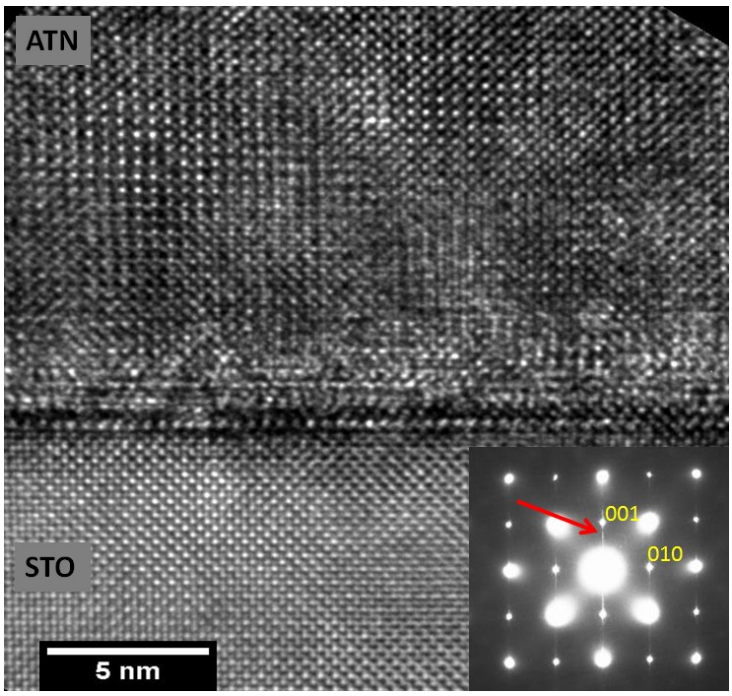

Figure 5-4: High resolution transmission electron microscopic image of the $Ag(Ta_{0.5}Nb_{0.5})O_3$ film on $SrTiO_3$ substrate. The image shows the film is homogeneous and free of secondary phases. Inset is an electron diffraction pattern obtained along the <100> zone axis. The pattern shows streaking along the *L*-direction (denoted by arrow) consistent with short range order of B-site cations.[43] The contrast at the interface is believed to be due to a combination of thickness differences and milling damage. Image courtesy of Y. Han.

The contrast near the interface in Figure 5-4 is likely due to a combination of thickness variation and ion milling effects. This noise can be reduced by first performing a Fast Fourier Transform (FFT) to the HRTEM image, then applying a filter to focus only on the main Bragg spots. An inverse Fast Fourier transform (iFFT) of this diffraction pattern will produce an image with less noise and contrast than the initial micrograph. Such a process is shown in Figure 5-5. The resulting calculated real space image is cleaner and shows the coherent nature of the film more clearly.

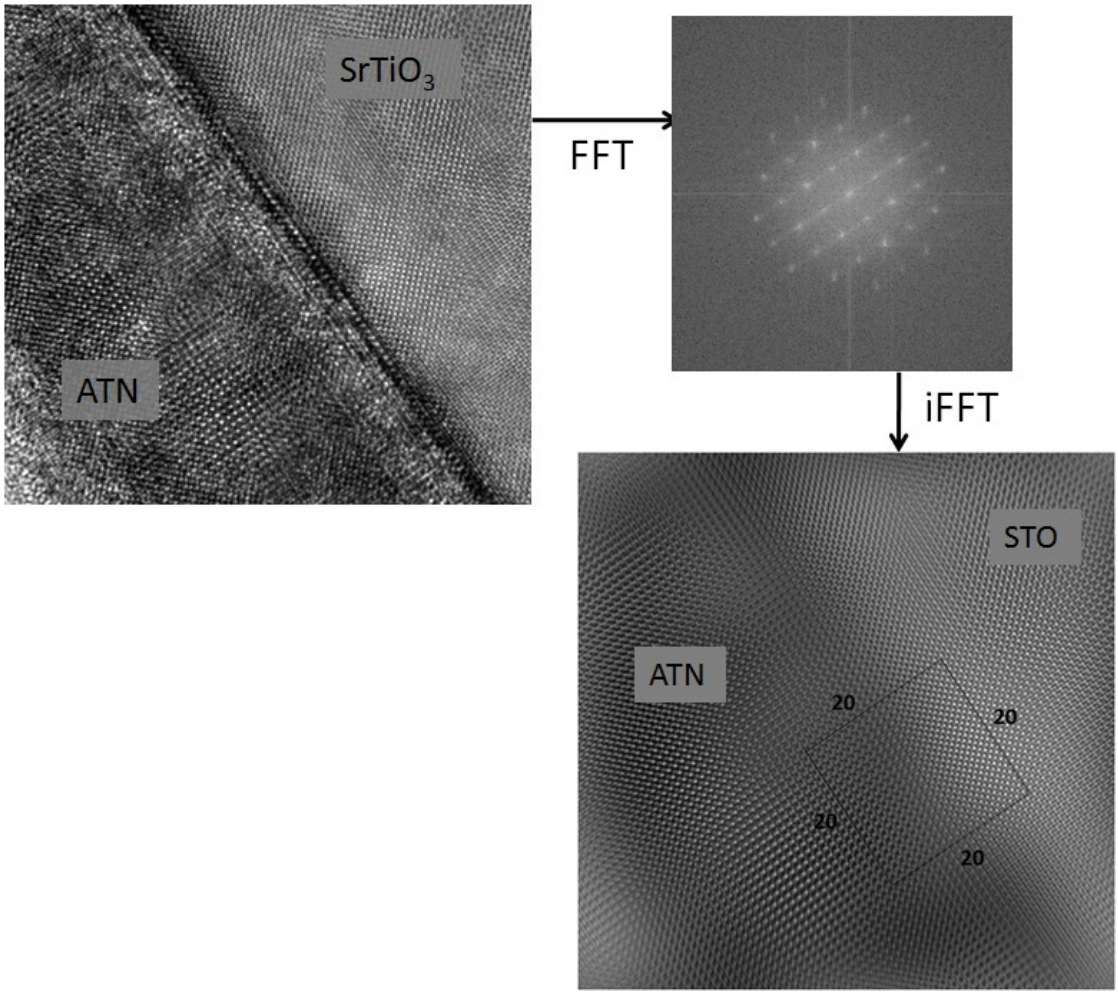

Figure 5-5 High resolution TEM image of ATN on $SrTiO_3$ with the corresponding calculated electron diffraction pattern. The Bragg spots were highlighted and a filter was applied to produce the calculated real space image as shown. FFT = Fast Fourier Transform.

The room temperature phase of coherently strained films can be determined by examining ½{*ooo*} ± ¼{00*L*} reflections (*o* = odd index). At room temperature, bulk ATN exhibits the M-type structure with the tilt system $a^-b^-c^-/a^-b^-c^+$. The resulting quadrupling of the unit cell along the c_{pc} axis can be detected through quarter-order peaks that flank ½{*ooo*}-type reflections.[43] Figure 5-6 shows XRD profiles of *H*, *K*, and *L* scans in reciprocal space around the ½311 reflection at 25 °C. Reciprocal lattice units *H*, *K*, and *L* are given with respect to the $SrTiO_3$ substrate. Figure 5-6c shows finite intensity at the ¼-order positions, suggesting that the

films are in the M phase at room temperature. Peaks were not observed at the ½311 ± ¼00 and ½311 ± 0¼0 positions, indicating that the combined in-phase/anti-phase tilting occurs only along the out-of-plane direction. This differs from relaxed films, in which the domain structure was such that the *c*-axis appeared in-plane as well as out-of-plane. The situation is counter-intuitive in the coherently strained films, given that the measured domain structure puts the long *b*-axis in the plane of the compressively strained film. From a strain perspective, the *b*-axis was likely to be the preferred out-of-plane axis.

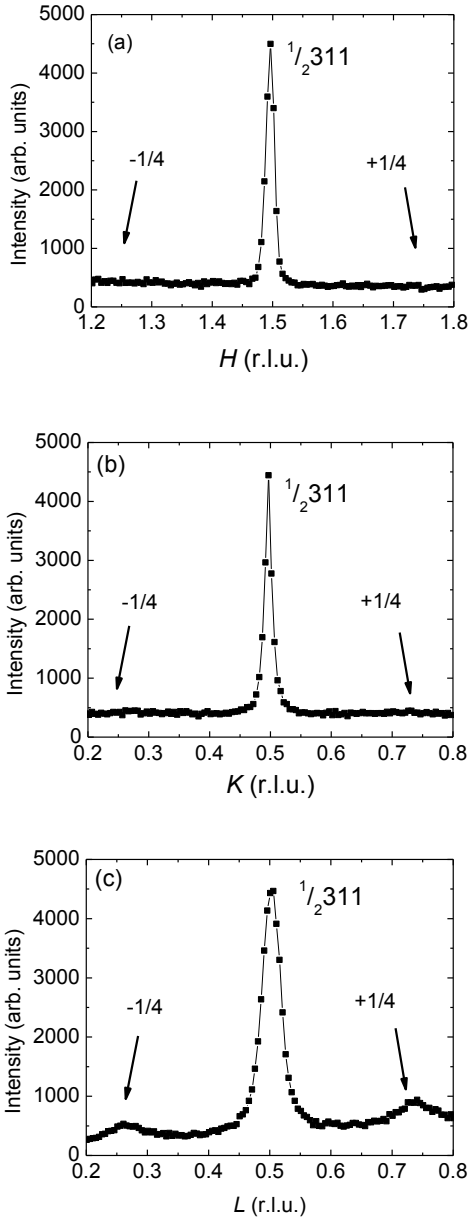

Figure 5-6 Intensity in reciprocal lattice units (r.l.u.) showing the *H*, *K*, and *L* regions of reciprocal space around the ½311 peak for $Ag(Ta_{0.5}Nb_{0.5})O_3$ films on $SrTiO_3$. The absence of intensity of ½311 ± ¼00 and ½311 ± 0¼0 indicate that the combined in-phase/anti-phase tilting occurs exclusively about the out-of-plane axis.

In addition to examining superlattice reflections due to octahedral tilting, superlattice reflections due to B-cation displacements were also characterized to determine which M phase exists at room temperature in the $Ag(Ta_{0.5}Nb_{0.5})O_3$ films. The M_3-M_2 phase transition marks the

point at which B-cation displacements undergo partial long-range ordering.[43] According to Levin *et al*.,[43] two consecutive B-site cations will displace along the [111] direction and the next two will displace along the [11$\bar{1}$]. The ordering of the B-site cations follows the periodicity imposed by the complex octahedral tilting about the *c*-axis and will also result in quarter-order superlattice reflections that flank the main Bragg peaks. Figure 5-7 shows diffraction around the ATN 011 / $SrTiO_3$ 011 peaks. The difference in reciprocal lattice units, ΔL, is given with respect to the $SrTiO_3$ substrate. The absence of quarter order reflections indicates either that the long range ordering of B-site cations is disrupted in the coherently strained $Ag(Ta_{0.5}Nb_{0.5})O_3$ films or that the peak intensity is below the detection threshold of the instrument. To assess which mechanisms dominate, compressively strained $AgNbO_3$ films were also examined. 011 ± 00¼ reflections (Figure 5-7b) were present, suggesting that there is considerably more disorder in the B-cation displacements in $Ag(Ta_{0.5}Nb_{0.5})O_3$ films. Increased B-cation displacement disorder at room temperature is commensurate with the bulk ceramic phase diagram in which the M phase transition temperatures decrease as Ta concentration increases[40, 43, 44, 75] and also with the observations on relaxed films by Han *et al*.[81]

For $Ag(Ta_{0.5}Nb_{0.5})O_3$ films, no quarter order peaks appeared in either the *H* or *K* directions of reciprocal space. The background signal was significantly higher in the *L* direction compared to the *H* and *K* directions. This diffuse scattering can be attributed to truncation rods. The electron diffraction pattern from the <100> zone axis pattern (ZAP) is shown in the inset in Figure 5-4. Similar to XRD results, the *c*-direction shows streaks of diffuse intensity which can be interpreted as truncation rods. These results suggest that the coherent $Ag(Ta_{0.5}Nb_{0.5})O_3$ films are in the M_3-like state with largely disordered local B-cation displacements at room temperature. Cryogenic measurements are required in order to determine the M_3-M_2 phase transition temperature in these films.

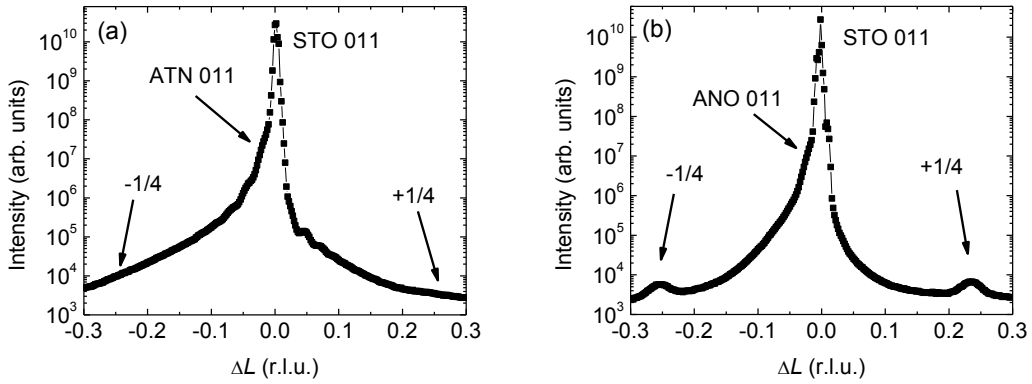

Figure 5-7 Diffraction from a room temperature *L*-scan in reciprocal space around the (a) 011 Bragg peak of $Ag(Ta_{0.5}Nb_{0.5})O_3$ and (b) 011 Bragg peak of $AgNbO_3/SrTiO_3$. In (a) there is no evidence of quarter order reflections (arrows), suggesting that the B-cations do not exhibit long range displacive order in the ATN films. In (b), peaks are observed at – ¼ and +¼ positions. ΔL is given in reciprocal lattice units referenced to the $SrTiO_3$ substrate.

5.1.3 Phase transitions

To assess the phase transition behavior of the coherently strained films, the lattice parameters were determined as a function of temperature. Due to the coherent nature of the ATN film, the film peak was too highly correlated with that of the substrate Bragg peak to enable acceptable fitting (Figure 5-8a). Thus, a Gaussian fit to the top of the film peak was used to determine the peak position as shown in Figure 5-8b. Because the lattice parameter of $SrTiO_3$ increased linearly as a function of temperature (Figure 5-9) anomalies in the difference between the out-of-plane lattice parameters, $\Delta z = z_{ATN} - z_{STO}$, indicate phase transitions in the ATN film. Figure 5-10a shows Δz versus temperature for $Ag(Ta_{0.5}Nb_{0.5})O_3$ with variations at 200 °C and 400 °C.

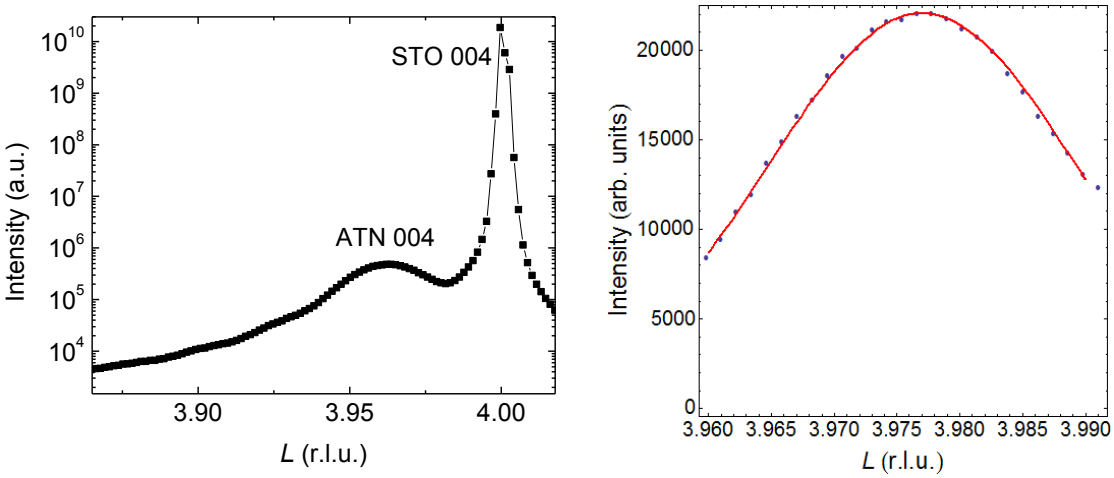

Figure 5-8 (a) *L*-scan in reciprocal space near the ATN and $SrTiO_3$ 004 reflection. The close nature of the two peaks did not allow for suitable fitting; as a result, (b) a Gaussian function was fit to the top of the ATN peak to record the peak position relative to the substrate. Data are shown in relative lattice units (r.l.u.) as referenced to the $SrTiO_3$. The blue circles represent raw data and the red curve corresponds to the Gaussian fit.

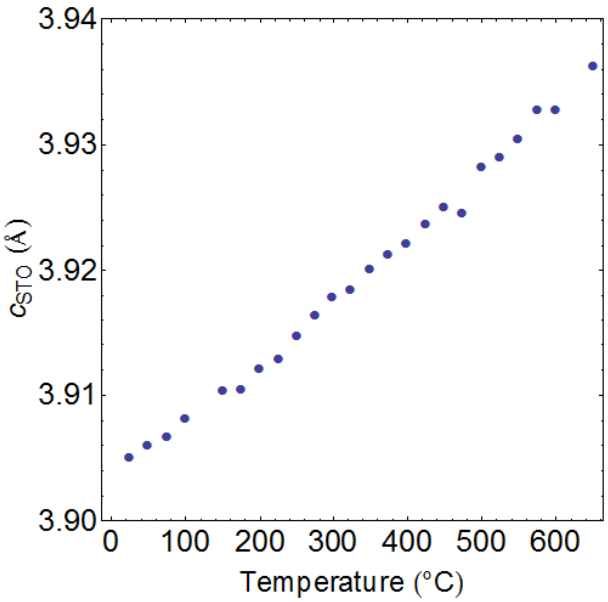

Figure 5-9 Out-of-plane lattice parameter of $SrTiO_3$ as a function of temperature. As expected, the substrate shows a linear response.

The anomalies in Figure 5-10a correspond to changes in the tilt system, as evidenced by changes to the superlattice reflections shown in Figure 5-10b. The T phase is tilted in-phase, which produces ½{*ooe*} superlattice reflections where *o* = odd and *e* = even indices.[3] Anti-

phase tilting, which occurs in the M_3 phase about the *a*- and *b*-axes, results in ½{*ooo*} superlattice reflections. The O phase is ascribed to a mixed tilt system, reported as $a^0b^-c^+$, which produces anti-phase tilting about the *b*-axis and in-phase tilting about the *c*-axis. Figure 5-10b shows the normalized integrated intensity of ½311 (anti-phase tilting) and ½312 (in-phase tilting) peaks. Regions where the integrated intensity of ½311 dominates correspond to the M phase while regions where the integrated intensity of ½312 dominates correspond to the T phase. The O phase has finite intensity of both the in-phase and anti-phase superlattice reflections.

Transition temperatures between phases were determined by performing linear fits to the integrated intensity data in Figure 5-10b. Scans of the ½312 and ½311 peaks were divided into intervals of 25 °C - 175 °C, 175 °C - 400°C and 400 °C - 650 °C. Each region was fitted with a straight line; the phase transition temperature was determined at the temperatures at which these lines intersected. Table 5-1 compares the transition temperatures of the compressively strained films to those of bulk $Ag(Ta_{0.5}Nb_{0.5})O_3$. The data demonstrate that the M_3-O phase transition in the films is suppressed by ~150 °C, while the C-T transition temperature is increased by ~130 °C. Thus, compressive biaxial strain expands the range of phase stability for the O and T phases.

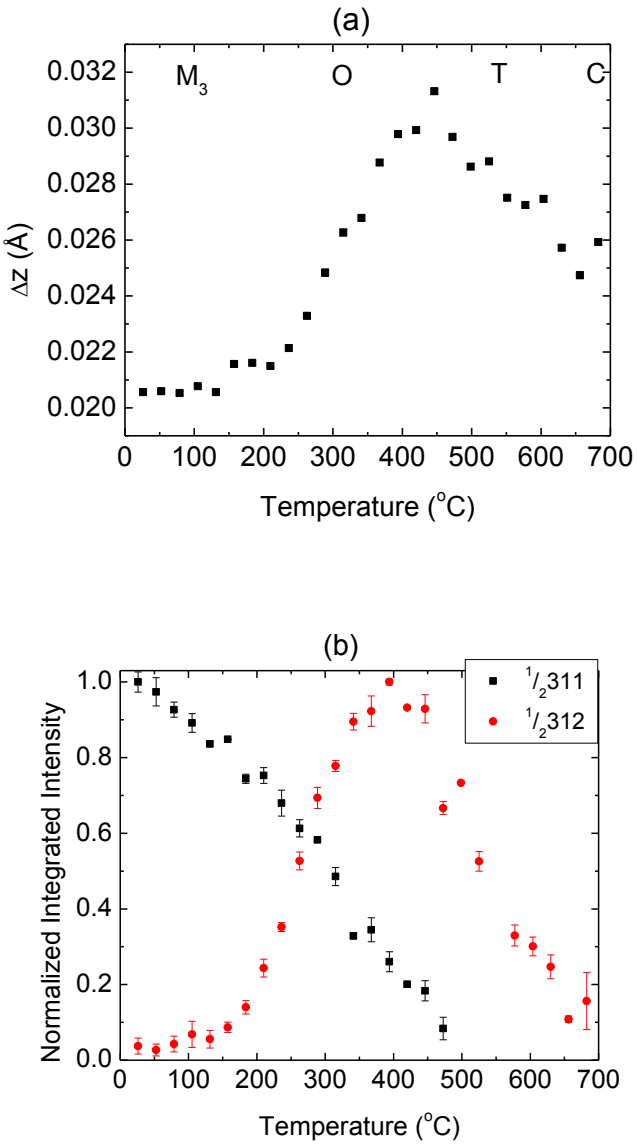

Figure 5-10 (a) Δz of $Ag(Ta_{0.5}Nb_{0.5})O_3$ films as a function of temperature. Because the lattice parameter of $SrTiO_3$ has a linear temperature dependence, anomalies in the data correspond to phase transitions in the ATN films. Error bars fall within the size of the data points. (b) Integrated intensity of ½311 and ½312 superlattice peaks normalized to the maximum intensity observed. In the M phase, anti-phase tilting dominates, whereas in the T phase, in-phase tilting dominates. The O phase has mixed in-phase and anti-phase tilting. This data show that the M-O phase transition occurs at 179 ± 12 °C, the O-T transition occurs at 378 ± 8 °C, and the T-C transition occurs at 682 ± 5 °C.

Table 5-1 Transition temperatures in compressively strained $Ag(Ta_{0.5}Nb_{0.5})O_3$ films compared to bulk $Ag(Ta_{0.5}Nb_{0.5})O_3$.

Transition Type	Bulk Transition Temperatures (°C)	Compressively Strained Films (°C)
C – T	552	682 ± 5
T – O	400	378 ± 8
O – M_3	326	179 ± 12

The M_3-O phase transition temperature was confirmed by examining the integrated intensity of ½311 + 00¼ as a function of temperature, as shown in Figure 5-11. The quarter-order reflection disappears above 250 °C, 50 °C below the relaxed films described by Han *et al*.,[81] thereby confirming that the M_3-O transition has been suppressed due to strain in the film in agreement with data presented in Figure 5-10. The non-abrupt nature of the data at the phase transition suggests that either the tilt angle decreases or the coherence length for the tilt is reduced, thereby making it difficult to ascertain the exact transition temperature with this data. This phenomenon can also be seen through the broadening of the full width at half maximum (FWHM) of a phi scan of the ½311 + 00¼ peak (Figure 5-11(b)) at temperatures near the phase transition. At this point, it is not clear whether a decrease in the tilt angle or a reduction in coherence length is dominant in producing the divergence in the FWHM of the quarter-order peak. An estimate of the phase transition temperature can be determined by performing two linear fits to the FWHM data; one 25 – 175 °C and the second 175 – 275 °C. The phase transition temperature was found to be ~ 180°C, which agrees very well with that found in Table 5-1.

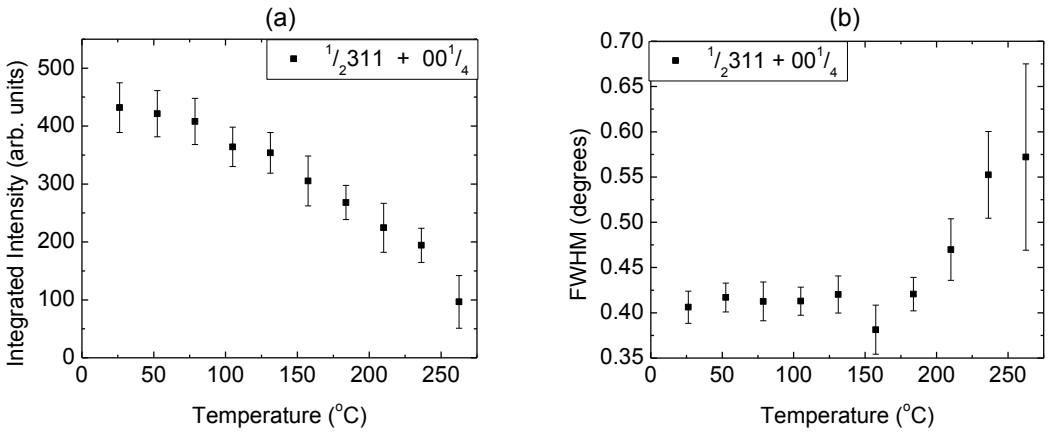

Figure 5-11 (a) Integrated intensity and (b) FWHM (phi scan) of the ½311 + 00¼ peak in $Ag(Ta_{0.5}Nb_{0.5})O_3$ films. As temperature increases, the integrated intensity of the quarter order peak was not observed above 250 °C, indicating the film is in the O phase. The upward movement of the FWHM data suggests a transition temperature occurs ~ 180 °C.

5.1.4 High temperature domain state

In order to determine the domain orientation in the tetragonal phase of these films, several ½{*ooe*} type reflections were recorded (*o* = odd, *e* = even). The tetragonal phase has a tilt system of $a^0a^0c^+$ with in-phase rotation around a single axis. Using rules for in-phase tilting developed by Glazer, the orientation of this unique axis may be determined. The Glazer rules are reproduced in Table 5-2 for convenience.[10] Figure 5-12 shows the intensities of the ½312, ½321 and ½123 peaks at 400 °C. Neither the ½321 or ½123 reflections showed measureable intensity, indicating that there are no rotations around the *y*-axis. It may be argued that for coherently strained films grown on a *P4mm* substrate, *x* and *y* are symmetrically equivalent. In this case, tilting about the *x*-axis should also be absent. In the figure, a well-developed ½312 is apparent. This suggests that the films exhibit in-phase tilt only along the out-of-plane *z*-axis. Thus, the compressive in-plane strain has forced the film to adopt a domain structure in which the tilt rotation axis is out-of-plane, consistent with theoretical predictions.[37]

Table 5-2 List of superlattice reflections that are produced for in-phase tilt about the *x*-, y- or z-axis. These rules are reproduced from Glazer.[10]

Tilt	Tilt Axis	Reflection
a^+	*x* or *y*	½{*eoo*} with $K \neq L$
b^+	*x* or *y*	½{*oeo*} with $H \neq L$
c^+	*z*	½{*ooe*} with $H \neq K$

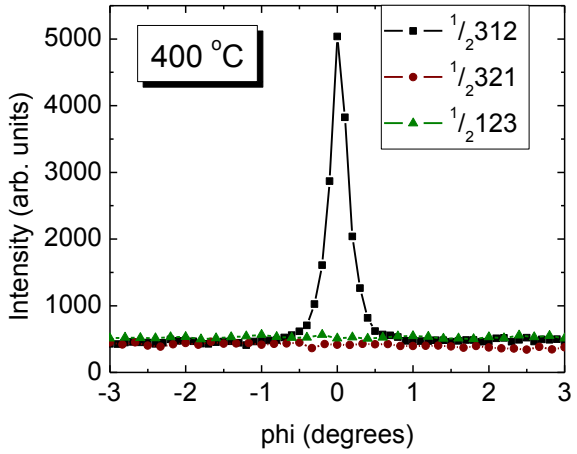

Figure 5-12 The intensity of superlattice reflections of the type ½{*ooe*} for $Ag(Ta_{0.5}Nb_{0.5})O_3$ films. The ½312 superlattice reflection is the only reflection that shows finite intensity in the tetragonal phase at 400 °C, suggesting that the in-phase tilt axis is out-of-plane and that domain states which would have put the tilt axis in-plane have been suppressed.

To date, there are no reports on the anisotropic properties of $Ag(Ta_{0.5}Nb_{0.5})O_3$ due to the difficulty of producing untwinned crystals. The technique of domain control demonstrated here allows for the possibility to perform such a study on ATN.

5.2 Discussion

The schematic in Figure 5-13 illustrates domain evolution in compressively strained ATN films as a function of temperature. It is worth noting that in bulk ATN, the *a* and *b* lattice parameters in the T and O phases are smaller than the *c* lattice parameter. Conversely, in the M phases in bulk, the *b* lattice parameter of ATN is larger than both *a* and *c*. The films are crystallized at 750 °C when the material is in the cubic phase. As the sample cools from the cubic phase down into the T and O phases, the lattice mismatch is a minimum if the *c*-axis is out-of-plane. Therefore, the material preferentially adopts domain states in the T and O phases with the *c*-axis out-of-plane as was observed in Figure 5-12. As the coherently strained film is cooled into the M phases, the domains do not re-orient with the *c*-axis in the plane, even though this would minimize strain along this axis. Presumably, this is a result of the high activation energy associated with reconfiguring the octahedral rotations. As a result, the complex tilt sequence develops normal to the substrate, and thus creates a domain state for M phase ATN in which the *c*-axis is exclusively along the out-of-plane direction.

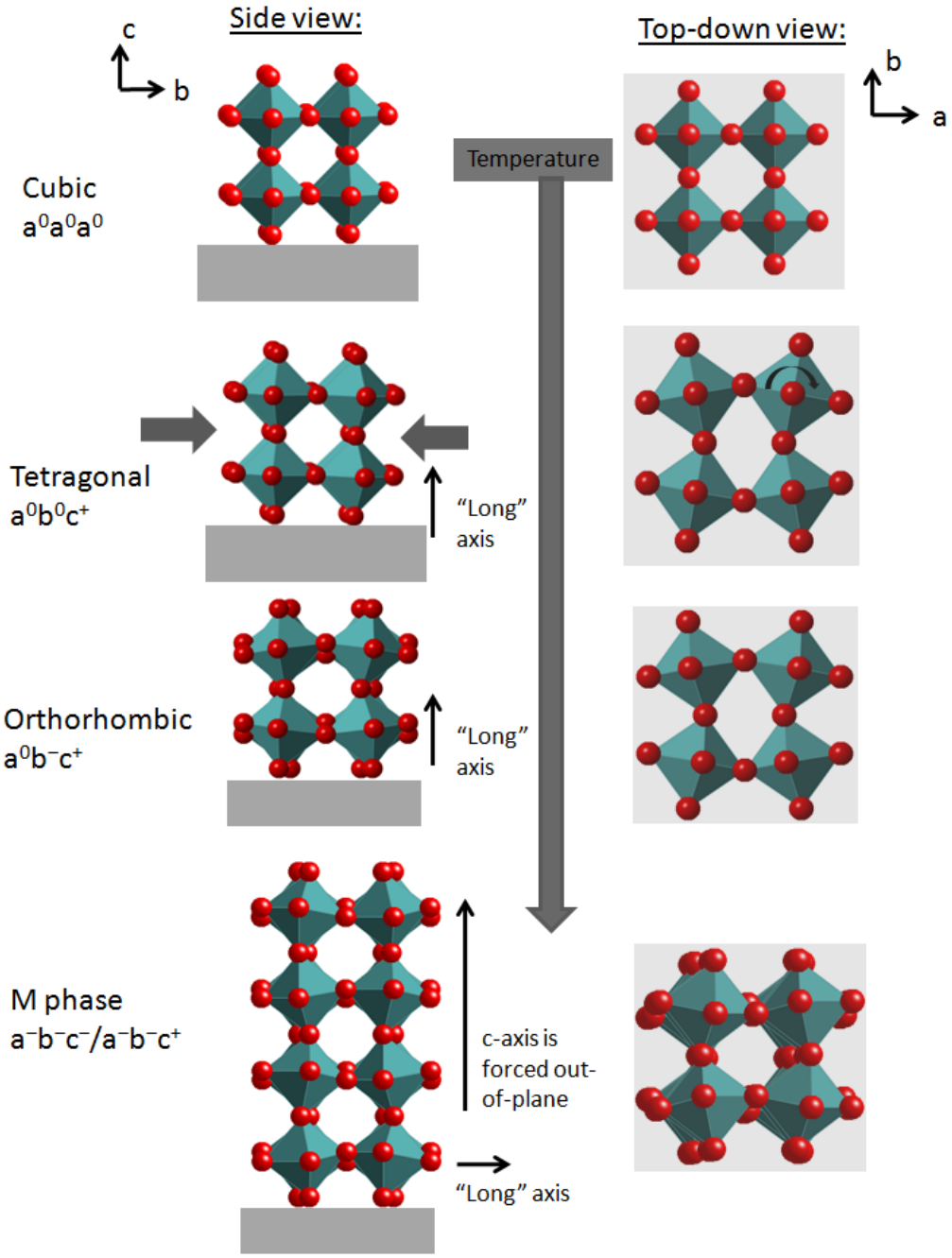

Figure 5-13 In $Ag(Ta_{0.5}Nb_{0.5})O_3$ films under compressive strain, the material is crystallized in the cubic phase. As it cools, the biaxial in-plane strain forces the shorter *a*- and *b*- axes to lie in-plane while the *c*-axis (the "long" axis) pops out-of-plane. This configuration stabilizes the tetragonal and orthorhombic phases, resulting in these phase fields having an expanded temperature region compared to bulk. As the material cools further, the *c*-axis remains in the out-of-plane orientation even though the "long" axis is the *b*-axis.

Combining the information on tilt transition temperatures and that of B-cation displacive ordering, the phase transition temperatures of compressively strained $Ag(Ta_{0.5}Nb_{0.5})O_3$ films can be superimposed on the bulk phase diagram, as shown in Figure 5-14. The phase transitions of the films, denoted by stars, show the expanded temperature region of the T and O phase fields. In addition, no indication of the M_2 phase was observed above room temperature.

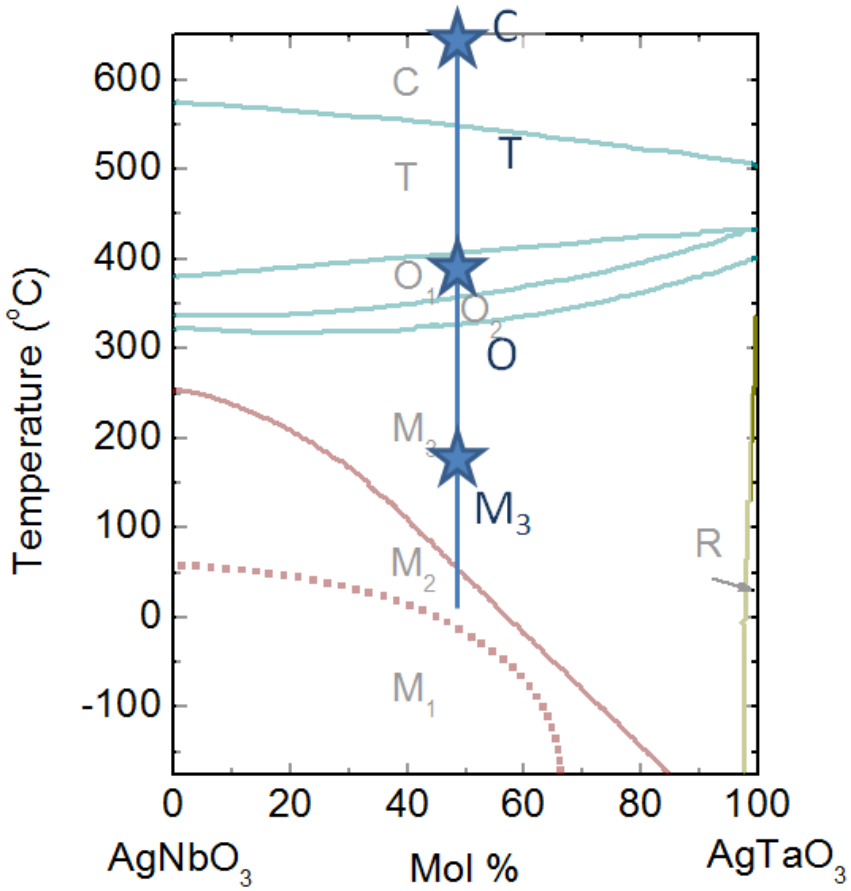

Figure 5-14 Phase diagram for compressively strained $Ag(Ta_{0.5}Nb_{0.5})O_3$ films on $SrTiO_3$ substrates superimposed on the bulk phase diagram for $AgTa_xNb_{1-x}O_3$ system. The stars indicate the phase transition temperatures observed in this work. The gray text represents the bulk phases while the black text refers to the films.

5.3 Conclusions

Coherent, compressively strained $Ag(Ta_xNb_{1-x})O_3$ thin films were deposited on (001) $SrTiO_3$ substrates. The in-plane compressive biaxial strain expanded the temperature region of the O and T phase fields by ~280 °C, and yielded a domain structure with the long axis out-of-plane. On further cooling, ferroelastic switching of the domain states was limited, which forced the complex tilt system to develop along the out-of-plane axis, despite the larger in-plane lattice mismatch. The strain control of the domain state in ATN films allows the possible study of anisotropy in such materials, as bulk materials and relaxed films are polydomain. As was the case for relaxed films, the coherently strained $Ag(Ta_{0.5}Nb_{0.5})O_3$ films are in the M_3 phase at room temperature, while bulk ceramics and crystals are in the M_2 phase. This work demonstrates the first steps in strain engineering functional materials with complex tilt systems and compound phase transition sequences and opens up the possibility of tailoring functional properties that are influenced by octahedral rotations.

Chapter 6

$Ag(Ta_xNb_{1-x})O_3$ Thin Films Under Tensile Strain

This chapter will discuss structural results of $Ag(Ta_xNb_{1-x})O_3$ (ATN) thin films under tensile strain. In this work, ATN was deposited on two different substrates: $KTaO_3$ and $(Ba_{0.4}Sr_{0.6})TiO_3$ (BST) on $LaAlO_3$. Prior to describing the ATN films, the structural properties of the BST layer will be discussed. Then, X-ray diffraction and TEM results of ATN under biaxial tensile strain will be presented. Finally, a discussion of how tensile strain influences the phase transitions in $Ag(Ta_{0.5}Nb_{0.5})O_3$ films is given.

6.1 Choice of substrate for tensile films

In the previous chapter, $Ag(Ta_{0.5}Nb_{0.5})O_3$ (ATN) thin films under compressive strain were described. The goal of this section was to perform a comparable study or ATN films with a tensile strain. Ideally, the underlying layer should be cubic with no rotation of the oxygen octahedra. For this work, two different substrates or pseudo-substrates were chosen. The first choice was a solid solution of $(Ba_{0.4}Sr_{0.6})TiO_3$ (BST) because it satisfies the conditions mentioned above. In addition, its lattice parameter of ~ 3.94 Å would induce a tensile strain in ATN of similar magnitude to that observed in ATN/STO, thus providing a comparable study between the compressive and tensile strain states. Unfortunately, single crystals of $(Ba_{0.4}Sr_{0.6})TiO_3$ are not commercially available. Therefore, a BST thin film was deposited via pulsed laser deposition to act as a pseudo-substrate for the $Ag(Ta_xNb_{1-x})O_3$ films. $(Ba_{0.4}Sr_{0.6})TiO_3$ should induce 0.85% tensile strain along the *a*-axis, negligible strain along the *b*-axis and 0.53% strain along the *c*-axis of coherent $Ag(Ta_{0.5}Nb_{0.5})O_3$. The underlying substrate of choice was $LaAlO_3$ (LAO) because its

lattice parameter was far enough from that of BST that peaks were readily differentiated in diffraction patterns. $LaAlO_3$ has a tilt system of $a^-a^-a^-$ and is twinned, however, the superlattice reflections are not in close proximity to tilt peaks in ATN. The ATN film thickness on BST/$LaAlO_3$ was ~ 15 nm.

The second substrate used in this study was $KTaO_3$. This crystal has a lattice parameter of 3.989 Å, which would induce a 2.0 % strain along the *a*-axis, 1.3 % strain along the *b*-axis and 1.8 % strain along the *c*-axis in $Ag(Ta_{0.5}Nb_{0.5})O_3$. Because of the larger strain, the ATN film was grown to a thickness of only 7.5 nm to increase the likelihood of coherency. The advantage of using $KTaO_3$ is that it has a smoother surface than the deposited BST film.

6.1.1 Structure and microstructure of $(Ba_{0.4}Sr_{0.6})TiO_3$ thin films

Prior to depositing $Ag(Ta_xNb_{1-x})O_3$, the structure and microstructure of $(Ba_{0.4}Sr_{0.6})TiO_3$ (BST) was examined to determine if the film was of acceptable quality. The experimental procedure for depositing BST films is described in detail in Chapter 3. Figure 6-1a shows the out-of-plane θ-2θ X-ray diffraction scan of BST on $LaAlO_3$. The film is free of second phases and shows no evidence of misorientation. The rocking curve about the 002 peak showed that the film mimicked the twinning of the underlying substrate. The FWHM of the stronger 002 film peak was 0.030 ± 0.002° and the lattice parameter was calculated to be 3.947 ± 0.015 Å. The $(Ba_{0.4}Sr_{0.6})TiO_3$ film exhibited epitaxy, as is demonstrated by the phi scan in Figure 6-1b. The FWHM of the 011 peak was 0.678 ± 0.002°.

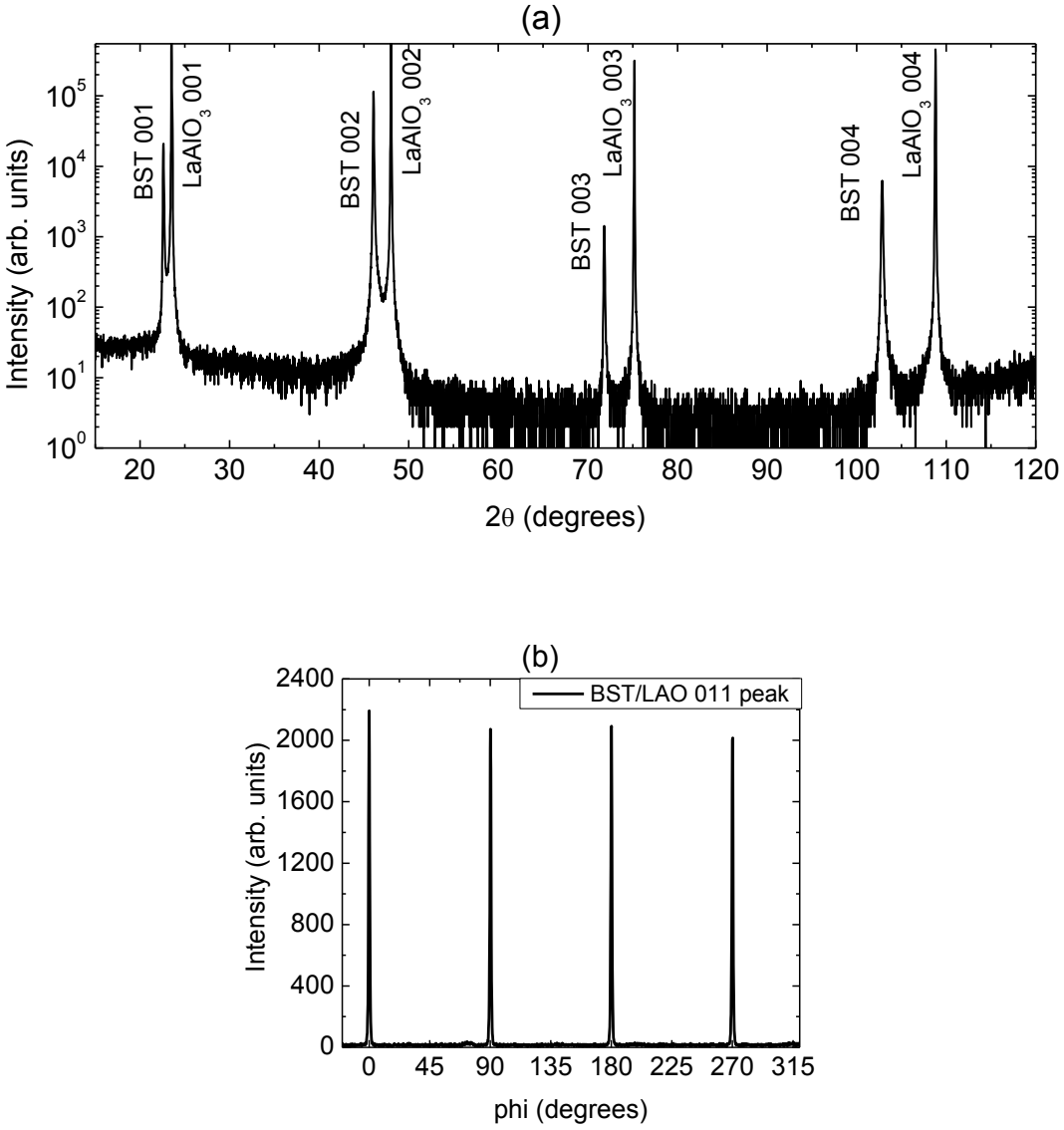

Figure 6-1 (a) Out-of-plane θ-2θ scan of a $(Ba_{0.4}Sr_{0.6})TiO_3$ film on $LaAlO_3$. (b) Phi scan showing epitaxy about the BST 011 peak.

The surface roughness of the BST film was critical because a coherent layer of ATN was to be deposited on top of this buffer layer. Any defects in the $(Ba_{0.4}Sr_{0.6})TiO_3$ could disrupt the crystalline quality of the ATN. Thus, the microstructure of the pseudo-substrate was examined using field-emission scanning electron microscopy (FE-SEM). Figure 6-2 shows a plan-view

micrograph of the BST surface. Although relatively dense and smooth, it should be noted that there are defects every few microns. A Digital Instruments Nanoscope Dimension 3100 Atomic Force Microscope (AFM) was used to measure the surface roughness of the film. The scan was performed in tapping mode with a standard tapping mode tip from Nanosensors. It was determined that the surface roughness had an rms value of ~10 Å. The defects observed in the FESEM image were pits in the film approximately 50-60 Å deep. Such a non-pristine surface may degrade the coherency of the ATN film.

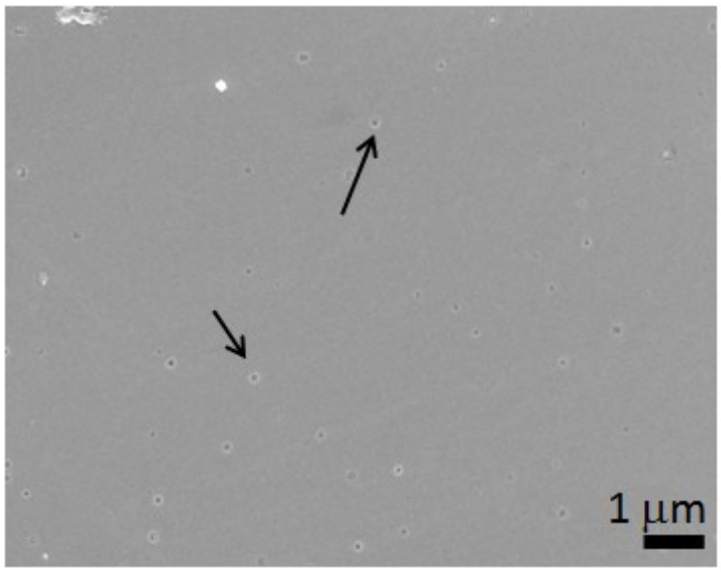

Figure 6-2 Field emission scanning electron micrograph of $(Ba_{0.4}Sr_{0.6})TiO_3$ film on $LaAlO_3$. The film shows a relatively smooth surface with visible defects (indicated by arrows).

6.2 Results of $Ag(Ta_{0.5}Nb_{0.5})O_3$ films under tensile strain

$Ag(Ta_xNb_{1-x})O_3$ thin films were deposited on a $(Ba_{0.4}Sr_{0.6})TiO_3$ (BST) pseudo-substrate as well as single crystal $KTaO_3$ to provide a tensile strain. Details of the experimental procedure are described in Chapter 3 of this dissertation. Figure 6-3 shows the sample stack consisting of the ATN film on a buffer layer of BST that was grown on a single crystal of $LaAlO_3$. The ATN layer

was ~15 nm and the BST layer was ~180 nm in thickness. $Ag(Ta_{0.5}Nb_{0.5})O_3$ films deposited on $KTaO_3$ were ~ 7.5 nm thick and were grown directly on the crystal surface.

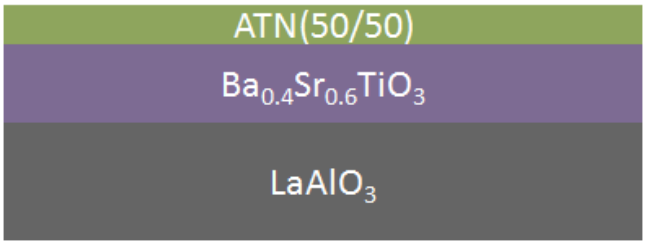

Figure 6-3 Schematic showing the substrate/pseudo-substrate stack that was used in this work. The $Ag(Ta_xNb_{1-x})O_3$ film was deposited on a buffer layer of $(Ba_{0.4}Sr_{0.6})TiO_3$ grown on an $LaAlO_3$ crystal.

6.2.1 X-ray diffraction of ATN/BST/$LaAlO_3$

Figure 6-4a shows the out-of-plane θ-2θ X-ray diffraction pattern of a ATN/BST/$LaAlO_3$ sample for a Ta:Nb ratio of 50:50. The shoulder from the ATN peak is clearly visible on the right hand side of the BST peak as shown in Figure 6-4b. No indication of second phases or misorientation was apparent in the sample. Due to the difficulty in separating an off-axis ATN peak from the BST reflections, no phi scan was performed.

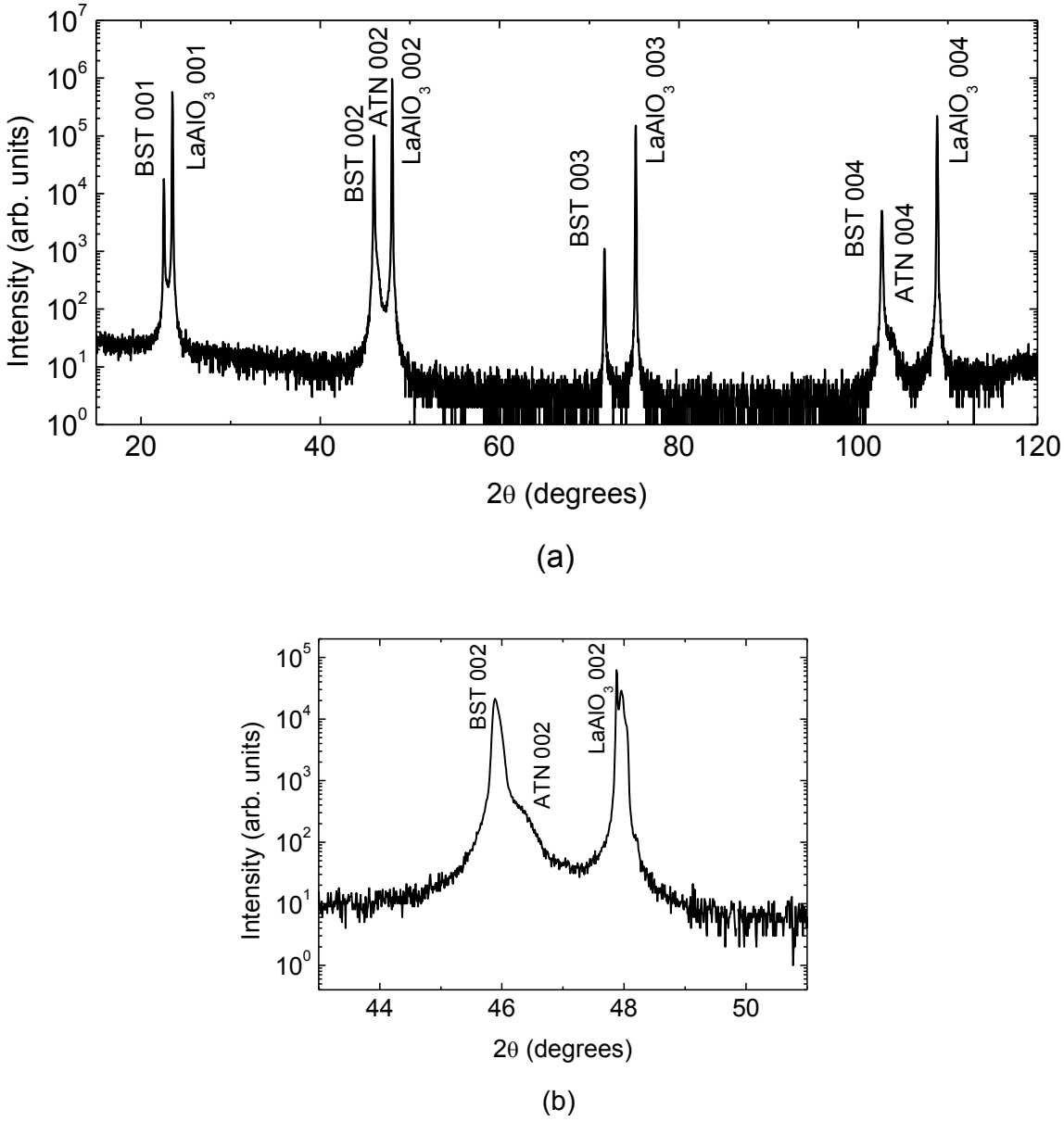

Figure 6-4 (a) θ-2θ X-ray diffraction pattern of coherent ATN (x=0.5)/BST/$LaAlO_3$ sample. (b) Higher resolution θ-2θ scan around the 002 peaks, showing the shoulder that represents the ATN film.

Rocking curves of the $Ag(Ta_{0.5}Nb_{0.5})O_3$ film, BST buffer layer and $LaAlO_3$ substrates are shown in Figure 6-5 for the 002 reflection. In this plot, the intensities are normalized and the peaks are centered on $\omega = 0°$. The double peak is due to twinning in the substrate, which propagates through the BST and ATN films. It appears that the ATN exhibits some portion of

material that is relaxed, based on the broad skirt seen in the rocking curve superimposed over the sharper peak. The FWHM of the left-hand peak for each of the materials is shown in Table 6-1.

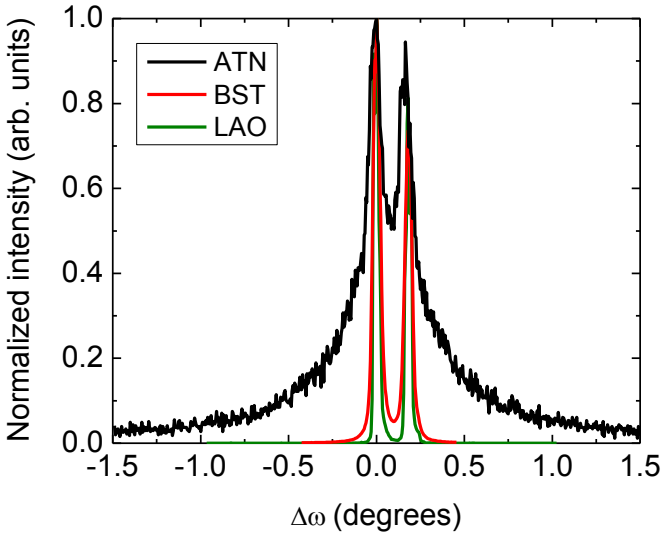

Figure 6-5 Normalized intensity of rocking curves for the $Ag(Ta_{0.5}Nb_{0.5})O_3$, BST, and $LaAlO_3$ layers. The double peak is a result of the twinning observed in $LaAlO_3$. The peaks were centered about $\omega = 0°$.

Table 6-1 FWHM of the 002 rocking curves for $LaAlO_3$, BST and ATN(x=0.5).

	FWHM rocking curve 002 (degrees)
$LaAlO_3$	**0.036 ± 0.002**
$(Ba_{0.4}Sr_{0.6})TiO_3$	**0.039 ± 0.004**
$Ag(Ta_{0.5}Nb_{0.5})O_3$	**0.111 ± 0.005**

6.2.2 X-ray diffraction of ATN on $KTaO_3$

Room temperature X-ray diffraction data of ATN on $KTaO_3$ are shown in Figure 6-6. The out-of-plane θ-2θ scan shows the films are free of secondary phases and exhibit only 00*L*

orientation. Rocking curves around the 002 peaks exhibited FWHM of 0.0167° ± 0.0005° and 0.058° ± 0.002° for $KTaO_3$ and ATN, respectively. The rocking curves are shown in Figure 6-6b.

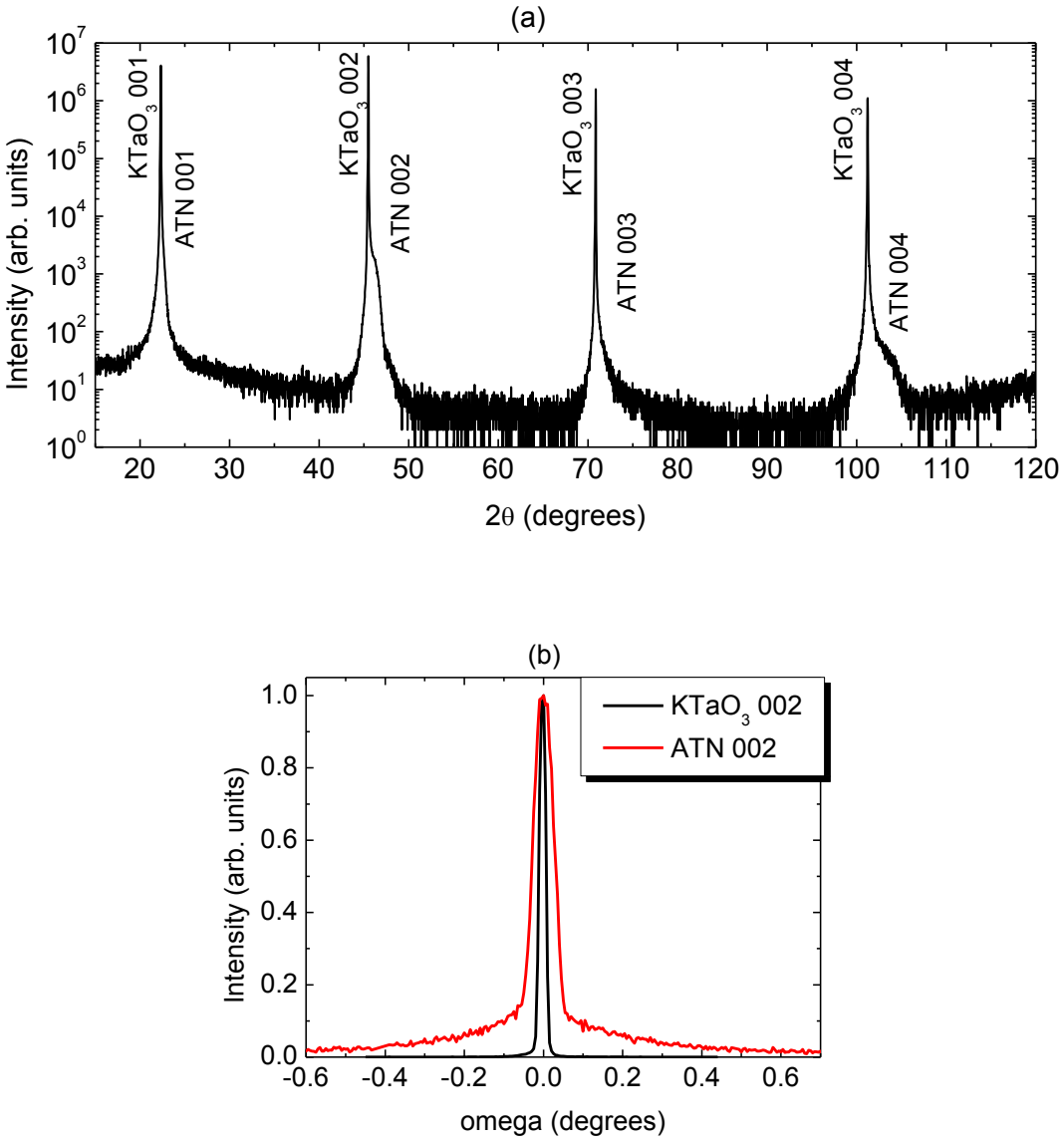

Figure 6-6 (a) θ-2θ X-ray diffraction pattern of $Ag(Ta_{0.5}Nb_{0.5})O_3$ on $KTaO_3$. (b) Rocking curve around the 002 reflection for both the film and substrate. The FWHM of $KTaO_3$ was 0.0167° ± 0.0005°. ATN had a FWHM of 0.058° ± 0.002°.

6.2.3 Room temperature TEM and synchrotron XRD

The room temperature phase of the tensile ATN films was determined through the use of TEM and synchrotron X-ray diffraction. Figure 6-7 shows a high-angle annular dark-field (HAADF) scanning tunneling electron microscope (STEM) micrograph of an $Ag(Ta_{0.5}Nb_{0.5})O_3$ film on a $(Ba_{0.4}Sr_{0.6})TiO_3$ buffer layer. The image shows the interface is clean and the ATN is coherent with the BST. It is believed that the bright spots in the ATN correspond to Nb/Ta atomic columns. The light regions in the BST are the Ba/Sr columns. The ATN film appears to be homogeneous and free of secondary phases.

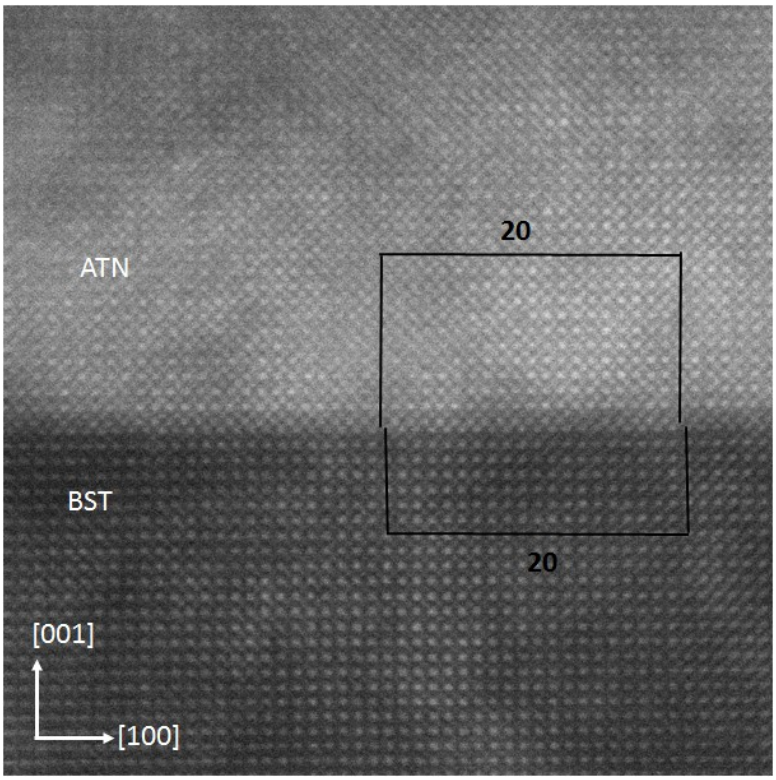

Figure 6-7 High-angle annular dark-field (HAADF) scanning tunneling electron micrograph (STEM) of an $Ag(Ta_{0.5}Nb_{0.5})O_3$ film on a $(Ba_{0.4}Sr_{0.6})TiO_3$ buffer layer. Coherency is demonstrated and a clear interface is observed between the two layers. Image courtesy of I. Levin.

6.2.3.1 ½{ooo} ± ¼{00L} reflections due to tilt

The room temperature phase can be determined, in part, by the existence or absence of quarter-order reflections flanking the ½{*ooo*}-type reflections. As was discussed in Section 2.3.3, such peaks indicate that the material has the complex tilt system $a^-b^-c^-/a^-b^-c^+$ and is in one of the M phases. The next two sub-sections will examine the ½{*ooo*} ± ¼{00*L*} reflections in both ATN/BST/$LaAlO_3$ and ATN/$KTaO_3$.

Complex tilt in ATN/BST/$LaAlO_3$

Figure 6-8 shows reciprocal space scans in the *H*, *K*, and *L* directions about the ½113 reflection for the $Ag(Ta_{0.5}Nb_{0.5})O_3$ film on a $(Ba_{0.4}Sr_{0.6})TiO_3$ buffer layer. In these films, no indication of the quarter-order reflection was observed. This suggests that the films are either in the O phase at room temperature, that the tilt angle is small, or that the long-range order of the octahedral rotations has been suppressed. To further investigate whether signal was present at the quarter order positions, phi and chi scans were performed at ½113 – 0¼0. These scans, shown in Figure 6-9, did not detect measureable intensity despite the long count time during the measurement.

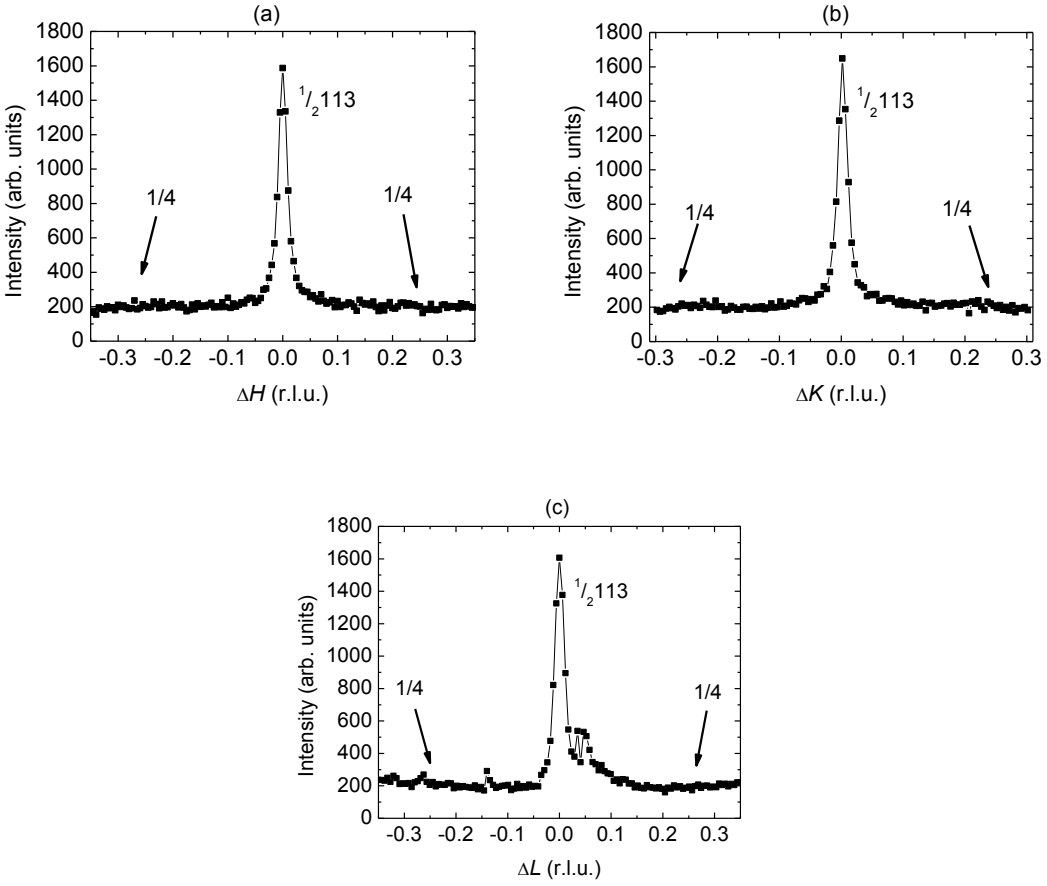

Figure 6-8 Room temperature reciprocal space scans in the (a) *H*, (b) *K*, and (c) *L* directions about the ½113 reflection for $Ag(Ta_{0.5}Nb_{0.5})O_3$ film on a $(Ba_{0.4}Sr_{0.6})TiO_3$. No evidence of quarter-order peaks is observed.

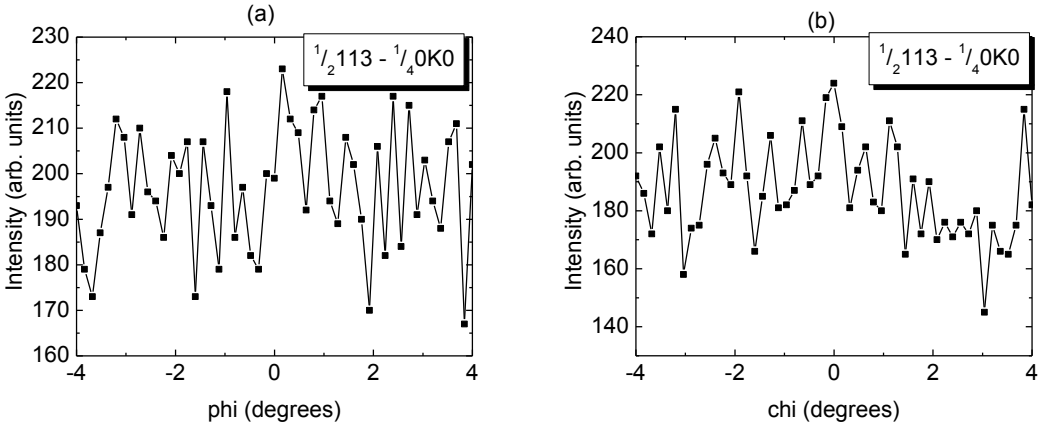

Figure 6-9 (a) Phi and (b) chi scans at the assumed ½113 – 0¼0 position for ATN/BST/$LaAlO_3$. There is no strong evidence for intensity at this location.

Transmission electron diffraction patterns were obtained at room temperature to examine whether or not the quarter order reflections associated with tilt were present. Figure 6-10a and Figure 6-10b show the diffraction patterns for ATN along the [130] and [013] zone axes, respectively. Similar to the X-ray results, no distinct ½{*ooo*} ± ¼{00*L*} spots were observed. However, streaks of diffuse intensity along the *c*-axis were discernable, suggesting that both the tilt angle and the correlation length for a complex sequence, $a^{-}b^{-}c^{-}/a^{-}b^{-}c^{+}$, are significantly reduced compared to bulk materials.

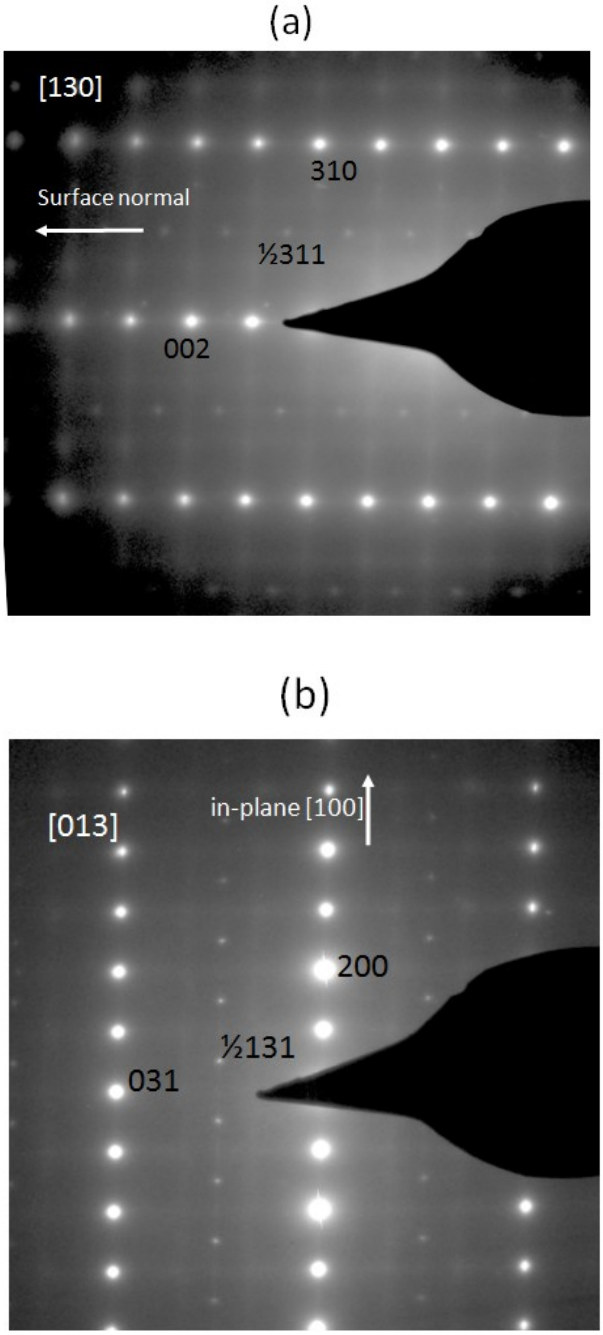

Figure 6-10 TEM electron diffraction patterns along the (a) [130] and (b) [013] zone axes for an $Ag(Ta_{0.5}Nb_{0.5})O_3$ film on a $(Ba_{0.4}Sr_{0.6})TiO_3$ buffer layer. Similar to the X-ray diffraction work, there was no evidence of quarter order reflections about the ½{*ooo*} spots. Sheets of diffuse intensity suggest that the long range order of the complex tilt is significantly reduced compared to bulk. Images provided courtesy of Igor Levin.

Complex tilt in ATN on $KTaO_3$

To further assess the room temperature phase of ATN films under tensile strain, a search for the ½{*ooo*} ± ¼{00*L*} reflections was performed on $Ag(Ta_{0.5}Nb_{0.5})O_3$ films on $KTaO_3$ substrates. Figure 6-11 shows synchrotron X-ray diffraction results of scans in reciprocal space near the ATN ½311 reflection. In Figure 6-11a, no clear peaks are apparent at the quarter-order positions in the *H*, *K*, or *L* directions when plotted on a scale which shows the main peak. However, closer examination at ½311 + 0¼0 position (Figure 6-11b) shows weak peaks suggesting that the films do exhibit the complex tilt system, $a^-b^-c^-/a^-b^-c^+$, along an in-plane direction. As is observed in Figure 6-11c, the ½311 + 00¼ region does not show obvious intensity. These results suggest that ATN films under tensile are in an M phase at room temperature and that the complex tilt is oriented in the plane of the film.

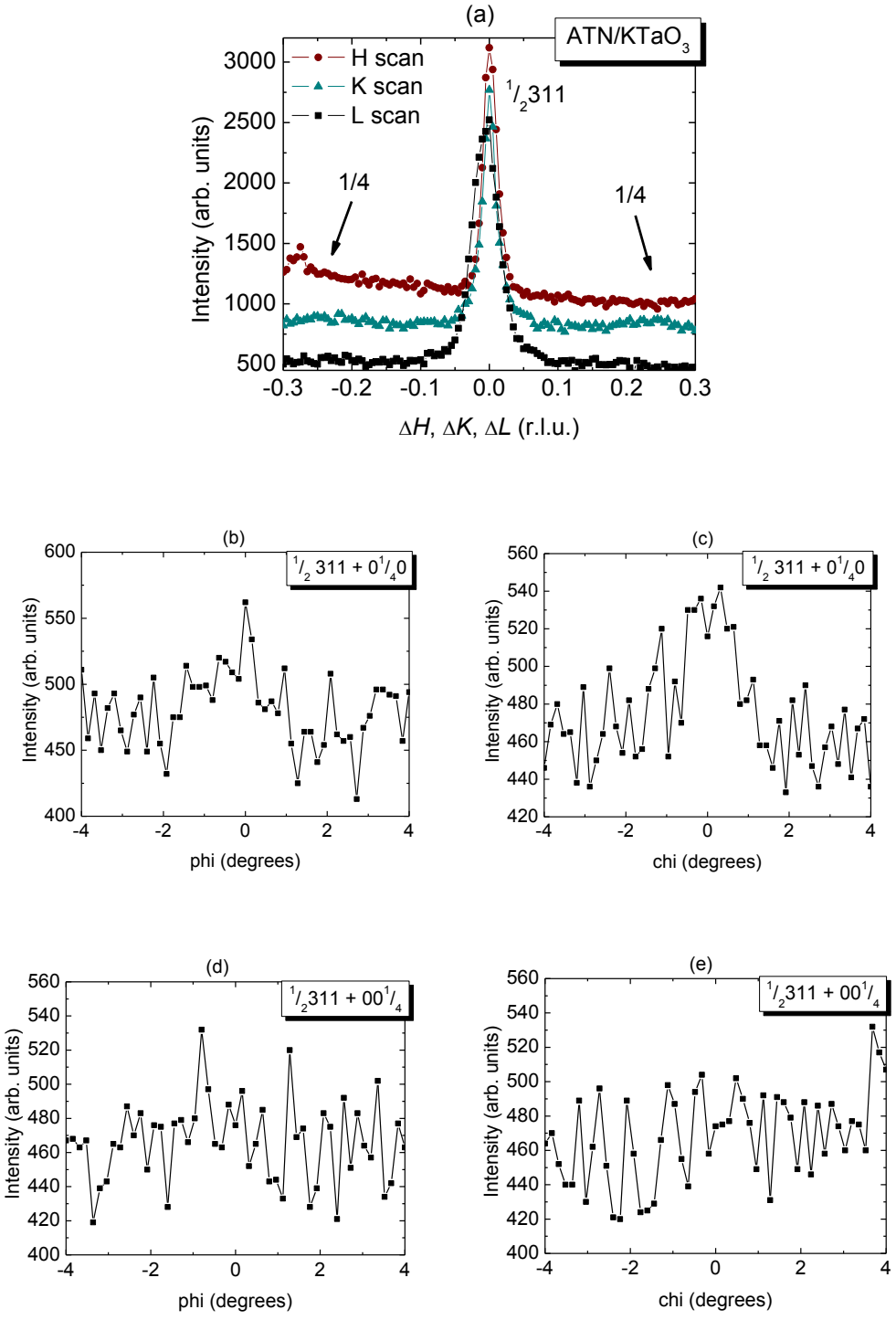

Figure 6-11 X-ray diffraction scans of $Ag(Ta_{0.5}Nb_{0.5})O_3$ film on $KTaO_3$. (a) Reciprocal space scans in the *H*, *K*, and *L* direction around the ½311 reflection. (b) Phi and (c) chi scans near ½311 + ¼{0*K*0} show slight hint of a peak. However, (d) phi and (e) chi scans about ½311 + ¼{00*L*} show no evidence of intensity. These results suggest the tilt axis lie in the plane of the film when ATN is under tensile strain.

6.2.3.2 ¼{00L} reflections due to local cation displacements

Figure 6-12 shows reciprocal space scans in the *H*, *K*, and *L* directions about the 101 reflection for $Ag(Ta_{0.5}Nb_{0.5})O_3$ film on $(Ba_{0.4}Sr_{0.6})TiO_3/LaAlO_3$. Such scans were designed to search for the ±¼{00*L*} peaks indicative of long range ordering of local cation displacements. Because the ATN film had similar lattice parameters to the $(Ba_{0.4}Sr_{0.6})TiO_3$ buffer layer, the more intense BST 101 peak was used as the center point in these measurements. Figure 6-12b and Figure 6-12c show only scans in the negative *K* and *L* directions; the ±¼{00*L*} peaks should be symmetric. Similar to the results of compressively strained ATN, no indication of quarter order reflections was observed. The TEM electron diffraction pattern in Figure 6-13 confirms that ±¼{00*L*} spots do not exist in the ATN/$(Ba_{0.4}Sr_{0.6})TiO_3/LaAlO_3$ samples. In addition, X-ray diffraction scans on ATN/$KTaO_3$ did not show evidence of the quarter-order reflections. One possibility is that this result suggests that tensile strain not only affects the octahedral rotations but also disrupts the long range ordering of local cation displacements. However, it is important to recognize that relaxed films also showed a suppression of the cation displacements. Thus, a second contribution to failure to observe these quarter order reflections could arise from the point defect concentrations in the films.

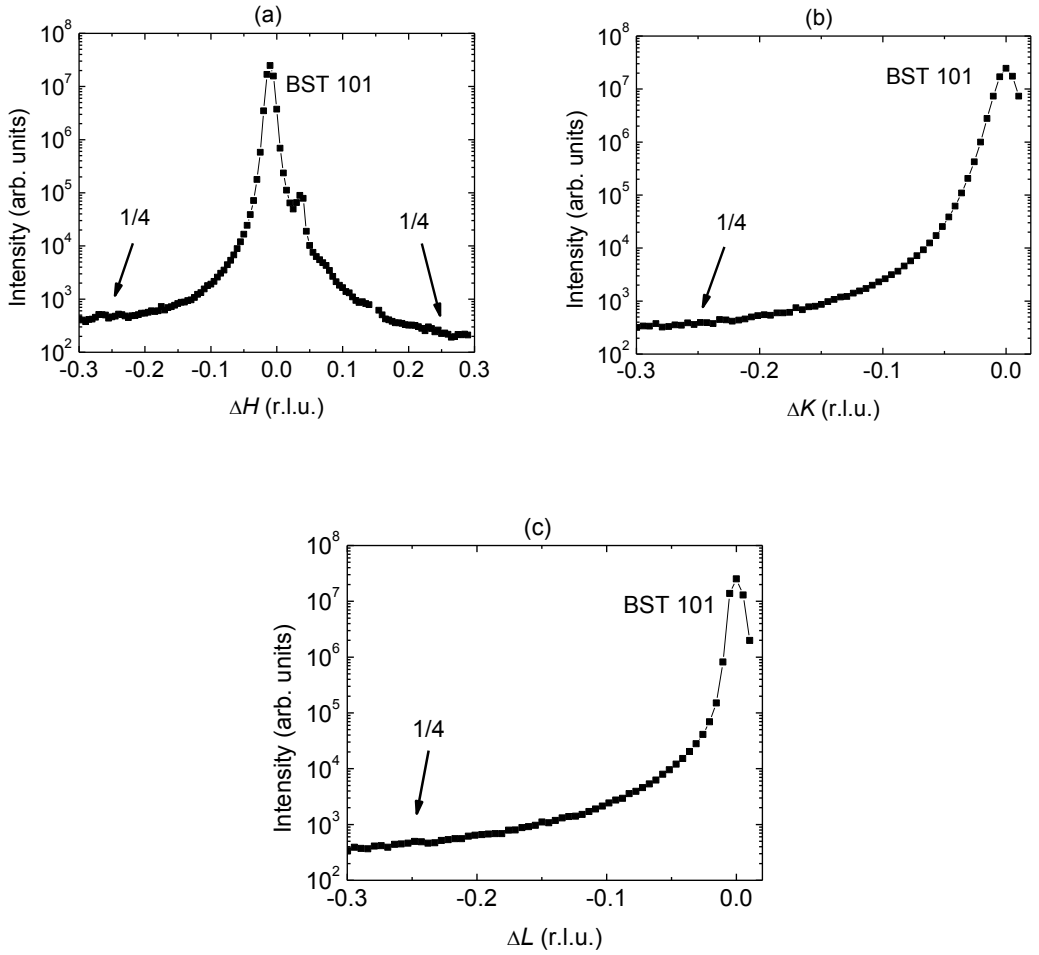

Figure 6-12 Reciprocal space scans in the (a) *H*, (b) *K*, and (c) *L* directions about the 101 reflection for $Ag(Ta_{0.5}Nb_{0.5})O_3$ on $(Ba_{0.4}Sr_{0.6})TiO_3/LaAlO_3$. There was no evidence of quarter order reflections, suggesting the long range ordering of local cation displacements is suppressed.

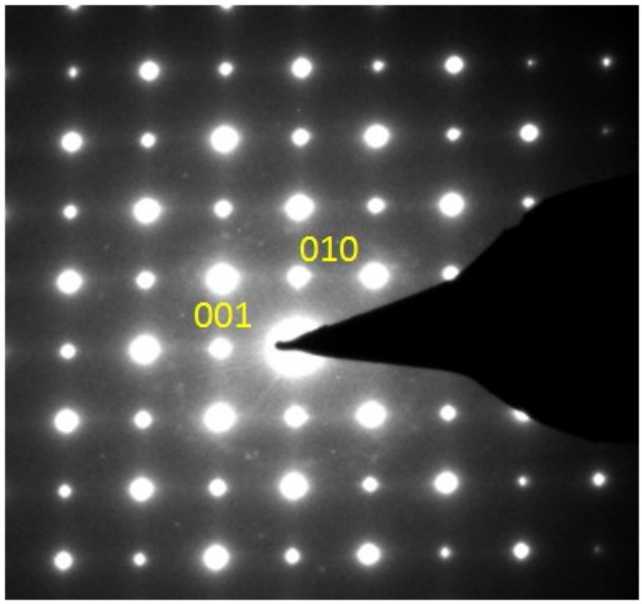

Figure 6-13 Selected area electron diffraction pattern along the [100] zone axis for ATN/BST/$LaAlO_3$. No ±¼{00*L*} reflections are observed, suggesting that tensile strain has affected the local cation displacements in $Ag(Ta_{0.5}Nb_{0.5})O_3$ films. The faint ring is likely due to redeposited Ag or Ag_2O. Images provided courtesy of Igor Levin.

6.2.4 Phase transition temperature determination of tensile films

The transition temperatures of $Ag(Ta_{0.5}Nb_{0.5})O_3$ films under tensile strain were determined by examining the integrated intensity of two superlattice reflections for the $Ag(Ta_{0.5}Nb_{0.5})O_3$ on $(Ba_{0.4}Sr_{0.6})TiO_3/LaAlO_3$ sample. No tilting of the oxygen octahedra exists in the cubic phase; therefore, no reflections would be expected. In the tetragonal phase, the in-phase tilt will produce ½{*ooe*}-type reflections.[3] Anti-phase tilting about the *a*- and *b*-axes exists in the M phases, producing superlattice reflections of the type ½{*ooo*}. The O phase exhibits a mixed tilt system, $a^0b^-c^+$, which gives rise to anti-phase tilting about the *b*-axis and in-phase tilting about the *c*-axis. Figure 6-14 shows the normalized integrated intensity for the ½113 (anti-phase) and ½123 peaks (in-phase). When the film is in the M phase, the ½113 peaks dominate

and when ATN is in the T phase, the ½123 reflection dominates. The region that shows finite intensity for both superlattice reflections occurs when the material is in the O phase. Interestingly, the intensity of the ½123 reflection was significantly weaker than a similar reflection in the compressively strained films. This suggests that the tilt angle or long range ordering of tilt in $Ag(Ta_{0.5}Nb_{0.5})O_3$ under tensile strain is smaller than that of ATN under compressive strain. As a consequence of the weaker intensity, the data shown in Figure 6-14 possesses more noise than was characteristic of the films on $SrTiO_3$.

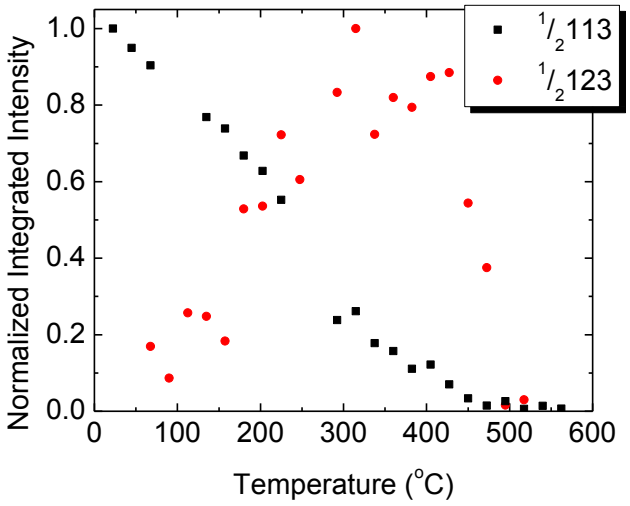

Figure 6-14 Normalized integrated intensities of the ½113 and ½123 reflections as a function of temperature in $Ag(Ta_{0.5}Nb_{0.5})O_3$ films on $(Ba_{0.4}Sr_{0.6})TiO_3/LaAlO_3$. In the M phase, anti-phase tilting dominates; the O phase shows both in-phase and anti-phase tilt and the T phase shows exclusively in-phase tilt.

The phase transition temperatures were determined by performing linear fits to the integrated intensity data in Figure 6-14. Data for the ½123 peak was divided into two regions; 75 °C – 300 °C and 300 °C – 525 °C. The ½113 response was fit with a line between 25 °C and 525 °C. Phase transition temperatures were determined at the intersections of these lines. Table 6-2 shows the transition temperatures determined in this work compared to those found in bulk $Ag(Ta_{0.5}Nb_{0.5})O_3$. The results indicate that tensile strain suppresses the M_3-O transition ~ 275 °C,

while the C-T transition temperature was comparable to bulk. As was observed in compressively strained films, tensile biaxial strain also stabilizes the O and T phase regime.

Table 6-2 Phase transition temperatures found in bulk $Ag(Ta_{0.5}Nb_{0.5})O_3$ and those determined for $Ag(Ta_{0.5}Nb_{0.5})O_3$ films on a $(Ba_{0.4}Sr_{0.6})TiO_3/LaAlO_3$.

Transition Type	Bulk Transition Temperatures (°C)	Films under tensile strain (°C)
C – T	552	551 ± 100
T – O	400	330 ± 72
O – M_3	326	52 ± 24

6.2.5 High temperature domain state of ATN under tensile strain

The domain state of $Ag(Ta_{0.5}Nb_{0.5})O_3$ thin films on $(Ba_{0.4}Sr_{0.6})TiO_3/LaAlO_3$ was determined through the examination of the ½{*ooe*}-type reflections at 400 °C. At this temperature, the material is in the tetragonal phase with tilt system $a^0a^0c^+$. According to rules developed by Glazer (shown in Table 5.2), the orientation of the tilt axis can be determined.[10] Figure 6-15 shows X-ray diffraction scans of the ½123, ½213 and ½312 reflections. As shown in the figure, finite intensity was observed for only the ½123 and ½213 peaks, indicating that the in-phase tilt occurs along the in-plane axes. The out-of-plane axis does not show presence of octahedral rotations as is evidenced by the fact that there was no intensity of the ½312 peak. This is in contrast to observations on compressively strained ATN films where the preferred rotation axis was along the out-of-plane direction. It is, however, in agreement with other reports which showed that biaxial tensile strain leads to an enhancement of octahedral rotations along the in-plane axis and suppression along the out-of-plane axis.[17, 22, 37] It can be concluded that in the T phase of tensile strained ATN films the tilt axis is along the *c*-axis, suggesting that the domain structure is arranged so that the *c*-axis lies in the plane.

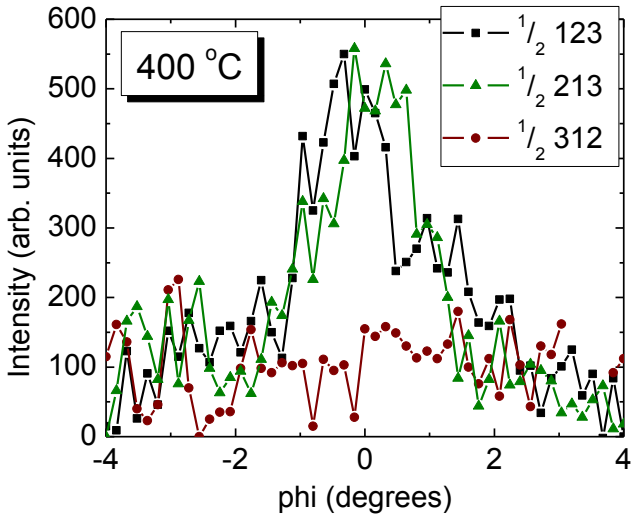

Figure 6-15 Phi scans near the ½123, ½213 and ½312 regions in the $Ag(Ta_{0.5}Nb_{0.5})O_3$ /$(Ba_{0.4}Sr_{0.6})TiO_3$/$LaAlO_3$ sample at 400 °C. The finite intensity of ½123 and ½213 reflections suggests that the in-phase tilt occurs exclusively around the in-plane axes.

6.3 Discussion

Figure 6-16 shows a schematic summarizing the evolution of the domain state in $Ag(Ta_{0.5}Nb_{0.5})O_3$ films under tensile strain as a function of temperature. When the films are at high temperatures, they are in the cubic phase. As the material cools, it transitions into the T phase with in-phase octahedral tilting about the in-plane axes. It is believed that the tensile strain forces this tilt axis along the in-plane directions to accommodate the smaller out-of-plane lattice parameter required.[37] In the O phase, the ATN film acquires anti-phase tilt in addition to the in-phase tilt from the T phase. At room temperature, the films are likely in the M_3 phase, as was evidenced by the disappearance of the ½123 peak. Based on the weak signal of the quarter-order reflections in ATN on $KTaO_3$, it is believed that the *c*-axis remains along the in-plane directions in this phase. As was observed with $Ag(Ta_{0.5}Nb_{0.5})O_3$ under compressive strain, it is likely that

the activation energy required to reconfigure octahedral rotations is too high, so that the domain state established at high temperatures templates the room temperature domain structure.

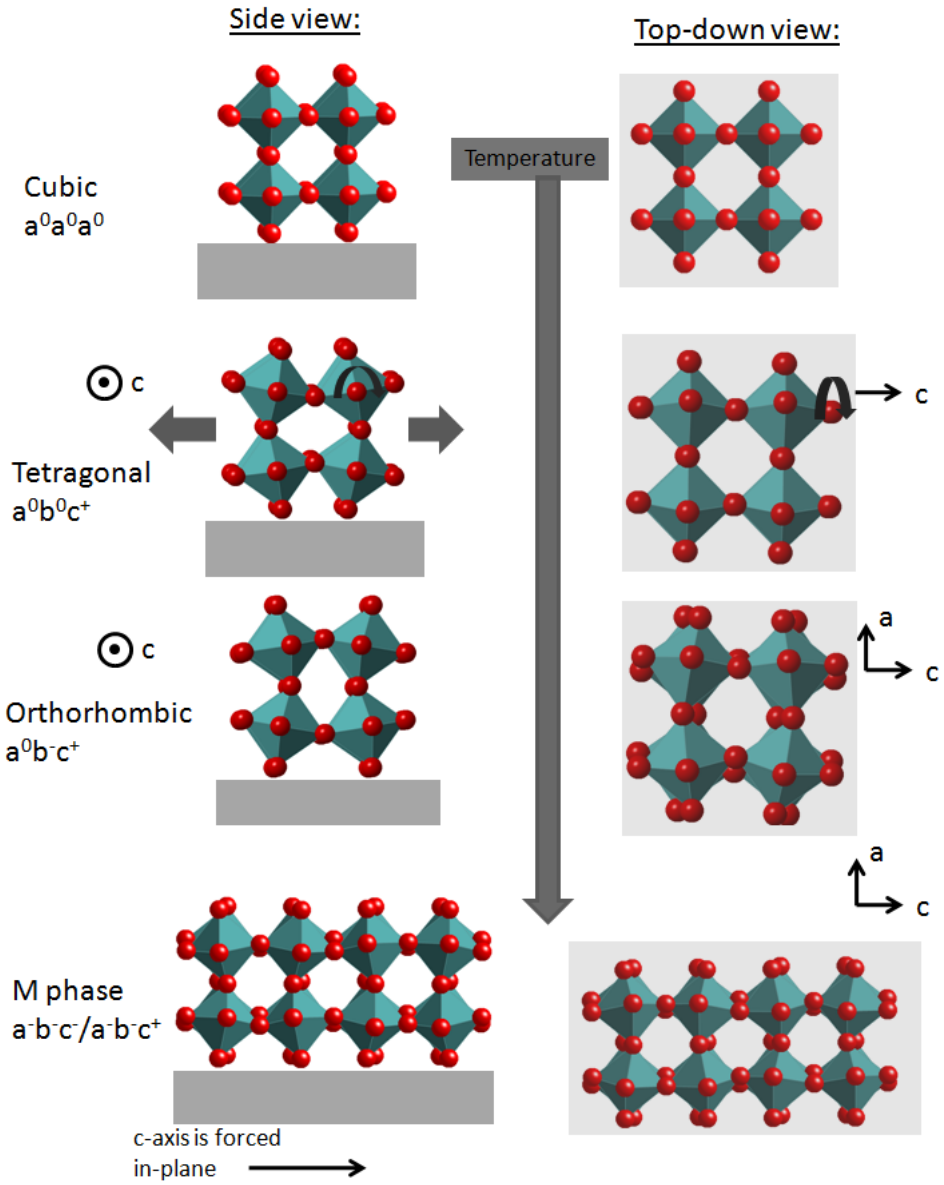

Figure 6-16 Schematic illustrating how the domains in ATN under tensile strain behave as a function of temperature. At high temperatures, the material is cubic. Then, as it cools through the tetragonal phase, an in-phase tilt develops along the in-plane axes. An anti-phase tilt is added in the O phase. The films are in the M_3 phase at room temperature. The domain structure is such that the complex tilt axis (i.e *c*-axis) lies in-plane.

The information described above can be summarized by superimposing the phase transition temperatures of ATN under tensile strain on the bulk phase diagram. This is shown in Figure 6-17. The results of $Ag(Ta_{0.5}Nb_{0.5})O_3$ on $(Ba_{0.4}Sr_{0.6})TiO_3/LaAlO_3$ are denoted using stars while the bulk data is shown as the solid lines. This figure demonstrates the expanded temperature regime experienced by the O and T phases. In addition, it shows that no indication of the M_2 phase was observed at room temperature.

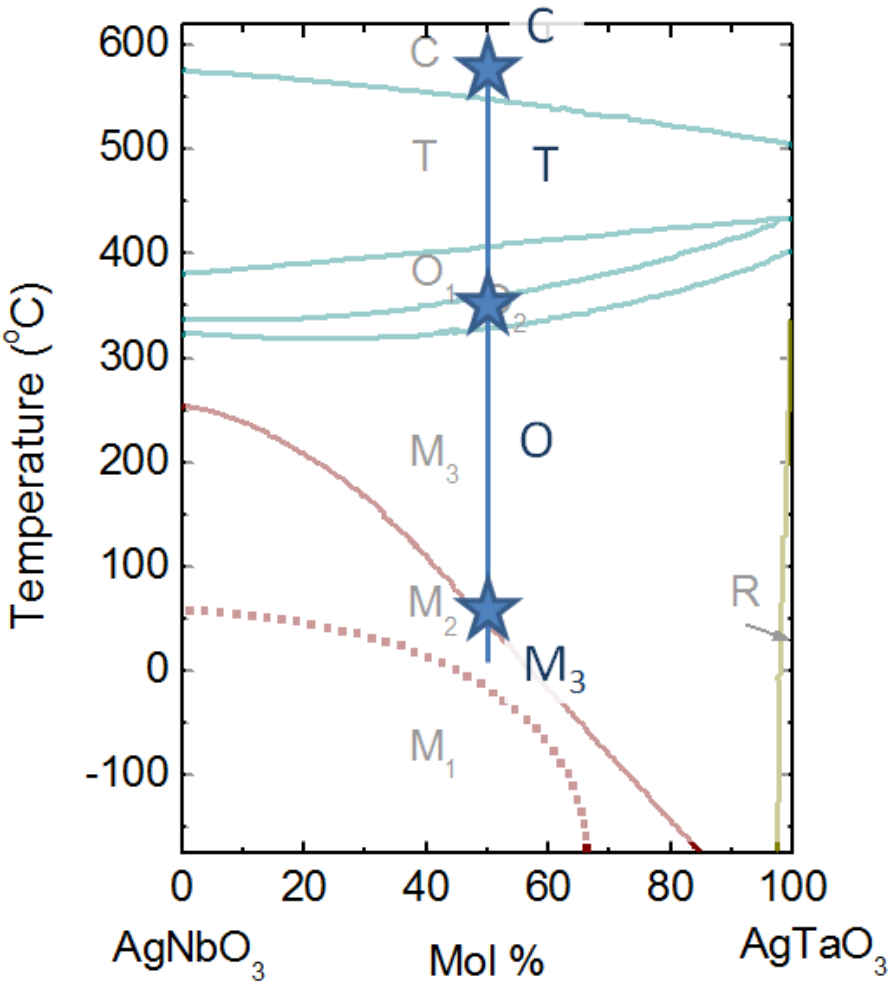

Figure 6-17 Phase transition temperatures of $Ag(Ta_{0.5}Nb_{0.5})O_3$ films on for $(Ba_{0.4}Sr_{0.6})TiO_3/LaAlO_3$ superimposed on the bulk phase diagram for $Ag(Ta_xNb_{1-x})O_3$. The paler areas represent bulk values while the black text refers to this work.

6.4 Conclusions

$Ag(Ta_{0.5}Nb_{0.5})O_3$ thin films were deposited on $(Ba_{0.4}Sr_{0.6})TiO_3/LaAlO_3$ (001) and $KTaO_3$ (001) substrates. The films were coherent in nature and, therefore, experienced a biaxial tensile stress. In the ATN/$KTaO_3$ films the strain induced in the film created a domain structure such that the *c*-axis aligned primarily along the in-plane axes. Both samples exhibited weak intensity of the superlattice reflections, suggesting the tilt angle is significantly reduced or the long range order of the complex tilt is suppressed compared to bulk and compressively strained thin films. In addition, the $Ag(Ta_{0.5}Nb_{0.5})O_3$ on $(Ba_{0.4}Sr_{0.6})TiO_3/LaAlO_3$ samples exhibited tetragonal and orthorhombic phase fields that were stabilized over a temperature region ~ 270 °C larger than that of bulk materials. Similar to relaxed and compressively strained films, both films were in the M_3 phase at room temperature. This work demonstrates that, in addition to compressive strain, tensile strain can be used to strain engineer materials with complex tilt systems and complicated phase transition sequences.

Chapter 7

Search for roto-electric effect in $AgNbO_3$

This chapter will first give an overview of theoretical work on roto-symmetry in structures that undergo rotation of polyhedra. Because, according to Neumann's Law, the symmetry of the geometrical representation of any physical property include the symmetry of the point group, new physical properties resulting from the new symmetries can be introduced by rotation. Then, an experimental method designed to assess the link between rotation and electric field will be outlined for $AgNbO_3$. Finally, results of experiments designed to search for the roto-electric effect will be discussed.

7.1 "Roto"-symmetry

Recently, Gopalan *et al.*[89] showed that the reversal of static structural rotations can be treated as a distinct symmetry operation. Examples include right- or left- handed helices, spirals, and antidistorted structures composed of rotations. These new symmetries are referred to as "roto" symmetries. Coupled with these "roto" symmetries is a prediction of new properties that include rotations such as rotoelectricity, piezorotation and rotomagnetism.

A symmetry operation is a set of actions performed on an object that will leave the object unchanged. The conventional symmetry operations include translations, mirrors, rotation and rotation inversion give rise to 32 crystallographic point groups and 230 space groups.[90] The symmetry of magnetic structures is often described with an additional symmetry operation, namely, time reversal (denoted 1'). This time reversal operation will invert time and hence the spin associated with magnetic moments. As a result, magnetic structures can be described with 90 magnetic point groups and 1421 magnetic space groups.[91]

Unfortunately, the conventional symmetry operations, including time reversal, do not do an adequate job of describing static rotations within a system. An example of a structure with static rotations is shown in Figure 7-1. Here, the oxygen octahedra of a perovskite structure may undergo tilt as shown in Figure 7-1b. The recently introduced roto-symmetry, denoted by the operation 1^{Φ}, will reverse the sense of static rotation of such structures. Using roto-symmetry as described by Gopalan *et al.,* there are 624 roto-point groups and 17,807 roto-space groups.[89]

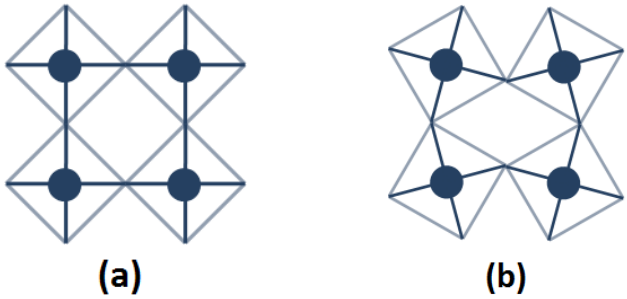

Figure 7-1 Schematic of a perovskite with (a) untilted oxygen octahedra and (b) tilted octahedra. Roto-symmetry has been shown to describe all the symmetry operations in perovskite structures with octahedral tilts.

Roto-symmetry describes finite rotations about an axis by +Φ and –Φ as shown in Figure 7-2. The images are color coded so that the purple octahedra denotes a +Φ rotation and orange represents a –Φ rotation. Applying rotation reversal symmetry, 1^{Φ}, to the image on the left will produce the image on the right and vice versa. In other words, rotation reversal symmetry will flip the sign of rotation (+Φ → –Φ) without translating the center of mass.[89]

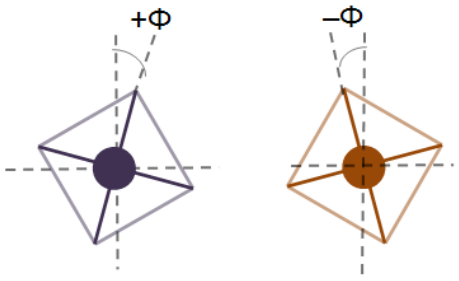

Figure 7-2 Static rotations, +Φ and –Φ, of oxygen octahedra. Roto-reversal symmetry will flip the sign of rotation.

Because a new symmetry operation has been introduced, a larger number of symmetry elements will exist for any particular system. This is shown in Figure 7-3 for the case of tilted octahedra. Using conventional symmetry, Figure 7-3 exhibits a mirror plane parallel to the *x*- and and *y*- axes as well as a 2-fold rotation about the *z*-axis. This system has the point group $m_x m_y 2_z$ which includes four symmetry elements. If rotation symmetry is considered, the same structure will exhibit all of the conventional symmetry element plus 4 new roto-symmetry elements. A mirror plane plus rotation reversal (denoted m^{Φ}) is parallel to an axis 45° between the *x* and *y* axes. In addition, a four-fold rotation plus reversal of tilt angle exists about the *z*-axis denoted by 4^{Φ} and $4^{-\Phi}$. The roto-point group is then $4^{\Phi} m_x m_{xy}{}^{\Phi}$. This new point group contains twice the number of symmetry elements as the conventional point group.[89] The larger number of symmetry elements indicates that more information on the structure is stored within the symmetry group.

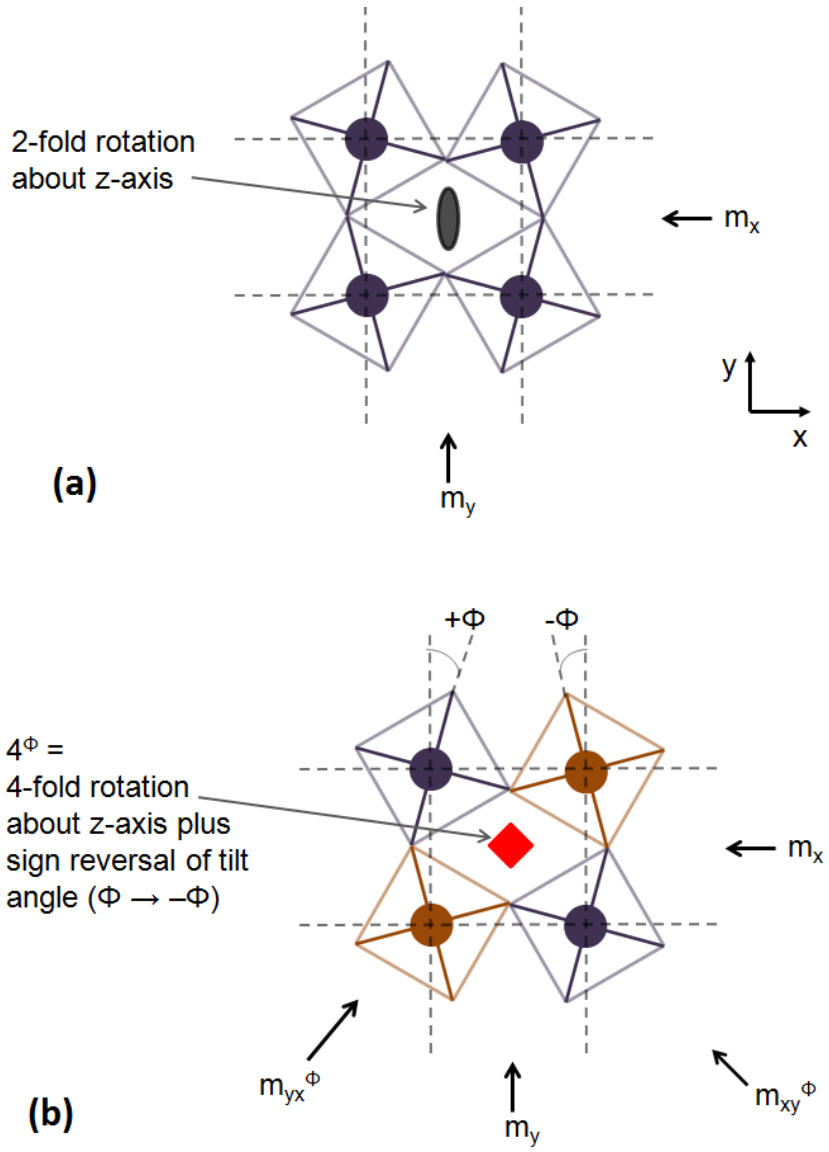

Figure 7-3 Schematic of a perovskite structure with tilted octahedra showing (a) the conventional symmetry elements and (b) the symmetry elements including roto-symmetry. Using conventional symmetry, the point group is $m_x m_y 2_z$. The point group including roto-symmetry is $4_z^{\Phi} m_x m_{xy}^{\Phi}$. Figure modeled after Gopalan *et al.*[89]

Using this technique, the symmetry elements of a real system can also be determined. For example, a perovskite structure with a tilt system of $a^+a^+c^+$ will have the orthorhombic space group *Immm1'*. However, if the new symmetries are considered, then a tetragonal space group *$I4^{\Phi}/mmm1'$* is determined.[89] All the symmetry elements for this system are shown in Figure

7-4. According to Gopalan *et al.*, the number of symmetry elements in the new space group is twice that of the conventional space group.

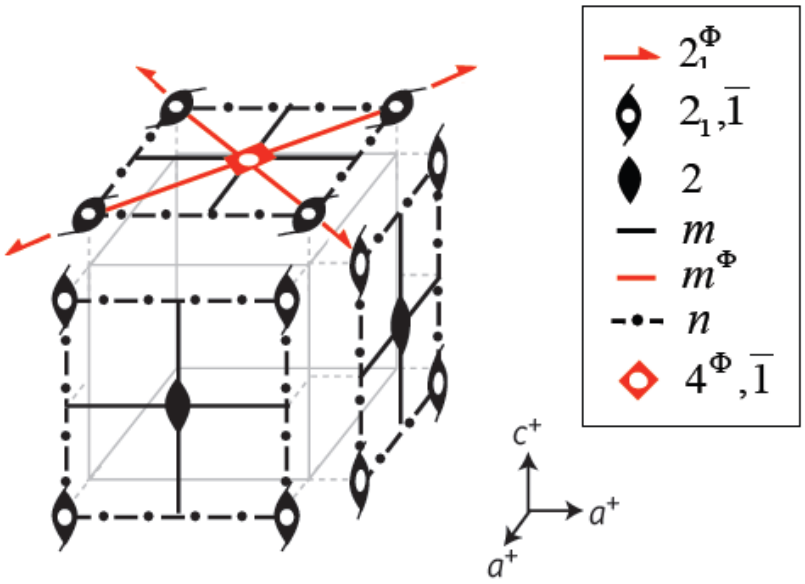

Figure 7-4 All the symmetry elements, including roto-symmetry, for a perovskite structure with an $a^+a^+c^+$ tilt system.[89]

7.1.1 New "roto" properties

A direct consequence of the discovery of new symmetries and new point groups is the possibility of predicting a wide range of new roto-properties that relate a property to static rotations in materials.[89] This concept follows from Neumann's law, which states "the symmetry of any physical property of a crystal must include the symmetry elements of the point group of the crystal." The finding of new symmetries associated with rotation reversal has opened up the door for new properties that relate static rotation to stress, strain, polarization, magnetism, and piezoelectricity to name a few. Table 7-1 shows select roto-property tensors.[89] The work

reported in this chapter will focus on the relationship between rotations and electric field, i.e. roto-electricity.

Table 7-1 Select roto-property tensors as described by Gopalan *et al.*[89]

Roto-property	***Tensor Form***
Static rotations	Φ
Linear rotoelectricity	$P_i = Q_{ij}\Phi_j$
Piezorotation	$\Phi_i = Q_{ijk}\sigma_j$
Piezorotoelectricity	$P_i = Q_{ijkl}\sigma_{jk}\Phi_l$
Quadratic rotomagnetism	$M_i = Q_{ijk}\Phi_j\Phi_k$
Piezorotomagnetism	$M_i = Q_{ijkl}\sigma_{jk}\Phi_l$
Quadratic rotoelectricity	$P_i = Q_{ijk}\Phi_j\Phi_k$
Rotostriction	$\varepsilon_{ij} = Q_{ijkl}\Phi_k\Phi_l$
Bi-quadratic rotoelectricity	$P_iP_j = Q_{ijkl}\Phi_k\Phi_l$

7.2 "Roto"-electric effect in $AgNbO_3$

The goal of this research was to design an experiment that tested for the roto-electric effect; linear, quadratic or bi-quadratic. Because $AgNbO_3$ is not polar, it should not exhibit linear or quadratic roto-electric effect. However, based on work by Gopalan,[92] the room temperature phase of $AgNbO_3$, M_1, should show bi-quadratic roto-electricity. Therefore, this work was designed to explore the possible relationship between electric field and octahedral rotations.

7.2.1 $AgNbO_3$ structure

At room temperature, $AgNbO_3$ possesses a perovskite-like structure with orthorhombic symmetry (*Pbcm* space group) and a unit cell with lattice parameters $\sqrt{2}a_{pc} \times \sqrt{2}a_{pc} \times 4a_{pc}$ (a_{pc} ~ 3.96 Å corresponds to the ideal perovskite).[43, 44] The superstructure is a result of cooperative motion of the oxygen octahedra. The tilt system, as defined by Glazer, is $a^-b^-c^-$/ $a^-b^-c^+$ which generates anti-phase tilting about the *a*- and *b*-axes and a combined in-phase and anti-phase tilt about the *c*-axis. At room temperature, the oxygen octahedra in $AgNbO_3$ have non-zero tilt about all three pseudo-cubic axes. According to Levin *et al.*,[43] bulk $AgNbO_3$ has a tilt angle of ~ 7.3° about the *c*-axis and a tilt angle of ~ 8.9° about the *b*-axis. Superlattice reflections in reciprocal space are produced as a result of non-zero tilt in this supercell. The intensity of the superlattice reflections is related to the magnitude of the rotation angle of a particular tilt system.

7.2.2 Calculation tilt angle in $AgNbO_3$

Prior to performing experiments, it was important to calculate the intensity of superlattice reflections as a function of tilt angle to determine if X-ray diffraction measurements could detect any changes in peak intensity. Recently, May *et al*. demonstrated quantification of tilt angle in perovskite structures based on the relationship between calculated and measured peak intensity of superlattice reflections.[22] The calculations presented here followed a similar procedure as that outlined by May *et al*.

In diffraction, the intensity of peaks is related to the square of the structure factor (which depends on scattering from atoms/electrons, the atomic positions and the indices of the peak in question). The calculated peak intensities are determined from

$$I = I_o \frac{1}{\sin(\eta)} \frac{1}{\sin(2\Theta)} \left(\sum_{j=1}^{4} D_j |F_{hkl}|^2 \right)$$

Equation 7-1

where I_O is the incident photon flux, $\frac{1}{\sin(\eta)}$ is a correction factor for the beam footprint, $\frac{1}{\sin(2\Theta)}$ is the Lorentz polarization correction, F_{hkl} is the structure factor for oxygen atoms and D_j is the relative volume fraction of the eight possible domains associated with tilt.[22] η is the incident photon angle (the angle between the sample and the incident beam, Figure 7-5) and Θ is the scattering angle. The scattering angle can be found from the relationship $\frac{\sin\Theta}{\lambda} = \frac{q}{4\pi}$ where q is the scattering vector; $q = \sqrt{\left(H\frac{2\pi}{a}\right)^2 + \left(K\frac{2\pi}{b}\right)^2 + \left(L\frac{2\pi}{c}\right)^2}$. Here, *H, K,* and *L* are the reciprocal space values of the peak in question and *a, b* and *c* are the lattice parameters.

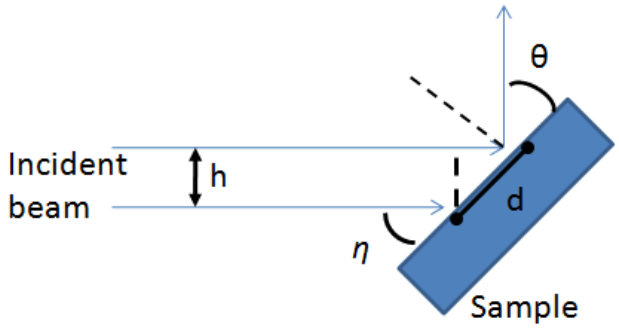

Figure 7-5 Schematic showing that the actual spotsize of the beam on the sample (i.e. beam footprint) can be calculated using simple geometry. The height of the incident beam is h. η is the angle between the sample and the incident beam. Θ is the scattering angle. d is the actual spot size or footprint on the sample.

The structure factor for each superlattice peak is obtained from

$$F_{hkl} = f_{O^{2-}} \sum_{n=1}^{48} \exp\left[2\pi i(hu_n + kv_n + lw_n)\right]$$

Equation 7-2

where the $f_{O^{2-}}$ is the oxygen ion form factor, the position of the n^{th} oxygen atom within the unit cell is given by (*u,v,w*) and *h*, *k*, and *l* are the Miller indices of the Bragg peak. The form factor

for O^{2-} was determined by fitting the data in Hovestreydt *et al*. for the appropriate wavelength (E = 21 keV) and then using the fit to calculate $f_{O^{2-}}$ for different q values.[93]

For $AgNbO_3$, only the contributions from the oxygen atoms are considered. As mentioned earlier, the octahedral rotations will double the unit cell along the *a*- and *b*- axis while quadrupling is observed along the *c* axis. This supercell gives rise to 48 oxygen positions. Each of these oxygen atoms was given a coordinate in the $AgNbO_3$ supercell. After tilt or rotation of the oxygen octahedra, the oxygen atoms adopted a new position that was calculated using the equations in Table 7-2. Here, Δx, Δy, or Δz represent the change in *x*, *y*, or *z* from the original oxygen position. $a_{\text{Nb-O}}$, $b_{\text{Nb-O}}$, and $c_{\text{Nb-O}}$ represent the Nb-O distance along the *a*, *b*, and *c* axes, respectively. In this case, *x*, *y*, and *z* and *a*, *b*, and *c* belong to the same coordinate system. *x*, *y*, and *z* represent the oxygen positions in the unit cell while *a*, *b*, and *c* refer to the lattice parameters of the supercell. In Table 7-2, α, β, and γ represent the tilt angle about the *a*-, *b*-, and *c*-axes of the crystal. Figure 7-6 shows a schematic of all the variables for the simple case when the oxygen octahedra tilt about the *c*-axis.

Table 7-2 Equations used to calculate the new oxygen positions after tilt or rotation of the oxygen octahedra about the *a*-, *b*- or *c*- axes.[94]

Tilt about *a*-axis	Tilt about *b*-axis	Tilt about *c*-axis
$\Delta y = y + c_{Nb-O}\frac{\text{Sin}\alpha}{4b}$	$\Delta x = x + c_{Nb-O}\frac{\text{Sin}\beta}{4a}$	$\Delta x = x + b_{Nb-O}\frac{\text{Sin}\gamma}{4a}$
$\Delta z = z + b_{Nb-O}\frac{\text{Sin}\alpha}{4c}$	$\Delta z = z + a_{Nb-O}\frac{\text{Sin}\beta}{4c}$	$\Delta y = y + a_{Nb-O}\frac{\text{Sin}\gamma}{4b}$

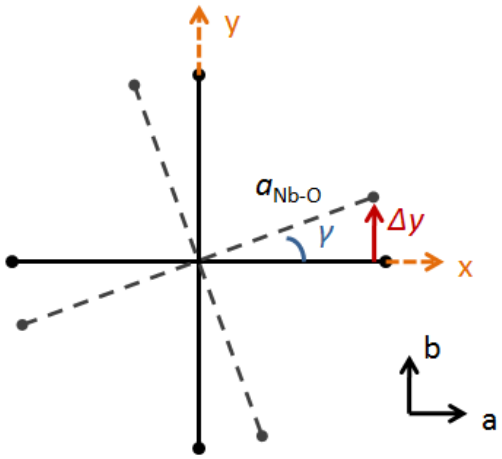

Figure 7-6 Schematic showing the variables needed to calculate the new oxygen positions after rotating the octahedral about the *c*-axis.

The new oxygen positions were calculated for each of the 48 oxygen atoms in the unit cell for different domain variants. For instance, the (+++) domain consisted of a clock-wise tilt about each of the *a*-, *b*- and *c*-axes. A (+–+) domain meant the octahedral rotated clockwise about the *a*- and *c*-axes, but rotated counter-clockwise about the *b*-axes. There are 8 possible domain variants in $AgNbO_3$. The structure factor was then calculated by taking into account the new positions for all 48 oxygen atoms and the *hkl* value of the Bragg peak. It is important to note that the *hkl* value is in reference to the supercell and not the simple pseudo-cubic unit cell. The intensity was calculated using Equation 7-1 for a number of reflections and a variety of different tilt angles.

7.2.3 Experimental procedure

The preparation of samples is described in detail in Chapter 3 and will be briefly outlined here. The sample set included single crystals of pure $AgNbO_3$, single crystals of

$(Ag_{0.95}Li_{0.5})NbO_3$, and thin films of $AgNbO_3$. The $AgNbO_3$ and $(Ag_{0.95}Li_{0.5})NbO_3$single crystals were donated from A. Kania and S. Wada, respectively. Crystals were polished with the 001 pseudo-cubic direction along the surface normal. Pt electrodes were sputtered on both sides of the samples. Thin films were prepared via a sol-gel method as described Section 3.2. Films were deposited on $SrRuO_3/LaAlO_3$ substrates. The film thickness was ~420nm. An interdigitated electrode pattern (Figure 7-7) was used to provide an electrical signal through the film. Due to the non-uniform distribution of electric field, only an estimate of the applied field will be quoted. Thus, all data will be reported as a function of voltage.

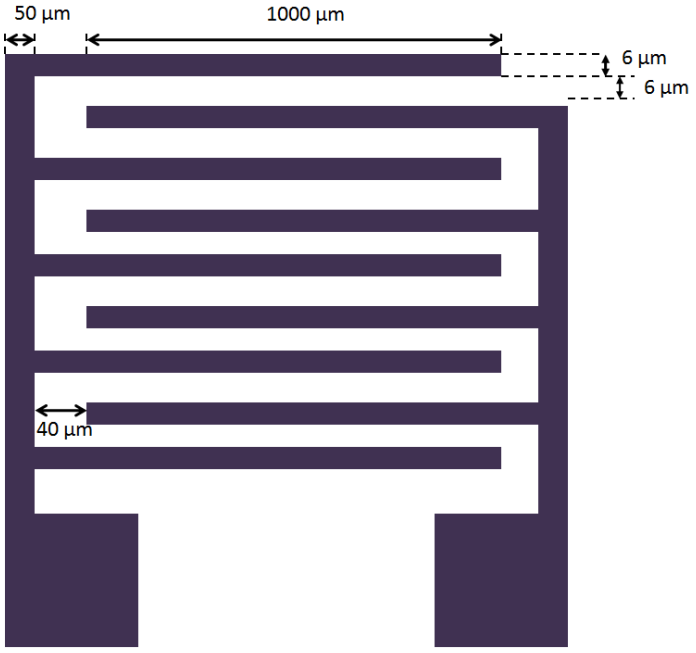

Figure 7-7 Schematic showing the interdigitated electrode pattern used for electrical measurements. Figure is not to scale. A total of 64 fingers were used in this work.

The experimental setup was designed to measure samples under zero field conditions as well as under the application of an electric field. For the single crystals, appropriately rated wires were fixed to the top and bottom Pt electrodes of the crystal using CircuitWorks® 2400 Conductive Silver Epoxy. The crystal was glued to a glass slide using silver epoxy. A portion of

the crystal hung over the edge of the glass slide to allow access to the bottom electrode. The glass slide was then mounted to an appropriate cylindrical sample holder designed for the Huber 4-circle diffractometer. The thin films were wirebonded to DIP packages. The package was then mounted to an appropriate sample holder so that the pins of the DIP package hung freely. Lead wires were soldered to desired pins of the package. Voltage was applied to the sample using a Keithley 2410 1100V SourceMeter. This device allowed for simultaneous output of voltage and measurement of current down to picoammeter levels. Current readings were monitored to ensure the crystal did not undergo breakdown. To improve the longevity of the crystal (by reducing the likelihood of long-range migration of oxygen vacancies), the polarity of voltage was reversed after each measurement.

Since the tilt angle is related to the intensity of superlattice reflections, these experiments were performed at the synchrotron at the Advanced Photon Source at beamline 33BM. The high brilliance and monochromatic nature of the X-rays allowed for easy detection of weak superlattice reflections. In addition, any changes in tilt angle due to the applied electric field should have resulted in intensity differences that are resolvable using a synchrotron.

7.3 Results and discussion

The next section will discuss the results obtained from measurements on the single crystals and thin films. First, initial characterization of the crystals and films will be reported. These include Laue, X-ray diffraction and some electrical measurements on the crystals. Then, calculations of tilt angle will be discussed. These calculations were performed to ensure detection of tilt angle was possible in the experiments. Finally, results on the search for the roto-electric effect will be outlined.

7.3.1 Initial characterization of crystals and films

Prior to measuring the crystals and films at the Advanced Photon Source, measurements to examine the crystal quality, dielectric properties and leakage currents were performed. Initial structural measurements on the $AgNbO_3$ and single crystals were performed to ensure the crystals were of good quality for roto-electric measurements.

7.3.1.1 Structural measurements on $AgNbO_3$ and (Ag,Li)NbO_3 single crystals

The orientation of the crystals was determined using Laue diffraction. Figure 7-8 shows the Laue pattern of the $<001>_{pc}$ pseudo-cubic crystallographic direction of the $AgNbO_3$ single crystal. After determining the orientation, the crystals were cut and polished so that the $<001>_{pc}$ direction was perpendicular to the cut. Details of the polishing process are described in Section 3.5.2. Platinum electrodes were sputter deposited on both sides of the crystal. The Pt thickness was ~1000 Å. The $AgNbO_3$ crystal thickness was 0.78 mm. ALN5 had a thickness of 0.33 mm.

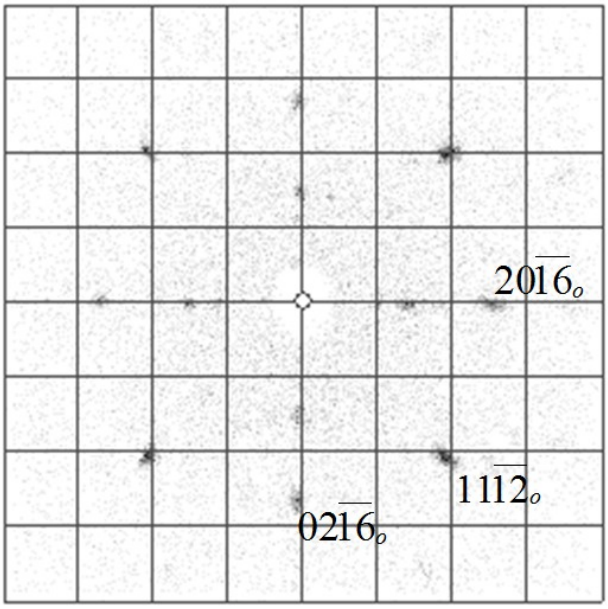

Figure 7-8 Laue diffraction pattern of $AgNbO_3$ crystal oriented along the <001> pseudo-cubic axis. Each line in the grid represents a 5 degree tilt of the crystal.

The quality of the crystals was examined using X-ray diffraction. Figure 7-9a shows the out-of-plane θ-2θ scan of the $AgNbO_3$ single crystal. The Pt peaks are from the Pt electrodes. Rocking curves about the 002_{pc} and 101_{pc} peaks are shown in Figure 7-9b and Figure 7-9c respectively. The multiple peaks about 002_{pc} are due to twinning in the film. A pseudo-Voigt function was fit to the three peaks and the FWHM values were found to be 0.462° ± 0.003°, 0.540° ± 0.013°, and 0.383° ± 0.006°. The FWHM of the 101_{pc} peak was 0.299° ± 0.002°. A phi scan was performed about the 101_{pc} peak to check for off-axis orientation. Figure 7-9d shows a phi scan about the 101_{pc} peak indicating the crystal is indeed a single crystal.

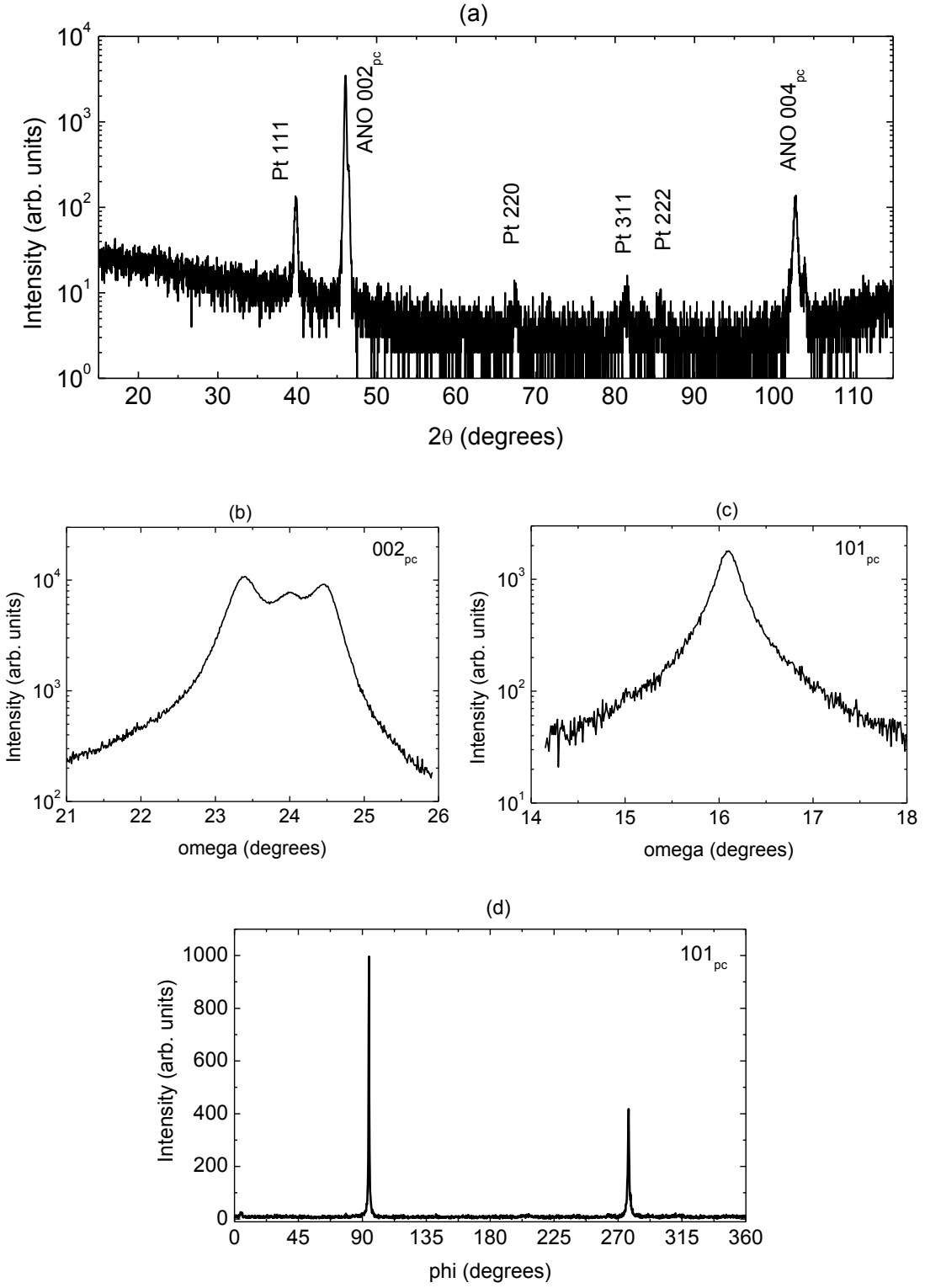

Figure 7-9 (a) Out-of-plane θ-2θ scan of the $AgNbO_3$ single crystal. The Pt peaks are due to the electrodes on the crystal. (b) and (c) show rocking curves for the 002_{pc} and 101_{pc} peaks respectively. (d) is the phi scan about the 101_{pc} peaks.

The out-of-plane θ-2θ scan of the ALN5 single crystal is shown in Figure 7-10a. Only 00*L* orientation peaks were found. Figure 7-10b and c show rocking curves about the 002_{pc} and 101_{pc} peaks, respectively. A pseudo-Voigt function was fit to the two peaks and the FWHM values were found to be 0.873° ± 0.004° and 0.709° ± 0.004°. The FWHM of the 101_{pc} peak was 1.081° ± 0.002°. A phi scan was performed about the 101_{pc} peak to check for crystallinity. Figure 7-9d shows a phi scan about the 101_{pc} peak, indicating the crystal is of good quality.

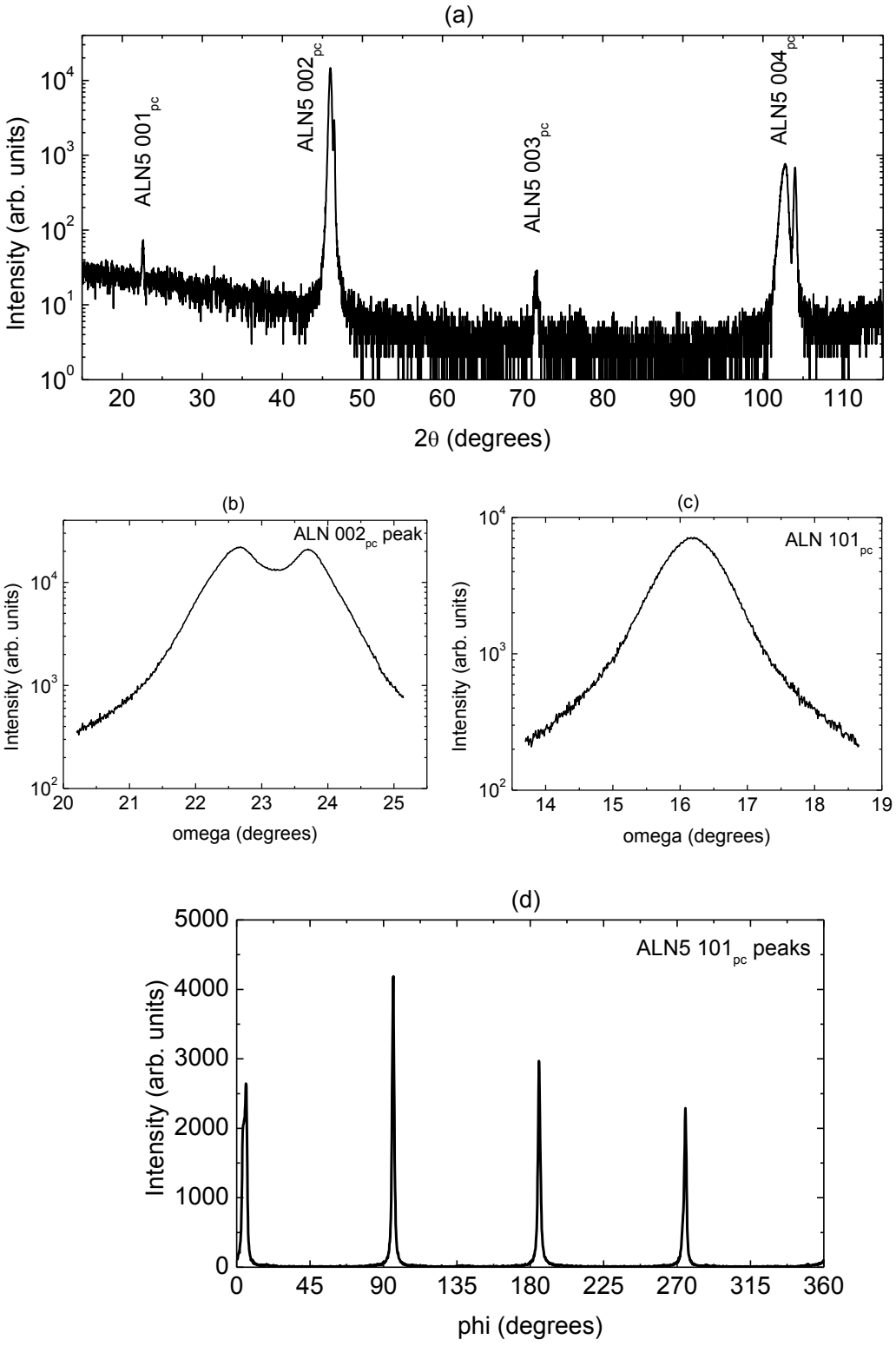

Figure 7-10 (a) Out-of-plane θ-2θ scan of the ALN5 single crystal. (b) and (c) show rocking curves for the 002_{pc} and 101_{pc} peaks respectively. The phi scan about the 101_{pc} peaks is shown in (d).

7.3.1.2 Temperature dependent permittivity and loss of single crystals

Electrical properties of the single crystals were also examined to ensure the crystals were not too lossy and could withstand high electric fields for extended periods of time. Figure 7-11 and Figure 7-12 show the permittivity and loss tangent as a function of temperature for $AgNbO_3$ and $(Ag_{0.95}Li_{0.5})NbO_3$ single crystals, respectively. These results agree well with reported data.[47, 95] For the $AgNbO_3$ crystals, the permittivity remains low at room temperature then increases to produce a broad maximum corresponding to the M_2-M_3 phase transition near 275 °C. The M_3-O transition can be observed ~ 375 °C. In the crystals with 0.05 % Li, the series of phase transitions, M_1-M_2, M_2-M_3, and M_3-O occur ~ 50 °C, 280 °C and 425 °C, respectively.

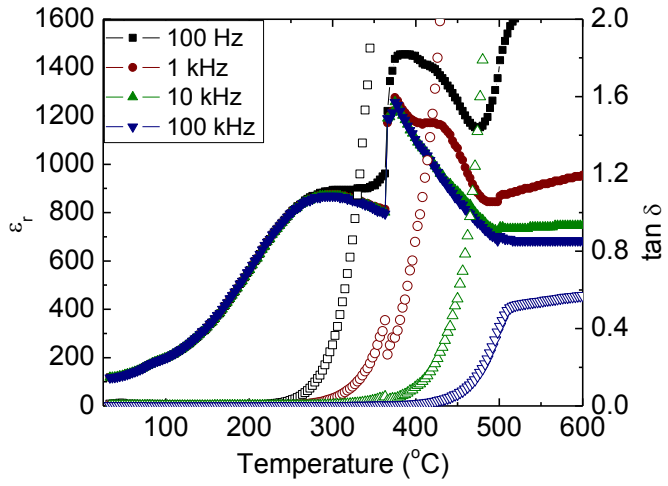

Figure 7-11 Temperature dependent permittivity (filled symbols) and loss data (open symbols) for $AgNbO_3$ single crystals.

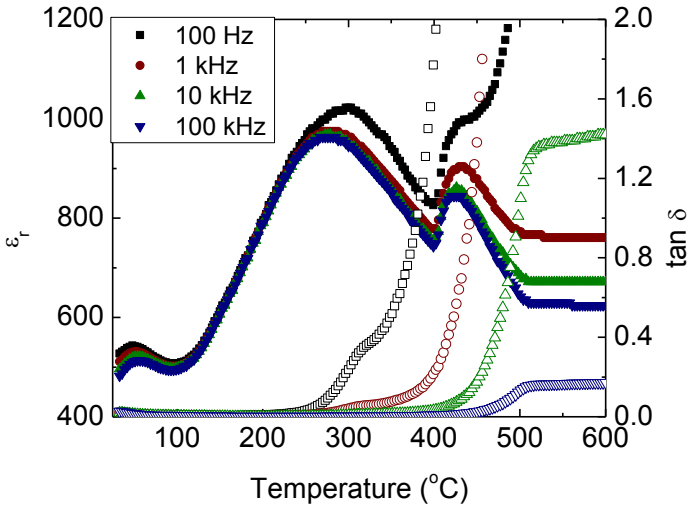

Figure 7-12 Temperature dependent permittivity of $(Ag_{0.95}Li_{0.5})NbO_3$ single crystals. Filled symbols show the permittivity, open symbols mark the loss tangent.

7.3.1.3 Polarization-electric field of single crystals

Polarization-electric (P-E) field hysteresis loops were recorded to determine the magnitude of electric field the crystals could sustain. Figure 7-13a and b show the P-E loops of the $AgNbO_3$ and ALN5 single crystals, respectively. As expected from the literature, the $AgNbO_3$ crystal was able to withstand 10 kV/cm.[60] At room temperature and these fields, the crystal behaved like a slightly lossy linear dielectric, although the M_1 is reportedly weakly ferroelectric. Higher driving fields were not attempted due to the fact that only one crystal was available for all measurements. The ALN5 crystal was able to tolerate higher fields. In addition, the loop was more open than that for pure $AgNbO_3$ suggesting stronger ferroelectric behavior.

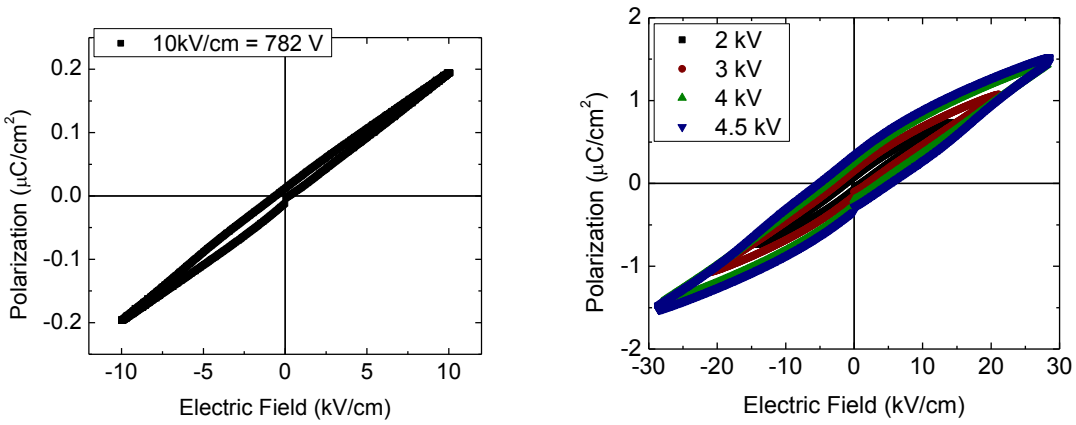

Figure 7-13 Polarization as a function of electric field for the (a) $AgNbO_3$ single crystal and (b) ALN5 crystal.

7.3.1.4 Leakage current

Leakage measurements were performed to ensure that the crystals could withstand electric fields for extended periods of time. Figure 7-14 shows the leakage current over a four minute timeframe for the $AgNbO_3$ single crystal. Current densities up to 200 nA/cm^2 were observed for electric fields near 10 kV/cm.

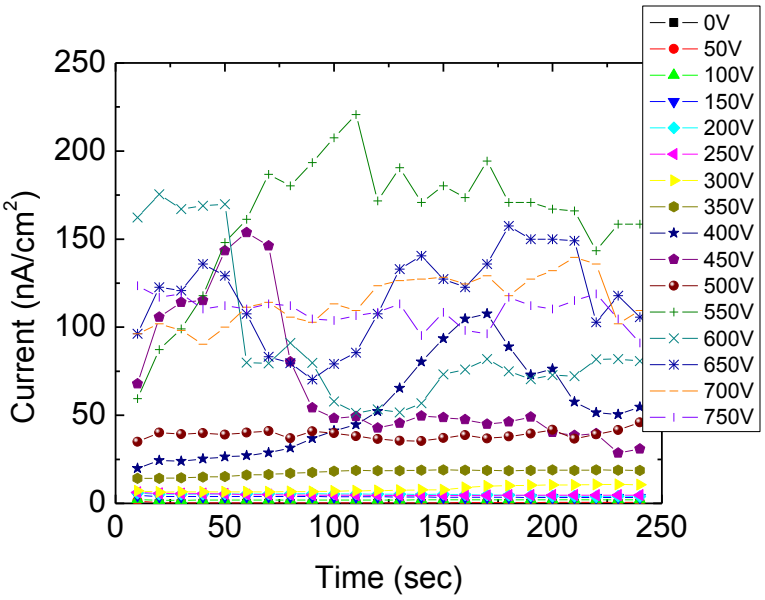

Figure 7-14 Leakage current as a function of time for the $AgNbO_3$ single crystal. 750 V = 9.6 kV/cm.

Leakage current measurements were also performed on the ALN5 crystals. These results are shown in Figure 7-15. The current densities became fairly high at 800 V at which point the measurement was stopped. The inset shows the current density values for lower applied voltages.

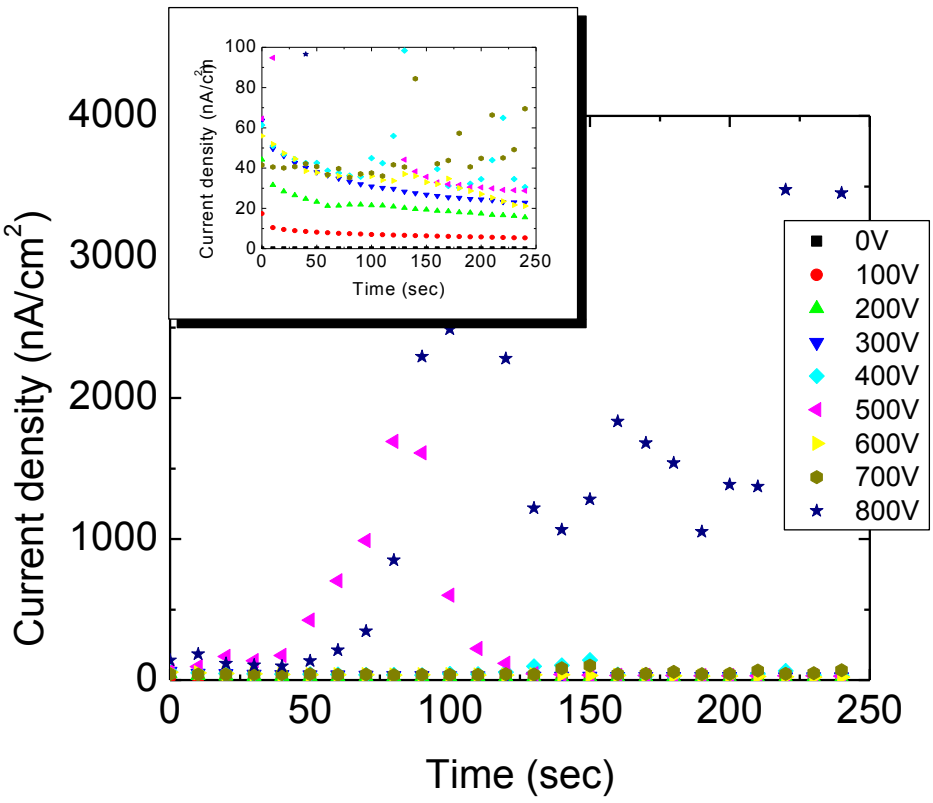

Figure 7-15 Leakage current as a function of time for the $(Ag_{0.95}Li_{0.5})NbO_3$ single crystal. Inset shows finer scale for the low field values. 800 V ~ 24.4 kV/cm.

7.3.2 Intensity calculations on tilted $AgNbO_3$

Prior to measuring the peak intensity experimentally, the peak intensity change as a function of tilt angle change was calculated to determine if the experiments were worth pursuing. The calculated intensity ratio as a function of tilt angle is shown in Figure 7-16 for three different superlattice reflections. Here, the square of the structure factor was calculated for $AgNbO_3$ in equilibrium with a ~ 7.3° tilt angle about the *c*-axis and ~ 8.9° tilt angle about the *b*-axis. Then, the square of the structure factor was calculated for changes in tilt angle up to 4° tilt from this

equilibrium condition. The ratio of these two values was then plotted as a function of tilt angle. Based on the results shown in Figure 7-16, the intensity ratio for the ½113 peak shows a weak field dependence; however, the intensity ratio for ½115 and ½117 show readily detectable changes.

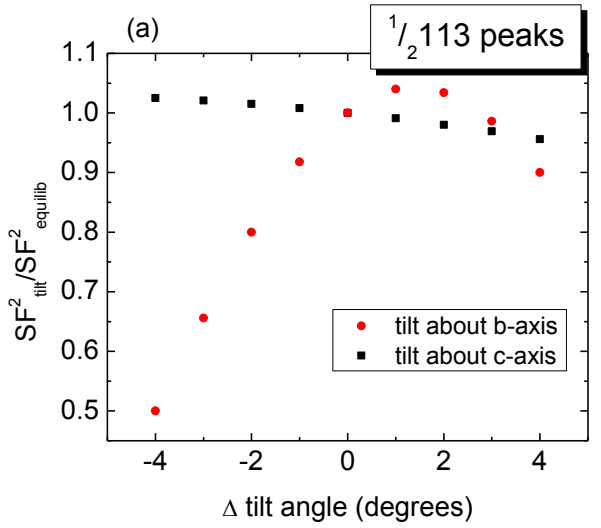

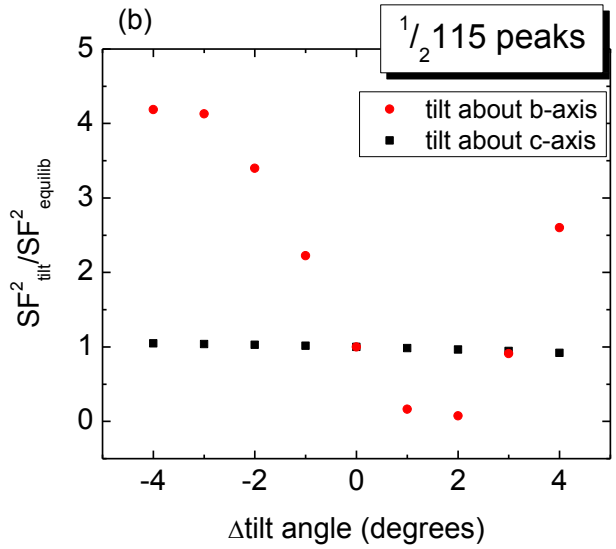

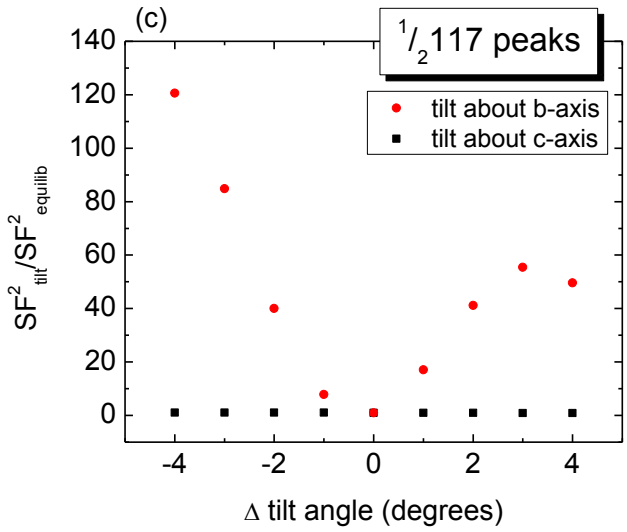

Figure 7-16 Calculated intensity ratios for (a) ½113, (b) ½115 and (c) ½117 superlattice reflections for $AgNbO_3$. The *x* axis is the change in tilt angle relative to the bulk tilt angle found at room temperature.

7.3.3 Synchrotron X-ray diffraction on $AgNbO_3$ single crystal

The next section provides results on electric field measurements performed at the synchrotron at the Advanced Photon Source on $AgNbO_3$ single crystals. For this sample, the ½1$\bar{1}$5 and ½$\bar{1}\bar{1}$3 + 0¼0 reflections were examined.

7.3.3.1 ½1$\bar{1}$5 peak

X-ray measurements were performed to look for changes in peak intensity as a function of electric field. Figure 7-17 shows the intensity of the ½1$\bar{1}$5 peak for the $AgNbO_3$ crystal at several electric fields. In this case, an initial measurement was performed under zero electric field to provide a baseline for field measurements. The voltage was increased and the data were retaken under bias. Finally, a measurement at zero electric field was obtained to compare to the

original state. The data for all 5 scans shown in Figure 7-17 look remarkably similar, suggesting that the field-induced changes in tilt angle are below the detection limit of the measurement.

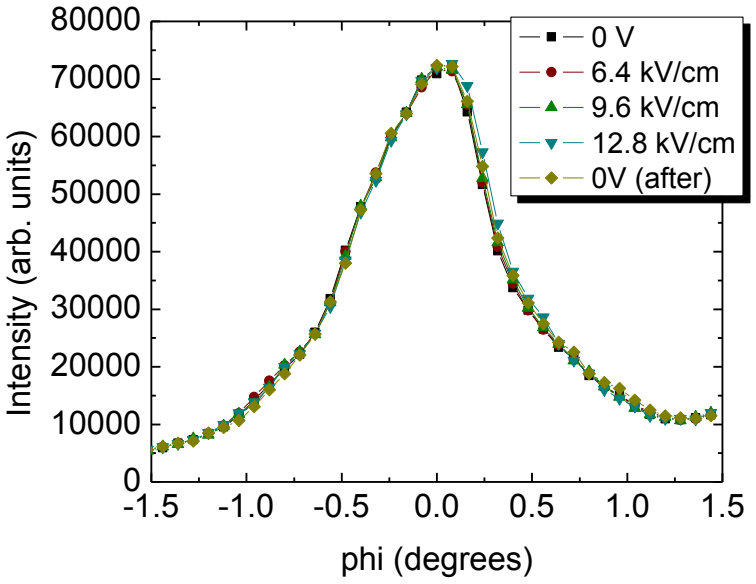

Figure 7-17 Intensity of ½$\mathbf{1\bar{1}5}$ peak for $AgNbO_3$ crystal as a function of electric field.

In order to better quantify the data, the peaks were fit with a pseudo-Voigt function. Then the amplitude of the peak and peak position were extracted for a series of scans. A typical measurement sequence included 2-3 scans at 0 V, 2-3 scans at a particular electric field and then 2-3 scans at 0 V. The time in between scans was not necessarily equal nor was the time between electric field steps. Figure 7-18a and b shows the peak intensity and peak position as a function of electric field for the ½$1\bar{1}5$ peak of the $AgNbO_3$ single crystal. The color differentiation indicates scans that were performed close to one another in time (i.e. there were several scans performed at 0 V near the time that scans were performed at +6.4 and –6.4 kV/cm as indicated by the black symbols). In Figure 7-18c, the center of mass of the ½$1\bar{1}5$ peak is plotted as a function of electric field. Upon first look, all three of the plots in Figure 7-18 suggest there might be a parabolic

dependence of peak intensity, position and center of mass on electric field. However, there was a time difference between scans, and as a result, the potential that the apparent field dependence was an artifact of time was examined.

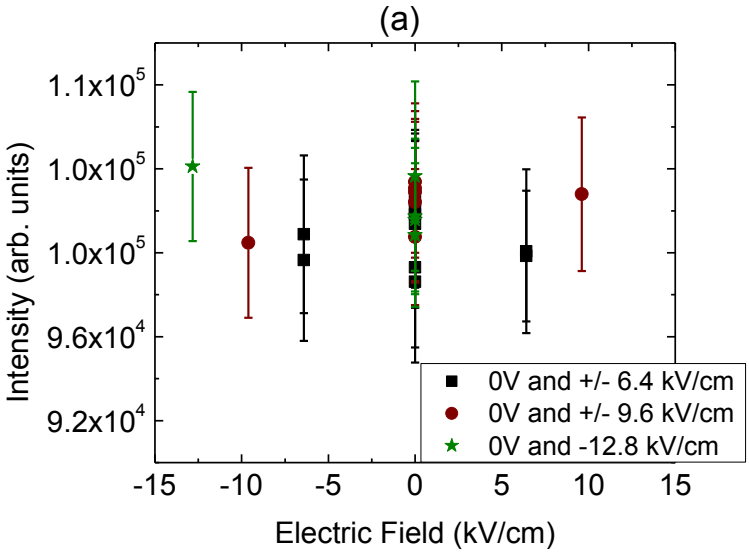

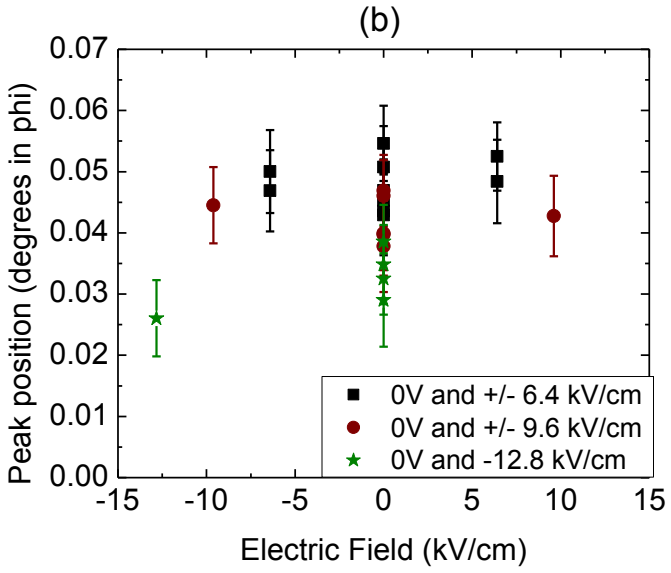

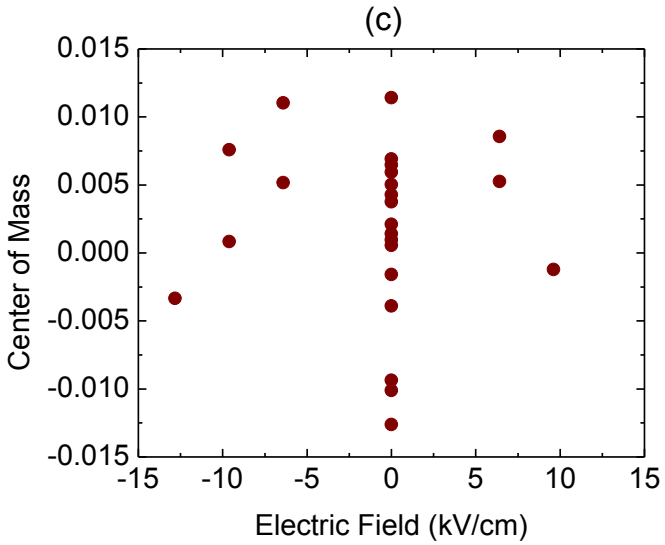

Figure 7-18 (a) Intensity, (b) peak position in phi, and (c) center of mass of ½$\mathbf{1\bar{1}5}$ peak as a function of electric field. The colors represent scans that were performed close to one another in time.

In order to determine whether or not a time dependent drift was present in the measurements, the peak intensity, peak position and center of mass were plotted as a function of time for the ½$1\bar{1}5$ peak of the $AgNbO_3$ single crystal. All measurements were performed at zero field. Figure 7-19 shows that the peak position (Figure 7-19b) and center of mass (Figure 7-19c) data have a definite time dependence suggesting that the parabolic shape in Figure 7-18b and c is likely due to drift rather than a field dependence. Thus, there does not seem to be any relationship between tilt angle and electric field.

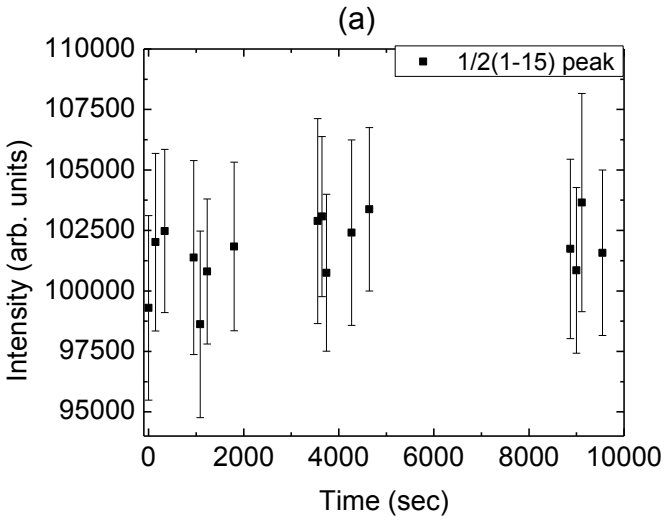
(a)
1/2(1-15) peak
Intensity (arb. units)
110000
107500
105000
102500
100000
97500
95000
0
2000
4000
6000
8000
10000
Time (sec)

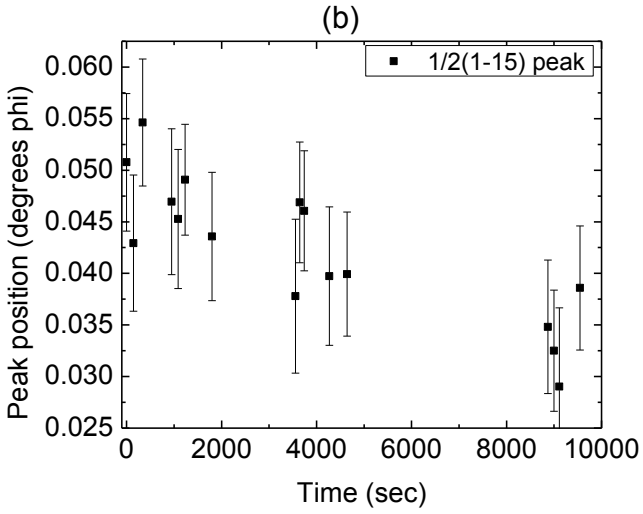
(b)
1/2(1-15) peak
Peak position (degrees phi)
0.060
0.055
0.050
0.045
0.040
0.035
0.030
0.025
0
2000
4000
6000
8000
10000
Time (sec)

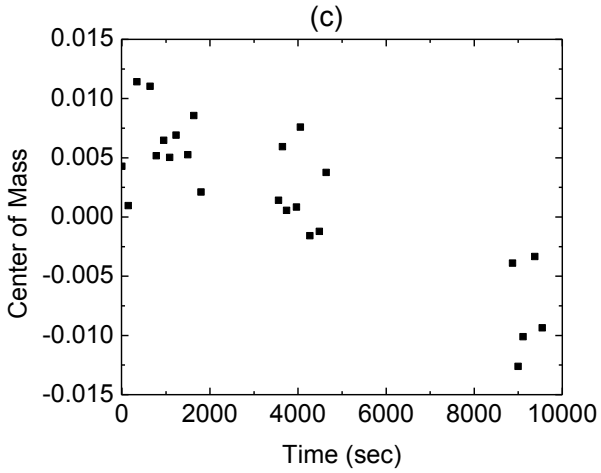

Figure 7-19 (a) Peak intensity, (b) peak position and (c) center of mass as a function of time for the ½1$\bar{1}$5 peak of the $AgNbO_3$ single crystal. The data shows drift in each of the parameters with time.

7.3.3.2 ½$\bar{1}\bar{1}$3 + ¼(0K0) peak

In addition to anti-phase tilting in $AgNbO_3$, the complex tilt system $a^-b^-c^-/a^-b^-c^+$ exists at room temperature. This tilt system produces quarter-order reflections about superlattice reflections of the type ½{*ooo*}. In this portion of the study, the ½$\bar{1}\bar{1}$3 + 0¼0 reflection was examined. Because the peak occurs along the *K* direction, the complex tilt is present along one of the in-plane directions of the crystal. In other words, the tilt will occur perpendicular to the direction of the electric field.

Figure 7-20 shows the peak intensity (a), peak position (b) and center of mass (c) as a function of electric field for the ½$\bar{1}\bar{1}$3 + 0¼0 superlattice reflection. Similar to the ½1$\bar{1}$5 peak, an apparent parabolic trend is observed. However, this is attributed to a drift in the data over time as seen in Figure 7-21. It was concluded that there is no electric field dependence on the tilt angle for the ½$\bar{1}\bar{1}$3 + 0¼0 superlattice reflection.

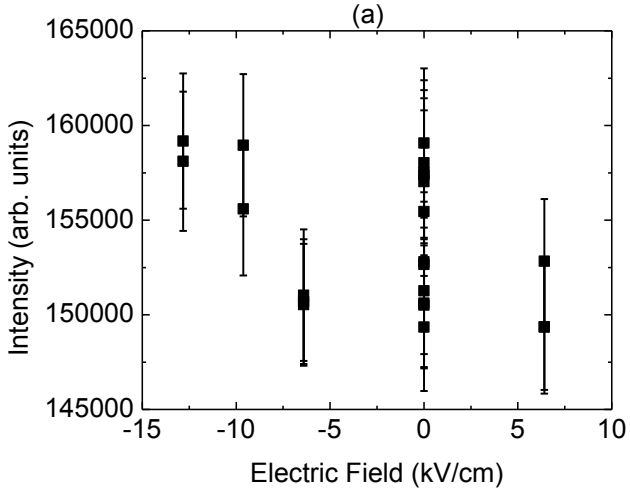
(a)
165000
160000
155000
150000
145000
Intensity (arb. units)
-15
-10
-5
0
5
10
Electric Field (kV/cm)

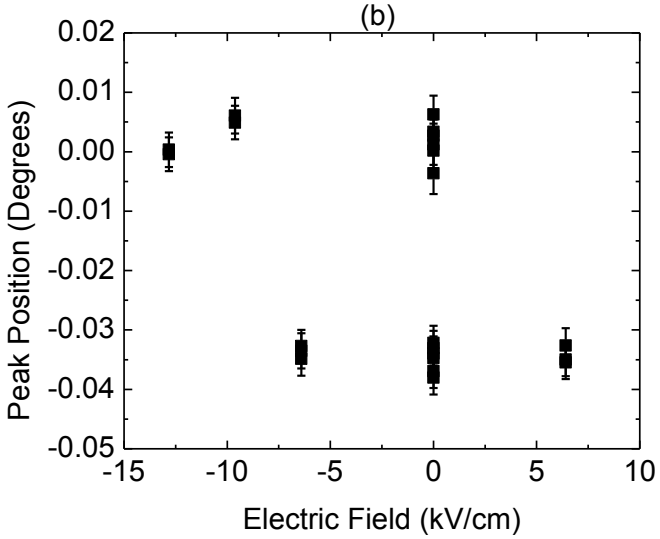
(b)
0.02
0.01
0.00
-0.01
-0.02
-0.03
-0.04
-0.05
Peak Position (Degrees)
-15
-10
-5
0
5
10
Electric Field (kV/cm)

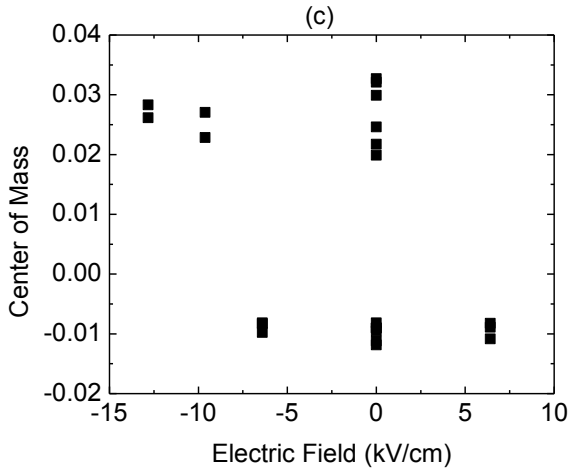

Figure 7-20 (a) Peak intensity, (b) peak position and (c) center of mass as a function of electric field of the ½$\overline{\mathbf{11}}$3 + 0¼0 superlattice reflection.

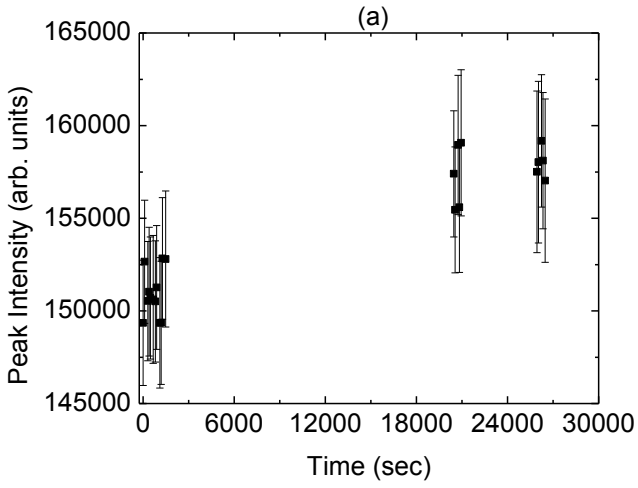

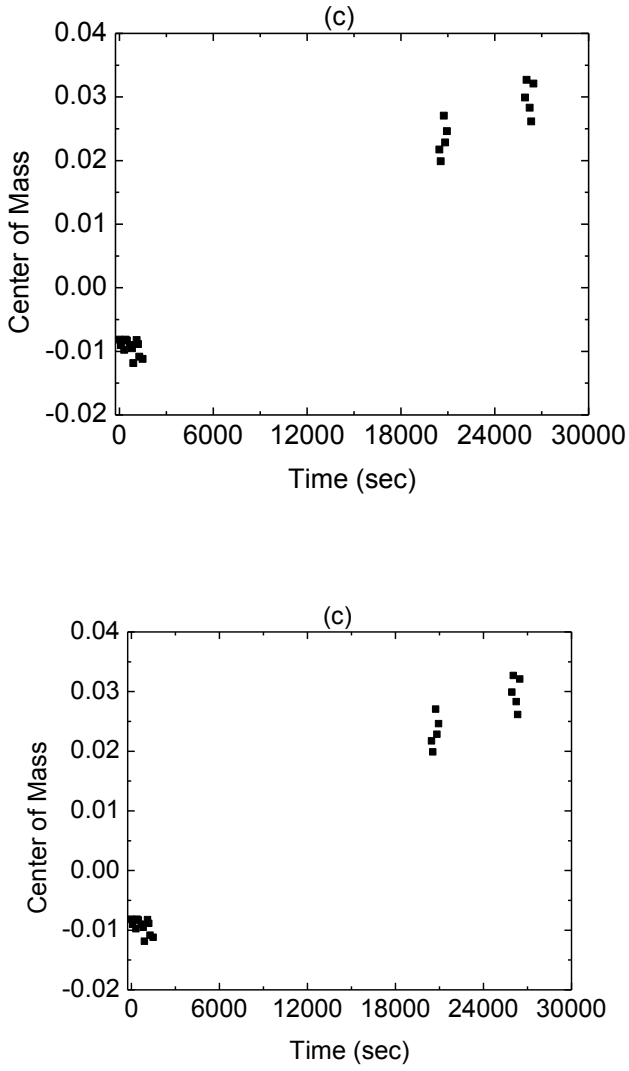

Figure 7-21 (a) Peak intensity, (b) peak position and (c) center of mass as a function of time for the ½$\bar{1}\bar{1}$3 + 0¼0 peak of $AgNbO_3$ single crystal. Between 0 and 2000 seconds, no field and ± 500 V measurements were recorded. Around 2000 seconds, data was collected for no field and -750 V. Near 2800 seconds, measurements for no field and -1000 V were recorded.

7.3.4 Synchrotron X-ray diffraction measurements on $(Ag_{0.95}Li_{0.5})NbO_3$ single crystal

The Li-doped $AgNbO_3$ single crystal was used because the sample could withstand higher electric fields, which should allow for easier detection of the roto-electric effect. For this sample, the ½117 superlattice reflection was chosen, because it should show the largest change in

intensity as a function of tilt angle as described in Section 7.3.2. Figure 7-22 shows the peak intensity, peak position and center of mass of the ½117 reflection as a function of electric field. Because of the high photocurrents generated in the direction of positive voltage, data were obtained with only negative field values to minimize the chances that the samples would fail prematurely. Similar to results on the $AgNbO_3$ single crystal, all data points at field fall within the error bars of the data points at zero field. The crystal experienced electrical breakdown at -1000 V (~30 kV/cm). No dependence of tilt angle on electric field was observed for the $(Ag_{0.95}Li_{0.5})NbO_3$ single crystals to the limit of accessible fields.

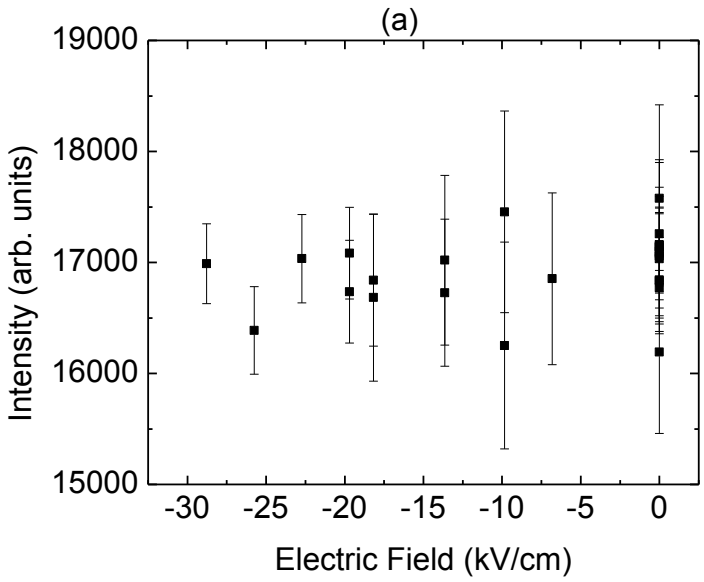

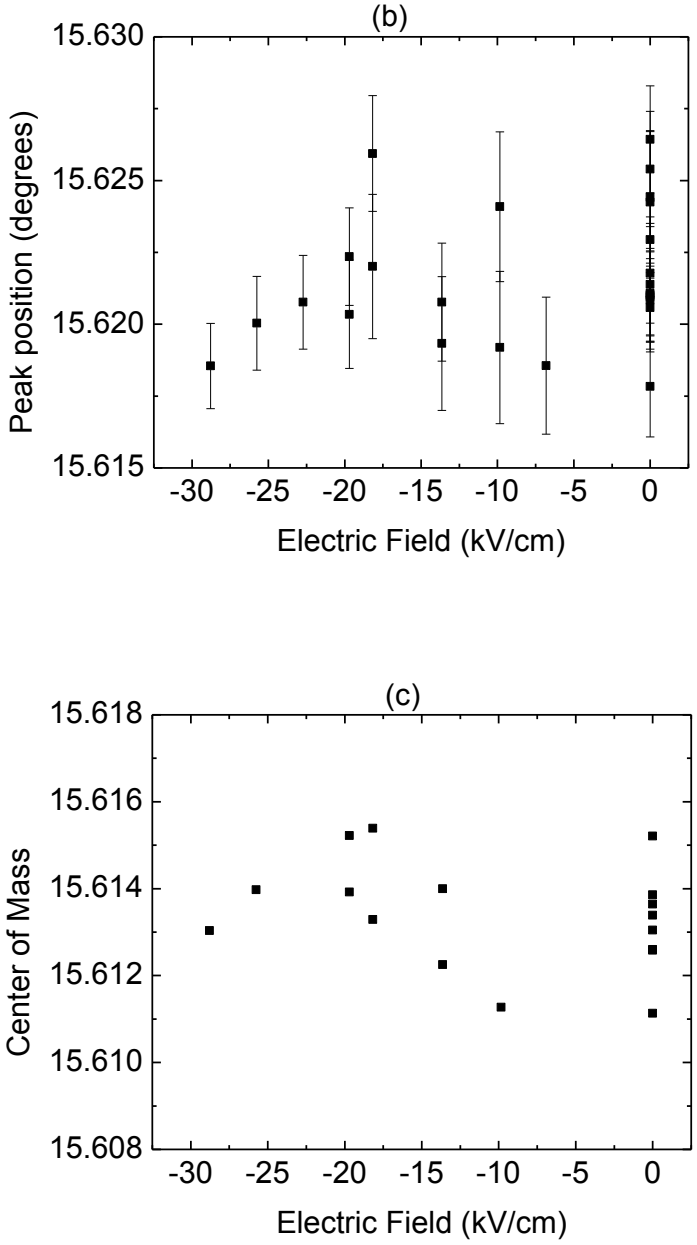

Figure 7-22 (a) Peak intensity, (b) peak position and (c) center of mass as a function of electric field for the ½117 peak of the ALN5 single crystal.

Similar to data on the $AgNbO_3$ crystals, the peak intensity, peak position and center of mass of the ½117 peak was plotted as a function of time to rule out drift in the measurement. Figure 7-23 shows these data.

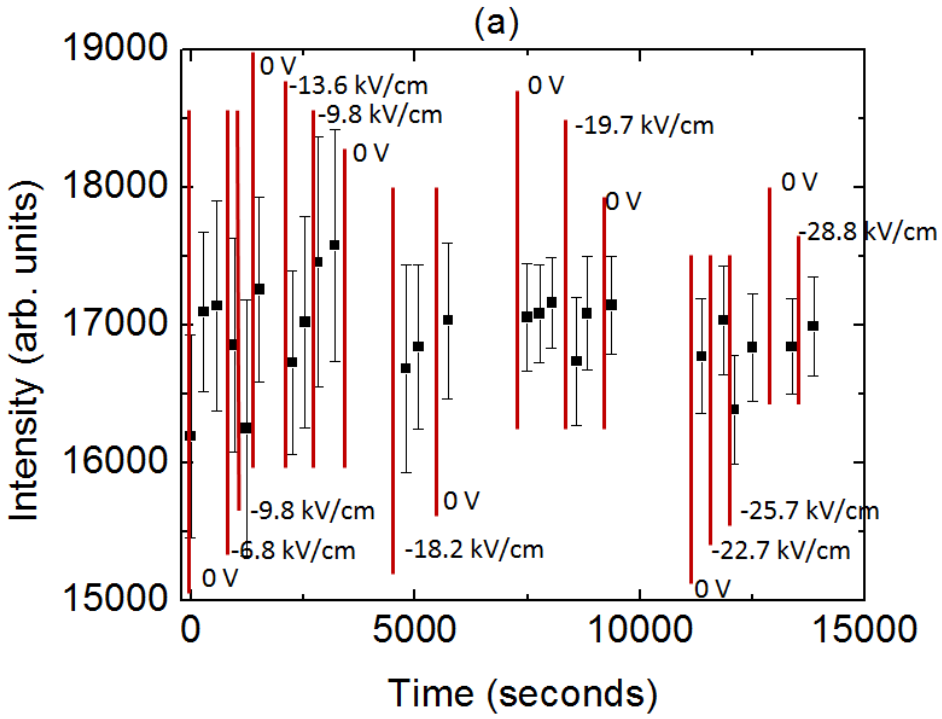

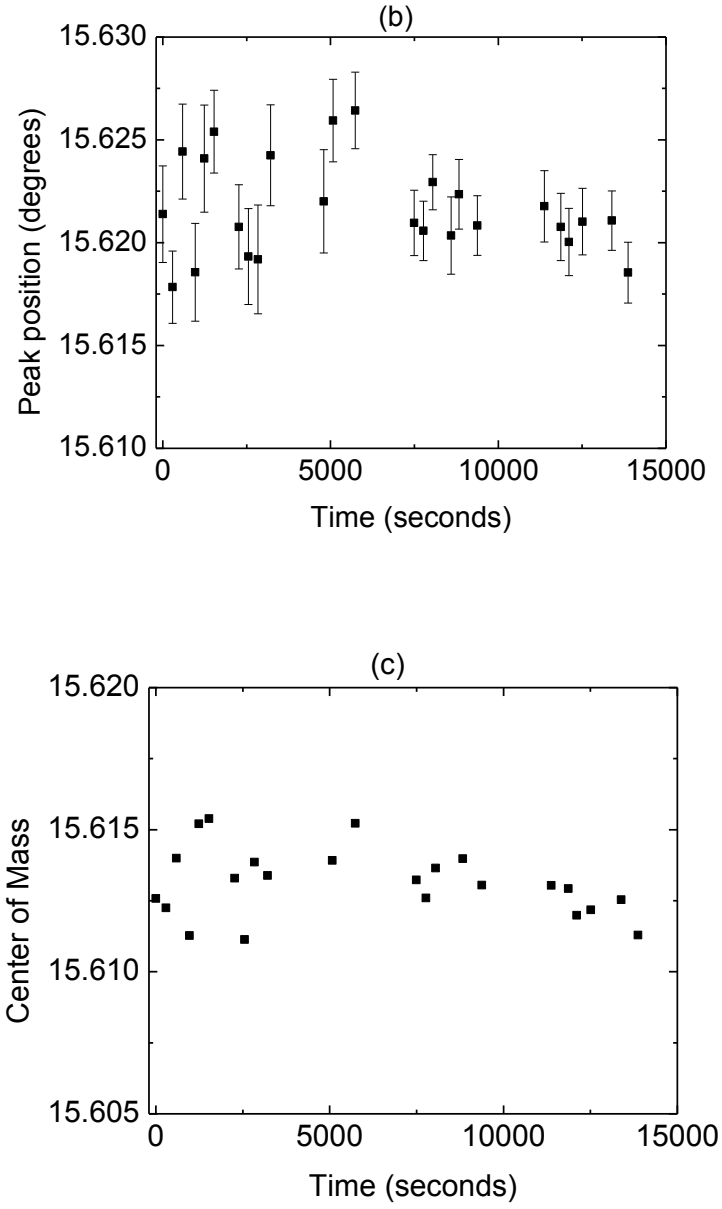

Figure 7-23 (a) Peak intensity, (b) peak position and (c) center of mass as a function of time for the ½117 peak of the ALN5 single crystal. The vertical red lines indicate when a given voltage was applied to the sample.

7.3.5 Synchrotron X-ray diffraction on $AgNbO_3$ thin films

In addition to measurements on single crystals, experiments were performed on $AgNbO_3$ thin films. Films were used because higher electric fields can be applied to the film as compared

to bulk single crystals. For the films, interdigitated electrodes (IDT) were deposited on the surface of the film and an electric field was applied so that most of the field was concentrated along the in-plane direction. This is contrary to the single crystals in which the field was applied along the surface normal. It is unknown whether the tilt angle would experience a larger change parallel or perpendicular to the applied electric field, the experiments on films provide a complement to the single crystal data. The films were epitaxial and fully relaxed with a multi-domain structure.

For the thin film experiments, IDT's were used which meant that the active area of the material was not the same as that of the parallel plate capacitor used for the single crystals. Based on the IDT dimensions (Figure 7-7), the active area of the sample was 1 mm *x* 0.378 mm. This active area can be compared to the footprint of the beam on the sample to determine how much of the sampled area was under the application of an electric field. The X-ray beam dimensions based on slit sizes were 1.0 mm *x* 0.5 mm (horizontal *x* vertical). For the ½113 peak measured in this experiment, the footprint of the beam was approximately 1.0 mm *x* 4.7 mm (see schematic in Figure 7-5 for geometrical considerations). Initially, multiple IDT electrodes were activated to increase the amount of material under field, however, all but one IDT failed at low voltages. Therefore, for the data reported in this dissertation, only one IDT was activated. That meant that the beam footprint was larger than the active area, which made detection of possible changes in tilt angles much more difficult.

Multiple superlattice reflections were examined. Unfortunately, the higher angle peaks (the peaks that would show the largest change in intensity due to a change in the tilt angle) had weak reflections due to the smaller volume of material that was sampled. Therefore, the $\frac{1}{2}\bar{1}\bar{1}3$ reflection was chosen.

Figure 7-24 shows the peak intensity, peak position and center of mass of the $\frac{1}{2}\bar{1}\bar{1}3$ reflection as a function of voltage for the $AgNbO_3$ thin film. No change in intensity of the peak was observed. A jump in the peak position was found, however, it was ascertained that this is

likely due to the measurement system and not representative of an actual peak shift due to applied electric field.

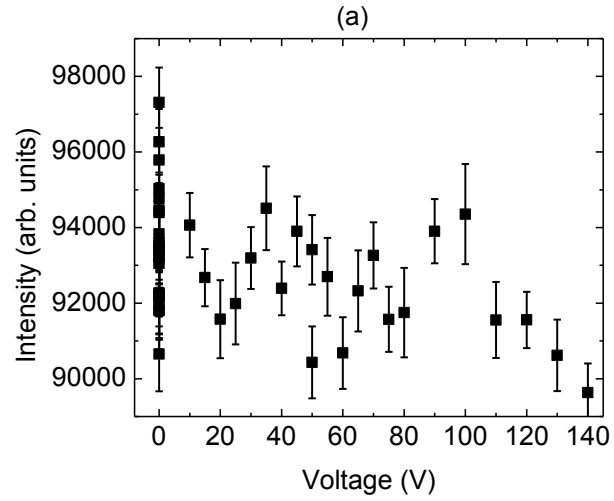

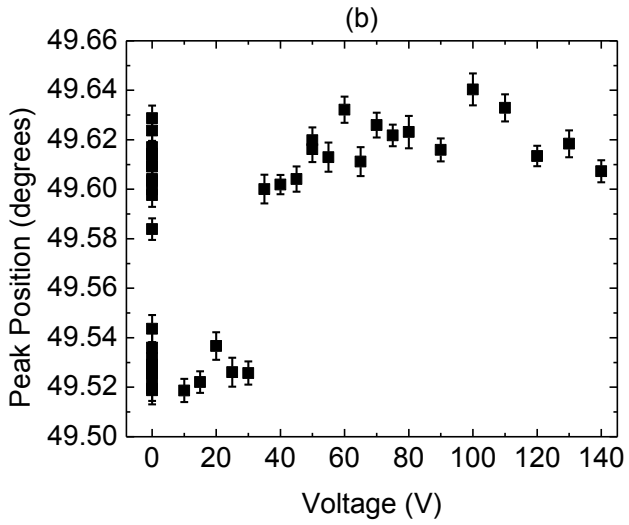

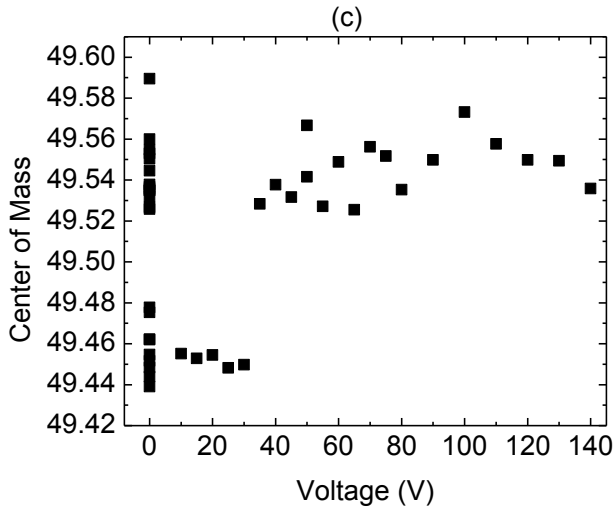

Figure 7-24 (a) Peak intensity, (b) peak position and (c) center of mass as a function of voltage for the ½$\bar{1}\bar{1}$3 peak of $AgNbO_3$ thin films. No significant trend was observed with voltage. The jump in data is related to the measurement system and not representative of a possible roto-electric effect.

Similar to the procedure performed on the single crystals, the peak intensity, peak position and center of mass were plotted as a function of time in order to rule out drift in the measurement. Figure 7-25 shows such data. The vertical red lines indicate when and what voltages were applied to the sample. Again, no obvious change was observed in any of the parameters. The jump observed in Figure 7-24 is more clearly due to the measurement system, rather than related to the roto-electric effect. Despite the fact that films allowed for higher applied electric fields, no change in tilt angle was observed, suggesting that the roto-electric effect in $AgNbO_3$ is below the detection limit of the measurement.

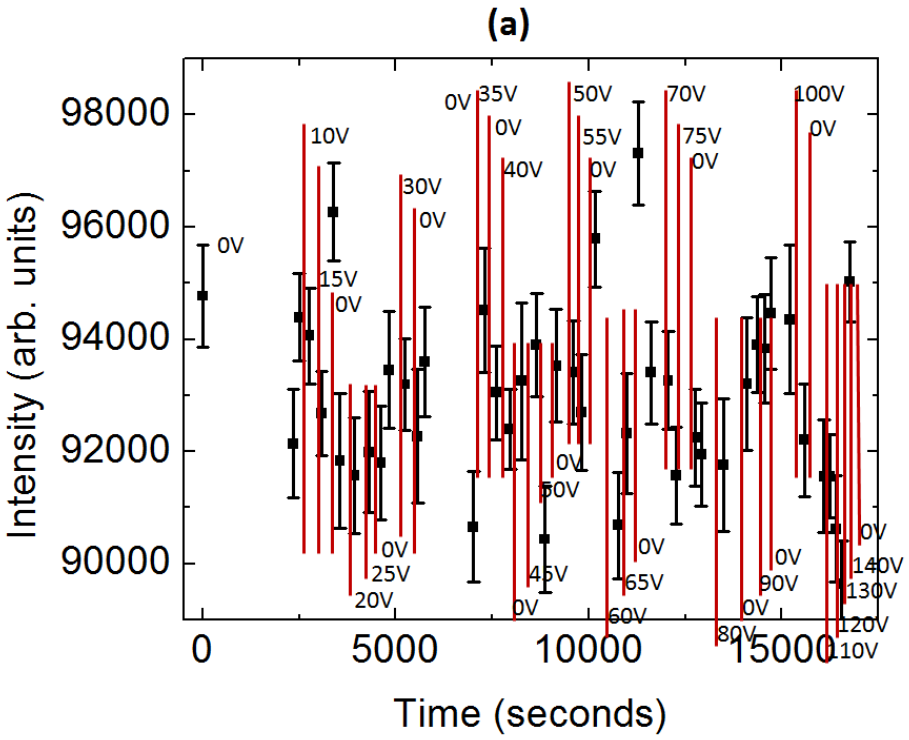
(a)
Intensity (arb. units)
Time (seconds)
98000
96000
94000
92000
90000
0
5000
10000
15000
0V
10V
15V
0V
20V
25V
0V
30V
0V
0V
35V
0V
40V
45V
0V
50V
0V
55V
0V
60V
65V
0V
70V
75V
0V
80V
90V
0V
100V
0V
110V
120V
130V
140V
0V

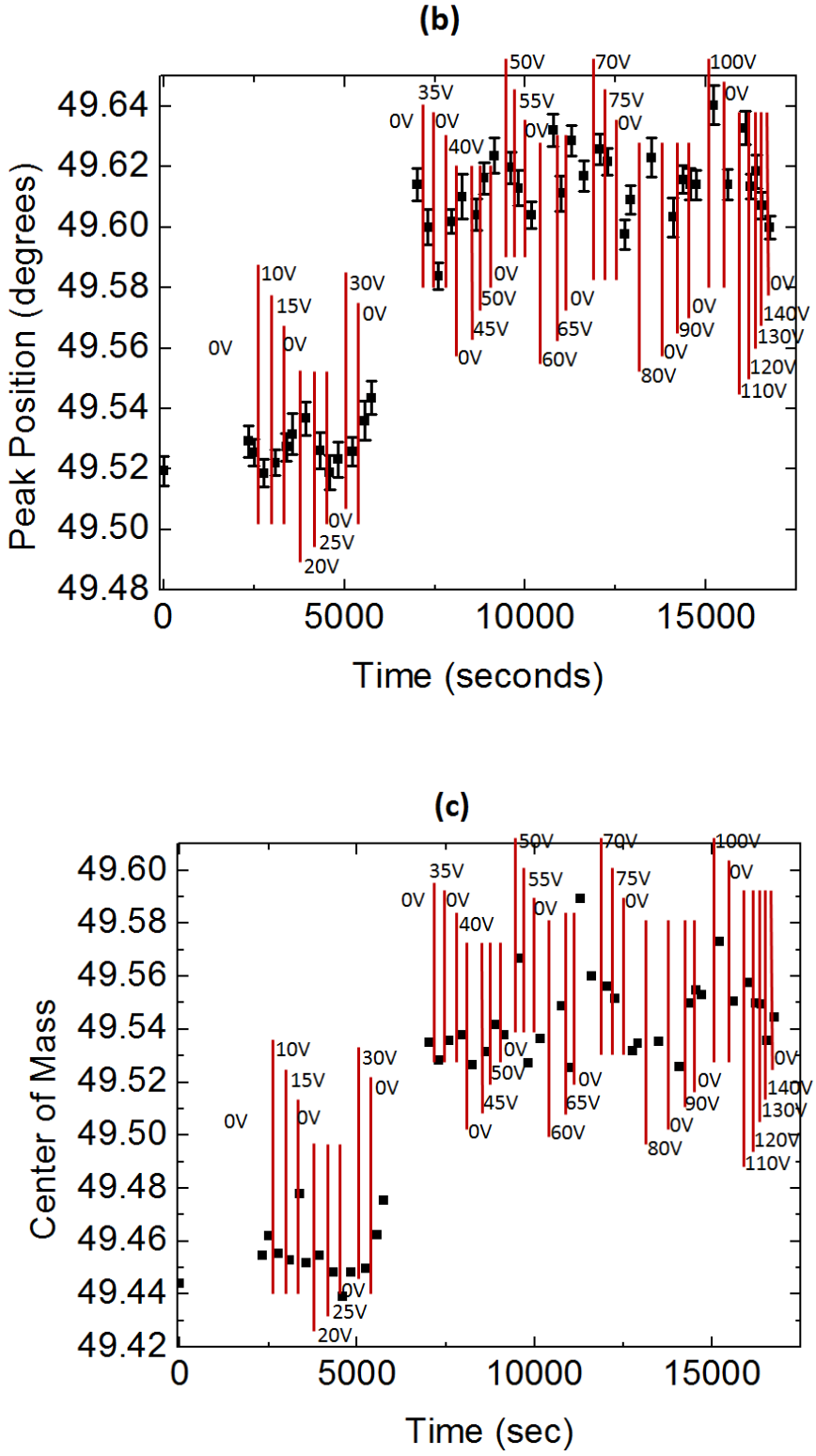

Figure 7-25 (a) Peak intensity, (b) peak position and (c) center of mass as a function of time for the ½$\bar{1}\bar{1}$3 peak of $AgNbO_3$ thin films. The vertical red lines indicate when a given voltage was applied to the sample.

7.4 Conclusions

In perovskite materials, rotation or tilting of the oxygen octahedra can lead to new symmetry considerations. As a result of these new symmetries, new properties related to these symmetries should exist. The work in this chapter aimed at carrying out an experiment designed to search for a relationship between tilt angle and applied electric field in the $AgNbO_3$ system. Calculations were performed to determine how much peak intensities changed as a function of tilt angle for several superlattice reflections. Then, experiments were carried out at the Advanced Photon Source to measure the intensity of superlattice reflections of a pure $AgNbO_3$ single crystal, a $(Ag_{0.95}Li_{0.5})NbO_3$ single crystal, and $AgNbO_3$ thin film. It was determined that no change was observed, suggesting that the tilt angle of the octahedra in $AgNbO_3$ was not influenced as a function of electric field.

Chapter 8

Conclusions and Future Work

8.1 Conclusions

The goal of this dissertation was to study octahedral tilt transitions in $Ag(Ta_xNb_{1-x})O_3$ thin films and crystals as a function of strain and electric field. The work on ATN films under compressive and tensile strain demonstrated that strain engineering in complex tilt systems is possible and thus suggests that manipulation of tilt transitions in a wide variety of functional ceramics is feasible. Although $AgNbO_3$ single crystals did not demonstrate an electric field dependence of octahedral tilt angle within the measurement limits, the groundwork for performing such experiments has been developed.

Synchrotron X-ray diffraction and TEM electron diffraction were used to confirm that relaxed $Ag(Ta_xNb_{1-x})O_3$ films deposited on $SrRuO_3/LaAlO_3(001)$ and $LaAlO_3(001)$ adopted the complex octahedral tilted structure at room temperature. This was demonstrated through the presence of $\frac{1}{2}\{ooo\} \pm \frac{1}{4}\{00L\}$ reflections. However, in the films, the intensity of such reflections was less than that observed in bulk, suggesting that the correlation length for the complex tilt is significantly reduced. In the ATN films, M_2-M_3 phase transition, which is associated with ordering of local displacements, occurs around ~ 210 °C (60 K) as opposed to ~ 40 °C (310 K) in bulk. These temperatures were confirmed through X-ray diffraction, TEM and electrical measurements. This suggests a strong suppression of B-cation displacive ordering in thin films. This was attributed to a significant concentration of point and planar defects which reduce the correlation length for complex octahedral rotations about the *c* axis and, thus, weaken the

interactions between the tilting and B-cation displacements which suppress the long range ordering.

Coherent $Ag(Ta_xNb_{1-x})O_3$ thin films were deposited on (001) $SrTiO_3$ substrates to produce a compressive biaxial strain state. This strain expanded the temperature region of the O and T phase fields by ~280 °C due to the closer lattice match in these regimes. As was predicted, the domain structure in these high temperature phases was oriented with the long axis out-of-plane. On further cooling, re-orientation of domain states was limited, which forced the complex tilt system to develop along the out-of-plane axis, despite the larger in-plane lattice mismatch. It was also found that the coherently strained $Ag(Ta_{0.5}Nb_{0.5})O_3$ films are in the M_3 phase at room temperature, while bulk ceramics and crystals are in the M_2 phase. Strain engineering in materials with complex tilt systems was demonstrated via control of the domain state and modification of the tilt transition temperatures of compressively strained $Ag(Ta_{0.5}Nb_{0.5})O_3$ films.

A biaxial tensile strain state was introduced in $Ag(Ta_{0.5}Nb_{0.5})O_3$ thin films via deposition on $(Ba_{0.4}Sr_{0.6})TiO_3/LaAlO_3$ (001) and $KTaO_3$ substrates. These films exhibited a domain structure with the *c*-axis aligned along the in-plane axes. Interestingly, the intensity of the superlattice reflections was significantly weaker than that observed in relaxed and compressively strained films. Thus, it is believed that the tilt angle has been significantly reduced. In the $Ag(Ta_{0.5}Nb_{0.5})O_3/(Ba_{0.4}Sr_{0.6})TiO_3/LaAlO_3$ samples, an expansion of the tetragonal and orthorhombic phase fields was observed, similar to films under compressive strain. For these films under tensile strain, the T and O phases were stabilized over a temperature region ~ 270 °C larger than that of bulk materials. In addition, the films were in the M_3 phase at room temperature rather than M_2 phase. This work demonstrates that, in addition to compressive strain, tensile strain can be used to engineer materials with complex tilt systems and complicated phase transition sequences.

A summary of the phase transition temperatures determined in relaxed, compressive and tensile strained $Ag(Ta_{0.5}Nb_{0.5})O_3$ thin films is shown in Figure 8-1. The high temperature phase transition for relaxed films, shown at a zero strain state, occurred at similar temperatures to those in bulk materials. For these films, only the M_2-M_3 transition temperature was suppressed; the lower temperature was tentatively attributed to a higher concentration of point defects disrupting the long range order of B-cation displacements. ATN films under compressive strain and tensile strain showed expanded tetragonal and orthorhombic phase fields as shown in Figure 8-1. Such changes in phase transition temperatures indicate that the tilt transition temperature was influenced by strain. In addition, the strain in these films modified the domain structure such that the complex tilt sequence lay along an out-of-plane direction for compressively strained films while the tilt axis was in-plane for films under tensile strain. The results presented in this dissertation show that strain can be used to alter tilt transition temperatures as well as control the domain states in oxide materials with complex tilt systems.

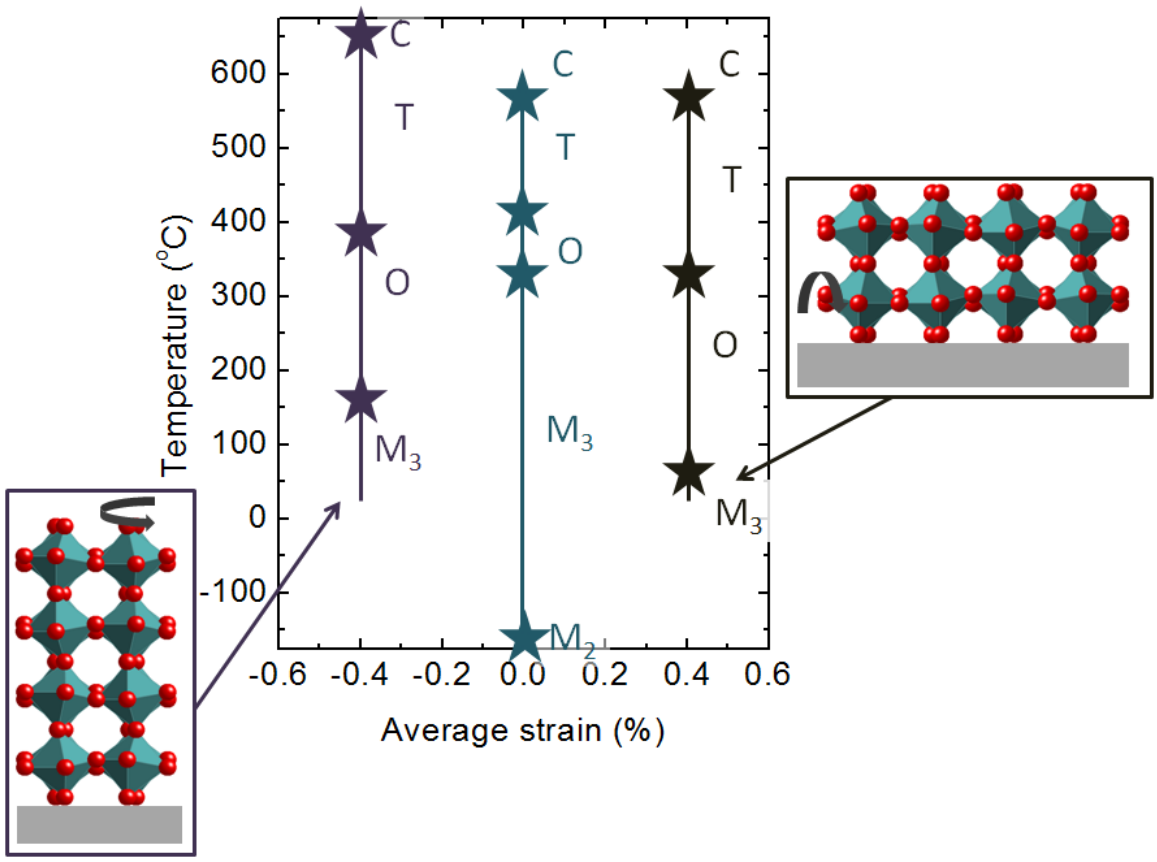

Figure 8-1 A strain phase diagram showing phase transition temperatures for thin films of $Ag(Ta_{0.5}Nb_{0.5})O_3$ in a relaxed, compressive and tensile strained state. The insets show the domain structure obtained when the film was under compressive and tensile strain.

Rotation or tilting of the oxygen octahedra can lead to new symmetry which, in turn, can introduce new properties related to these symmetries. An experiment was designed and implemented to search for a relationship between tilt angle and applied electric field in the $AgNbO_3$ system. Measurements were performed at the Advanced Photon Source to measure the intensity of superlattice reflections of a pure $AgNbO_3$ single crystal, a $(Ag_{0.95}Li_{0.05})NbO_3$ single crystal, and $AgNbO_3$ thin film. Since tilt angle and intensity of the superlattice peaks are related, a change in peak height was expected if the rotation angle deviated. However, in the samples tested, no change was observed, suggesting that the octahedra in $AgNbO_3$ do not undergo a substantial change in tilt as a function of electric field.

8.2 Recommendations for future work

8.2.1 Further studies on the $Ag(Ta_xNb_{1-x})O_3$ system

This section will describe two possible for future experiments focused specifically on the $Ag(Ta_xNb_{1-x})O_3$ system. Both experiments will provide more information into the complicated ATN system, thereby providing a base understanding for other complex oxides.

8.2.1.1 Quantification of tilt angles

The work presented in this dissertation relied on relative intensities of superlattice reflections to determine phase transition sequences. No quantitative measurements were performed that allowed for exact tilt angle determination. Recent work by May *et al.* introduced a method for calculating octahedral rotation angles in the perovskite system $LaNiO_3$.[22] As an extension of the work presented here, a similar method of calculations can be performed on ATN to more fully understand the impact of strain on tilt. Such an experiment would help answer the question of how the tilt angle is affected by strain. It would also provide some information on the suppression of the M_2-M_3 transition (especially in relaxed films) since the local cation displacements are strongly coupled to the octahedral tilting.

8.2.1.2 ATN as a function of strain

In this dissertation, only two biaxial strain states of ATN were examined, therefore, another set of possible experiments would include measurements on a variety of substrates that induce different levels of strain. Due to the difficulty in finding commercially available substrates with a cubic, no-tilt structure, it is recommended that a buffer layer of $(Ba,Sr)TiO_3$ be used. The

Ba/Sr ratio can be adjusted to provide a wide range of strain states in the ATN film (~2% tensile to ~1% compressive). These experiments would help complete the strain phase diagram for ATN. The work would determine how the phase transitions, specifically the tilt transition, depend on strain (i.e. linear dependence or other). This information would provide a basis for phase transitions in other complex oxide materials under various strain states.

Another avenue for studying different strain levels in ATN would be to deposit a set of films with different thicknesses. The thinnest film would be fully coherent to the given substrate. As the thickness increases, the formation of dislocations would start to relax the strain level in the film thus providing a range of strain states. The goal of this work would be to understand how different levels of strain affect octahedral tilting. Ultimately, a strain phase diagram for ATN could be completed.

8.2.1.3 Investigation of the suppression of the M_2-M_3 transition temperature in ATN thin films

In relaxed ATN films, the suppression of the M_2-M_3 phase transition temperature was attributed to the larger concentration of point and planar defects found in films compared to bulk, however, the defect type or concentration was not examined in detail. A study can be designed that uses electrical measurements to determine transition temperatures of films with different cation stoichiometry or films that have been annealed in a controlled environment of silver vapor. Changing these conditions can alter the type and concentration of defects in the film. Such a study, which designed to pinpoint why the B-cation displacements were disrupted, would be useful as it provides a deeper understanding into the suppression of the M_2-M_3 phase transition temperature found in films.

8.2.2 The continued search for the "roto" electric effect

Based on the results presented in this dissertation, there was no detectable change in tilt angle as a function of electric field for $AgNbO_3$ single crystals and thin films. However, this does not mean that the roto-electric effect is not present in some materials. Therefore, one avenue of future research is to explore this phenomenon in another material. An excellent candidate is lead germanate, $Pb_5Ge_3O_{11}$, because it exhibits rotation of polyhedra and is polar.[96-98] $Pb_5Ge_3O_{11}$ has a *P3* space group at room temperature in which the oxygen atoms form tetrahedra centered about Ge (Figure 8-2). Lead germanate is a well studied material that undergoes a ferroelectric phase transition coupled with a change in optical activity at 450 K.[96, 98] Below the Curie temperature, the optical handedness inverts when the polarization switches under the application of an electric field.[96] This relationship between optical activity and electric field is known as the electro-gyration effect.[98-100]

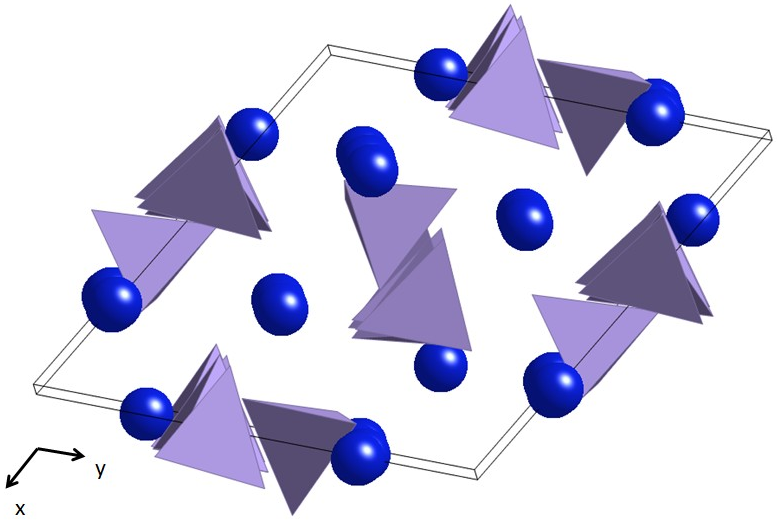

Figure 8-2 Room temperature crystal structure of lead germanate as viewed down the *c*-axis. The blue spheres represent Pb atoms, the Ge atoms sit at the center of the tetrahedra and the oxygen atoms occupy the corners of the tetrahedra.

No direct link between electric field and tetrahedral rotations has been reported $Pb_5Ge_3O_{11,}$ however, it is believed that the optical activity is associated with rotations of the Ge polyhedra.[98] Therefore, lead germanate is a natural choice for experiments searching for the roto-electric effect. Structural measurements will be performed in a manner similar to those outlined in Chapter 7 using synchrotron X-ray diffraction. The superlattice reflections due to the tilting of the polyhedra will be examined as a function of electric field. The intensities of these reflections would then be compared. Any change in rotation angle would lead to deviations in peak intensity. Highly insulting $Pb_5Ge_3O_{11}$ single crystals should enable diffraction measurements performed at DC fields. If, however, the conductivity of lifetime under field is too low, then AC field measurements may be required. If this is the case, a measurement set-up designed to synchronize the AC field with the X-ray beam using time resolved X-ray diffraction is essential.[101] The measurements outlined in Chapter 7 provide a strong basis for measurements on lead germanate and other potential materials. The proposed study could potentially open the door for studying new physical properties and ultimately provide new devices that exploit such properties.

8.2.3 Quantifying domain wall motion in $Pb(Zr,Ti)O_3$ thin films

Thin films of lead zirconate titanate, $Pb(Zr,Ti)O_3$ (PZT), exhibit large piezoelectric responses at low voltages and, as such, are among the most promising candidates for miniaturized actuators and sensors in microelectromechanical systems (MEMS). In bulk PZT, much of the electromechanical coupling is associated with the motion of ferroelectric domain walls. In thin films, the underlying substrate clamps the domain walls and significantly lowers the magnitudes of piezoelectric and dielectric responses. Currently, comprehensive understanding of domain wall motion and its contribution to piezoelectric properties in PZT thin films is missing in part because

only indirect measurements of these effects have been reported. The proposed research seeks to address this problem by combining *in situ* X-ray diffraction and transmission electron microscopy to develop fully quantitative measurements of the motion of non-180° domain walls in PZT films having different compositions and stress states. These measurements could be used to develop a comprehensive model of the domain wall phenomena, as needed to optimize piezoelectric properties of PZT films in MEMS devices.

A series of quantitative measurements of domain wall motion in thin film PZT materials should be undertaken using *in situ* X-ray diffraction and transmission electron microscopy (TEM). Previous research on bulk ceramics shows that the degree of domain switching in the tetragonal and rhombohedral structures can be calculated directly from the changes in relative intensities of Bragg peaks.[101, 102] Here, a similar procedure should be developed for thin films. Samples of different compositions across the PZT phase diagram could be used to compare the behavior of tetragonal, rhombohedral, and MPB-type structures. Clamped films should be compared to diaphragm structures where the film has been fully released from the underlying substrate.

Data obtained using synchrotron X-ray diffraction and would be analyzed to assess both the intrinsic electric field-induced lattice strains as well as non-180° domain wall motion. The lattice strain induced by the electric-field is calculated from

$$\varepsilon_{hkl} = \frac{d^{+}_{hkl} - d^{-}_{hkl}}{d^{-}_{hkl}}$$

where d^{+}_{hkl} and d^{-}_{hkl} are the *d*-spacings during the application of maximum positive and minimum negative electric fields, respectively.[101] The converse piezoelectric coefficient, d_{ijk}, can be determined through the relationship $\varepsilon_{jk} = d_{ijk}E_i$ where E_i is the applied electric field. The volume fraction of non-180° domains can be calculated from the intensities of certain diffraction

peaks.[101, 103-105] For tetragonal perovskite structures, a volume fraction of domains having their *c*-axis aligned with a given direction is given by

$$v_{002} = \frac{\frac{I_{002}}{I'_{002}}}{\frac{I_{002}}{I'_{002}} + 2\left(\frac{I_{200}}{I'_{200}}\right)}$$

where I_{hkl} is the integrated area of the *hkl* diffraction peak and I'_{hkl} is the integrated area of the same peak for a sample with random orientations of 90° domains. The factor of 2 in the denominator accounts for the multiplicity of {200} lattice planes in the tetragonal structure. The volume fraction of 111 domains can be determined using a similar method. The change in volume fraction of the non-180° domains under square wave electric fields can be given by $\Delta\eta = \eta^+ - \eta^-$, where η^+ and η^- are values of η (the volume fraction of domains) for maximum positive and minimum negative electric fields. For tetragonal structures, $\eta_{002} = v_{002} - \frac{1}{3}$ while for rhombohedral structures, $\eta_{111} = v_{111} - \frac{1}{4}$. The fractions correspond to an equal distribution of possible ferroelastic domain variants. This technique will provide a direct method of quantifying non-180° domain wall motion in PZT thin films.

The measurements outlined above could be used to develop a comprehensive model for the ensemble average motion of domain walls in PZT thin films. This would allow the behavior of films to be compared on a quantitative basis with bulk materials. The proposed study would also provide key fundamental information to theorists on the interaction between domain wall motion and clamping conditions, and could help to elucidate the origins of correlated motion of domain walls in thin films.

Appendix A

Mathematica code for fitting Bragg peaks

A sample Mathmatica code that was used to fit Bragg peaks is shown in this appendix. This example is given for a two temperatures points, however, all temperature data can be analyzed in a similar manner. The room temperature example uses one pseudo-Voigt peak to fit the data. The fitting of the data at 400 °C uses two pseudo-Voigt peaks. A file called "TXRFtools" is required to run the program. The code embedded in this document will provide commands for reading the SPEC output file obtained at APS.

Load functions

```
 Needs["PlotLegends`"]
<<PlotLegends`

Needs["ErrorBarPlots`"]
Needs["HypothesisTesting`"]
$TextStyle={FontFamily->"Arial",FontSize->26};
SetDirectory["C:\\Users\\RWilke\\Documents\\Raegan\\Research\\data\\Argonne
Data"];
<<TXRFtools`

plotoptionsLegend = Sequence[Frame->True,BaseStyle->{FontFamily->"Arial",
FontSize->30},Frame->True, FrameTicksStyle-> {FontSize->25,FontSize->
25},ImageSize->700,
FrameTicksStyle->Directive[Thick],LegendShadow->None];

plotoptions = Sequence[Frame->True,BaseStyle->{FontFamily→"Arial", FontSize->
30},Frame->True,FrameTicksStyle->{FontSize->20,FontSize->20},ImageSize->500,
FrameTicksStyle->Directive[Thick]];
```

File Import

```
atn008T450C=Import["C:\\Users\\RWilke\\Documents\\Raegan\\Research\\data\\Argon
ne Data\\2009_2 - July 2009\\July09\\jul2409_3","Table"];

atn008T25C=Import["C:\\Users\\RWilke\\Documents\\Raegan\\Research\\data\\Argonn
e Data\\2009_2 - July 2009\\July09\\jul2509_10","Table"];
```

(*Note: files for other temperatures can be imported in a similar manner *)

Name assignment

```
atn008T400CL=Transpose[getSpecScan[atn008T400C,#,17]&/@{"L","signal"}];
atn008T400CHK=Transpose[getSpecScan[atn008T400C,#,17]&/@{"H","K"}];

atn008T25CL=Transpose[getSpecScan[atn008T25C,#,23]&/@{"L","signal"}];
atn008T25CHK=Transpose[getSpecScan[atn008T25C,#,23]&/@{"H","K"}];

ListLinePlot[atn008T25CL,PlotMarkers→Automatic, Frame->True,FrameLabel->{"L
(rlu)","Intensity"},GridLines->Automatic]
```

Convert to d-spacing

```
aLAO=3.79965;
bLAO=3.79957;
cLAO=3.79174;
```

(* Note: these values obtained from orientation matrix at APS *)

d-spacing equations

```
atn008DSpace400C = (1/Sqrt[(atn008T400CHK[[All,1]],aLAO)^2 + (atn008T400CHK[[All,2]],aLAO)^2
+ (atn008T400CL[[All,1]],aLAO)^2]);


atn008DSpace25C=(1/Sqrt[(atn008T25CHK[[All,1]],aLAO)^2 + (atn008T25CHK[[All,2]],aLAO)^2 +
(atn008T25CL[[All,1]],aLAO)^2]););
```

d-spacing name assignment

```
atn008DSpace400C=Transpose[{atn008DSpace400C,atn008T400CL[[All,2]]}];
atn008DSpace25C=Transpose[{atn008DSpace25C,atn008T25CL[[All,2]]}];
```

Test

```
ListPlot[{atn008DSpace450C}, PlotRange-> Automatic, PlotMarkers->{Automatic,8},
Frame->True, FrameLabel->{"d-spacing 008 (Å)","Signal"},LabelStyle->14]
```

Fitting Functions

```
pV1 = amp0(mu0*(2/pi)*(fwhm0/(4(x-cen0)^2+fwhm0^2))+(1-
mu0)*Sqrt[4*Log[2]]/((Sqrt[pi]*fwhm0))* Exp[-((4Log[2])/fwhm0^2)*(x-cen0)^2]) +
amp2*x + const;

pV2 = amp0(mu0*(2/pi )*(fwhm0/(4(x-cen0)^2+fwhm0^2))+(1-mu0)*
Sqrt[4*Log[2]]/((Sqrt[pi ]*fwhm0))* Exp[-((4Log[2])/fwhm0^2) (x-cen0)^2]) +
amp1(mu1*(2/pi )*(fwhm1/(4(x-cen1)^2+fwhm1^2))+(1-mu1)*
Sqrt[4*Log[2]]/((Sqrt[pi]*fwhm1))* Exp[-((4Log[2])/fwhm1^2)*(x-cen1)^2]) + amp2*x
+ const;
```

Truncate data

```
atn008DSpace400CTrunc=atn008DSpace400C[[5;;180]];
atn008DSpace25CTrunc=atn008DSpace25C[[5;;180]];
```

Peak Fitting

400 °C

2 peak fit

```
atn008DSpaceT400CRegress =
NonlinearModelFit[atn008DSpace400CTrunc,{pV2,{20>amp0>0, 0.491<cen0<0.496,
0<fwhm0<0.002, 0<mu0<1, 10>amp1>0, 0.493<cen1<0.498, 0<fwhm1<0.002, 0<mu1<1,
amp2<0, const>0}}, {{amp0,10}, {fwhm0,0.001}, {cen0,0.4945}, {mu0,0.87},
{amp1,8}, {fwhm1,0.001}, {cen1,0.496}, {mu1,0.87}, {amp2,-500}, {const,2200}},
x, Weights→(1/#^0  &), MaxIterations->150];


atn008DSpaceT400CfitsL2pks=atn008DSpaceT400CRegress["BestFitParameters"]
atn008DSpaceErr400CL2pks=atn008DSpaceT400CRegress["ParameterErrors"]
atn008DSpaceBIC400CL2pks=atn008DSpaceT400CRegress["BIC"]


Show[ListPlot[atn008DSpace400CTrunc,PlotRange->{{0.488,0.499},{1500,4000}},plot
options,FrameLabel->{"d-spacing 008c (Å)","Intensity"},LabelStyle->16,
AspectRatio->1,PlotMarkers->{Automatic,8}],Plot[pV2/.atn008DSpaceT400CfitsL2pks
, {x,0.487,0.5},PlotStyle->{Red,Thick}]]
```

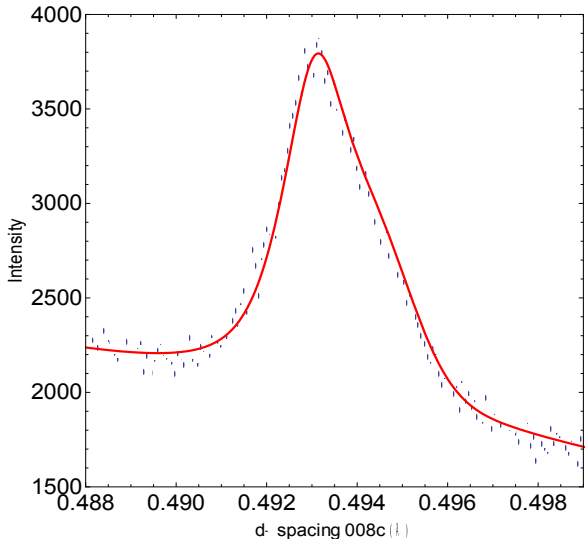

25 °C

One peak fit

```
atn008DSpaceT25CRegress =
NonlinearModelFit[atn008DSpace25CTrunc,{pV1,{20>amp0>0, 0.489<cen0<0.498,
0<fwhm0<0.006, 0<mu0<1, amp2<0, const>0}}, {{amp0,10}, { ,0.002},
{cen0,0.4915}, {mu0,0.87}, {amp2,-10}, {const,2000}}, x, Weights→(1/#^0
&),MaxIterations->150];

atn008DSpaceT25CfitsL=atn008DSpaceT25CRegress["BestFitParameters"]
atn008DSpaceErr25CL=atn008DSpaceT25CRegress["ParameterErrors"]
atn008DSpaceBIC25CL=atn008DSpaceT25CRegress["BIC"]
```

```
Show[ListPlot[atn008DSpace25CTrunc,PlotRange->Automatic,plotoptions,FrameLabel
->{"d-spacing 008c (Å)","Intensity"}, LabelStyle->16, AspectRatio->1,
PlotMarkers->{Automatic,8}],Plot[pV1/.atn008DSpaceT25CfitsL,{x,0.484,0.4975},
PlotStyle->{Red,Thick}]]
```

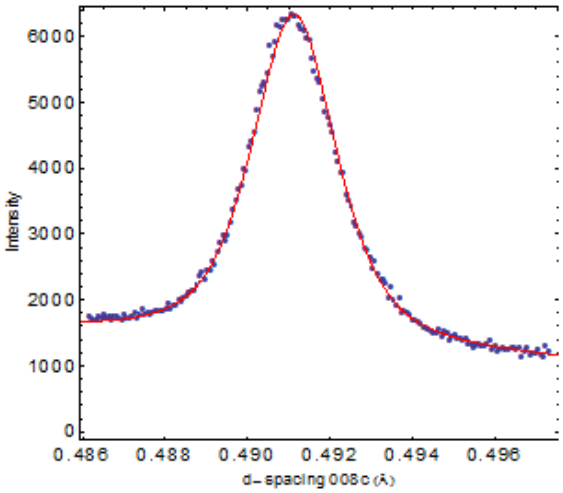

d-spacing vs. Temperature

```
atn008DSpaceandError =
{{{600,cen0/.atn008DSpaceT600CfitsL},ErrorBar[atn008DSpaceErr600CL[[3]]]},
{{575,cen0/.atn008DSpaceT575CfitsL},ErrorBar[atn008DSpaceErr575CL[[3]]]},
{{550,cen0/.atn008DSpaceT550CfitsL},ErrorBar[atn008DSpaceErr550CL[[3]]]},
{{525,cen0/.atn008DSpaceT525CfitsL2pks},ErrorBar[atn008DSpaceT525CfitsL2pks[[3]
]]},
{{525,cen1/.atn008DSpaceT525CfitsL2pks},ErrorBar[atn008DSpaceT525CfitsL2pks[[7]
]]},
{{500,cen0/.atn008DSpaceT525CfitsL2pks},ErrorBar[atn008DSpaceT525CfitsL2pks[[3]
]]},
{{500,cen1/.atn008DSpaceT500CfitsL2pks},ErrorBar[atn008DSpaceT500CfitsL2pks[[7]
]]},
{{475,cen0/.atn008DSpaceT475CfitsL2pks},ErrorBar[atn008DSpaceErr475CL2pks[[3]]]
},
{{475,cen1/.atn008DSpaceT475CfitsL2pks},ErrorBar[atn008DSpaceErr475CL2pks[[7]]]
},
{{450,cen0/.atn008DSpaceT450CfitsL2pks},ErrorBar[atn008DSpaceErr450CL2pks[[3]]]
},
{{450,cen1/.atn008DSpaceT450CfitsL2pks},ErrorBar[atn008DSpaceErr450CL2pks[[7]]]
},
{{425,cen0/.atn008DSpaceT425CfitsL2pks},ErrorBar[atn008DSpaceErr425CL2pks[[3]]]
},
{{425,cen1/.atn008DSpaceT425CfitsL2pks},ErrorBar[atn008DSpaceErr425CL2pks[[7]]]
},
{{400,cen0/.atn008DSpaceT400CfitsL2pks},ErrorBar[atn008DSpaceErr400CL2pks[[3]]]
},
{{400,cen1/.atn008DSpaceT400CfitsL2pks},ErrorBar[atn008DSpaceErr400CL2pks[[7]]]
},
```

```
{{375,cen0/.atn008DSpaceT375CfitsL2pks},ErrorBar[atn008DSpaceErr375CL2pks[[3]]]
},
{{375,cen1/.atn008DSpaceT375CfitsL2pks},ErrorBar[atn008DSpaceErr375CL2pks[[7]]]
},
{{350,cen0/.atn008DSpaceT350CfitsL2pks},ErrorBar[atn008DSpaceErr350CL2pks[[3]]]
},
{{350,cen1/.atn008DSpaceT350CfitsL2pks},ErrorBar[atn008DSpaceErr350CL2pks[[7]]]
},
{{325,cen0/.atn008DSpaceT325CfitsL2pks},ErrorBar[atn008DSpaceErr325CL2pks[[3]]]
},
{{325,cen1/.atn008DSpaceT325CfitsL2pks},ErrorBar[atn008DSpaceErr325CL2pks[[7]]]
},
{{275,cen0/.atn008DSpaceT275CfitsL2pks},ErrorBar[atn008DSpaceErr275CL2pks[[3]]]
},
{{275,cen1/.atn008DSpaceT275CfitsL2pks},ErrorBar[atn008DSpaceErr275CL2pks[[7]]]
},
{{250,cen0/.atn008DSpaceT250CfitsL},ErrorBar[atn008DSpaceErr250CL[[3]]]},
{{225,cen0/.atn008DSpaceT225CfitsL},ErrorBar[atn008DSpaceErr225CL[[3]]]},
{{200,cen0/.atn008DSpaceT200CfitsL},ErrorBar[atn008DSpaceErr200CL[[3]]]},
{{175,cen0/.atn008DSpaceT175CfitsL},ErrorBar[atn008DSpaceErr175CL[[3]]]},
{{150,cen0/.atn008DSpaceT150CfitsL},ErrorBar[atn008DSpaceErr150CL[[3]]]},
{{125,cen0/.atn008DSpaceT125CfitsL},ErrorBar[atn008DSpaceErr125CL[[3]]]},
{{100,cen0/.atn008DSpaceT100CfitsL},ErrorBar[atn008DSpaceErr100CL[[3]]]},
{{75,cen0/.atn008DSpaceT75CfitsL},ErrorBar[atn008DSpaceErr75CL[[3]]]},
{{50,cen0/.atn008DSpaceT50CfitsL},ErrorBar[atn008DSpaceErr50CL[[3]]]},
{{25,cen0/.atn008DSpaceT25CfitsL},ErrorBar[atn008DSpaceErr25CL[[3]]]}};
```

Plot

```
Show[ErrorListPlot[atn008DSpaceandError],ListPlot[atn008DSpaceandError[[All,1]]
, PlotMarkers->{Automatic,12}], ImageSize->700, plotoptions,
FrameLabel->{"Temperature (°C)","d-spacing of 008c
(Å)"},LabelStyle->20,PlotRange->Automatic]
```

Appendix B

Mathematica code for fitting superlattice reflections

The following pages provide sample Mathmatica code that was used to fit superlattice reflections and calculate the integrated intensity of such peaks. The fitting in this example is shown for one temperature point, however, all temperature data can be analyzed in a similar manner. The code used to find the integrated intensity vs. temperature is also given. A file called "TXRFtools" is required to run the program. The code embedded in this document will provide commands for reading the SPEC output file obtained at APS.

Load Functions

```
Needs["PlotLegends`"]
<<PlotLegends`

Needs["ErrorBarPlots`"]
Needs["HypothesisTesting`"]
$TextStyle={FontFamily->"Arial",FontSize→26};
SetDirectory["C:\\Users\\RWilke\\Documents\\Raegan\\Research\\data\\Argonne
Data"];
<<TXRFtools`

plotoptionsLegend=Sequence[Frame→True,BaseStyle→{FontFamily->"Arial",FontSize->
30},Frame->True,FrameTicksStyle->{FontSize->25,FontSize->25},
ImageSize->700,FrameTicksStyle->Directive[Thick],LegendShadow->None];

plotoptions=Sequence[Frame->True,BaseStyle->{FontFamily->"Arial",FontSize->30},
Frame->True,FrameTicksStyle->{FontSize->25,FontSize->25},
ImageSize->500,FrameTicksStyle->Directive[Thick]];
```

File Import

```
Data=Import["C:\\Users\\RWilke\\Documents\\Raegan\\Research\\data\\Argonne
Data\\2009_3 - Oct 2009\\Oct 2009\\nov0109_5","Table"];

Data25C=Transpose[getSpecScan[Data,#,44]&/@{"phi","signal"}];
```

Test plot:

```
ListPlot[Data25C,PlotMarkers->Automatic,Joined->True,
PlotMarkers->{Automatic,10},PlotRange->All]
```

Center about ϕ = 0

```
Data25C[[All,1]]=Mean[Data25C [[All,1]]]- Data25C [[All,1]]-10^-15;

ListPlot[Data25C,PlotMarkers->Automatic,Joined->True,PlotMarkers->{Automatic,10
},PlotRange->All]
```

Pseudo-Voigt function

```
pV1=amp1(mu1*(2/pi)*(fwhm1/(4(x-cen1)^2+fwhm1^2))+(1-mu1)*Sqrt[4Log[2]]
/(2Sqrt[pi]*fwhm1)*
Exp[-((4Log[2])/fwhm1^2)*(x-cen1)^2])+const;
```

Peak Fitting

```
Data25CRegress=NonlinearModelFit[Data25C,{pV1,{6000>amp1>0,
-.8<cen1<0.8,0<fwhm1<2,
0<const<1000,0<mu1<1}},{{amp1,3400},{fwhm1,0.7},{cen1,0},{mu1,.266},{const,300}
},x,Weights→(1/#^0 &),MaxIterations->150];

Data25Cfits= Data25CRegress["BestFitParameters"]
Data25CErr= Data25CRegress["ParameterErrors"]
Data25CphiConfInt= Data25CRegress["ParameterConfidenceIntervals"]
Data25CphiBIC= Data25CRegress["BIC"]

Show[ListPlot[Data25CRegress,PlotRange->All,plotoptions,FrameLabel->{"Phi
(degrees)","Intensity"},AspectRatio->1,PlotMarkers->{Automatic,8}],Plot[pV1/.
Data25Cfits,{x,-2,2},PlotRange->All]]
```

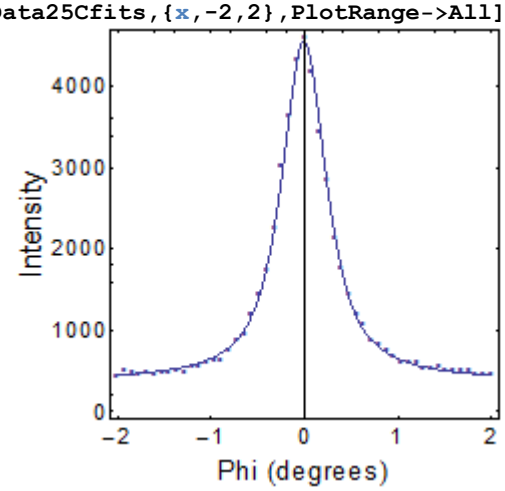

Integrated Intensity

```
IInt25C=Integrate[pV1/.Data25Cfits,{x,-2 ,2}]-(const/.Data25Cfits)*4;
```

```
IIvsTemp={{25,IInt25C},{50,IInt50C},(*add data for other temperatures*)};

ListPlot[IIvsTemp, PlotRange-> Automatic, Frame-> True,
FrameLabel->{"Temperature (°C)","Integrated Intensity"}, LabelStyle->18,
FrameStyle->Thick, PlotMarkers->{Automatic,12}]
```

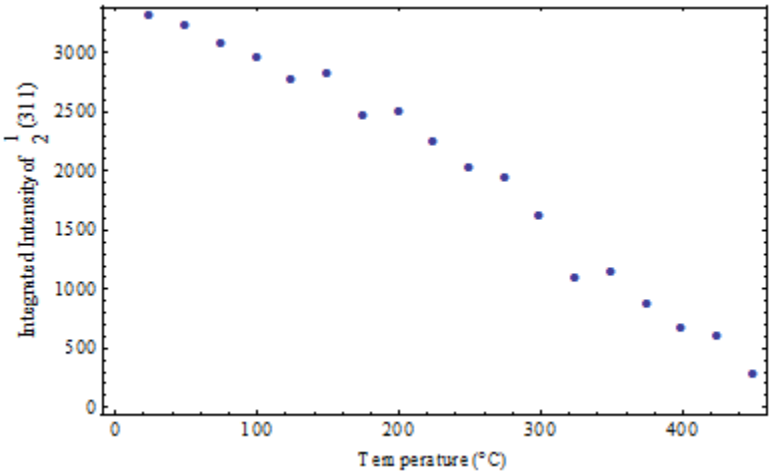

Error calculation:
Integrated intensity calculation of lower confidence limit:

```
Err25CLower=Integrate[(Data25CphiConfInt[[1,1]]*(Data25CphiConfInt
[[4,1]]*2/pi* Data25CphiConfInt[[2,1]]/(4*(x - Data25CphiConfInt[[3,1]])^2+
Data25CphiConfInt [[2,1]]^2)+(1-
Data25CphiConfInt[[4,1]])*(Sqrt[4*Log[2]/(2*Sqrt[2]* Data25CphiConfInt [[2,1]])
* Exp[-((4Log[2])/(4*Data25CphiConfInt[[2,1]]^2))*(x- Data25CphiConfInt
[[3,1]])^2])+ Data25CphiConfInt[[5,1]]),{x,-2 ,2}]-(const/. Data25CphiConfInt)*4;

IInt25CErr=Abs[(Err25CLower - IInt25C)/1.96];
(* NOTE: The factor of 1.96 is needed to convert from confidence limits to standard error *)

IIntError={{IInt25CErr},{IInt50CErr},(*add data for other temperatures*)};

IIntandError={{{25,IInt25C},ErrorBar[IInt25CErr]},{{50,IInt50C},ErrorBar[IInt50
CErr]}, (*add data for other temperatures*)};
```

Plot

```
Show[ErrorListPlot[IIntandError],ListPlot[IIntandError[[All,1]],
PlotMarkers->{Automatic,12}],PlotRange->All, Frame-> True,
FrameLabel->{"Temperature (°C)","Integrated Intensity"}, LabelStyle->18,
FrameStyle->Thick, ImageSize->700, BaseStyle->{FontFamily->"Arial",
FontSize->30}]
```

References

1. Trolier-McKinstry, S. and P. Muralt, *Thin film piezoelectrics for MEMS.* Journal of Electroceramics, 2004. **12**(1-2): p. 7-17.

2. Glazer, A.M., *Classification of tilted octahedra in perovskites.* Acta Crystallographica Section B-Structural Science, 1972. **B 28**(NOV15): p. 3384-&.

3. Woodward, D.I., Reaney, I. M., *Electron diffraction of tilted perovskites.* Acta Crystallographica Section B-Structural Science, 2005. **61**: p. 387-399.

4. Schlom, D.G., Chen, L. Q., Eom, C. B., Rabe, K. M., Streiffer, S. K., Triscone, J. M., *Strain tuning of ferroelectric thin films.* Annual Review of Materials Research, 2007. **37**: p. 589-626.

5. Haeni, J.H., Irvin, P., Chang, W., Uecker, R., Reiche, P., Li, Y. L., Choudhury, S., Tian, W., Hawley, M. E., Craigo, B., Tagantsev, A. K., Pan, X. Q., Streiffer, S. K., Chen, L. Q., Kirchoefer, S. W., Levy, J., Schlom, D. G., *Room-temperature ferroelectricity in strained $SrTiO_3$.* Nature, 2004. **430**(7001): p. 758-761.

6. He, F.Z., Wells, B. O., Ban, Z. G., Alpay, S. P., Grenier, S., Shapiro, S. M., Si, W. D., Clark, A., Xi, X. X., *Structural phase transition in epitaxial perovskite films.* Physical Review B, 2004. **70**(23): p. 235405.

7. He, F.Z., Wells, B. O., Shapiro, S. M., *Strain phase diagram and domain orientation in $SrTiO_3$ thin films.* Physical Review Letters, 2005. **94**(17): p. 176101.

8. Choi, K.J., Biegalski, M., Li, Y. L., Sharan, A., Schubert, J., Uecker, R., Reiche, P., Chen, Y. B., Pan, X. Q., Gopalan, V., Chen, L. Q., Schlom, D. G., Eom, C. B., *Enhancement of ferroelectricity in strained $BaTiO_3$ thin films.* Science, 2004. **306**(5698): p. 1005-1009.

9. Streiffer, S.K., Eastman, J. A., Fong, D. D., Thompson, C., Munkholm, A., Murty, M. V. R., Auciello, O., Bai, G. R., Stephenson, G. B., *Observation of nanoscale 180 degrees stripe domains in ferroelectric $PbTiO_3$ thin films.* Physical Review Letters, 2002. **89**(6): p. 067601.

10. Glazer, A.M., *Simple ways of determining perovskite structures.* Acta Crystallographica Section A, 1975. **31**(NOV1): p. 756-762.

11. Reaney, I.M., Colla, E. L., Setter, N., *Dielectric and structural characteristics of Ba-based and Sr-based complex perovskites as a function of tolerance factor.* Japanese Journal of Applied Physics Part 1-Regular Papers Short Notes & Review Papers, 1994. **33**(7A): p. 3984-3990.

12. Howard, C.J., Stokes, H. T., *Octahedral tilting in cation-ordered perovskites - a group-theoretical analysis.* Acta Crystallographica Section B-Structural Science, 2004. **60**: p. 674-684.

13. Stokes, H.T., Kisi, E. H., Hatch, D. M., Howard, C. J., *Group-theoretical analysis of octahedral tilting in ferroelectric perovskites.* Acta Crystallographica Section B-Structural Science, 2002. **58**: p. 934-938.

14. Axe, J.D., Shirane, G., Mueller, K. A., *Zone-boundary phonon instability in cubic $LaAlO_3$.* Bulletin of the American Physical Society, 1969. **14**(1): p. 61.

15. Woodward, D.I., Reaney, I. M., Eitel, R. E., Randall, C. A., *Crystal and domain structure of the $BiFeO_3$-$PbTiO_3$ solid solution.* Journal of Applied Physics, 2003. **94**(5): p. 3313-3318.

16. Woodward, D.I., Knudsen, J., Reaney, I. M., *Review of crystal and domain structures in the $PbZr_xTi_{1-x}O_3$ solid solution.* Physical Review B, 2005. **72**.

17. Vailionis, A., Boschker, H., Siemons, W., Houwman, E. P., Blank, D. H. A., Rijnders, G., Koster, G., *Misfit strain accommodation in epitaxial ABO_3 perovskites: Lattice rotations and lattice modulations.* Physical Review B, 2011. **83**(6): p. 064101.

18. Biegalski, M.D., Haeni, J. H., Trolier-McKinstry, S., Schlom, D. G., Brandle, C. D., Ven Graitis, A. J., *Thermal expansion of the new perovskite substrates $DyScO_3$ and $GdScO_3$.* Journal of Materials Research, 2005. **20**(4): p. 952-958.

19. Kennedy, B.J., Hunter, B. A., Hester, J. R., *Synchrotron x-ray diffraction reexamination of the sequence of high-temperature phases in $SrRuO_3$.* Physical Review B, 2002. **65**(22): p. 224103.

20. Kennedy, B.J., Howard, C. J., Chakoumakos, B. C., *Phase transitions in perovskite at elevated temperatures - a powder neutron diffraction study.* Journal of Physics-Condensed Matter, 1999. **11**(6): p. 1479-1488.

21. Sakowski-Cowley, A.C., Lukaszew, K, Megaw, H. D., *Structure of sodium niobate at room temperature and the problem of reliability in pseudosymmetric structures.* Acta Crystallographica Section B-Structural Crystallography and Crystal Chemistry, 1969. **B 25**: p. 851-&.

22. May, S.J., Kim, J. W., Rondinelli, J. M., Karapetrova, E., Spaldin, N. A., Bhattacharya, A., Ryan, P. J., *Quantifying octahedral rotations in strained perovskite oxide films.* Physical Review B, 2010. **82**(1): p. 014110.

23. Ohring, M., *Materials Science of Thin Films: Deposition & Structure,* 2002, San Diego, CA: Academic Press.

24. Smith, D.L., *Thin-Film Deposition: Principles & Practice.* 1995: McGraw-Hill, Inc.

25. Matthews, J.W., Blakeslee, A. E., *Defects in epitaxial multilayers 1. Misfit dislocations* Journal of Crystal Growth, 1974. **27**(DEC): p. 118-125.

26. Choi, K.J., Baek, S. H., Jang, H. W., Belenky, L. J., Lyubchenko, M., Eom, C. B., *Phase-Transition Temperatures of Strained Single-Crystal $SrRuO_3$ Thin Films.* Advanced Materials, 2010. **22**(6): p. 759.

27. Vailionis, A., Siemons, W., Koster, G., *Strain-induced single-domain growth of epitaxial $SrRuO_3$ layers on $SrTiO_3$: A high-temperature x-ray diffraction study.* Applied Physics Letters, 2007. **91**(7): p. 071907.

28. Vailionis, A., Siemons, W., Koster, G., *Room temperature epitaxial stabilization of a tetragonal phase in $ARuO_3$ (A=Ca and Sr) thin films.* Applied Physics Letters, 2008. **93**(5).

29. Maria, J.P., McKinstry, H. L., Trolier-McKinstry, S., *Origin of preferential orthorhombic twinning in $SrRuO_3$ epitaxial thin firms.* Applied Physics Letters, 2000. **76**(23): p. 3382-3384.

30. Theis, C.D., *Investigation of growth and domain structure of epitaxial lead titanate thin films*, 1996, The Pennsylvania State University.

31. He, H., Tan, X., *Electric-field-induced transformation of incommensurate modulations in antiferroelectric $Pb_{0.99}Nb_{0.02}[(Zr_{1-x}Sn_x)_{(1-y)}Ti_y]_{(0.98)}O_3$.* Physical Review B, 2005. **72**(2): p. 024102.

32. Pertsev, N.A., Tagantsev, A. K., Setter, N., *Phase transitions and strain-induced ferroelectricity in $SrTiO_3$ epitaxial thin films.* Physical Review B, 2000. **61**(2): p. R825-R829.

33. Pertsev, N.A., Tagantsev, A. K., Setter, N., *Phase transitions and strain-induced ferroelectricity in $SrTiO_3$ epitaxial thin films (vol 61, pg R825, 2000).* Physical Review B, 2002. **65**(21): p. 219901.

34. Li, Y.L., Choudhury, S., Haeni, J. H., Biegalski, M. D., Vasudevarao, A., Sharan, A., Ma, H. Z., Levy, J., Gopalan, V., Trolier-McKinstry, S., Schlom, D. G., Jia, Q. X., Chen, L. Q., *Phase transitions and domain structures in strained pseudocubic (100) $SrTiO_3$ thin films.* Physical Review B, 2006. **73**(18): p. 184112.

35. Biegalski, M., *Epitaxially Strained Strontium Titanate*, 2006, The Pennsylvania State University.

36. Tinberg, D.S., *Phase transitions in epitaxial rhombohedral Pb($Zr_{1-X}Ti_X$)O3 thin films*, 2010, The Pennsylvania State University.

37. Hatt, A.J., Spaldin, N.A., *Competition between polar distortions and octahedral rotations in epitaxial strained $LaAlO_3$*, in *arXiv:0808.3792v1*2008.

38. May, S.J., Smith, C.R., Kim, J.-W., Karapetrova, E., Bhattacharya, A., Ryan, P.J., *Control of octahedral rotations in $(LaNiO_3)_n/(SrMnO_3)_m$ superlattices.* Physical Review B, 2011. **83**: p. 153411.

39. Rondinelli, J.M., Spaldin, N. A., *Substrate coherency driven octahedral rotations in perovskite oxide films.* Physical Review B, 2010. **82**(11): p. 113402.

40. Levin, I., Woicik, J. C., Llobet, A., Tucker, M. G., Krayzman, V., Pokorny, J., Reaney, I. M., *Displacive Ordering Transitions in Perovskite-Like $AgNb_{1/2}Ta_{1/2}O3$.* Chemistry of Materials, 2010. **22**(17): p. 4987-4995.

41. Pawelczyk, M., *Phase-transitions in $AgTa_xNb_{1-x}O3$ solid-solutions.* Phase Transitions, 1987. **8**(4): p. 273-292.

42. Ratuszna, A., Pawluk, J.,Kania, A., *Temperature evolution of the crystal structure of $AgNbO_3$.* Phase Transitions, 2003. **76**(6): p. 611-620.

43. Levin, I., Krayzman, V., Woicik, J. C., Karapetrova, J., Proffen, T., Tucker, M. G., Reaney, I. M., *Structural changes underlying the diffuse dielectric response in $AgNbO_3$.* Physical Review B, 2009. **79**(10): p. 104113.

44. Sciau, P., Kania, A., Dkhil, B., Suard, E., Ratuszna, A., *Structural investigation of $AgNbO_3$ phases using x-ray and neutron diffraction.* Journal of Physics-Condensed Matter, 2004. **16**(16): p. 2795-2810.

45. Shannon, R.D., *Revised effective ionic-radii and systematic studies of interatomic distances in halids and chalcogenides.* Acta Crystallographica Section A, 1976. **32**(SEP1): p. 751-767.

46. Hafid, M., Kugel, G. E., Kania, A., Roleder, K., Fontana, M. D., *Study of the phase-transition sequence of mixed silver tantalate niobate ($AgTa_{1-x}Nb_xO_3$) by inelastic light-scattering.* Journal of Physics-Condensed Matter, 1992. **4**(9): p. 2333-2345.

47. Francombe, M.H., Lewis, B., *Structural and electrical properties of silver niobate and silver tantalate.* Acta Crystallographica, 1958. **11**(3): p. 175-178.

48. Lufaso, M.W., *Crystal structures, modeling, and dielectric property relationships of 2:1 ordered $Ba_3MM'_2O_9$ (M = Mg, Ni, Zn; M ' = Nb, Ta) perovskites.* Chemistry of Materials, 2004. **16**(11): p. 2148-2156.

49. Comes, R., Lambert, M., Guinier, A., *Chain structure of $BaTiO_3$ and $KNbO_3$* Solid State Communications, 1968. **6**(10): p. 715.

50. Valant, M., Suvorov, D., *New high-permittivity $AgNb_{1-x}Ta_xO_3$ microwave ceramics: Part II, Dielectric characteristics.* Journal of the American Ceramic Society, 1999. **82**(1): p. 88-93.

51. Valant, M., Axelsson, A. K., Alford, N., *Review of $Ag(Nb, Ta)O_3$ as a functional material.* Journal of the European Ceramic Society, 2007. **27**(7): p. 2549-2560.

52. Kim, H.T., Shrout, T., Randall, C., Lanagan, M., *Low-temperature sintering and dielectric properties of $Ag(Nb,Ta)O_3$ composite ceramics.* Journal of the American Ceramic Society, 2002. **85**(11): p. 2738-2744.

53. Petzelt, J., Kamba, S., Buixaderas, E., Bovtun, V., Zikmund, Z., Kania, A., Koukal, V., Pokorny, J., Polivka, J., Pashkov, V., Komandin, G., Volkov, A., *Infrared and microwave dielectric response of the disordered antiferroelectric $Ag(Ta,Nb)O_3$ system.* Ferroelectrics, 1999. **223**: p. 235-246.

54. Fu, D.S., Endo, M., Taniguchi, H., Taniyama, T., Itoh, M., *$AgNbO_3$: A lead-free material with large polarization and electromechanical response.* Applied Physics Letters, 2007. **90**(25): p. 252907.

55. Fu, D.S., Endo, M., Taniguchi, H., Taniyama, T., Itoh, M., Koshihara, S., *Ferroelectricity of Li-doped silver niobate (Ag, Li)NbO_3.* Journal of Physics-Condensed Matter, 2011. **23**(7): p. 075901.

56. Fu, D.S., Itoh, M., Koshihara, S., *Dielectric, ferroelectric, and piezoelectric behaviors of $AgNbO_3$-$KNbO_3$ solid solution.* Journal of Applied Physics, 2009. **106**(10): p. 104104.

57. Kania, A., *An additional phase transition in silver niobate $AgNbO_3$.* Ferroelectrics, 1998. **205**(1-4): p. 19-28.

58. Kania, A., *Dielectric properties of $Ag_{1-x}A_xNbO_3$ (A : K, Na and Li) and $AgNb_{1-x}Ta_xO_3$ solid solutions in the vicinity of diffuse phase transitions.* Journal of Physics D-Applied Physics, 2001. **34**(10): p. 1447-1455.

59. Kania, A., Roleder, K., *Ferroelectricity in $AgNb_{1-x}Ta_xO_3$ solid-solutions.* Ferroelectrics Letters Section, 1984. **2**(2): p. 51-54.

60. Kania, A., Roleder, K., Lukaszewski, M., *The ferroelectric phase in $AgNbO_3$* Ferroelectrics, 1984. **52**(4): p. 265-269.

61. Miga, S., Kania, A., Dec, J., *Freezing of the Nb^{5+} ion dynamics in $AgNbO_3$ studied by linear and nonlinear dielectric response.* Journal of Physics-Condensed Matter, 2011. **23**(15): p. 155901.

62. Valant, M., Suvorov, D., *New high-permittivity $AgNb_{1-x}Ta_xO_3$ microwave ceramics: Part I, Crystal structures and phase-decomposition relations.* Journal of the American Ceramic Society, 1999. **82**(1): p. 81-87.

63. Valant, M., Suvorov, D., Hoffmann, C., Sommariva, H., *$Ag(Nb,Ta)O_3$-based ceramics with suppressed temperature dependence of permittivity.* Journal of the European Ceramic Society, 2001. **21**: p. 2647-2651.

64. Volkov, A.A., Gorshunov, B. P., Komandin, G., Fortin, W., Kugel, G. E., Kania, A., Grigas, J., *High-frequency spectra of $AgTaO_3$-$AgNbO_3$ mixed ceramics.* Journal of Physics-Condensed Matter, 1995. **7**(4): p. 785-793.

65. Koh, J.H., Grishin, A., *$Ag(Ta, Nb)O_3$ thin-film low-loss variable interdigital capacitors.* Applied Physics Letters, 2001. **79**(14): p. 2234-2236.

66. Koh, J.H., Khartsev, S. I., Grishin, A., *Ferroelectric silver niobate-tantalate thin films.* Applied Physics Letters, 2000. **77**(26): p. 4416-4418.

67. Koh, J.H., Moon, B. M., Grishin, A., *Dielectric properties and Schottky barriers in silver tantalate-niobate thin film capacitors.* Integrated Ferroelectrics, 2001. **39**: p. 1361-1368.

68. Kim, J.Y., Grishin, A. M., *$Ag(Ta_{0.5}Nb_{0.5})O_3$ thin film microwave coplanar waveguide tunable capacitors.* Integrated Ferroelectrics, 2005. **77**: p. 13-20.

69. Kim, J.Y., Grishin, A. M., *$AgTaO_3$ and $AgNbO_3$ thin films by pulsed laser deposition.* Thin Solid Films, 2006. **515**: p. 615-618.

70. Telli, M.B., *Chemical solution deposition of silver tantalate niobate, $Ag(Ta_xNb_{1-x})O_3$, thin films* in *Materials Science and Engineering,* 2005, The Pennsylvania State University: University Park, PA, U.S.A.

71. Sakurai, H., Yamazoe, S., Wada, T., *Ferroelectric and antiferroelectric properties of $AgNbO_3$ films fabricated on (001), (110), and (111)$SrTiO_3$ substrates by pulsed laser deposition.* Applied Physics Letters, 2010. **97**(4): p. 042901.

72. Sakurai, H., Yamazoe, S., Wada, T., *oral presentation*, International Symposium on the Application of Ferroelectrics, Edinburgh, Scottland, 2010.

73. Telli, M.B., Trolier-McKinstry, S., Woodward, D. I., Reaney, I. M., *Chemical solution deposited silver tantalate niobate, $Ag_{1-x}(Ta_{0.5}Nb_{0.5})O_{3-y}$, thin films on (111)Pt/Ti/SiO_2/(100)Si substrates.* Journal of Sol-Gel Science and Technology, 2007. **42**(3): p. 407-414.

74. Telli, M.B., Bharadwaja, S. S. N., Biegalski, M. D., Trolier-McKinstry, S., *(00l) epitaxial $AgTaO_3$ and $AgNbO_3$ thin films on (001)$SrRuO_3$/(001)$LaAlO_3$ substrates by chemical solution deposition.* Applied Physics Letters, 2006. **89**(25): p. 252907.

75. Telli, M.B., Bharadwaja, S. S. N., Biegalski, M. D., Cheng, J. G., Trolier-McKinstry, S., *(001) epitaxial $Ag(Ta_{0.5}Nb_{0.5})O_3$ thin films on (001)$SrRuO_3$/(001)$LaAlO_3$ substrates by chemical solution deposition.* Journal of Applied Physics, 2007. **101**(1): p. 014101.

76. Grinberg, I., Rappe, A. M., *Silver solid solution piezoelectrics.* Applied Physics Letters, 2004. **85**: p. 1760-1762.

77. Carter, A.C., Horwitz, J. S., Chrisey, D. B., Pond, J. M., Kirchoefer, S. W., Chang, W. T., *Pulsed laser deposition of ferroelectric thin films for room temperature active microwave electronics.* Integrated Ferroelectrics, 1997. **17**(1-4): p. 273-285.

78. Rios, S., Scott, J. F., Lookman, A., McAneney, J., Bowman, R. M., Gregg, J. M., *Phase transitions in epitaxial $Ba_{0.5}Sr_{0.5}TiO_3$ thin films.* Journal of Applied Physics, 2006. **99**(2): p. 024107.

79. Qadri, S.B., Horwitz, J. S., Chrisey, D. B., Auyeung, R. C. Y., Knauss, L. A., *X-ray characterization of epitaxial (Sr,Ba)TiO_3 films grown by pulsed laser deposition.* Surface & Coatings Technology, 1995. **76**(1-3): p. 348-351.

80. Koh, J.H., B.M. Moon, and A. Grishin, *Dielectric properties and Schottky barriers in silver tantalate-niobate thin film capacitors.* Integrated Ferroelectrics, 2001. **39**(1-4): p. 1361-1368.

81. Han, Y., Reaney, I.M., Johnson-Wilke, R.L., Telli, M.B., Tinberg, D.S., Levin, I., Fong, D.D., Fister, T.T., Streiffer, S.K., Trolier-McKinstry, S., *Phase Transitions in $Ag(Ta_xNb_{1-x})O_3$ thin films on $SrRuO_3/LaAlO_3(001)_{pc}$ substrates.* Journal of Applied Physics, 2010. **107**(12): p. 123517.

82. Tinberg, D.S., *Pulsed laser deposition of $xBiScO_3(1-x)BaTiO_3$ thin films for Pb-free dielectric applications*, in *Materials Science and Engineering,* 2006, The Pennsylvania State University.

83. Munkholm, A., et al., *Antiferrodistortive reconstruction of the $PbTiO_3$(001) surface.* Physical Review Letters, 2002. **88**(1).

84. Nelson, J.B., Riley, D.P., *An experimental investigation of extrapolation methods in the dimensions of crystals derivation of accurate unit.* Phys. Soc., 1944. **57**: p. 160.

85. Touloukain, Y.S., *Thermal Expansion--Nonmetallic Solids* in *Thermophysical Properties of Matter,* 1977, IFI/Plenum, vol. 13, p. 570.

86. Chakoumakos, B.C., Schlom, D. G., Urbanik, M., Luine, J., *Thermal expansion of $LaAlO_3$ and $(La,Sr)(Al,Ta)O_3$, substrate materials for superconducting thin-film device applications.* Journal of Applied Physics, 1998. **83**(4): p. 1979-1982.

87. Young, R.A., Wiles, D. B., *Profile shape functions in Rietveld refinements.* Journal of Applied Crystallography, 1982. **15**(AUG): p. 430-438.

88. Origin Lab, I. *Pseudo-Voigt I*. http://www.originlab.de/www/helponline/origin/en/UserGuide/PsdVoigt1.html.

89. Gopalan, V., Litvin, D. B., *Rotation-reversal symmetries in crystals and handed structures.* Nature Materials, 2011. **10**(5): p. 376-381.

90. Newnham, R.E., *Properties of Materials; Anisotropy, Symmetry, Structure,* 2005: Oxford University Press.

91. Birss, R.R., *Symmetry and Magnetism,* 1964, Amsterdam: North-Holland Publishing Co.

92. Gopalan, V., *personal communication*, 2010.

93. Hovestreydt, E., *On the atomic scattering factor for O^{-2}* Acta Crystallographica Section A, 1983. **39**(MAR): p. 268-269.

94. May, S.J., *personal communication*, 2011.

95. Wada, S., Saito, A., Hoshina, T., Kakemoto, H., Tsurumi, T., Moryoshi, C., Kuroiwa, Y., *Growth of large-scale silver lithium niobate single crystals and their piezoelectric properties.* Japanese Journal of Applied Physics Part 1-Regular Papers Brief Communications & Review Papers, 2006. **45**(9B): p. 7389-7396.

96. Newnham, R.E., Wolfe, R. W., Darlington, C.N., *Prototype structure of $Pb_5Ge_3O_{11}$* Journal of Solid State Chemistry, 1973. **6**(3): p. 378-383.

97. Adamenko, D.I., Klymiv, I. M., Vasylkiv, Y., Duda, V. M., Ermakov, A. S., Vlokh, R. O., *Optical activity and the critical exponent of order parameter in lead germanate crystals. 2. Electrogyration and dielectric properties of $Pb_5Ge_3O_{11}:Cu^{2+}$*. Ukrainian Journal of Physical Optics, 2009. **10**(4): p. 194-200.

98. Adamenko, D.I., Klymiv, I. M., Vasylkiv, Y., Vlokh, R. O., *Optical activity and critical exponent of the order parameter in lead germanate crystals. 1. The case of diffused phase transition in $Pb_5Ge_3O_{11}$ doped with Cu, Ba and Si ions.* Ukrainian Journal of Physical Optics, 2009. **10**(4): p. 182-193.

99. Aizu, K., *Reversal in optical rotatory power-gyroelectric crystals + hypergyroelectric crystals* Physical Review a-General Physics, 1964. **133**(6A): p. 1584.

100. Konak, C., Kopsky, V., Smutny, F., *Gyrotropic phase-transitions* Journal of Physics C-Solid State Physics, 1978. **11**(12): p. 2493-2518.

101. Pramanick, A., Daniels, J. E., Jones, J. L., *Subcoercive Cyclic Electrical Loading of Lead Zirconate Titanate Ceramics II: Time-Resolved X-Ray Diffraction.* Journal of the American Ceramic Society, 2009. **92**(10): p. 2300-2310.

102. Jones, J.L., Pramanick, A., Nino, J. C., Motahari, S. M., Ustundag, E., Daymond, M. R., Oliver, E. C., *Time-resolved and orientation-dependent electric-field-induced strains in lead zirconate titanate ceramics.* Applied Physics Letters, 2007. **90**(17): p. 172909.

103. Subbarao, E.C., McQuarrie, M. C.,Buessem, W. R., *Domain effects in polycrystalline barium titanate.* Journal of Applied Physics, 1957. **28**(10): p. 1194-1200.

104. Pramanick, A., Damjanovic, D., Daniels, J. E., Nino, J. C., Jones, J. L., *Origins of Electro-Mechanical Coupling in Polycrystalline Ferroelectrics During Subcoercive Electrical Loading.* Journal of the American Ceramic Society, 2011. **94**(2): p. 293-309.

105. Jones, J.L., Slamovich, E. B., Bowman, K. J., *Domain texture distributions in tetragonal lead zirconate titanate by x-ray and neutron diffraction.* Journal of Applied Physics, 2005. **97**(3): p. 034113.

VITA

Raegan Johnson

Raegan Johnson was born in Minnesota on March 23, 1979. She earned her bachelor's degree in physics from Gustavus Adolphus College in 2001. Following graduating *cum laude*, she worked as a student intern for Honeywell in Minneapolis. After the year-long internship, she enrolled in a master's degree program at Iowa State. In 2005, she graduated with her M.S. degree in Electrical Engineering. After a short stint in Australia, she found herself in State College, PA searching for a job. Fortunately, Dr. Susan Trolier-McKinstry was in need of a research assistant for a one-year project. Knowing the traits of a phenomenal advisor, Raegan remained in the group, enrolling in the Ph.D. program in the summer of 2007.